Spin-Resolved Microscopy of Strongly Correlated Fermionic Many-Body States

Timon Alexander Hilker

München 2017

Spin-Resolved Microscopy of Strongly Correlated Fermionic Many-Body States

Timon Alexander Hilker

Dissertation
an der Fakultät für Physik
der Ludwig–Maximilians–Universität
München

vorgelegt von
TIMON ALEXANDER HILKER
aus Wuppertal

München, 23.10.2017

Erstgutachter: Prof. Dr. Immanuel Bloch
Zweitgutachter: Prof. Dr. Lode Pollet
Tag der mündlichen Prüfung: 27.11.2017

Zusammenfassung

Mit ultrakalte Gasen in optischen Gittern lassen sich stark wechselwirkende Quantenvielteilchensysteme auf der Ebene einzelner Spins untersuchen. Diese Doktorarbeit fasst den Aufbau und die ersten Ergebnisse eines Quantengasmikroskops mit fermionischen ^{6}Li Atomen zusammen. Wir konnten erstmals antiferromagnetische Spinkorrelationen in Hubbard-Systemen beobachten und in eindimensionalen Systeme die Trennung von Ladungs- und Spinfreiheitsgraden mit Korrelationen nachweisen, die im thermischen Gleichgewicht gemessen wurden.

Die Grundlage für diese Experimente ist das Quantengasmikroskop, welches während der Doktorarbeit geplant und aufgebaut wurde. Die Bilder, die man damit nehmen kann, sind Momentaufnahmen eines Quantenvielteilchensystems, auf denen man alle Atome einzeln auf ihren jeweiligen Gitterplätzen erkennen kann. Wir produzieren ein ultrakaltes Quantengas mit Standardverfahren wie Laserkühlung, optischen Fallen und Verdunstungskühlung und laden es in eine einzelne Ebene eines dreidimensionalen optischen Gitters. Vor dem Abbilden wird jedes Atom entsprechend seines Spin mit einem Stern-Gerlach-Magnetfeld um einen halben Gitterplatz nach links oder rechts verschoben. Zur Abbildung der Atome messen wir die Fluoreszenz eines Raman-Seitenbandkühlprozesses, welcher in einem zusätzlichen sehr tiefen optischen Gitter abläuft, und können so 97% der Atome erfolgreich detektieren. Ein Kapitel dieser Arbeit widmet sich den Details dieses Prozesses und kann die verbliebenen Verluste durch eine Nichtgleichgewichtsverteilung der lokalen Anregungen erklären.

Die Messung der Dichteverteilung der stark wechelwirkenden Atome im inhomogenen Gitter erlaubt es die Zustandsgleichung des Fermi-Hubbard-Models zu bestimmen. Dabei beobachten wir die starke Unterdrückung der Kompressibilität in der Mott-Isolator-Phase. Mit unseren hochaufgelösten Bildern können wir auch die Dichtekorrelationen des Systems messen und so das Fluktuations-Dissipations-Theorem bestätigen, welches die Kompressibilität in Beziehung zu der Summe aller Dichtefluktuationen setzt.

Für eine Entropie pro Teilchen von weniger als $\log(2)k_B$ zeigt der Mott-Isolator antiferromagnetische Spinkorrelationen aufgrund der Austauschwechselwirkung. In eindimensionalen Spinketten konnten wir diese magnetische Ordnung bis zu einer Distanz von vier Gitterplätzen direkt messen. Die Stärke der beobachteten Korrelationen stimmt sehr gut überein mit Quanten-Monte-Carlo-Rechnungen bei einer Temperatur von einem Achtel der Bandbreite, welches einer Entropie von $0.4k_B$ pro Atom entspricht. Für Spinketten mit weniger als einem Atom pro Gitterplatz sehen wir eine charakteristische Verschiebung der Spinkorrelationen zu größeren Wellenlängen, die der einer Luttinger Flüssigkeit entspricht.

Besonders interessante physikalische Phänomene treten auf, wenn man den Spinfreiheitsgrad mit der Bewegung der Atome koppelt. In eindimensionalen Systemen tritt hier die Spin-Ladungs-Trennung auf, die einem Loch eine freie Bewegung durch eine Spinkette ermöglicht. Allerdings scheint diese Delokalisierung zu einer Reduktionen der magnetischen Ordnung zu führen, da die Position der Teilchen nun fluktuiert. Normale Zweipunktkorrelatoren messen so kleinere Werte. Allerdings konnten wir zeigen, dass die Spins um einzelne Löcher herum primär antiparallel ausgerichtet sind und so nachweisen, dass die Spinordnung fast unabhängig vom Grad der Dotierung ist, wenn man die Lochposition mitberücksichtigt. Diese Messungen lassen sich als erster direkten Nachweis von Spin-Ladungs-Trennung durch Gleichgewichtskorrelationen interpretieren.

Diese Arbeit umfasst die ersten Messungen von Spin-Loch-Korrelationen mit ultrakalten Atomen und sie stellt damit einen wichtigen Schritt auf dem Weg zu Quantensimulationen dotierter Antiferromagneten dar, die einen Beitrag zum Verständnis von Hochtemperatursupraleitern leisten könnten.

Abstract

Ultracold fermionic atoms in optical lattices allows to simulate the behavior of electrons in strongly correlated materials. In this thesis, we demonstrate the preparation and site- and spin-resolved imaging of Hubbard systems with fermionic ^{6}Li atoms. We realize and measure strong antiferromagnetic spin correlations and study their amplitude for various temperatures, interactions and dopings. In one-dimensional systems we observe spin-charge separation signatures by measuring equilibrium correlations for spin and density.

The basis for these measurements is a quantum gas microscope for fermionic ^{6}Li atoms, which was built during this PhD thesis. It allows to take snapshots of the quantum many-body system with single-atom and single-site resolution. Using standard techniques of laser cooling, optical trapping, and evaporative cooling, ultracold Fermi gases are prepared and loaded into a single plane of a three-dimensional optical lattice of tunable geometry. The spin of each atom is converted to a spatial information via a local Stern-Gerlach splitting. The imaging is performed by collection of fluorescence light from Raman sideband cooling in an additional, deep optical lattice. A detailed analysis of this cooling process, which explains our imaging fidelity of 97% from the non-thermal distribution of excitations is presented.

A study of the density distribution of the strongly interacting atoms in the lattice allows to derive the equatioän of state of the Fermi-Hubbard model, which shows a strongly reduced compressibility in the Mott insulating regime. From the high-resolution images we can, in addition, extract all density correlations. This allows us to experimentally confirm the fluctuation-dissipation theorem linking the compressibility to the sum of all density fluctuations.

At entropies below $k_B \log(2)$ per particle, antiferromagnetic correlations arise from exchange interactions in a Mott insulator. We directly observe magnetic correlations up to four sites in one-dimensional spin chains. The measured antiferromagnetic spin correlations agree well with quantum Monte-Carlo calculations at temperatures of 1/8 of the band width, which corresponds to an entropy per particle of only 0.4 k_B. At fillings below one atom per site, we observe characteristic oscillations of the spin correlations vs density as predicted by Luttinger liquid theory.

Interesting physics arises when one couples the spin degree of freedom with the motion of the quantum particles. In one dimension, the phenomenon of spin-charge separation allows the holes to propagate through a spin chain without energy cost. Their motion, however, hides the magnetic order from local observables. Thanks to our simultaneous imaging of spins and holes, we can directly study the spin alignment around individual holes. We reveal spin correlations which are almost fully independent of the degree of hole doping with string spin-density correlation functions. These measurement are the first experimental observation of spin-charge separation in equilibrium correlation measurements.

This work demonstrates the experimental study of doped quantum magnetism with individual spin resolution and paves the way for quantum simulations of doped two-dimensional antiferromagnets relevant to high temperature superconductivity.

Contents

To my family and friends

"Erwin with his psi can do
Calculations quite a few.
But one thing has not been seen:
Just what does psi really mean?
– Felix Bloch & Erich Hückel

Chapter 1

Introduction

One of the great and most impactful frontiers of physics is the quantum many-particle problem. What happens when many quantum particles - like quarks, electrons or atoms - meet and strongly interact with each other? The problem spans systems from the large scales of nuclear matter in neutron stars via the electron transport in photosynthesis or unconventional superconductors to the tiny scales of gluons inside a proton.

Atomic gases at nano-Kelvin temperatures trapped with lasers in an ultra-high vacuum provide a platform to study such quantum many-body effects with unparalleled precision and control [1]. In the spirit of Richard Feynman's proposal [2], quantum simulations with ultracold atoms are an approach to understand a complicated quantum system by simulation of its behavior with a second, more controlled quantum system. Especially the physics of strongly correlated electrons associated with high-temperature superconductivity [3] still contains many open questions [4], which could be addressed with ultracold fermions in optical lattices.

Ultracold atoms

The origin of the research with ultracold atoms reaches back to the first proposal of laser cooling by Hänsch and Schawlow in 1975 [5], which was built upon an earlier idea by Ashkin [6]. Such cooling by light was achieved with trapped ions in 1978 [7, 8] (Nobel prize 1989 to Dehmelt and Paul) and the first deceleration of a beam of *neutral* atoms with a laser force was demonstrated by Phillips and Metcalf in 1982 [9]. With a magneto-optical trap neutral atoms can be stored [10] and cooled to temperatures below 1 mK (Nobel prize 1997 to Chu, Cohen-Tannoudji and Phillips). Even colder temperatures can be realized with additional evaporative cooling, a technique rewarded by the first Bose-Einstein condensates (BEC) in 1995 [11–13] (Nobel prize 2001 to Cornell, Ketterle and Wiemann). The low temperatures allow to gain full control of the state of individual quantum objects like ions or atoms in cavities (Nobel prize 2012 to Wineland and Haroche).

Since the first BEC, the field of ultracold atoms has seen an exceptional growth. The cooling of Fermionic atoms to quantum degeneracy, especially challenging due to their lack of thermalization, was achieved by the use of a spin-mixture [14] or a second atomic species via sympathetic cooling [15]. In a next step, the development of optical lattices [16] allowed the field of ultracold gases to enter the regime of strong correlations, prominently demonstrated in the superfluid to Mott insulator transition with bosons [17]. A second route to strong correlations is being realized since 1998 [18] through the use of Feshbach resonances, which allow to tune the interatomic interaction [19]. This enables the experimental simulation of some of the most relevant Hamiltonians of solid state theory in a clean and even time-resolved manner.

Quantum gas microscopes Ultracold quantum gases can be probed with a variety of measurement techniques. The most common approach is to image the cloud of atoms after a free expansion period with absorption or fluorescence imaging (time-of-flight imaging [1]). After

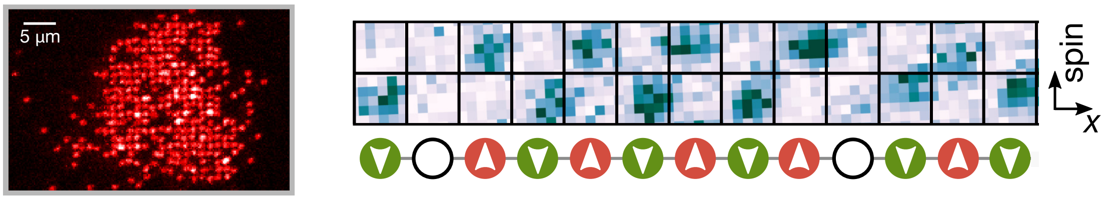

Figure 1.1. Images of individual atoms in a quantum many-body state. *Left: Image of ^{6}Li atoms in an optical lattice. Every red dot is one atom. Right: Zoom into a one-dimensional chain of atoms imaged with spin encoded in the vertical position showing antiferromagnetic order and holes.*

a long expansion without interactions, the spatial density distribution of the cloud mirrors the momentum distribution of the trapped atoms. Improved momentum mapping with shorter expansion times can be achieved by releasing the atoms into a large harmonic trap (momentum focusing [20, 21]). In-situ images i.e. images of atoms inside the trap, on the other hand, give direct access to the density distribution. They require higher optical resolution and some approach to deal with the high optical density, but allow to directly extract e.g. the equation-of-state of the system ([22–24] and many more).

All these techniques, however, return observables, which are averaged over some set of the microscopic quantum particles by the measurement itself. In contrast, *quantum gas microscopes*, as pioneered with bosonic Rubidium in 2009/10 [25, 26], can observe individual atoms on every site of an optical lattice via fluorescence imaging. With this technique it is not only possible to measure the average density distribution with highest resolution, but also to detect all orders of correlations. Individual thermal and quantum fluctuation have been observed [27] and tracked with time [28] in early experiments.

In particular, there is an great interest to simulate the behavior of electrons, which are fermions. Thus, when we started our work, it was a natural decision to build a machine that applies this advanced imaging technique to a fermionic atom, ^{6}Li in our case. Fermions are, however, much harder to cool to temperatures much below the Fermi temperature and the imaging of lithium is a special challenge due to the low atomic mass. Optical molasses cooling, as applied in the Rb experiments, does not exist for lithium and, in addition, the maximal relative lattice depths, which can be achieved with available laser power, are much lower. On the other hand, the low mass allows for a lattice with a larger lattice constant, which makes the optical resolution less demanding.

This thesis summarizes the technical realization of this microscope for Fermions and presents some of the first measurements with this novel machine. We solved the imaging challenge by Raman sideband cooling in an additional deep pinning lattice and could even realize a spin resolution with a local Stern-Gerlach separation. The observed images are snapshots of the quantum many-body state in real space with single-spin resolution on every lattice sites (Fig. 1.1).

The first single-atom resolved images of fermions were achieved in the spring 2015 by three groups [29–31], but the temperature of their atoms was too high to observe the fermionic nature of the atoms. We observed the first resolved atoms in the summer 2015 and our temperatures were low enough to image a degenerate Fermi gas that showed Pauli blocking [32].

Strongly correlated materials

Strongly correlated systems can be defined as many-body systems whose properties can not be mapped to non-interacting quasi particles [33]. In the early 1960s, the main motivation to study strong correlations in condensed matter physics came from experiments on transition metal oxides and the Mott metal-insulator transition [34]. The discovery of heavy fermion compounds [35, 36] and high-temperature cuprate superconductors [3] has revived the interest in the 1980s, which continues up to the present days. These materials show unusual electronic and magnetic properties, which are often of technological interest, but their theoretical understanding presents a considerable challenge already for decades. The theoretical progress in the field of strongly correlated systems has been slowed by the difficulties of applying approximations. Due to the non-perturbative nature of the problem, it is often hard to say whether a theoretical prediction is a real feature of the Hamiltonian studied or an artifact of the applied approximations. Direct numerical studies are slowed by the exponential growth of the computations with system size [37], while Quantum Monte Carlo calculations suffer from the *sign-problem* at low temperatures [38].

Nevertheless, there has been tremendous progress in the last 30 years to identify the d-wave nature of these high-T_c superconductors [39–42], to characterize the influence of resonating-valence bonds [4, 43] and charge waves [44, 45] in the anomalous pseudo-gap phase and to gain a general understanding of the relevant processes. Nevertheless, many open questions remain [46] especially about the pseudo-gap phase with several competing orders [47]. What is the order of its ground state? What is the role of topology? Which is the most simple model that captures all relevant effects? Or the related question of how much of the phase diagram can be described within the single-band Fermi-Hubbard model (FHM) [48]. Although the presence of a d-wave state in the FHM is supported strongly by numerical calculations [49] and models with minor additions [50], an unambiguous proof has been prevented by the complexity of calculations in the doped Hubbard model.

Doped antiferromagnets Microscopically, the complexity arises from the competition between the delocalization of the holes and the antiferromagnetic spin order. As one can see in figure 1.2, a moving hole in a Néel background produces a string of flipped spins. The associated linear increase of energy naively leads to a confinement of the holes. On self-retracing paths, a single hole can, however, undo the flipping of spins and move on so-called *background-*

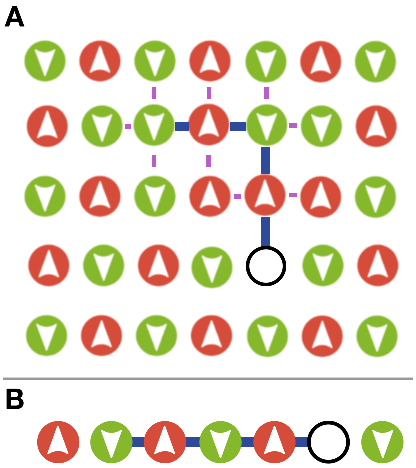

Figure 1.2. Hole propagation in AFM background. ***(A)*** *In two dimensions, the propagation of a hole along some path (blue line) produces a string of flipped spins with an associated energy cost. Broken bonds are indicated in purple.* ***(B)*** *In one dimension, a hole is free to propagate through an AFM spin chain without an energy cost.*

restoring paths. In addition, a hole can hop 1.5 times around a local plaquette, moving each of the three spins twice and thus propagate without changing its background and without energy cost. Due to the high order of this processes, the effective amplitude of this hopping process is, however, so low that it is irrelevant in most cases.

Also a second hole moving on the same path repairs the flipped spins. So two holes can freely propagate together, which leads to an effective attraction of the holes. This pairing is dominantly of $d_{x^2-y^2}$-nature[1] [51] and can be understood as a *paramagnon exchange*: In analogy to BCS-Pairing [52], where the electronic charge attracts surrounding ions, whose polarization attracts a second electron once the first electron moved away, a spin creates a local spin polarization which attracts or repels a second electron depending on its spin [51]. In addition to these pairing mechanisms, there can be bound states of more than two particles e.g. stripes of holes (Fig. 7.1) leading to charge-density waves [53]. These stripes can be seen as one-dimensional (1d) doped spin-chains and within the 1d structure the competition of antiferromagnetic spin order and hole delocalization is absent. This is due to the phenomenon of spin-charge separation in one-dimensional systems [54].

It becomes clear that already on the microscopic level many competing processes exist in doped antiferromagnets. The direct observation of these effects by experiments with single-spin resolution is one of the great goals with ultracold atoms in optical lattices.

Simulation of the Fermi-Hubbard model

The microscopic physics of antiferromagnetism and doping can be described within the Fermi-Hubbard model. This model has been central within the description of strongly correlated systems since its introduction in 1963 by Hubbard [55]. It covers the dynamics of particles in a lattice by just two terms: A hopping rate t and an on-site interaction U. Fermionic atoms in an optical lattice are very well described by the Fermi-Hubbard model and, thus, they are well suited to simulate the physics of this foundational model. An optical lattice is a defect-free potential for ultracold atoms and the ability to control the tunneling rate of atoms via the depth of the optical lattice and to control the interaction between the particles via a Feshbach resonance allows to tune the parameters t and U to almost arbitrary values, even dynamically during the experiment. This enables to study not only the static properties but also the dynamical evolution of a non-trivial many-body quantum system [56] and brings the experiments close to a realization of a *quantum simulator* [2]. Hence, ultracold atoms in optical lattices can give valuable insights to strongly correlated systems that can not be obtained on a classical computer nor in a condensed-matter experiment.

Quantum magnetism Despite its simple form, the Fermi-Hubbard model gives rise to rich physics, some of which has already been observed with ultracold gases. Most prominently the transition from a metal to a Mott insulator was demonstrated with fermionic atoms in 2008 [57, 58]. For even lower temperatures the system shows a phase transition to an antiferromagnetically (AFM) ordered state [59] in three dimensions and strong magnetic correlations in lower dimensions [60]. The realization of such quantum magnetism with ultracold atoms had been prevented for a long time by the temperature requirements, which are given by the small exchange energy $J = 4t^2/U$ and by a lack of a sensitive probes for spin correlations. To reach the antiferromagnetic *phase* with long range order in 3d, entropies per particle be-

---

[1] For $d_{x^2-y^2}$ pairing, the superconducting gap is zero at four line nodes located at the diagonals of the Brillouin zone.

low $k_B \log(2)/2 = 0.35 k_B$ are required [61], while AFM *correlations* beyond nearest neighbor appear below an entropy of $\log(2) k_B$ [60] in all dimensions. In addition, the detection of AFM order with methods that rely on global parameters like Bragg scattering [62] is difficult because the antiferromagnetic phase first occurs in a limited region in the center of the trap. Many proposals were developed with novel cooling mechanisms [63] to reach an AFM state, which include Pomeranchuk cooling [61], cooling by shaping the confinement [64], adiabatic splitting of a band insulator [65] and in-lattice evaporation [66].

With ultracold fermions, the first AFM spin correlations in the FHM were demonstrated by measuring singlets on neighboring sites [67] and by global Bragg spectroscopy [68] in 2012 and 2014 respectively.[1] Soon after the completion of the first fermionic quantum gas microscopes, longer-ranged spin correlations were observed by us [71] and three other groups [72–74] in 2016. This is the one of the central results of this thesis. Even stronger order, which extents through the full system, was achieved since then by shaping of the confining potential [75]. Also the analog charge order on the attractive side of the FHM was recently observed [76]. This tremendous progress within a short amount of time demonstrates how much a new detection technique (quantum gas microscope) can advance a long standing problem (cooling of lattice fermions). These novel cooling methods are summarized under the name *entropy management* because they rely on a redistribution of entropy within the atom cloud to produce certain regions with very low entropy and they will most likely lead to further progress in the near future.

Spin-hole correlations in one dimension One-dimensional systems are different from materials in higher dimensions. Even weakly interacting systems can not be described in terms of the bare particles, but the relevant degrees of freedom are always collective modes [54].

Most notably, one-dimensional systems show spin-charge separation. This does not only refer to a different velocity of spin and charge excitations, but also includes the structure of the ground state. Correlations of pure spin and charge variables factorize i.e. spin and charge degrees of freedom are independent.

Although the effect of spin-charge separation is well understood theoretically and represents a fundamental property of materials in one dimension, there is only limited experimental evidence based on spectroscopic [77–79] or transport measurements [80, 81] in condensed matter systems. In this thesis we present results which show a direct consequence of spin-charge separation: The independence of spin and charge sector in equilibrium correlation measurements [82].

This thesis

The main topic of this thesis is the analysis of antiferromagnetic spin correlations of ultracold fermions with single-site resolution in an optical lattice. To achieve this goal, we realized a quantum gas microscope with full density and spin resolution and cooled a gas of ^{6}Li atoms to deep quantum degeneracy. We implemented a large scale, three-dimensional optical superlattice, which allows to perform a local adiabatic Stern-Gerlach splitting for spin read-out. The single-atom resolved imaging is performed via the fluorescence of a Raman sideband cooling scheme in an additional deep pinning lattice.

---

[1] With bosons an AFM Ising quantum magnet was realized in a tilted lattice [69] and classical frustrated magnetism could be simulated on a triangular lattice [70].

We observed antiferromagnetic spin correlations in one-dimensional chains over at least four sites and found excellent agreement with the spin properties of the Fermi-Hubbard model as derived from quantum Monte Carlo calculations at entropies as low as 0.4 k_B per particle. In doped spin chains, we could show that the apparent reduction of spin correlations due to holes is rooted in the two-point spin correlation function and that, in fact, the spin order is almost unaffected by the presence of holes. Our results are a confirmation of spin-charge separation with equilibrium correlation measurements.

- Chapter 2 first summarizes the physics of ultracold fermions in optical lattices and their description by the Fermi-Hubbard model. In the second part, an overview of Luttinger liquid theory is given and its application to doped spin chains is reviewed.
- Chapter 3 gives a brief summary of the experimental setup, which is described in detail in earlier PhD theses.
- Chapter 4 describes a modeling of Raman sideband cooling, which we use to image and cool the atoms simultaneously. We derive the Raman couplings and analyze the relevant cooling and heating rates. To understand the residual losses of atoms, we employ a rate equation, which predicts a non-thermal occupation distribution of the local excitations with a long tail to large energies.
- In Chapter 5 we briefly summarize the algorithm to reconstruct the lattice occupation from the fluorescence images and present potential improvements.
- Chapter 6 is covers the density and spin analysis of one-dimensional Hubbard systems. We emphasize the possibility to sort the data by global properties and carefully study mean density, density variance and density correlations as a function of the chemical potential. This allows to confirm the fluctuation-dissipation theorem for compressibility and density fluctuations. In the second part, we present our results on antiferromagnetic spin correlations and show its application as a spin thermometer. For densities lower than one, we observe incommensurate spin correlations as predicted by the Luttinger liquid description.
- Chapter 7 covers our results of spin-charge correlations in doped spin chains. Making use of higher order correlation functions, we show that holes act as a domain wall of the parity of the antiferromagnetic order and, thus, reduce the spin correlations as measured by two-point functions. In analogy to the spin-1 Haldane chain, a non-local string correlations analysis, however, shows that the relative spins alignment remains unchanged even at strong doping. This is a direct consequence of spin-charge separation, which allows to describe the spin sector by a Heisenberg model regardless of the amount of doping.

The work in this thesis has been carried out with Ahmed Omran, Martin Boll, Guillaume Salomon, Immanuel Bloch and Christian Gross.

Publications

The main results of my PhD work have been published in these papers:

- *'Microscopic observation of Pauli blocking in degenerate fermionic lattice gases'*.
  A. Omran, M. Boll, T. A. Hilker, K. Kleinlein, G. Salomon, I. Bloch, and C. Gross. Physical Review Letters **115**, 263001 (2015).

- *'Spin- and density-resolved microscopy of antiferromagnetic correlations in Fermi-Hubbard chains'*.
  M. Boll*, T. A. Hilker*, G. Salomon*, A. Omran, J. Nespolo, L. Pollet, I. Bloch, and C. Gross. Science **353**, 1257 (2016).
  * *Equal contributions*

- *'Revealing hidden antiferromagnetic correlations in doped Hubbard chains via string correlators'*.
  T. A. Hilker, G. Salomon, F. Grusdt, A. Omran, M. Boll, E. Demler, I. Bloch, and C. Gross. Science **357**, 484 (2017).

Chapter 2

The Hubbard Model with Ultracold Fermions - Theory

This chapter summarizes some of the relevant theory for the simulation of the Fermi-Hubbard model with ultracold atoms in optical lattices. The first section introduces the basic atom-light interactions and sketches the properties of an optical lattice (Sect. 2.1). Then the main phases of the Fermi-Hubbard model are discussed and we show spin correlations from quantum Monte Carlo calculations for different interactions, temperatures and entropies, which are later compared to experimental measurements (Sect. 2.2). Finally we present the most relevant aspects of Luttinger liquid theory and spin-charge separation (Sect. 2.3).

2.1 Fermions in optical lattices

A neutral alkaline atom can be described as a positively charged core and a single bound electron. The interaction of these atoms with the oscillating electric field of laser light is the most important tool for the creation, manipulation and detection of ultracold atoms [83]. There are two parts to this interaction: A recoil force due to the absorption or emission of a photon and a dispersive interaction. The relative strength of the two forces depends on the detuning $\Delta = \omega_{\mathrm{Las}} - \omega_{\mathrm{Atom}}$ of the laser frequency ω_{Las} to the relevant transition frequency of the atom ω_{Atom}. In general, the absorptive interaction due to scattering of photons is used to cool the atoms and to take images, while the dispersive interaction allows to build optical traps and lattices. This section deals with the dispersive interactions for the simplified case of a two-level atom.

Dipole potential The dispersive interaction with far detuned light can be modeled by a virtual excitation of the atom. The resulting dipole potential for a light intensity $I(\mathbf{r})$ is given by [84]

$$V_{\mathrm{dip}}(\mathbf{r}) = \frac{3\pi c^2 \Gamma}{2\omega_{\mathrm{Atom}}^3} \left(\frac{1}{\Delta} - \frac{1}{\omega_{\mathrm{Las}} + \omega_{\mathrm{Atom}}} \right) I(\mathbf{r}), \tag{2.1.1}$$

where c is the speed of light, Γ is the scattering rate of the excited state and the last term is the counter-rotating correction, which is relevant for detunings on the order of the transition frequency. In the expression, the fine-structure splitting has been ignored[1]. The dipole potential is directly proportional to the intensity of light and an attractive potential for the atom can be realized with a red detuned laser beam ($\Delta < 0$).

---

[1] A more detailed treatment of light shifts can be found in chapter 4.

2.1.1 Optical lattices

Interference of laser beams lead to a periodic intensity modulation, which is the basis of an optical lattice. For an attractive three-dimensional optical lattice constructed from three independent pairs of beams with the lattice constants d_x, d_y, d_z and lattice depths $V_{0,x}$, $V_{0,y}$, $V_{0,z}$, the potential is

$$V(\mathbf{r}) = -V_{0,x}\cos^2(\pi x/d_x) - V_{0,y}\cos^2(\pi y/d_y) - V_{0,z}\cos^2(\pi z/d_z). \tag{2.1.2}$$

The lattice depths is best expressed in terms of the lattice recoil energies E_r^{Lat}

$$E_r^{\mathrm{Lat},i} = h^2/(8md_i^2) \tag{2.1.3}$$

along axis $i = x, y, z$.

The quantum mechanical eigenstates of such a potential for non-interacting particles can be found from the single-particle Hamiltonian

$$\hat{H} = -\frac{\hbar^2}{2m}\nabla^2 + V(\mathbf{r}). \tag{2.1.4}$$

For a square lattice, the potential separates into the three axis, which can be treated independently. A band calculation for the x-axis via Bloch's theorem [85] gives delocalized eigenstates, that can be written as the product of plane waves with quasi momentum q and a periodic function $u_{n,q}(x)$

$$\Psi_{n_x,q_x}(x) = e^{iq_x x}u_{n_x,q_x}(x), \tag{2.1.5}$$

where n denotes the band index. The Mathieu equation allows for an explicit solution of the Bloch equation for a square lattice [86]. The resulting energy bands increase in widths with index n, while the band gaps decrease.

Wannier states The Bloch states can be combined into Wannier states, which are maximally localized at the different lattice sites $\mathbf{r}_j$ and orthogonal to each other:

$$w_{n,j}(\mathbf{r}) = \frac{1}{\sqrt{N}}\sum_q e^{-i\mathbf{q}\cdot\mathbf{r}_j}u_{n,\mathbf{q}}(\mathbf{r}) \tag{2.1.6}$$

Lowest band At temperatures and chemical potentials which are small relative to the first band-gap, only the lowest band is occupied. For lattice depths $V_0 \gtrsim 5E_r^{\mathrm{Lat}}$, the tight-binding approximation can be applied, which results in a simplified Hamiltonian for the lowest band

$$\hat{H}_{\mathrm{t.b.}} = -\sum_{\langle i,j\rangle} t_{i,j}\left(\hat{a}_i^\dagger\hat{a}_j + \hat{a}_j^\dagger\hat{a}_i\right). \tag{2.1.7}$$

Here the indices $\langle i,j\rangle$ run over all neighboring sites, the fermionic operator $\hat{a}_i^\dagger$ creates a particle in the Wannier state $w_i = w_{0,i}$ and the tunneling parameter $t_{i,j}$ is given by

$$t_{i,j} = \int d\mathbf{r}^3 w_i^*(\mathbf{r})\hat{H}w_j(\mathbf{r}) \tag{2.1.8}$$

with $\hat{H}$ from equation 2.1.4. For a homogeneous system the hopping strength t only depends on the direction of $\mathbf{r}_i - \mathbf{r}_j$ i.e. the system is characterized by t_x, t_y, and t_z.

The energy of an eigenstate with quasi-momentum $\mathbf{q} = (q_x, q_y, q_z)$ is given by

$$E(\mathbf{q}) = -2t_x \cos(q_x d_x) - 2t_y \cos(q_y d_y) - 2t_z \cos(q_z d_z) \tag{2.1.9}$$

The dispersion relation, thus, has the shape of a cosine along each axis, the bandwidth is given by $W = 2(t_x + t_y + t_z)$ and the maximal group velocity is $v_g = 2t_i d_i/\hbar$ along axis i[1]. This description includes the cases of reduced dimensionality because for very strong lattice depths along some directions the associated tunneling parameters vanish.

Energy levels for deep lattices For very deep lattices, the tunneling is effectively zero for all deeply bound states. The local energy levels E_n in one axis are given by (c.f. [87])

$$E_n = \hbar\omega_0 \left(n + \frac{1}{2}\right) - \left(\frac{1}{2}(n^2 - n) - \frac{1}{8}\right) E_r^{\mathrm{Lat}}, \quad \hbar\omega_0 = \left(2\sqrt{\frac{V_0}{E_r^{\mathrm{Lat}}}} - \frac{13}{12}\right) E_r^{\mathrm{Lat}}, \tag{2.1.10}$$

for a lattice depth V_0 if this axis. The second term contains the correction due to anharmonicities and ω_0 has been defined as the lowest energy difference $E_1 - E_0$. This leads to a level splitting between consecutive energy levels n and $n+1$, which decreases with increasing n by one E_r^{Lat} per level due to the anharmonicity of the cosine potential:

$$E_{n+1} - E_n = \hbar\omega_0 - nE_r^{\mathrm{Lat}} \tag{2.1.11}$$

Note that the term due to the anharmonicity is independent of the lattice depths. These results become important for Raman sideband cooling (Chapter 4), where one couples different energy levels resonantly.

2.1.2 Interactions of ultracold atoms

The interaction of cold atoms are described by low energy quantum mechanical scattering theory [88]. The ultracold regime, in consequence, is defined as the temperature range, where only s-wave scattering is relevant. In this case, the strength of the interaction is given by the s-wave scattering length a_s and interactions can be described via an on-site potential[2]

$$V_{\mathrm{int}}(\mathbf{r}_1, \mathbf{r}_2) = g\delta(\mathbf{r}_1 - \mathbf{r}_2) = \frac{4\pi\hbar^2 a_s}{m}\delta(\mathbf{r}_1 - \mathbf{r}_2) \tag{2.1.12}$$

Due to the antisymmetry of the wavefunction, identical fermions can not scatter via s-wave scattering. Thus, a spin-polarized cloud of ultracold fermionic atoms is always non-interacting.

The interaction between atoms in different spin states can be tuned via Feshbach resonances by applying a magnetic field [19]. Lithium-6 has a very broad Feshbach resonance (see Fig. 3.4), which makes it experimentally easy to adjust the scattering length to any required value.

---

[1] Thus, the wavefront of an initially localized particle in a lattice with $t = (2\pi\hbar) \cdot 1\,\mathrm{kHz}$ moves by about 12 sites per millisecond.

[2] If the potential acts on a function which is not regular at $r = 0$, the expression $g\delta(\mathbf{r})\frac{\partial}{\partial r}(r\ldots)$ should be used.

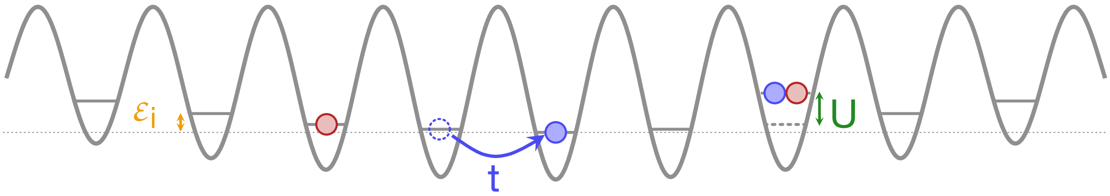

Figure 2.1. Bare processes of the Fermi-Hubbard model. *Spin-1/2 fermionic particles in a lattice can tunnel from site to site with a rate t. Two atoms at the same site have an interaction energy U and there is a global confinement with local energy shifts ε_i. Image adapted from [89].*

In an optical lattice, equation (2.1.12) leads within the tight-binding description of the lowest band to a local interaction term

$$\hat{H}_{\text{int}} = U \sum_i \hat{n}_{i,\uparrow} \hat{n}_{i,\downarrow} \tag{2.1.13}$$

with the density $\hat{n}_{i,\nu} = \hat{a}^\dagger_{i,\nu} \hat{a}_{i,\nu}$ for spin ν. The interaction strength U can be related to the scattering length a_s via [1]

$$U = \frac{4\pi\hbar^2 a_s}{m} \int d\mathbf{r}^3 \, |w(\mathbf{r})|^4 \tag{2.1.14}$$

with the Wannier function $w(\mathbf{r})$ (Eq. 2.1.6).

2.2 Fermi-Hubbard model

The (Fermi)-Hubbard Model (FHM) has been introduction in 1963 by Hubbard [55] and it has been central for the description of strongly correlated fermionic systems.

Its Hamiltonian is the sum of the tight-binding lattice Hamiltonian (Eq. 2.1.7) with an on-site interaction term (Eq. 2.1.13) for spin-1/2 fermions

$$\hat{H} = -t \sum_{\langle i,j \rangle, \nu} (\hat{a}^\dagger_{i,\nu} \hat{a}_{j,\nu} + \text{h.c.}) + U \sum_i \hat{n}_{i,\uparrow} \hat{n}_{i,\downarrow} + \sum_{i,\nu} \varepsilon_i \hat{n}_{i,\nu} \, . \tag{2.2.1}$$

Here the density operator $\hat{n}_i = \hat{n}_{i,\uparrow} + \hat{n}_{i,\downarrow}$ measures the occupancy at site i. The last term allows to describe an additional (confining) potential with local energy shifts ε_i, which are present for ultracold atoms due to the finite waist of the lattice laser beams. This potential is a central aspect of the experimental system and it represents the largest deviation from the ideal, homogeneous Hubbard model.

The three terms of equation 2.2.1 are the three competing processes that govern the physics explored in this thesis

- The hopping term (t) describes the tunneling of atoms from one lattice site to a neighboring lattice site. It is the kinetic energy of the system and tries to delocalize particles over the system.
- The interaction term (U) is the energy cost (gain) if two atoms which occupy the same lattice site. It tends to localize the particles.

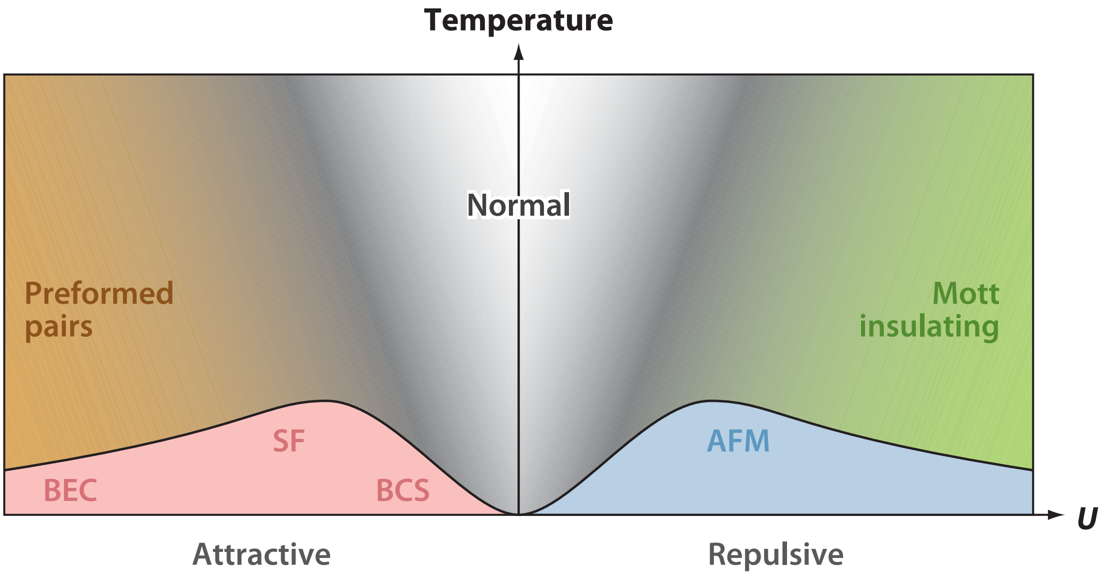

Figure 2.2. Phase diagram of the Fermi-Hubbard model at half filling. *At the special point of half filling and zero polarization the Fermi-Hubbard model shows a symmetry between the attractive and repulsive side. This thesis deals with the crossover from a metal (Normal) to a Mott insulator at repulsive interactions and with the antiferromagnetic (AFM) correlations at low temperatures. On the attractive side particles form bound pairs for strong attraction and a superfluid (SF) emerges for low temperatures. At small attractive interaction there are weakly bound pairs of BCS type, while the strongly bound pairs at large negative U can be seen as bosons, which form a Bose-Einstein condensate (BEC). The phase diagram is for three spatial dimensions, but if one interprets the phase as dominant correlations, it also describes lower-dimensional systems. Figure adjusted from [90].*

- The confinement (ε_i) is a large scale potential, which makes the system inhomogeneous and exerts a force towards the center of the trap. The relative change between neighboring sites is typically the smallest energy scale of the system, which allows to ignore it in a local analysis. This leads to the presence of several phases in different regions of the trap.

In certain regimes i.e. where one term dominates, the FHM can be approximated by simpler models. For strong repulsions the FHM for example maps to the Heisenberg model (or the t-J model if there is doping), which is covered in section 2.2.2.

In principle, the Fermi-Hubbard Hamiltonian can be applied to any lattice geometry, but we restrict the discussion to the case of simple square lattices in one, two or three dimensions (1d, 2d, 3d).

2.2.1 Phases at half filling

The Fermi-Hubbard model shows a rich set of phases with many competing orders. For the analysis in this section we ignore the local potential ε. The full phase diagram has four dimensions in this case, e.g. the temperature[1] T/t, the interaction U/t, the mean density n and the spin polarization (magnetization) M. In addition, the model can be analyzed in different

---

[1] In this thesis, we express temperatures in units of energy i.e. $k_B = 1$.

spatial dimensions. At the special symmetry point of half filling per spin ($n = 1$) and zero polarization ($M = 0$), the phase diagram is well understood (see Fig. 2.2).

Repulsive interactions At very high temperatures relative to U/t, the system is a metal. In two or more spatial dimension this is a Fermi liquid [91], while in one dimension Luttinger liquid theory applies (see Appendix A). The particles are mobile and there are strong density and spin fluctuations.

At lower temperatures or stronger repulsions $(T/U \ll 1)$, the interactions start to dominate and there is a crossover into a Mott insulator, where the occupation of a lattice site with two atoms is suppressed. The Mott-insulating phase behaves in many ways like a band insulator and it is incompressible. However, the spin of the atom is still a fluctuating degree of freedom, thus, the Mott insulator can carry a spin entropy of up to $\log(2)$ per site.

At even lower temperatures, the spins of the localized particles start to order. A second order exchange process, where two opposite spins on neighboring sites flip via a an intermediate doubly occupied state, has an energy of $J = 4t^2/U$. It leads to an antiferromagnetic coupling, which drives the system into a Heisenberg antiferromagnet at the Néel temperature T_N (Sect. 2.2.2). This temperature depends on interaction strength and dimensionality.

- In three dimension, there is a phase transition at a finite $T_N > 0$, which peaks at $U = 8t$ with $T_N = 0.3t$ [59]. The corresponding entropy per particle at this transition point is approximately $\log(2)/2$ [61], thus, half the maximal entropy of the Heisenberg model.

- In two dimensions, the Mermin-Wagner theorem [92] does not allow for a transition into an ordered state at $T > 0$. Long-ranged stagged spin order in an infinite system is only reached for $T = 0$, but the spin-spin correlation length ξ grows with decreasing temperature. A finite size system, thus, is fully ordered already at a finite temperature once ξ exceeds the size of the system.

- In one dimension, there can be no long range spin order for a SU(2) symmetric system. Instead, the Fermi-Hubbard model shows algebraic order at $T = 0$ and exponentially decaying spin-spin correlations for finite temperature (for details see Sects. 2.3.2 and A.3).

Attractive interactions For $U < 0$ opposite spins attract each other and the phases of the FHM show very different properties. However, the Lieb-Mathis transformation [93]

$$\hat{a}_{i,\uparrow} \to (-1)^{i_x+i_y+i_z}\hat{a}^\dagger_{i,\uparrow}, \quad \hat{a}_{i,\downarrow} \to \hat{a}_{i,\downarrow} \tag{2.2.2}$$

maps the states with attractive interaction ($U < 0$) onto states from the repulsive model ($U > 0$) for any bipartite lattice. It is a partial particle-hole transformation with an addition phase shift on one sublattice. A detailed discussion in appendix A.2 shows, that this transformation corresponds to a mapping of the spin sector onto the density sector and vice versa. There is, thus, a direct correspondence between the phases, their order parameter and even the excitation spectrum for repulsive and attractive interactions: The Mott insulator maps onto bound pairs of atoms. The antiferromagnetic spin order in z-direction corresponds to an ordering of these doublons in a checkerboard pattern, while the x and y spin order maps onto the complex superfluid order order parameter Δ. At weak attraction, the system show BCS (Bardeen-Cooper-

Schrieffer) superfluidity with Cooper pairs [52], while there are superfluid tightly bound pairs for strong attraction[1].

Away from half filling or zero imbalance, the transformation maps a finite doping onto a spin imbalance and vice versa. In the experiment, this can be used to relate measurements to phases, which are otherwise inaccessible [93].

2.2.2 t-J model

In the limit $t/U \gg 1$, the Fermi-Hubbard model maps onto the $t-J^*$ model with antiferromagnetic spin couplings [96]:

$$H_{t-J} = \hat{\mathscr{P}}_s \left[-t \sum_{i,j,\nu} \hat{a}^{\dagger}_{i,\nu} \hat{a}_{j,\nu} + J \sum \left(\hat{\vec{S}}_i \cdot \hat{\vec{S}}_j - \frac{\hat{n}_i \hat{n}_j}{4} \right) + H_{\text{NNN}} \right] \hat{\mathscr{P}}_s, \tag{2.2.3}$$

The spin operators are defined as $\hat{\vec{S}}_j = \frac{1}{2}\sum_{\nu,\nu'} \hat{a}^{\dagger}_{j,\nu} \vec{\sigma}_{\nu,\nu'} \hat{a}_{j,\nu'}$ with $\vec{\sigma}$ denotes a vector of Pauli matrices. Note that the Hamiltonian in Eq. (2.2.3) must be projected onto the subspace of single-occupied sites, which is ensured by the projection operators $\hat{\mathscr{P}}_s$.

The first term in Eq. (2.2.3) describes hopping processes of a fermion to an unoccupied neighboring site. The second term in Eq. (2.2.3) corresponds to the usual spin-exchange interaction between two fermions on neighboring sites. Its energy scale is set by $J = 4t^2/U$ because it derives from a second order tunneling processes where a state with two fermions on the same site is virtually occupied. The exchange interaction between two neighboring spins leads to a zero-point energy of $J/4$, which manifests itself by the nearest-neighbor density-density interaction $J\hat{n}_i\hat{n}_j/4$ in Eq. (2.2.3). The last term $\hat{\mathscr{H}}_{\text{NNN}}$ describes hole-assisted next-nearest-neighbor hopping events, which are discussed in section 7.5.2. In the ordinary t-J model these processes are often ignored, but they can be relevant as shown in our measurements of chapter 7.

Heisenberg model For half filling ($n_\uparrow = n_\downarrow = 1/2$), every site is occupied, there is no hopping and equation 2.2.3 becomes the SU(2) Heisenberg Hamiltonian

$$H_{\text{Heis.}} = J \sum_{\langle ij \rangle} \hat{\vec{S}}_i \cdot \hat{\vec{S}}_j = J \sum_{\langle ij \rangle} \hat{S}^z_i \hat{S}^z_j + \frac{1}{2} \left(\hat{S}^+_i \hat{S}^-_j + \hat{S}^-_i \hat{S}^+_j \right) \tag{2.2.4}$$

In the second expression the raising (lowering) operator have been introduced $\hat{S}^{\pm} = \hat{S}^x \pm i\hat{S}^y$, which create coherent spin exchanges.

In one dimension, the Heisenberg model correctly describes the spin degree of freedom even away from half filling for strong U. This is due to the effect of spin-charge separation [54] and we investigated these connections in detail in our experiments on doped spin chains (see Chap. 7).

---

[1] If one ramps the interaction of ultracold atoms through a Feshbach resonance coming from the attractive site, these pairs become real bound molecules [94] on the repulsive site which form a BEC (BEC-BCS crossover [95]). This transition is not included in the FHM and the molecular BEC is very different from the repulsive side of the FHM discussed above. Expressed diffidently, there are always lower lying molecular state *below* the repulsive side of the FHM. This can lead to spontaneous creation of molecules for strong repulsive interactions, which occur as losses.

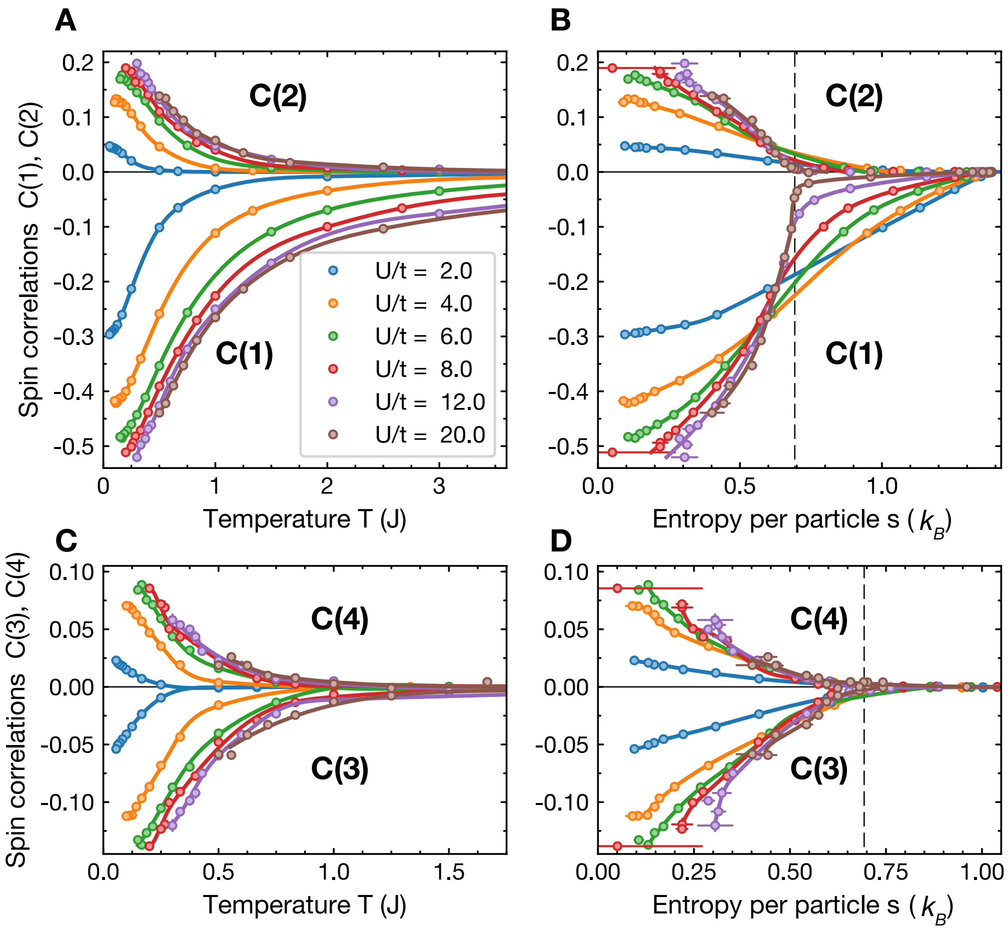

Figure 2.3. Spin correlation for 1d Fermi-Hubbard chains. *The spin-spin correlations $C(d)$ for different temperature, entropies and interactions from QMC calculations (by J. Nespolo). The spin correlations plotted vs temperature in units of the exchange coupling $J = 4t^2/U$ **(A,C)** and vs the entropy per particle s **(B,D)** approach the Heisenberg results for $U/t \to \infty$. The color lines are guides based on spline interpolations and the vertical dashed lines indicate the maximal entropy of the Heisenberg model, $s = k_B \log(2)$.*

2.2.3 Spin correlations

One of the main observable to characterize the spin order of a system is the spin-spin correlation function

$$C(\mathbf{d}) = 4\left(\left\langle S^z_{\mathbf{i}} S^z_{\mathbf{i+d}}\right\rangle - \left\langle S^z_{\mathbf{i}}\right\rangle \left\langle S^z_{\mathbf{i+d}}\right\rangle\right), \tag{2.2.5}$$

which measures the spin orientation on a site **i+d** relative to the spin on site **i**. The unconnected second part ensures that the correlator is zero if there are no correlations between the spins. For the spin balanced case this part vanishes. The prefactor, four, normalizes the correlations such that a perfect (anti-) ferromagnet has correlations 1 (-1).

Antiferromagnetic correlations as in the Hubbard model are characterized by a staggered spin correlator $C(d)$ i.e. the sign of the correlator switches when d is changed by one site. Figure 2.3 shows the spin correlations for the Fermi-Hubbard model for distance $d = 1$ to 4 for one-dimensional chains from quantum Monte Carlo (QMC) calculations[1]. All correlations except $d = 1$ are almost zero for $T > J$ or an entropy per particle greater than $k_B \log(2)$. But for lower temperatures spin correlations quickly build up. The maximal nearest-neighbor correlations ($d = 1$) for $T = 0$ in the Heisenberg limit are $C(1) = -0.6$, which is much smaller than in a Néel state due to quantum spin fluctuations. For weaker interactions U/t, the spin correlations decrease due to charge fluctuations. This trend is inverted at constant entropy for nearest-neighbor interactions with entropies above $\log(2)$. Here it is the less favorable to store entropy in spin fluctuations the higher t^2/U is. Thus more entropy goes into energetically less costly charge excitations and the spin correlations grow with t/U.

Due to the strong temperature dependence of $C(d)$ for $T < 2J$, measured spin correlations provide a good thermometer for the system by comparison to theoretical values (see Sect. 6.4.2).

2.3 Luttinger liquid theory

One-dimensional interacting systems show very different properties compared to systems of higher dimensions. While most many-body systems in two or more dimensions are described by Fermi liquid theory [91] with quasi-particle excitations that can be adiabatically connected to free Fermions, most one-dimensional systems can be treated by a harmonic-fluid approach [97–99]. Its basic excitations are collective waves with a simple linear dispersion. In contrast to higher dimensions these excitations are bosonic and show negligible overlap with the microscopic fermions. Such systems have been termed *Luttinger liquids* [100, 101] and its main properties are summarized in appendix A, while an extensive coverage of this theory can be found in the book by T. Giamarchi [54].

The special properties of one-dimensional systems arise from the fact that identical fermions in one dimension can not pass trough one another, but they merely push each other. So no particle can move without moving all the others leading to the aforementioned collective excitations. In momentum space, this can be understood by a linearization of the dispersion relation around each of the two Fermi points: Each excitation $k \to k+q$ has an energy $E = u\hbar q$, which is independent of the initial momentum $\hbar k$ and only depends on the group velocity[2] u. As all excitations with fix q have the same energy, any interaction couples them and the eigenmodes are excitations with momenta q, which are collectively shared by all particles close to one Fermi point.

2.3.1 Spin-charge separation

This special structure even holds for fermions with spin, leading to two types of collective excitations: a density wave, called charge wave for electrons, and a spin wave. The effective Hamiltonian of the low-lying excitations of an interacting one-dimensional system can very generally be written as

$$H_{LL} = \sum_q u_\sigma \hbar \, |q| \, \hat{b}^\dagger_{\sigma,q} \hat{b}_{\sigma,q} + u_\rho \hbar \, |q| \, \hat{b}^\dagger_{\rho,q} \hat{b}_{\rho,q}, \tag{2.3.1}$$

---

[1] The QMC calculations have been done by J. Nespolo from L. Pollet's group [71].

[2] For non-interacting particles $u = v_F = \left.\frac{\partial E(p)}{\partial p}\right|_{p=p_F}$ is the group velocity at the Fermi point. For interacting particles u depends on the interactions, but the simple form $E = u\hbar q$ remains.

where the $\hat{b}^\dagger_{\rho,q}$ ($\hat{b}^\dagger_{\sigma,q}$) are *bosonic* operators, which create charge (spin) waves with wavevectors q and velocity u_ρ (u_σ). Thus, there is a separation into independent charge and spin sectors already on the level of the (effective) Hamiltonian and the charge excitations (holons) and spin excitations (spinons) travel with different velocities.

Accuracy of spin-charge separation Spin-charge separation in 1d systems is based on the validity of the Luttinger Hamiltonian (2.3.1). For the Tomonaga-Luttinger model with a linear dispersion [97, 98], the Hamiltonian is exact. For typical dispersion with a band curvature, a linearization around the two Fermi points provides a valid effective description in terms of the Luttinger liquid theory. The band curvature is only an irrelevant correction for the leading long-wavelength physics [101], but it nevertheless changes the behavior on sub-leading time and length scales. This leads to a finite dispersion of the sound modes, a finite lifetime of the excitations and the breakdown of spin-charge separation [102]. The relevance of this correction, thus, depends on the length and time scales probed relative to the effects of the band curvature.

As long as all physical processes only affect states for which the linearization is valid, Luttinger liquid applies, the sound modes are undamped, and spin and charge separate. For the FHM, this applies to the limit of low interactions, where the energy U is much smaller than E_F or the band width W. But it also applies to the $U \to \infty$ limit [103] because, when U is larger than the bandwidth $4t$, the low temperature system can be described by a (partially) occupied ground band and an empty Mott band. The relevant interactions in this case are the spin-exchange processes (virtual excitations to the Mott band) with an energy scale $J = 4t^2/U$. So in this sense the interactions are again weak relative to the band width $4t$ and one can expect spin-charge separation. That this reasoning is correct can be shown by the exact factorization of the many-body wavefunction in the limit of $U \to \infty$ [104]:

$$\Psi\left(\{x_{j,\nu}\}\right) = \Psi_\rho\left(\{x_j\}\right)\Psi_\sigma\left(\{\tilde{x}_{j,\nu}\}\right) \tag{2.3.2}$$

The full wavefunction $\Psi\left(\{x_{j,\nu}\}\right)$ of all fermions with spin ν is a product of a wavefunction Ψ_ρ, which only depends on the position of the particles independent of their spin, and a spin wavefunction Ψ_σ in *squeezed space* [104–107], i.e. whose configuration space are the spins on the occupied sites $\tilde{x}$ only (see Sect. 7.5 for details).

For strong but finite interactions U, this description remains approximately valid leading to spin-charge separation not only for the excitations, but also for the structure of all low energy states including the ground state. Only in an intermediate U/t regime, the corrections from band curvature can become strong e.g. visible in a binding of spin and charge excitations.

2.3.2 Correlation functions

The description in terms of bosons, introduced above, allows to explicitly calculate correlation functions of spin and charge, which are the main observables of our measurements. At zero temperature, Luttinger liquids show correlations which decay algebraically. The most important ones in the repulsive FHM are the density-density correlations, which describe the tendency of the system to form a charge density wave, and the spin-spin correlations towards an antiferromagnet. In leading order, one obtains at a temperature T and mean density n (see Appx. A.3)

$$\begin{aligned} R(x) &= \langle \hat{n}_0 \hat{n}_x \rangle - \langle \hat{n}_0 \rangle \langle \hat{n}_x \rangle \\ &= -\frac{K_\rho}{(\pi x_\rho \sinh(x/x_\rho)^2} + A_2 \frac{\cos(\pi n x)}{\left(x_\rho \sinh(x/x_\rho)\right)^{K_\rho} \left(x_\sigma \sinh(x/x_\sigma)\right)^{K_\sigma}} \end{aligned} \tag{2.3.3}$$

$$\begin{aligned} C(x) &= 4 \left(\langle \hat{S}^z_0 \hat{S}^z_x \rangle - \langle \hat{S}^z_0 \rangle \langle \hat{S}^z_x \rangle \right) \\ &= -\frac{K_\sigma}{(\pi x_\sigma \sinh(x/x_\sigma)^2} + A'_2 \frac{\cos(\pi n x)}{\left(x_\rho \sinh(x/x_\rho)\right)^{K_\rho} \left(x_\sigma \sinh(x/x_\sigma)\right)^{K_\sigma}} \end{aligned} \tag{2.3.4}$$

where A_2, A'_2 are proportionality constants that depend on the microscopic physics of the system and $x_\chi = u_\chi/(\pi T)$ $(\chi = \rho, \sigma)$ are characteristic thermal length scales of the charge and spin sector. At distances $x > x_\chi$ the correlations decay exponentially due to thermal excitation with . At shorter distances, however, the decay is algebraically because excitations with high energy are not thermally activated and long wavelength excitations do not affect short distances. The Luttinger parameters are ($K_\sigma = 1$, $K_\rho = 0$) in the Mott insulator and ($K_\sigma = 1$, $K_\rho \approx 0.5$) for doped, strongly repulsive systems [103]. Thus the first term decays faster then the cos-term and we get the high temperature result for $x \gg x_\rho, x_\sigma$:

$$R(x) \sim C(x) \sim \cos(\pi n x)\, e^{-x/\xi} \quad \text{with:} \quad \xi^{-1} = \left(\frac{u_\rho}{\pi K_\rho T} \right)^{-1} + \left(\frac{u_\sigma}{\pi K_\sigma T} \right)^{-1} \tag{2.3.5}$$

Although spin and density correlations show the same functional form, the amplitude of spin correlations is much stronger i.e. $A_2 \ll A'_2$ (see .

Finite doping The periodicity of the oscillations in equation 2.3.4 is $2\pi/(2k_F) = 2/n$. This gives the staggered AFM correlations at $n = 1$. At finite hole doping the wavelength of the spin and charge oscillations, thus, increases due to the dilution of the chain with holes. In addition, the amplitude of the oscillations decays faster compared to the Mott phase because $K_\rho \geq 0.5 > 0$. This can be attributed to the following processes: While the holes move through a spin chain, they shift the positions of the spins. This does not change the sequence of spins, but adds uncertainty to their position on the lattice. The two-point correlator (Eq. 2.3.4) can not distinguish this effect from a true reduction of spin correlations i.e. the relative alignment of spins irrespectively of the position of holes. To describe these bare spin correlations, one needs to turn to an analysis in *squeezed space*: All unoccupied *sites* are removed, the particles are squeezed into a spin chain and then, correlations are evaluated. This can be achieved either directly or with a string-correlation function [107]. We applied both approached successfully to our measurement data and could show that the true spin correlations are (almost) independent of doping (see chapter 7).

Chapter 3

Experimental Setup

In this chapter, the setup of the experiment is briefly described. After an overview (Sect. 3.1), some of the important properties of lithium are presented (Sect. 3.2). Then, we summarize the steps to produce a degenerate quantum gas in a single layer of an optical lattice (Sect. 3.3). We introduce and characterize, in the following, all optical lattices used in the experiment (Sect. 3.4). Finally, the setup for Raman sideband cooling and fluorescence imaging is briefly presented (Sect. 3.5). The focus of these parts is on a general understanding of the experiment. Detailed descriptions of various parts can be found in other theses [108–112] with a full overview given in [89].

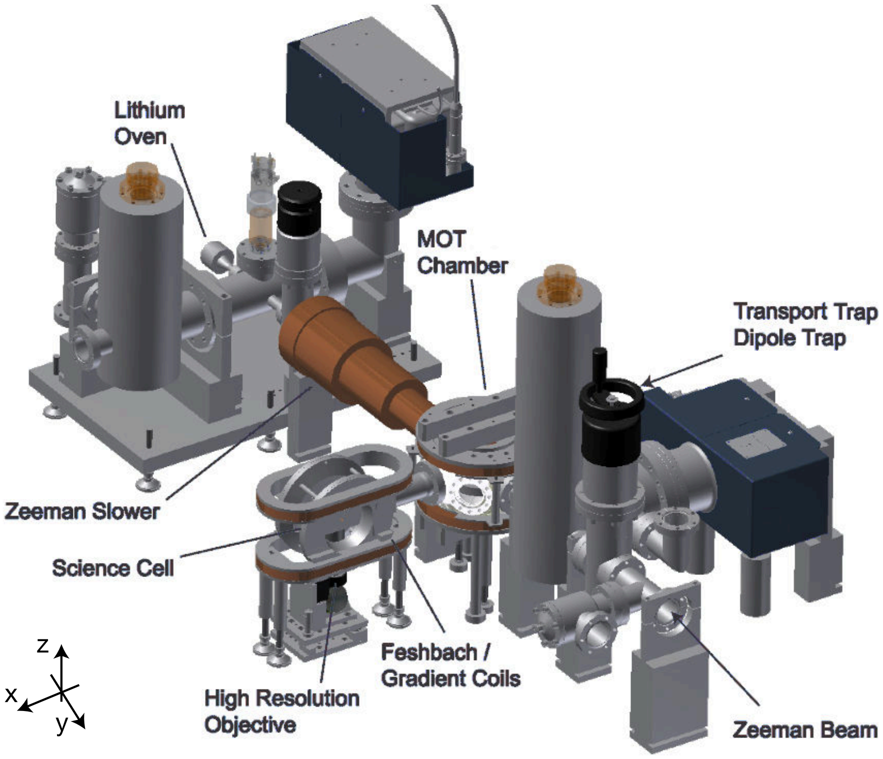

Figure 3.1. Overview of the vacuum setup. *The* ^{6}*Li atoms are emitted from an oven, cooled by a Zeeman slower and captured in a magneto-optical trap. From there, they are transferred with an optical transport to the science cell, where the main experiment takes place.*

3.1 Overview of the experiment

The first three years of work for this thesis were focused on constructing an ultracold quantum gas machine for fermionic ^{6}Li atoms. The goal to image a strongly correlated quantum gas with single-site and single-spin resolution, poses a considerable technical challenge. We put effort into designing the experiment to be flexible and to operate with fast cycle times of currently 15 seconds.

The experiment is performed in a chamber with ultrahigh vacuum (about $2 \cdot 10^{-11}$ mbar) that consists of a oven section, a MOT chamber and a science cell (Fig. 3.1). We load our (red) three-dimensional magneto-optical trap (MOT) from a Zeeman slower. An additional second MOT operated on the narrow $2S$ - $3P$ transition cools the atoms further to load them directly into a strong dipole trap (Fig. 3.2A). After an optical transport into the science cell, we efficiently evaporate the cloud to quantum degeneracy. With a tightly focused dimple trap we can load directly a single plane of our optical lattice (Fig. 3.2B). The experiment can then be performed in the variable geometries of a three-dimensional optical superlattice and atomic interactions are controlled by the broad ^{6}Li Feshbach resonance. For the imaging, we perform

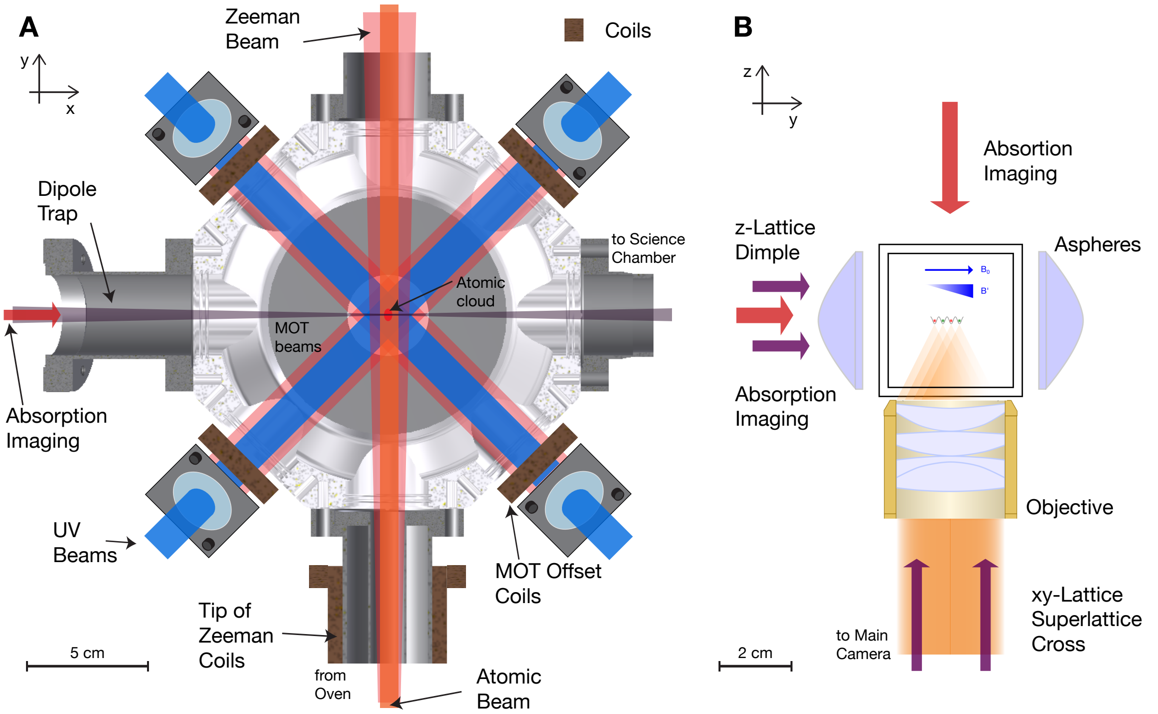

Figure 3.2. Overview MOT and Science chamber. *(**A**) MOT chamber seen from top with its most important elements. MOT coils (not shown) are horizontal. (**B**) Science chamber (glass cell) seen from front with high-resolution lenses. The main images are taken by collection of fluorescence light through the objective. Absorption images are only used for characterization of the cooling steps.*

Raman sideband cooling in an additional, very deep 3d-lattice and collect the florescence with a high-resolution objective.

3.2 Properties of ^{6}Li

Lithium-6 is one of only two alkali isotopes for a fermionic experiment with ultracold atoms. It is the third element in the periodic table and its small mass is the main reason lithium was chosen for the setup. The tunneling dynamics in an optical lattice scales with $1/(ma^2)$, where a is the lattice constant. Thus small masses allow for fast time scales or large lattice spacings, which are more easily resolved in single-site imaging. Even more important, large lattice sites allow to manipulate the atoms on sub-lattice distances, which we employed to circumvent the loss of doublons [25, 26] during imaging and to implement a full spin resolution of our microscope [32].

There are two stable isotopes of lithium: ^{6}Li and ^{7}Li. Both contain a single valence electron, thus the number of nucleons make ^{6}Li a composite fermion and ^{7}Li a composite boson. Although the natural abundance of ^{6}Li is an order of magnitude smaller, almost pure ^{6}Li samples are available, as ^{6}Li is used to produce tritium for fusion and as a neutron absorber. Enrichment is done by the COLEX (Column exchange) electrochemical process that utilizes the affinity to mercury [118]. Large stockpiles were produced during the 1950s and early 60s for hydrogen bombs.

As a bulk, solid lithium has a silvery-gray appearance. Like all alkali atoms, it reacts with water and contact with moist air quickly corrodes the surface, but the reaction is far less violent

Property	Symbol	Value ^{6}Li	Value ^{7}Li	Unit	Ref.
Natural abundance	χ	7.59	92.41	%	[113]
Density (at $T = 300$ K)	n	0.534		g/cm^3	[114]
Melting point	T_M	453.69		K	[114]
Boiling point	T_B	1615		K	[114]
Mass	m	9.9883	11.6503	10^{-27} kg	[113]
Total electronic spin	S	1/2	1/2		
Total nuclear spin	I	1	3/2		
Magnetic dipole constant	A (GS)	152.14	401.75	$(2\pi)\cdot$ MHz	[115]
Total electronic g-factor	g_S (GS)	2.0023010			[115]
Total nuclear g-factor	g_I	-0.448	-1.182	10^{-3}	[115]
Wavelength	λ	670.977497	670.962024	nm	[116]
Frequency	ν	446.799571	446.809875	$(2\pi)\cdot$ THz	
Lifetime	τ	27.102		ns	[117]
Natural linewidth	Γ	5.8724		$(2\pi)\cdot$ MHz	
Fine-structure	Δ_{FS}	10.052837	10.053184	$(2\pi)\cdot$ GHz	[116]
Doppler temperature	T_D	140.92		μK	
Recoil velocity	v_R	9.89	8.48	cm/s	
Recoil energy	E_R	73.675	63.167	$(2\pi)\cdot$ kHz	
Recoil temperature	T_R	3.536	3.032	μK	

Table 3.1. Properties of lithium. *An overview of some properties of ^{6}Li and ^{7}Li . Optical properties (where applicable) have been expressed for the stretched D_2 transition. The ^{7}Li in our machine is currently not used. GS-Ground State.*

compared to the heavier alkali metals. As laser cooling only works with atoms in the gas phase, the most important property of solid/liquid lithium is its vapor pressure. Unlike rubidium the vapor pressure at room temperature is effectively zero and lithium needs to be heated to above 300°C. This is beyond the melting point of lithium, which is listed among other important quantities in Table 3.1.

Consequences of the light mass Acceleration scales inversely proportional to the mass, thus the time evolution of atomic motion for lithium happens on fast timescales and/or over larger distances. This becomes relevant when compared to other time or length scales which are not affected by the mass. A simple example is the free fall due to gravity, which is the same for all atoms on absolute scales, but slow for lithium on its relative scale. A brief analysis of the consequences of the light mass i.e. fast time scales and large distances of lithium in comparison to heavier elements for ultracold atom experiments:

- The optical resolution of the D-line is given by the wavelength $\lambda/2$, which is similar for all alkali atoms. Relative to intrinsic distances, lithium is, thus, easier to resolve than other atoms. We make use of this by construction of a large scale optical lattice.

- The excited state lifetime for all alkali atoms is about 25 ns which is thus long on relative scales for lithium. This limits the number of photons one can scatter, which makes absorption as well as fluorescence imaging harder for lithium.

- Relative to its recoil timescale $E_r/h = (2\pi)\cdot 74\,\text{kHz}$, the excited P-state decay rate of $\Gamma = (2\pi)\cdot 5.9\,\text{MHz}$ is only a factor of 100 faster. Thus there can be be a significant

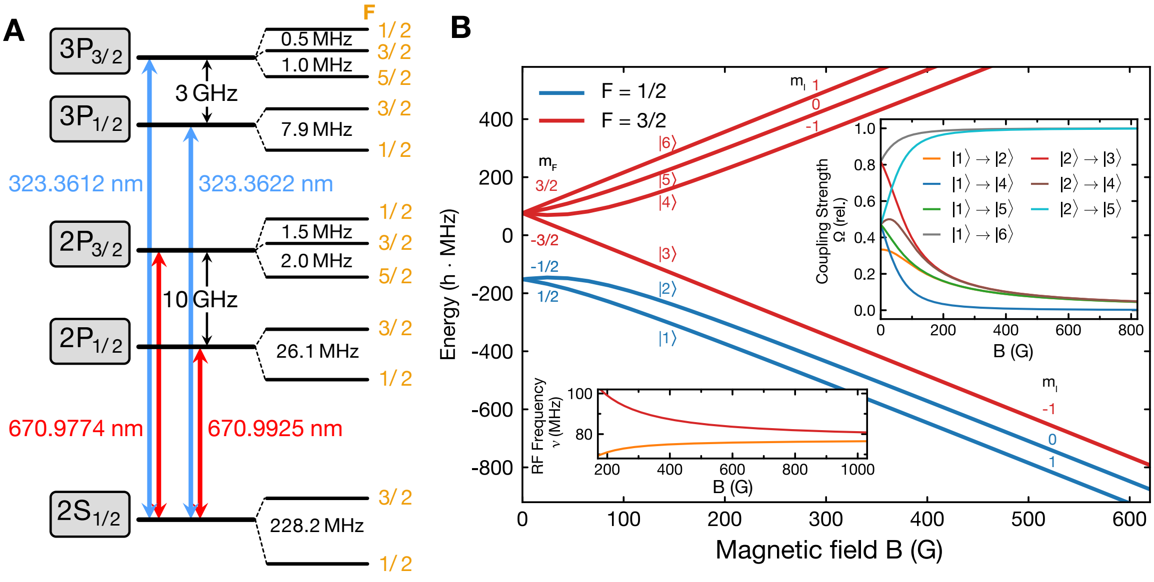

Figure 3.3. ***States of ^{6}Li .*** ***(A)*** *The 2S, 2P, and 3P states with fine and hyperfine structure and their splittings. Image taken from [89].* ***(B)*** *Breit-Rabi diagram of ^{6}Li with the Zeeman regime on the left (F-Basis) and the Paschen-Back regime on the right (JI-Basis). Left inset shows the energy splitting of the three lowest states, which approach $\sim (2\pi\hbar)\cdot 80\,MHz$ at high magnetic fields. Right inset shows the transition strength (Rabi frequency) for magnetic RF transitions between states of the 2S manifold normalized to a pure electron rotation i.e. $|m_J, m_I\rangle \rightarrow |m_J+1, m_I\rangle$. At high magnetic field the coupling between the $|1\rangle, |2\rangle$, and $|3\rangle$ state become very small.*

atomic movement in a potential of several E_r depths during the time spent in the P-state for any photon scattered (see Section 4).

- The effective vacuum lifetime, which typically sets the bound for the time of an experiment, is longer for lithium.
- The faster timescales are associated with higher energies, which require deeper traps. Thus, the required power for optical traps scales inversely with the mass if length scales are kept constant. This can be a problem because site-resolved fluorescence imaging requires low-noise, deep lattices, which are limited by available laser power.

Consequences of the small fine- and hyperfine-structure The fine-structure splitting of the D-line is only $(2\pi\hbar)\cdot 10.05\,\text{GHz}$ for lithium. The hyperfine splitting in the ground state (2S) is $(2\pi\hbar)\cdot 228.205\,\text{MHz}$ and in the excited states it is even on the order of the linewidth Γ (see Fig. 3.3).

- The unresolved hyperfine-structure in the P-states prevents the continuous scattering on a closed line. Thus laser cooling requires a strong repumper. Only at very large magnetic fields, the optical transitions become almost closed.
- Standard molasses cooling [119, 120] does not work for lithium as it requires the selective driving of hyperfine transitions. Grey molasses cooling on the other hand has been demonstrated for lithium [121].

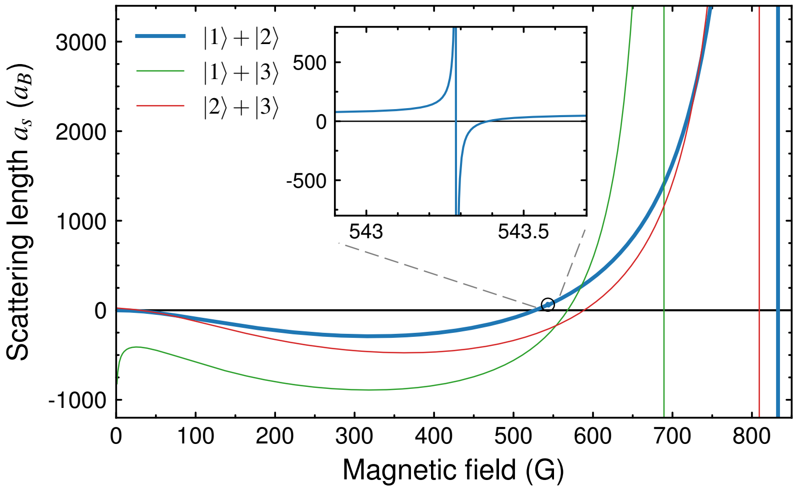

Figure 3.4. Scattering length of ^{6}Li . *The scattering length of the lowest states of ^{6}Li in the experimentally explored region. The broad Feshbach resonance is used to tune the interactions. There is an additional narrow ($0.1\,G$) resonance at $B = 543.286(3)\,G$ [126] (inset). Data of the main plot is taken from the supplementary material of [127].*

- The small fine-structure allows to easily offset-lock lasers operating on the D_1 and D_2 lines.

- The small hyperfine-structure can be bridged by acousto-optical modulators (AOM) allowing for simple pairs of Raman lasers.

- The relatively small ground state splitting leads to additional scattering in the detuned target F-manifold during optical pumping. This results in additional heating for Raman side-band cooling (Sect. 4) and prevented us from a successful implementation of EIT-cooling [122] for the imaging of lithium. On the other hand, EIT cooling for potassium-40, which has a $(2\pi\hbar) \cdot 1.3\,\mathrm{GHz}$ ground state splitting, has been used successfully for imaging [29, 123].

- The ratio of Raman coupling Ω between the two F-levels to off-resonant scattering rate Γ_{ph} is limited to 140 for large detunings due to negative interference of couplings via the D_1 and D_2 line [124]. Thus off-resonant scattering can not be fully suppressed for Raman transitions.

- The same ratio applies to differential light shifts between different m_F-states due to a single laser beam. This makes it practically impossible to implement state-dependent lattices for ^{6}Li. Optical addressing schemes as implemented for ^{87}Rb [125], which rely on differential light shifts, would thus be less coherent.

- At finite magnetic fields the nuclear spin quickly decouples from the electron spin (see Fig. 3.3 B) and for $B > 22\,\mathrm{G}$ state $|2\rangle = |F = 1/2, m_F = -1/2\rangle$ becomes high field seeking (Paschen-Back). The RF-coupling between the three $|J = -1/2\rangle$ states quickly drops (right inset), while their energy difference approaches about $(2\pi\hbar) \cdot 80\,\mathrm{MHz}$.

3.3 Cooling to quantum degeneracy

Zeeman Slower and MOTs The ^{6}Li atoms are ejected from a steel oven operated at 380°C. The atomic beam is decelerated in a Zeeman slower [9] with a decreasing magnetic field peaking at about 800 G. The field merges smoothly into the gradient of a standard 3d MOT operated on the D_2-line. We can load up to 10^9 ^{6}Li atoms in 5 seconds. But due to the small atom number required in the lattice experiments, we keep our oven temperature lower to minimize the coating with lithium of the window through which the Zeeman beam enters. We typically load the MOT for only 3 seconds and after a compression stage we obtain $80 \cdot 10^6$ atoms at $400\,\mu$K. For details about the setup, laser settings and loading rates see [108].

In order to load the atoms directly into an optical dipole trap of 60 W, we cool the atoms with a 13 ms pulse of a UV-MOT on the narrow 2S-3P transition [89, 128]. This reduces the temperature to about $60\,\mu$K, while keeping about 30% of the atoms. There is a trade-off between temperature and losses, which we resolved by optimizing the number of atoms that can be loaded into the subsequent dipole trap. At the end, we optically pump the atoms to the lowest two hyperfine states.

Optical transport and Evaporations Next, we load as many atoms as possible into an optical dipole trap and transport the atoms with two mirrors on a translation stage into the science cell. The volume of a dipole trap scales with the 4th power of its waist. At the same time the relevant axial trapping frequency for optical transport scales with the inverse 3rd power. This makes it impossible to use the same dipole trap both for loading of large atom numbers and for a fast transport. Thus, we use two dipole traps. The first operates at the magic wavelength of the UV-MOT at 1070 nm and can, thus, be turned on during the UV-MOT phase. It has a large waist of $100\,\mu$m and we typically load up to 5 million atoms into this trap.

In order to transfer the atoms efficiently into the second dipole trap (3 W, 1064 nm, $28\,\mu$m waist), both traps are overlapped and we run an optical evaporation by lowering the depth of the first dipole trap from 60 W to zero in 2 seconds ($-290\,a_B$ scattering length). This allows to start the transport with up to 2 million atoms at about $20\,\mu$K. In 0.5 seconds an air-bearing translation stages moves the focus of the trap with the atoms by 28 cm to the focal point of our objective in the science cell.

Here we form a crossed dipole trap by ramping up an intersecting laser beam (2.5 W, 1064 nm, $75\,\mu$m waist) that travels through the objective. Due to the uncoated surface of our glass cell, we angle the beam by 20 degree to avoid a back reflex that would create a standing wave. In this crossed dipole trap, we perform a 3 second evaporation by first decreasing the power of the transport beam and then both beams. This allows to produce degenerate Fermi gases of little over 10^5 atoms at $T/T_F = 0.15$ in a total time of 8.5 sec.

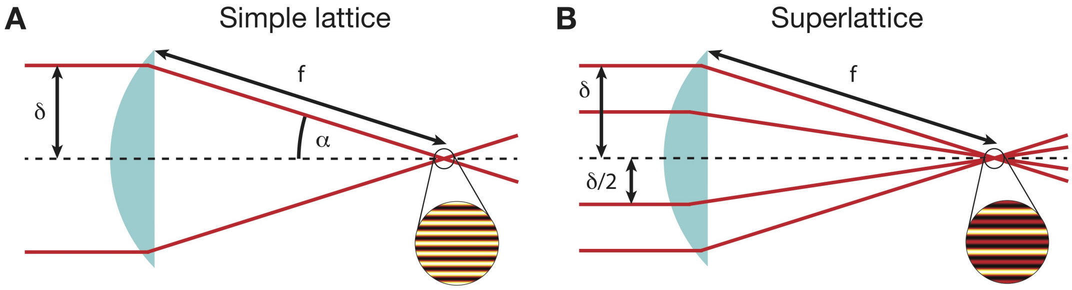

__Figure 3.5. Optical lattices by interferences under an angle.__ We use the interference of angled beams to generate the large-spacing optical lattices. Beams with different angles produce the lattice and superlattice. Images taken from [109].

3.4 Optical lattices

We designed and built three 3-dimensional cubic optical lattices for the experiment. These provide a large degree of flexibility to realize many geometries for the quantum simulation and to manipulate the atoms on the length scale of the lattice constants. The lattices that are used to generate the Hubbard lattice sites are termed *physics lattice*, while we call the deep lattice used only for imaging *pinning lattice*.

3.4.1 Physics lattice

Our physics lattices is an optical superlattice with lattice constants of $1.15\,\mu$m and $2.3\,\mu$m in both x and y direction and $1.55\,\mu$m and $3.1\,\mu$m in the vertical direction (z). They are created in a somewhat unusual way because we do not retro-reflect the lattice beams, but interfere pairs of beams under various angles (see Fig. 3.5). This allows to realize the desired lattice constants with a standard high-power, low noise laser source (*Mephisto* by *Coherent*) at 1064 nm. Two coherent beams, which intersect under an total angle of 2α, generate a 1-dimensional lattice with a lattice constant given by

$$d_L = \frac{\lambda_{Laser}}{2\sin(\alpha)}. \tag{3.4.1}$$

We generate six times parallel pairs of beams in two interferometric setups [109] and focus these onto the atoms by our imaging objective (x and y direction) and an aspheric lens on the site (see Figs. 3.2 B and 3.6). The frequencies of the beam pairs are detuned relative to each other by at least $(2\pi)\cdot 80$ MHz to avoid cross interferences.

The large lattice constants are a big advantage for imaging and sub-lattice site manipulations, but in order to keep the trap confinement by the lattice beams on the same level, one would need to scale the lattice waists accordingly. Unfortunately it is hard to realize large foci after a high-NA objective. Our optical access before the objective puts an upper limit to the lattice waists at $125\,\mu$m. This allows to realize Mott-insulators up to about 16 sites in diameter[1].

When we want to measure our atom distribution, we ramp up the physics lattices to their maximum value of $50E_r$ (3 W per lattice pair), sufficient to freeze the motion of the atoms.

---

[1] Parameters used for this estimate: $V_x = 5E_r$, $U = (2\pi\hbar)\cdot 2.8\,\mathrm{kHz}$, $k_BT = t/2$ and $< 1\%$ thermal doublons. Experimentally confirmed.

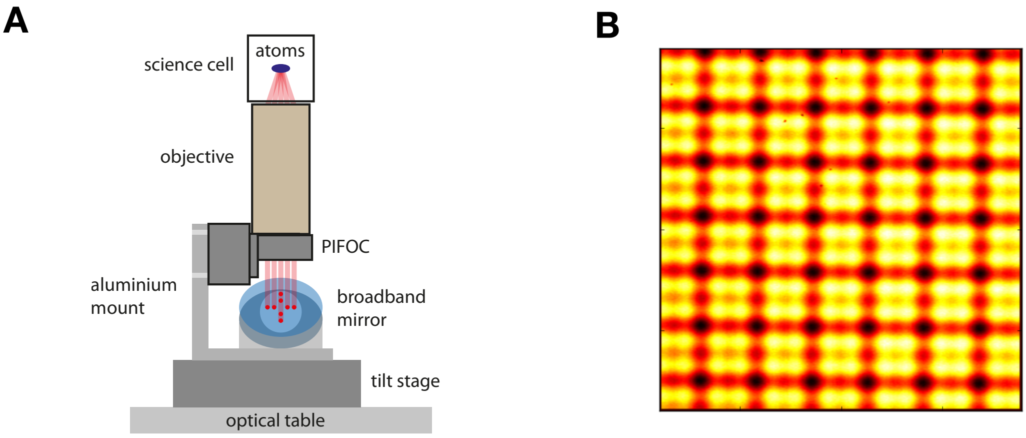

Figure 3.6. Projection of physics lattice through the objective. ***(A)*** *We send four pairs of coherent beams into the imaging objective to generate the x and y lattices and superlattices.* ***(B)*** *Example of a 2d superlattice in plaquette configuration. The plot shows the light intensity of the optical lattices imaged onto a camera. Images taken from [109].*

The ramp time of 1 ms is fast compared to our highest tunneling rates ($t_{\text{max}} \approx (2\pi\hbar) \cdot 400$ Hz) and slow relative to the lowest on-site frequency ($\omega_z = (2\pi) \cdot 7$ kHz) to avoid band excitations.

Superlattice We use six additional beams at half the distance to the optical axis to create the superlattices with 2.3 μm and 3.1 μm. These allow to generate more complicated geometries like double wells, plaquettes, ladders or staggered lattices. In addition, they can be used to create non-trivial initial density distributions like spin-density waves. Not all lattice beams are used in all experiments. In the experiments presented in this thesis, we mainly used the superlattice in y-direction for spin-resolved imaging.

The combined potential of the superlattices depends critically on the relative phase between the short and the long component. This phase is stabilized in the interferometric setup and can be adjusted with a piezo voltage to any value between zero and 2π. For details on the stabilization and a recent characterization see [109] and [112].

Imperfect confining potential The lattices that we generate with beams propagating through the microscope objective show deviations from a perfect Gaussian envelope. Imperfections on the laser beams due to tiny surface errors of optical elements (mirrors, lenses or the objective itself) appear as irregular modulations of the optical potential. Similar problems have been reported for the Bosonic microscope in Harvard [129] and recently in 1d optical lattice in Paris, which both also send the lattice beams through strong lenses. On large scales this leads to a deviations of the mean density of our clouds from a round shape and on short scales it results in small site-to-site offsets (Fig. 3.7). We characterized the strength of these fringes by detailed measurements of site-resolved densities and calculation of the mean deviation from an harmonic confinement per site $\Delta\varepsilon_i$. We found $\langle|\Delta\varepsilon_i|\rangle = (2\pi\hbar) \cdot 240(30)$ Hz at $(2\pi\hbar) \cdot (31, 42, 15)$ kHz lattice depth along the three axis, which is sufficiently below the band width $W_x = (2\pi\hbar) \cdot 1.6$ kHz and has no major effect on the physical results. The strength of $\Delta\varepsilon_i$ scales linearly with lattice depths, while tunneling rates decrease (Eq. 2.1.8). As long as $\Delta\varepsilon_i$ is small compared the tunneling energy scales or temperatures, its effect is small, but as

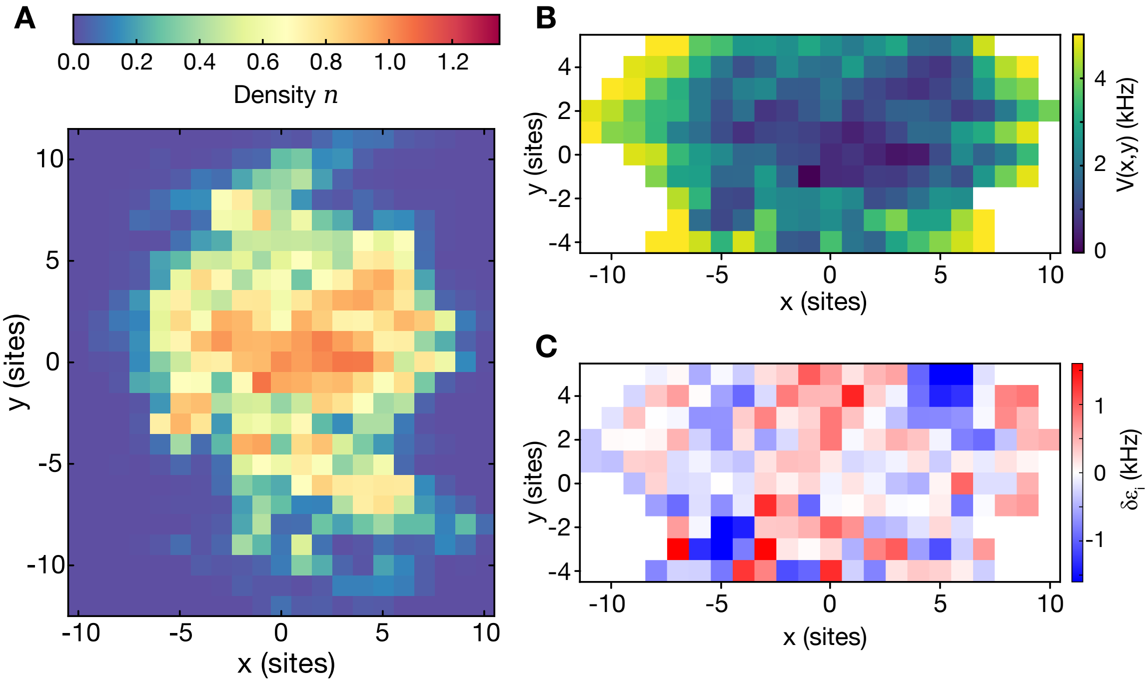

Figure 3.7. Optical lattice potential. ***(A)*** *The average density distribution $n(x,y$ is given by the confining potential, which shows deviations from a simple harmonic shape.* ***(B)*** *Reconstructed potential landscape per site $V(x,y)$ for $(2\pi\hbar)\cdot(31,42,15)\,$kHz lattice depth in the x, y, z lattice.* ***(C)*** *Deviations $\Delta\varepsilon_i$ of (B) from a two-dimensional harmonic potential with $\omega_x = (2\pi)\cdot 250(5)\,$Hz and $\omega_y = (2\pi)\cdot 210(5)\,$Hz.*

we approach lower energy scales e.g. holes can get trapped in local humps. Note that spin correlations from second order exchange processes are almost unaffected by these fringes.

3.4.2 Lattice loading

Single-plane preparation For the imaging it is very important to have atoms only in a single plane of the vertical lattice because any atom in neighboring planes adds disturbing signals to the image. With a tightly confined elliptical dimple beam ($w_z = 1.7\,\mu$m, $w_x = 10\,\mu$m) we can directly transfer the atoms into just one plane of the z-superlattice ($d = 3.1\,\mu$m). The dimple trap is derived from a distributed feedback (DFB) diode laser at 780 nm and it is focused onto the crossed dipole trap through the z-lattice asphere (Fig. 3.2) already during the optical evaporation. Once the transport trap is switched off, about 15 000 atoms remain in the dimple/cross-trap. Due to their fermionic nature, the atomic cloud has a vertical size larger than 3μm. Thus before the transfer into the z-lattice, we reduce the lattice depth briefly to spill out half of the atoms and then re-raise to full power to get the maximum confinement. This allows us to deterministically load about 8000 atoms at 1 μK into a single plane.

Magnetic evaporation The final evaporation is done in the z-superlattice and cross trap. In order to have a constant strong confinement and to avoid tunneling into neighboring z-planes, we drive the evaporation with a strong horizontal magnetic gradient. In the Paschen-Back regime both spin states, $|1\rangle$ and $|2\rangle$, have almost the same magnetic moment (Fig. 3.3), so they are pushed out to the same direction (y-direction). We run the evaporation at 599 G offset field (353 a_B scattering length), which is still far away from the losses of the large Feshbach resonance (834 G). To ramp the magnetic field to this point, one has to cross the small Feshbach resonance (543 G, Fig. 3.4), which we do while the atoms are spread out in the plane (low cross power) with a quick jump (< 1 ms). The evaporation is done by linearly increasing the magnetic gradient within 2.5 s. The final value between 20 and 30 G/cm allows to set the atom number for the experiment very precisely. For example, in a 24 hour measurement with 131 atoms in the mean, we recorded a root-mean-square fluctuation of only 5.5 atom, which is less than half of the shot noise value. As we have about 97% detection efficiency (see Chap. 4), the number squeezing in the preparation is even slightly higher than the recorded one.

XY Lattice Ramps The ramp-up of the two remaining lattice axes is one of the most delicate processes as it determines the final temperature of the lattice gas. One tries to stay as adiabatic as possible in a given finite time. After the evaporation, we therefore deconfine the cloud by lowering the power in the cross beam. It is important to bring the density of the cloud to a similar distribution that we want to obtain later in the lattice. This minimizes mass transport during the lattice ramp up, which is one of the main sources for heating. For the same reason, we increase the scattering length to the desired value already prior to the lattice ramps. For a scattering length above 800 a_B, we noted first losses due to inelastic scattering processes in the 2d-cloud without a lattice. Any increase of interactions above this values, thus, has to be done during the lattice ramps, where three body collisions are suppressed by the repulsive interaction U.

The details of the optimized lattice ramp depend on the final state we want to reach. We typically use two piecewise linear ramps per axis with a total period of 80 ms and optimized the relative timing of the x, y and Feshbach ramps. For the case of strongly doped 1d-chains, ramps are described in Appendix B.1.

At the end of the lattice ramps, we prepared the quantum state that we want to study. We, then, hold the atoms for about 15 ms to allow small excitations to thermalize before we freeze the distribution by a quick 1 ms ramp of all lattices to their maximum depths. No further tunneling happens after this point in time.

3.4.3 Spin resolved imaging

In order to measure the spin of each atom, we need to convert the spin-state into a spatial information. As detailed in [112], we apply a strong magnetic gradient (95 G/cm) along the y-direction and adiabatically split the y-superlattice sites with the short scale y-lattice in 10 ms. Close to zero magnetic field the magnetic moment of the two spin states $(|1\rangle, |2\rangle)$ are opposite (Fig. 3.3) thus they are transferred to opposite sites of the short lattice (see Fig 3.8). This process requires a phase stability of lattice to superlattice below 200 mrad and relative match of the lattice constants to better than 1‰.

A direct spin-resolved imaging, as obtained by scattering light with one spin component while the other is kept in a dark state has recently been demonstrated with ^{87}Rb in tight tweezers [130], but this would be very challenging in our experiment due to the high number of photons required for imaging in a lattice and a lack of a sufficiently closed transitions at experimental magnetic fields.

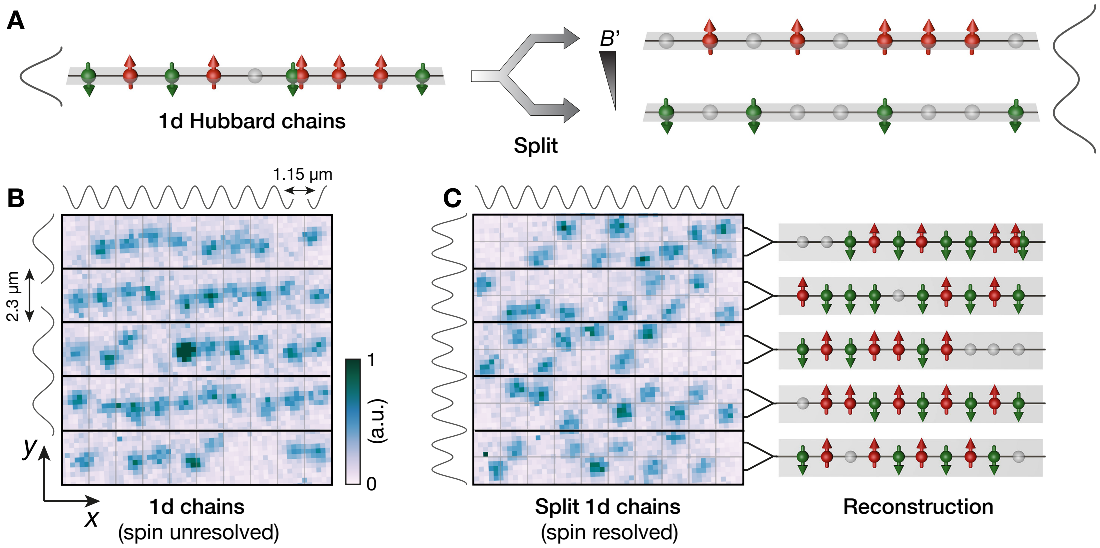

Figure 3.8. Schematic of the spin and density resolved detection. ***(A)*** *Schematic of the spin resolved imaging. Each site is split spin-dependently into a local double well potential. During the splitting process a magnetic field gradient* B' *is applied to separate the two spins. This allows for the simultaneous detection of* $|\uparrow\rangle$ *(green),* $|\downarrow\rangle$ *(red) spins, doublons (red and green spins overlapping) and holes (gray spheres) and thus for a full characterization of the Hubbard state.* ***(B)*** *Typical fluorescence image of atoms in five one-dimensional tubes imaged prior to splitting. The lattice potentials are indicated by the black lines next to the images with a spacing along the tubes oriented in x-direction of* $1.15\,\mu m$ *and a transverse inter-tube separation of* $2.3\,\mu m$*.* ***(C)*** *Typical image with spin resolved detection. A superlattice in y-direction (indicated on the left of the image) is used to split each chain in a spin dependent manner. The* $|\downarrow\rangle$ *spins are pulled down, while the* $|\uparrow\rangle$ *spins are pulled upwards. The right image illustrates the reconstructed occupations.*

3.4.4 Pinning lattice

The lattice depths of the physics lattices are limited by the amount of power that we can send into the interferometer and the objective. As the recoil heating from lithium for light scattering is especially severe, we need an extra lattice to hold the atoms in place during imaging[1]. We use three Nufern 50 W fiber amplifiers seeded by a low-noise laser (Mephisto) to create an additional retro-reflected optical lattice with $d_{PL} = 532\,\text{nm}$ lattice spacing and about $500\,E_r$ lattice depths. The tight confinement is necessary to allow for efficient Raman sideband cooling and to prevent the atoms from tunneling even in the excited bands[2]. The pinning lattice axis have relative angles of 90° to ensure symmetric on-site trap frequencies of $(2\pi)\cdot 1.3\,\text{MHz}$. Relative to the physics lattice plane, the pinning lattice is rotated by 10° in plane and 44° out of the plane (see Fig. 3.9). There is no need for stabilization of the relative phases because the pinning lattice oversamples each physics site by a factor of ten i.e. $(1150/532)^3$.

---

[1] In addition to the limited power, the large lattice spacing makes Raman sideband cooling in the physics lattice practically impossible because even at unreasonable 50 W per axis, one would only reach $(2\pi)\cdot 500\,\text{kHz}$ on-site frequency.

[2] There are about 14 bound states per site, out of which 8 have tunnel-couplings $t < 0.1\,\text{Hz}$.

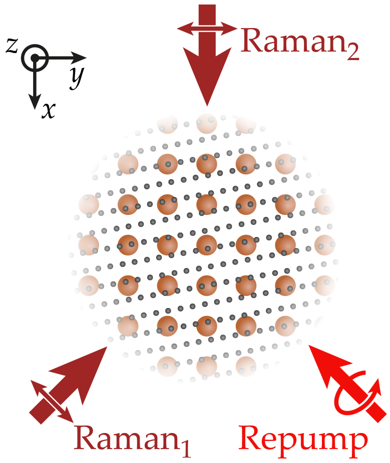

Figure 3.9. ***Lattices and raman beams.*** *Brown dots mark the physics lattice sites and grey dots show the pinning lattice sites in a vertical range of* $\pm 250\,\mathrm{nm}$ *from the lattice plane. Due to the smaller lattice spacing of the pinning lattice, each physics site is connected with many pinning sites. We perform Raman sideband cooling in the pinning lattice with the geometry shown. All three beams are in the x-y plane. Image taken from [89].*

3.5 Raman cooling

Raman sideband cooling is a powerful technique to cool particles whose motion is confined by a strong harmonic potential. We discuss the details of this process in chapter 4. Experimentally it requires at least one pair of Raman beams and one repump beam in addition to the strong pinning lattice.

Raman beams One is free to choose any two states of the electronic ground state for the Raman coupling. We are working with the $F = 1/2$ and $F = 3/2$ manifolds at zero magnetic field, which has the advantage that all states participate in the cooling process and no additional m_F-repumper is necessary[1]. Raman cooling for lithium thus requires two coherent Raman beams with a frequency difference close to $E_{HFS} + \hbar\omega_0 = (2\pi\hbar) \cdot 229.5\,\mathrm{MHz}$[2]. These beams are generated from a single TA running $(2\pi) \cdot 7.3\,\mathrm{GHz}$ red detuned to the D_1-line. After splitting the beam at a polarizing beam splitter, one arm is frequency shifted by an AOM double pass. The beams are independently fibered and at the position of the atoms they intersect with a relative angle of 135° and a linear polarization in the plane (see Fig. 3.9). In this configuration the momentum transfer $\Delta\vec{k}$ is at an angle of 55° to all three pinning axes, providing equal Raman coupling on all axes. With 0.6 mW and 6.5 mW power of the Raman beams, we can achieve Raman coupling strengths of $(2\pi) \cdot 50\,\mathrm{kHz}$ on the first red sideband.

Repump beam The repump beam is a single beam resonant on the D_1-line with circular polarization that is in the plane of the Raman beams. At a waist of $500\,\mu\mathrm{m}$ only a few $\mu\mathrm{W}$ of power are required, which are derived from a diode laser (Toptica). The power is stabilized with a photo-diode and a PI-controller before the beam is attenuated to the final value.

---

[1] At a close analysis this statement is only partially true (see Sect. 4.2).

[2] The plus sign for the red sideband arises from repumping on the lower $F = 1/2$ state.

Chapter 4

Raman Sideband Cooling for Fluorescence Imaging

This chapter contains a detailed theoretical treatment of Raman sideband cooling used for fluorescence imaging of alkali atoms. We start by deriving the Raman couplings in a three-dimensional geometry (Sect. 4.2). We then calculate the cooling (Sec. 4.3) and heating rates (Sect. 4.4) involved in the process and finally analyze a rate equation to predict the evolution of the occupation of vibrational levels and the residual loss rate (Sect. 4.5). The results are compared with experimental measurement of the tunneling and losses during our imaging (Sect. 4.6). Throughout the chapter, the numbers and figures are taken from our experiment, but the analysis in the text stays more general.

4.1 Introduction

To take fluorescence images with single-site resolution, we scatter photons and image these with our high-resolution objective ($NA = 0.5$) onto an EMCCD camera. We need to collect more than 100 photons per atom to identify individual atoms with high fidelity on densely filled images (see Chapter 5). As we collect only about 5% of all scattered photons and every photon heats the atom by at least one photon recoil, each atom is heated-up by more than 5 mK. This is much more than the largest pinning lattice depth we can create with available laser power and the atoms thus need to be cooled during imaging.

The first quantum gas microscopes with Rb [25, 26] used optical molasses cooling [120] for fluorescence imaging. All the microscopes with fermionic atoms (Li,K) implemented some version of Raman sideband cooling either the far detuned version discussed in this chapter or a similar electromagnetically-induced-transparency (EIT) cooling [122], which uses additional interference effects[1]. Microscopes with heavy Ytterbium atoms even demonstrated single-atom resolved images without cooling [131] and with Faraday imaging [132].

Sideband cooling techniques have first been used to cool trapped ions [8, 133], opto-mechanical systems [134, 135] and alkaline earth atoms [136, 137]. The technique relies on resolved sidebands due to the quantized motion in a trap with a harmonic frequency that is large compared to the linewidth of the transition (called *festina lente regime* [138]) such that individual sidebands can be addressed with a laser. To provide such a sufficiently narrow line, *Raman sideband cooling* uses a two-photon Raman process, which is a coherent coupling of two states via a detuned third state. This allows to selectively address sidebands in traps with frequencies that are small compared to the large natural linewidth Γ of neutral alkali atoms. Raman sideband cooling has been successfully demonstrated with ions [139] in 1995 and with heavy neutral atoms in 1d [140], 2d [141] and 3d [142] optical lattices already in 1998. Recently, the method has been successfully implemented for the fluorescence imaging of single

---

[1] We tried EIT cooling, but we saw too large heating rates due to the small hyperfine structure of ^{6}Li .

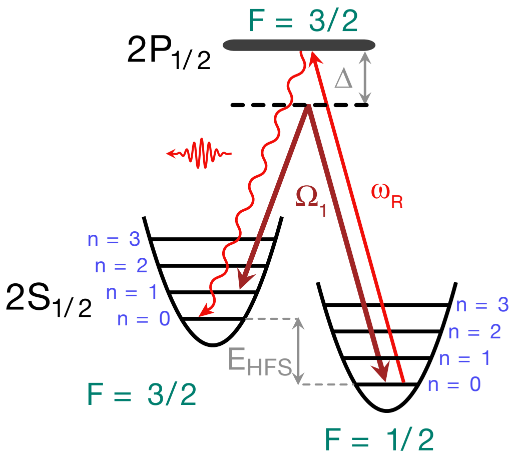

Figure 4.1. Overview of Raman cooling. *The two F-levels of the ground state are coupled on the red sideband of the local oscillator levels with a pair of Raman beams. A repumper incoherently pumps the population back to the $F = 3/2$ state and the emitted photon carries away the entropy.*

atoms in optical tweezers [143], for large clouds in optical lattices [144] and for quantum gas microscopes of lithium [30, 32, 74] and potassium [29, 31, 123]. Even cooling without tight confinement has been achieved by addressing of higher order sidebands [145].

Raman sideband cooling for fluorescence imaging in an optical lattice is different from traditional Raman cooling in so far as one starts with a cold sample in the lowest band. The goal is to scatter photons and at the same time to prevent the atoms from heating-up into unbound states or into high-exited harmonic oscillators states, which have a finite tunneling amplitude. Thus, the focus is no longer on the maximization of the ground state occupation, but rather on the minimization of a population tail to high excited states.

The calculations in this chapter confirm our observation that it is not possible to optimize the cooling with our given lattice to a loss rate better than ~2%. In a regime where the cooling is much stronger than all heatings, the loss rate is still expected to be non-zero and it becomes a fixed fraction of the photon scattering rate. The value of this fraction only depends on the depth of the lattice in units of the lattice recoil, the ratio of lattice constant to wavelength of resonant light and the repump efficiency.

Basic cooling scheme Raman sideband cooling is a two step process: A coherent pair of Raman lasers resonantly couples two spin states ($|1\rangle, |2\rangle$) of the electronic ground state of the atom. The frequency difference of the two beams is adjusted to remove one (or more) excitations from the motional harmonic oscillator (h.o.) state of the atom. As a coherent process, this coupling alone leads to Raman oscillations between the states and does not cool. A repump beam, thus, incoherently pumps population from the second to the first state via an excited P-state and the emitted photon carries away the entropy. The harmonic oscillator state is conserved during repumping if the Lamb-Dicke parameter, η, is much smaller than one:

$$\eta^2(n+1) \equiv \frac{E_r^\gamma}{\hbar\omega_0}(n+1) \ll 1 \tag{4.1.1}$$

Here n is the current harmonic oscillator level, $\hbar\omega_0$ is the energy splitting between the levels and $E_r^\gamma = \frac{\hbar^2 k_\gamma^2}{2m}$ is the recoil energy of the repump light with wavevector k_γ. One successful cycle cools the atom by an energy $\hbar\omega_0$.

The process can either be done in a pulsed sequence, with alternating Raman and repump pulses, or continuously, with all beams turned on at the same time. We implemented the continuous version, which is treated also in this analysis. Many of the aspects can however directly be applied to the pulsed system as well.

The motional ground state of $|1\rangle$ is a dark state to both the Raman coupling and the repump beam. The state is, however, not dark to detuned single-photon excitations from the Raman beams. This gives a sufficient fluorescence rate, which we use to image the atoms, while they remain on their lattice sites.

Our system We are working with ^{6}Li in a 532 nm lattice (see Sect. 3.4.4), thus, the photon recoil energy is $E_r^\gamma = (2\pi\hbar) \cdot 74\,\mathrm{kHz}$ and the lattice recoil energy (Eq. 2.1.3) is $E_r^{\mathrm{Lat}} = (2\pi\hbar) \cdot 29.3\,\mathrm{kHz}$. Our pinning lattice has a depths of 517 $E_r^{\mathrm{Lat}} = k_B \cdot 0.73$ mK per axis and the on-site frequency is $\omega_0 = (2\pi) \cdot 1.3$ MHz corresponding to 60 μK.

4.2 Raman coupling

4.2.1 Coupling strength

A Raman process is a two-photon coupling of two states with different spins via a detuned third state. In a three-level atom, the coupling rate Ω is related to the single-photon Rabi frequencies $\Omega_{Rm,i}$ via

$$\Omega = \frac{\Omega_{Rm,1}\Omega_{Rm,2}}{2\,|\Delta_{Rm}|}, \tag{4.2.1}$$

where Δ_{Rm} is the detuning to the third state.

In a multilevel atom, the couplings are more complicated because contributions via different excited states need to be summed and these different paths interfere. A general operator for light shifts and couplings between ground state i and j of alkali atoms can be expressed as [146]

$$\hat{V}_{i,j} = \sum_l \frac{|j\rangle\langle j|\hat{\mathbf{d}} \cdot \mathbf{E}^*(x,t)|l\rangle\langle l|\hat{\mathbf{d}} \cdot \mathbf{E}(x,t)|i\rangle\langle i|}{4\hbar\Delta_l}, \tag{4.2.2}$$

which is a straightforward generalization of the usual light-shift operator to the case $i \neq j$. Here $\hat{d}$ is the atomic dipole operator, $\mathbf{E}(x,t)$ is the electric field of all Raman beams in the rotating frame of one laser at frequency ω_{Las} [1] and $\Delta_l = \omega_{\mathrm{Las}} - \omega_{il}$ is the detuning from the transition to the excited state l. In the case where this detunings Δ_l is much larger than the hyperfine

---

[1] The remaining t dependence allows for a detuned second laser, whose electric field oscillates with $(\omega_{\mathrm{Las2}} - \omega_{\mathrm{Las}})t$ in the rotation frame.

structure of the atom, the expression can be simplified. Following the detailed derivation in [147], one can write

$$\hat{V} = V(x,t) + \mathbf{B}_{\text{eff}}(x,t) \cdot \hat{\mathbf{S}}_{\mathbf{e}} \quad \text{with:} \tag{4.2.3}$$

$$V(x,t) = V_0 \left|\boldsymbol{\epsilon}(x,t)\right|^2, \quad \mathbf{B}_{\text{eff}}(x,t) = V_0 D_{FS} \frac{i}{2\hbar} \left(\boldsymbol{\epsilon}^*(x,t) \times \boldsymbol{\epsilon}(x,t)\right)$$

$$V_0 = \frac{\hbar\Gamma^2}{8\Delta_{\text{avg}}} \frac{I}{I_S}, \quad \Delta_{\text{avg}} = 3\left(\Delta_{1/2}^{-1} + 2\Delta_{3/2}^{-1}\right)^{-1}, \quad D_{FS} = 2\frac{\Delta_{3/2} - \Delta_{1/2}}{\Delta_{3/2} + 2\Delta_{1/2}}.$$

The detuning $\Delta_{3/2(1/2)}$ is measured with respect to the $D_2(D_1)$ line and $\boldsymbol{\epsilon}(x,t)$ is the (not necessary normalized) local polarization of the electric field $\mathbf{E}(x,t) = \sqrt{2I/\varepsilon_0 c}\,\boldsymbol{\epsilon}(x,t)$ with averaged intensity I. I_S is the saturation intensity of the D_2-line. The light shift $V(x) = \langle V(x,t) \rangle_t$ is the same for all ground states of the atom, while the differential light shifts and coupling matrix elements are expressed as an effective magnetic field $\mathbf{B}_{\text{eff}}$, that couples to the electron spin $\hat{\mathbf{S}}_{\mathbf{e}}$. There are a few effects to emphasize in equation 4.2.3.

- The factor D_{FS} describes the interference of the D_1 and D_2 line. For detunings much larger than the fine-structure $E_{FS}/\hbar = \Delta_{3/2} - \Delta_{1/2}$, the atom looks to the laser like a two-level atom and the effective magnetic field drops like Δ^{-2} instead of Δ^{-1}. At this point there is no further gain of the coherent coupling relative to the off-resonant scattering by larger detunings. This leads to a fundamental limit per alkali atom in achievable coherence [124]. Lithium has a fine-structure splitting of only 10 GHz and is, thus, the worst choice in this respect.

- The diagonal terms of $\mathbf{B}_{\text{eff}}(x,t) \cdot \hat{\mathbf{S}}_{\mathbf{e}}$ written in an $|F, m_F\rangle$-basis are the tensor light shifts, which can be expressed as the Zeeman shifts of the fictitious magnetic field: $g_F m_F \mathbf{B}_{\text{eff}}(x)$.

- The expression $\mathbf{B}_{\text{eff}}(x,t) \cdot \hat{\mathbf{S}}_{\mathbf{e}}$ can be expanded as $\frac{1}{2}\left(B^-_{\text{eff}}(x,t)\hat{S}^+_e + B^+_{\text{eff}}(x,t)\hat{S}^-_e\right) + B^z_{\text{eff}}(x,t)\hat{S}^z_e$, driving $\Delta m_F = \pm 1, 0$ and ΔF-transitions.[1]

- For a multi-laser setup, the time-dependence of $\mathbf{B}_{\text{eff}}(x,t)$ has Fourier components at the pairwise differences in frequency between the lasers. This allows to resonantly couple states of different energies e.g. the two F-levels.

- The spatial dependence of $\mathbf{B}_{\text{eff}}(x,t)$ is given by the two photon momentum transfers $k_i - k_j$. It is needed to couple different atomic wave functions e.g. the h.o. levels n, n'.

---

[1] $\Delta m_F = \pm 2$ transitions are forbidden ($E_{HFS}/(\hbar\Delta)$ suppressed) in the regime of large detunings relative to the hyperfine splitting of the P-state because its coupling elements via one P_J manifold sum to zero.

Our system As introduced in the last chapter (see Sect. 3.5), we are using Raman beams that are intersecting at an angle $\phi \approx 135^\circ$ in the xy-plane, whose polarization is linear and in this plane. Inserting the corresponding electric fields in Eq. 4.2.3 gives

$$\begin{aligned}
\mathbf{B}_{\text{eff}}(r,t) &= \frac{V_0 D_{FS}}{\hbar} \sin\phi \sin\left(\boldsymbol{\Delta_k}\,\mathbf{r} - \delta_\omega t\right) \vec{e}_z \\
&= \frac{\Omega_{Rm,1}\Omega_{Rm,2}}{2\Delta_{1/2}} \frac{E_{FS}}{3\hbar\Delta_{3/2}} \sin\phi \sin\left(\boldsymbol{\Delta_k}\,\mathbf{r} - \delta_\omega t\right) \vec{e}_z && (4.2.4) \\
\frac{\hbar}{2}\Omega_{Fm_F \leftrightarrow F'm'_F} &= \langle F m_F | \mathbf{B}_{\text{eff}}(r,t) \cdot \hat{\mathbf{S}}_{\mathbf{e}} | F' m'_F \rangle && (4.2.5) \\
&= \delta_{m_F,m'_F} \left(\delta_{F,F'} g_F m_F \mathbf{B}_{\text{eff}}(r,t) + \delta_{F,F'+1} \mathbf{B}_{\text{eff}}(r,t) \underbrace{\langle F m_F | \hat{S}^z | F-1, m_F \rangle}_{-\hbar\sqrt{F^2 - m_F^2}/2F \overset{^6\text{Li}}{=} -\hbar\sqrt{2}/3} \right),
\end{aligned}$$

with the relative k-vector $\boldsymbol{\Delta_k} = \boldsymbol{k}_2 - \boldsymbol{k}_1$ and two-photon detuning δ_ω. In the second line the term has been expressed with the single-photon Rabi frequencies to emphasize the relation with respect to the simple 3-level expression in Eq. 4.2.1. Note that the diagonal terms of $\Omega_{Fm_F \leftrightarrow F'm'_F}$ vanish[1] upon time average due to the fast time oscillation δ_ω. For ^{6}Li ($I = 1$) in free space there is, thus, a single Raman coupling rate Ω_{free} coupling the $|F, m_F\rangle = |1/2, 1/2\rangle \leftrightarrow |3/2, 1/2\rangle$ and $|1/2, -1/2\rangle \leftrightarrow |3/2, -1/2\rangle$ states.

$$\Omega_{\text{free}} = \frac{\Omega_{Rm,1}\Omega_{Rm,2}}{2\Delta_{1/2}} \frac{2\sqrt{2}}{9} \frac{E_{FS}}{\hbar\Delta_{3/2}} \sin\phi \tag{4.2.6}$$

We measured our Raman coupling Ω_{free} via coherent Rabi oscillations (Fig. 4.2 B) in a large crossed dipole trap. For low intensities of $I_1 = 0.32\,\text{W/cm}^2$ and $I_2 = 3.2\,\text{W/cm}^2$ we measured $\Omega_{\text{free}} = (2\pi) \cdot 30.6\,\text{kHz}$ [89]. From equation 4.2.4 we obtain from the experimental intensities and detunings $|B_{\text{eff}}| = 43\,\text{mG}$ and $\Omega_{Fm_F \leftrightarrow F-1,m_F} = (2\pi) \cdot 29\,\text{kHz}$, which matches the experimental Raman coupling quite well. In the cooling protocol we use much larger intensities.

Dark state As shown in equation 4.2.5 an oscillating effective magnetic field along the z-axis can only drive $\Delta m_F = 0$ transitions. For our $F = 3/2 \rightarrow F = 1/2$ scheme this results in two states $|F = 3/2, m_F = \pm 3/2\rangle$ that are dark with respect to the Raman coupling, thus those do not participate in the cooling cycle. For a $F \rightarrow F' < F$ transition, this is unavoidable as there are always $2(F - F')$ dark states when coupling to a manifold with fewer states [148]. We also tried the inverted repump scheme (repump on $F = 3/2$, Raman coupling $F = 1/2 \rightarrow 3/2$), which has no dark state. But the repump efficiency α (see Sect. 4.3-4.5) in this case is worse, leading to higher loss and tunneling rates.

The dark states of the Raman coupling are not as detrimental as it might seem as they are not dark to the off-resonant single-photon Raman excitations 4.4.3. These depopulate the dark states and bring the atom back into the cooling cycle. The $n = 0$ state is dark to the $n \rightarrow n - 1$ transfers anyway. Thus, the main effect of the Raman dark states is that half of the ground state is not exposed to the (detuned) $n \rightarrow n$ carrier heating (see Sect. 4.4.4). This compensates

---

[1] There are residual light shifts even for linear polarization. From the hyperfine structure we calculate shifts of about $(2\pi) \cdot 70\,\text{kHz}$ between the $F = 3/2$ and $F = 1/2$ states. Those need to be considered for the 2-photon Raman detuning.

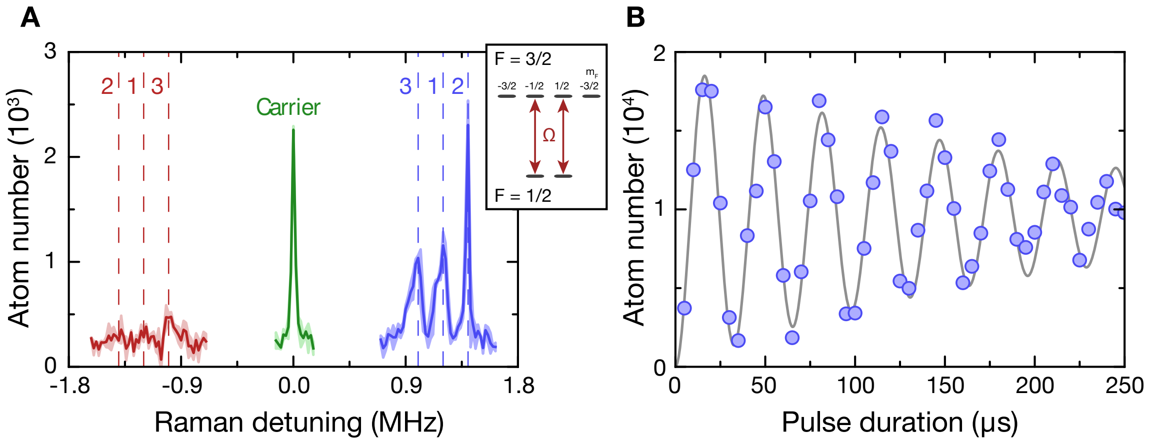

Figure 4.2. Raman processes in the pinning lattice. ***(A)*** *The Raman spectroscopy of the $F = 1/2 \to 3/2$ transition in the 3d pinning lattice shows a carrier transition (green) and one blue sideband per axis. The power of the three axes differ in this measurements to allow for three separate peaks. The red sidebands are strongly suppressed for a cold gas. The shaded area mark the statistical uncertainty.* ***(B)*** *Rabi oscillations on the Raman carrier transition fitted by an exponentially decaying cosine function showing $\Omega_{free} = (2\pi)\cdot 30.6\,kHz$. The central inset shows the coupled m_F states. Figures adjusted from [89].*

most of the effect on the cooling at the expense of a reduced total scattering rate (see Sect. 4.5). The exact role of these Raman dark states needs to be clarified in a careful three-dimensional analysis.

4.2.2 Sideband transitions

As mentioned, the Raman transitions can connect different spatial wave functions while they flip the spin of an atom. The corresponding rate is simply given by the matrix element between the initial h.o. state $\mathbf{n} = (n_1, n_2, n_3)$ and the final h.o. state $\mathbf{n}'$

$$\begin{aligned}\Omega_{\mathbf{n},\mathbf{n}'} e^{\delta_\omega t} &= \langle \mathbf{n}' F' m_F | \mathbf{B}_{\text{eff}}(r,t) \cdot \hat{\mathbf{S}}_{\mathbf{e}} | \mathbf{n} F m_F \rangle \\ &= \Omega_{\text{free}} \langle n_1' n_2' n_3' | e^{-i\boldsymbol{\Delta}_{\boldsymbol{k}} \boldsymbol{r}} | n_1 n_2 n_3 \rangle \\ &= \Omega_{\text{free}} \langle n_1' | e^{-i\eta_{R1}(\hat{a}_1 + \hat{a}_1^\dagger)} | n_1 \rangle \langle n_2' | e^{-i\eta_{R2}(\hat{a}_2 + \hat{a}_2^\dagger)} | n_2 \rangle \langle n_3' | e^{-i\eta_{R3}(\hat{a}_3 + \hat{a}_3^\dagger)} | n_3 \rangle, \qquad (4.2.7)\end{aligned}$$

where the counter-rotating term was dropped and $\hat{a}_i$ ($\hat{a}_i^\dagger$) is the lowering (raising) operator of the h.o. along axis $i = 1, 2, 3$ that forms an angle θ_i with $\boldsymbol{\Delta}_{\boldsymbol{k}}$. The last expression introduced the Lamb-Dicke parameter of the Raman coupling

$$\eta_{R,i} = \sqrt{\frac{\hbar^2 \, |\Delta_k \cos\theta_i|^2}{2m\hbar\omega_0}}, \qquad (4.2.8)$$

which governs the strength of $n \to n' \neq n$ transitions. Note that these are different from the Lamb-Dicke parameter of the repumper η (Eq. 4.1.1). At our geometry the angle is $\theta_i \approx 55°$ for all axes resulting in symmetric couplings in the axis with $\eta_R = 0.25$.

Matrix elements The operator $\hat{D}(i\eta_R) = e^{-i\eta_R(\hat{a}+\hat{a}^\dagger)}$ is the well-know translation operator of coherent states and its matrix elements are given by [149]

$$\begin{aligned} D_{n',n} &= \langle n'|\hat{D}(i\eta_R)|n\rangle = \langle n+\Delta n|e^{-i\eta_R(\hat{a}+\hat{a}^\dagger)}|n\rangle \\ &= \sqrt{\frac{n!}{(n+\Delta n)!}}(i\eta)^{\Delta n} L_n^{\Delta n}(\eta^2)\, e^{-|\eta|^2/2}, \end{aligned} \tag{4.2.9}$$

where $L_n^{\Delta n}(\eta^2)$ are the generalized Laguerre polynomials [150]. In general, this leads to couplings between arbitrary n and n' with amplitudes that oscillate as a function of n, Δ_n and η. Only in the Lamb-Dicke regime ($\eta^2 n \ll 1$) the expression can be simplified:

$$D_{n+\Delta n,n} \approx \frac{(i\eta)^{\Delta n}}{\sqrt{(\Delta n)!}}\sqrt{\begin{pmatrix} n+\Delta n \\ n \end{pmatrix}}\left(1-\frac{1}{2}\left(1+\frac{2n}{1+\Delta n}\right)\eta^2+\dots\right) \tag{4.2.10}$$

$$\approx \begin{cases} -i\eta\sqrt{n}, & \Delta n = -1 \\ 1-\frac{1}{2}\eta^2(2n+1), & \Delta n = 0 \\ i\eta\sqrt{n+1}, & \Delta n = 1. \end{cases} \tag{4.2.11}$$

In the first line, Δn is taken large or equal to zero and $\Delta n < 0$ can be obtained from $D_{n',n} = D_{n,n'}$. For $\eta \approx 0.25$, the expansion is a good approximation for the lowest n, but it quickly breaks down for even medium n leading to higher order coupling at excited h.o. levels. In addition, the couplings shows zero crossings even for $\Delta n = 1$ for specific large n. These prevent e.g. the direct cooling by just ($\Delta n = -1$)-couplings in ion experiments [151]. In our case, this effect plays no role as even in the deep pinning lattice we have only about 10 bound states and, in addition, the anharmonicities of the cosine potential dominate for large n.

For the rest of this chapter we use $\Omega_n = \Omega_1\sqrt{n}$ for our ($\Delta n = -1$)-Raman coupling in analytic expressions and estimations of coupling rates, but take the full expression $\langle \mathbf{n}'|e^{-i\eta_R(\hat{a}+\hat{a}^\dagger)}|\mathbf{n}\rangle$ in the numerical rate equation.

Raman spectroscopy We measured our level spacings $\omega_0 = E_1 - E_0$ of the pinning lattice sites via Raman sideband spectroscopy (Fig. 4.2 A) of the blue sidebands. For the measurement we use a different power in each axis to resolve three individual sidebands and then scale to the power P used for imaging, using (cf. Eq. 2.1.11)

$$\hbar\omega_0 \simeq 2\sqrt{V_0 E_r^{\mathrm{Lat}}} \sim \sqrt{P} \tag{4.2.12}$$

In the center of the lattice, we determine $\hbar\omega_0 = (2\pi)\cdot 1.32(5)\,\mathrm{MHz}$ and a clear decrease of the on-site frequency is visible towards the edges of the cloud, due to the finite waist of the pinning lattice beams of only 60 μm. To compensate for this shift to smaller ω_0 (and for the shift due to the anharmonicity of the sites), we modulate our two-photon detuning from 0.98 MHz to 1.34 MHz. Still this limits the region of the trap that we can image to about 2000 sites.

4.3 Cooling rate

A full description of the Raman sideband cooling process requires a master equation including all 24 states of the 2S and 2P level of the atom and at least the N_b bound states of the 3d harmonic oscillators in the local lattice well with the spin- and spin-orbit-couplings from the three laser beams. While numerically feasible, it is more instructive to separate the full process into suitably chosen subsystems and to analyze these separately.

4.3.1 Master equation 3-level system

The main subsystem of Raman cooling is a three level system consisting of the states $|1,n\rangle, |2,n-1\rangle$ and $|3,n^*-1\rangle$, where n labels the harmonic oscillator levels, while n^* is just a spatial quantum number for the excited state, which has a different optical potential. Depending on the laser wavelength of the optical lattice, the excited state is not even trapped. The ground states are coupled by the two-photon Raman process on the first sideband at a rate $\Omega_n = \Omega_1\sqrt{n}$ and the state $|2,n-1\rangle$ is coupled to some combination of excited P-states called $|3,n^*-1\rangle$ with a Rabi coupling ω_R of the repumper. This is described by the Hamiltonian

$$H = \frac{\hbar}{2}\begin{pmatrix} -2\delta_1 & \Omega_n & 0 \\ \Omega_n & 0 & \omega_R \\ 0 & \omega_R & -2\delta_2 \end{pmatrix}, \tag{4.3.1}$$

where δ_1 is the detuning of the Raman process relative to the sideband and δ_2 describes the repump detuning. For notational simplicity, the couplings are assumed to be real.
The state $|3,n^*-1\rangle$ decays incoherently back to the ground states (for details see section 4.5.2). There is a branching fraction into state $|1\rangle$ called α and the distribution to the different n-levels is given by the matrix elements $\left|D_{n,n'}\right|^2$. In our scheme $\alpha \approx 0.6$, but the value depends on the exact polarizations and detunings of all beams as those set the quantization axis of the system and, thus, determine the excited state $|3\rangle$. In the Lamb-Dicke regime $\left(\eta^2 n \ll 1\right)$ the decay rates are:

- to state $|1,n\rangle$: $\Gamma_{\to 1} \approx \alpha\eta^2 n\Gamma$
- to state $|2,n-1\rangle$: $\Gamma_{\to 2} \approx (1-\alpha)(1-\eta^2(2n-1))\Gamma$
- to all other states: $\Gamma_{\to \text{other}} = \Gamma - \Gamma_{\to 1} - \Gamma_{\to 2}$

Note that for a successful cooling the atom decays to $|1,n-1\rangle$, which is in a different n-manifold and thus included in $\Gamma_{\to \text{other}}$.

The time evolution of the sub-system can be described in the rotating-frame approximation with a modified master equation [152] of the density matrix ρ

$$\frac{d\rho}{dt} = -\frac{i}{\hbar}[H,\rho] + \underbrace{\sum_{i=1,2,\text{other}} \Gamma_{\to i}\left(\sigma_{i3}\rho\sigma_{3i} - \frac{1}{2}\sigma_{33}\rho + \frac{1}{2}\rho\sigma_{33}\right)}_{\mathscr{L}(\rho)} \tag{4.3.2}$$

$$\mathscr{L}(\rho) = \begin{pmatrix} \Gamma_{\to 1}\rho_{33} & 0 & -\Gamma\rho_{13}/2 \\ 0 & \Gamma_{\to 2}\rho_{33} & -\Gamma\rho_{23}/2 \\ -\Gamma\rho_{31}/2 & -\Gamma\rho_{32}/2 & -\Gamma\rho_{33} \end{pmatrix}$$

Solving this equation for the population ρ_{33}, one can determine the total scattering of the n-manifold by

$$\Gamma_{n,\mathrm{eff}} = \rho_{33}\Gamma. \tag{4.3.3}$$

The rate of cooling is given by the fraction that is decaying into the $|1, n-1\rangle$ state (see Eq. 4.2.9)

$$\Gamma_{cool} = \rho_{33}\alpha \left|D_{n-1,n-1}\right|^2 \Gamma \tag{4.3.4}$$

which is still directly proportional to the population of the excited state.

Steady state Note that equation 4.3.2 has no steady-state solution because the 3-level system is not closed (for $\Gamma_{\mathrm{other}} \neq 0$). Instead one can look for solutions with constant decay rates $\dot{\rho} = -\lambda\rho$. As $\dot{\rho}$ is linear in the elements of ρ, this requires to solve for the eigensystem of a 9×9 matrix (3 real diagonal elements, 3 complex off-diagonal elements), which can only be done numerically. In the full system, i.e. taking all n-manifolds, there is, however, additional decay *into* the considered n-manifold, which equals Γ_{other} in a global steady-state situation. It is, thus, helpful to consider $\Gamma_{\to\mathrm{other}} = 0$ i.e. $\Gamma_{\to 1} = \alpha_{n,\mathrm{eff}}\Gamma = \Gamma - \Gamma_{\to 2}$ with an effective branching $\alpha_{n,\mathrm{eff}}$ that depends on the population of all n levels and could be determined self-consistently in a full calculation.
In this case, it is possible to give an analytic solution ρ^{st} to the steady-state equation ($\dot{\rho} = 0$) of Eq. 4.3.2 for arbitrary parameters (cf. [148]):

$$\rho_{33}^{st} = \tag{4.3.5}$$

$$\frac{\omega_R^2\Omega_n^2}{2\Omega_n^2(\Gamma^2 + \Omega_n^2 + (1-\alpha_{n,\mathrm{eff}})(2\delta_1^2 + \omega_R^2) + 4\delta_{12}(\delta_2 - 2\alpha_{n,\mathrm{eff}}\delta_1)) + \alpha_{n,\mathrm{eff}}\left(4\Gamma^2\delta_1^2 + (\omega_R^2 + 4\delta_1\delta_{12})^2\right)}.$$

Here the relative detuning $\delta_{12} = \delta_2 - \delta_1$ was introduced. The resulting scattering rate is now given by

$$\Gamma_{n,\mathrm{eff}} = \Gamma\rho_{33}^{st}, \tag{4.3.6}$$

When the atom decayed to the state $|1, n-1\rangle$, the system lost one vibrational quantum. The total cooling Λ_{Cool} rate can, thus, finally be obtained by adding the processes in the three axis, which remain independent as long as the excitation probabilities are low.

$$\Lambda_{\mathrm{Cool}} = 3\Gamma_{n,\mathrm{eff}}\hbar\omega_0\alpha \left|D_{n-1,n-1}\right|^2 \tag{4.3.7}$$

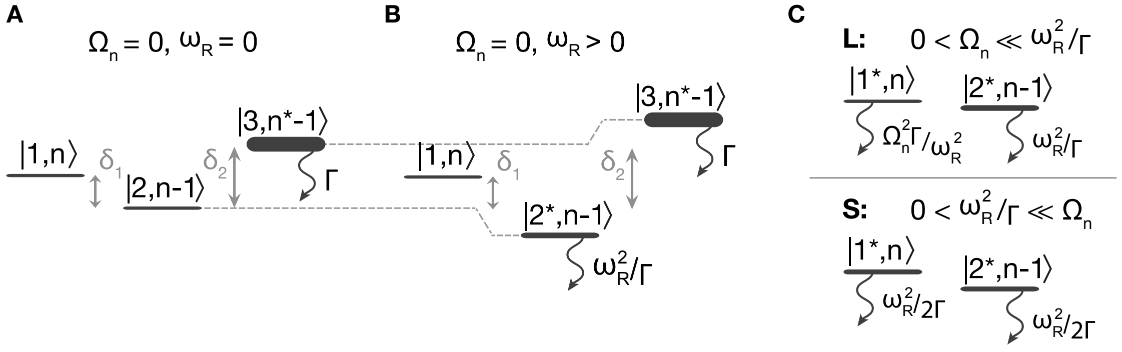

Figure 4.3. Dressed states in n-manifold. ***(A)*** *The three uncoupled dressed states with the 2-photon Raman detuning δ_1 and the repump detuning δ_2.*[1] ***(B)*** *The repump coupling $\omega_R < \Gamma$ weakly mixes states $|2\rangle$ and $|3\rangle$, which gives the state $|2^*\rangle$ a scattering rate ω^2/Γ.* ***(C)*** *For Raman coupling weaker than this rate (L), the scattering of the n manifold (and thus the cooling rate) is quadratic in the Raman coupling Ω_n. For strong Raman coupling, the states $|1\rangle$ and $|2^*\rangle$ mix. The modifications due to finite detunings are captured by expression 4.3.5.*

4.3.2 Dressed state picture

For a typical hierarchy of coupling rates $\Gamma \gg \omega_R \gg \Omega_n$ (see Table 4.1), one can get an intuitive picture for the cooling rate by first dressing the state $|2,n-1\rangle$ with the state $|3,n^*-1\rangle$, which results in a new state $|2^*,n-1\rangle$, that is weakly decaying with a rate $\Gamma_{2^*} = \omega_R^2\Gamma/(\Gamma^2+4\delta_2^2)$. The Raman coupling can then be applied to the effective 2-level system $|1,n\rangle \leftrightarrow |2^*,n-1\rangle$ with a modified detuning (see Fig. 4.3).

Taking Γ much larger than the 2-photon-Raman detuning δ_1 and larger than all couplings, Eq. 4.3.5 simplifies to

$$\rho_{33}^{st} \approx \frac{\omega_R^2\Omega_n^2}{2\Omega_n^2(\Gamma^2+4\delta_2^2)+4\alpha_{n,\mathrm{eff}}\delta_1^2\Gamma^2+\alpha_{n,\mathrm{eff}}(\omega_R^2+4\delta_1\delta_{12})^2} \tag{4.3.8}$$

$$\overset{\delta_1=\delta_2=0}{=} \frac{\omega_R^2\Omega_n^2}{2\Omega_n^2\Gamma^2+\alpha_{n,\mathrm{eff}}\omega_R^4}. \tag{4.3.9}$$

As in a two-level atom, one can identify two regimes, the low-coupling regime (L) and the saturated regime (S) with respect to the Raman laser. At low coupling of the Raman laser (L) the state $|2^*,n-1\rangle$ mixes weakly to the state $|1,n\rangle$ and the scattering rate is linear in the squared Raman Rabi coupling.

$$\Gamma_{n,\mathrm{eff}} = \rho_{33}^{st}\Gamma$$

$$\overset{\Omega_n\to 0}{=} \frac{\omega_R^2\Omega_n^2\Gamma}{\alpha_{n,\mathrm{eff}}\left(4\delta_1^2\Gamma^2+(\omega_R^2+4\delta_1\delta_{12})^2\right)} \tag{4.3.10}$$

$$\overset{\delta_1=0}{=} \frac{\Omega_n^2}{\alpha_{n,\mathrm{eff}}\omega_R^2}\Gamma \tag{4.3.11}$$

---

[1] Both detunings are measured relative to state $|2\rangle$. In our case, where $|1\rangle$ is the energetically higher $F = 3/2$ state and $|2\rangle$ is the $F = 1/2$ state, this means that the absolute frequency of the repumper is $E(|P_{1/2},F = 3/2\rangle)/\hbar - E(|S,F = 1/2\rangle)/\hbar + \delta_2$, while the difference of the two Raman lasers is $E(|S,F = 3/2\rangle)/\hbar - E(|S,F = 1/2\rangle)/\hbar + \omega_0 - \delta_1$.

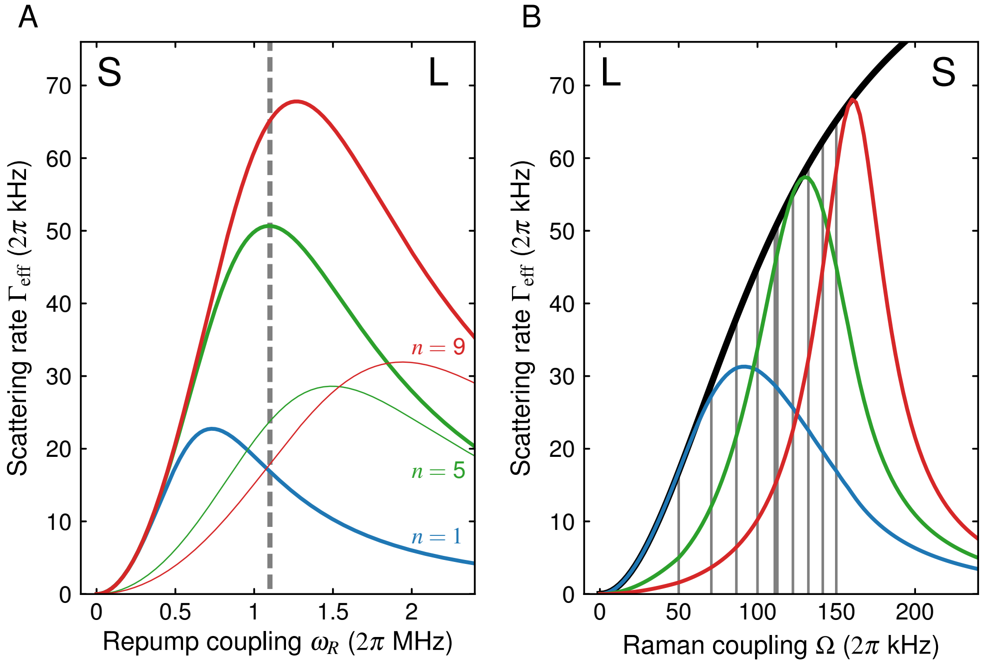

Figure 4.4. Scattering rate of the three level system. *The scattering rate Γ_{eff} is directly proportional to the cooling rate of the Raman sideband process.* ***(A)*** *Scattering rate from the solution of the optical Bloch equation (Eq. 4.3.5) with Raman coupling $\Omega_n = \sqrt{n}\,50\,(2\pi\ kHz)$ for three $[n,(n-1)]$-manifolds as a function of the resonant ($\delta_2 = 0$) repump coupling ω_R. The bold lines show the behavior for a Raman coupling resonant on the red sideband ($\delta_1 = 0$), while the thin lines take into account the anharmonicity of the lattice wells, $\delta_1 \approx n \cdot 32\,(2\pi\ kHz)$. At low repump power the Raman laser saturates the $|1\rangle \leftrightarrow |2^*\rangle$ transition (S) and at strong repump power the Raman transfer is suppressed by the strong decay of $|2^*\rangle$ (L). The dashed gray line marks the experimental value of the repump coupling of $(2\pi)\cdot 1.1\,MHz$.* ***(B)*** *Scattering rate at a repump coupling of $(2\pi)\cdot 1.1\,MHz$ vs Raman coupling Ω. The bold black line gives the result for $\delta_1 = 0$ and $\delta_2 = 0$ and the vertical gray lines mark the $n \rightarrow n-1$ couplings of the $n = 1$ to $n = 9$ h.o. states (left to right). The colored lines take into account the anharmonicity of the wells $\delta_{ah,n}$ by linking the Raman coupling to the levels $n(\Omega)$ at $\Omega_0 = (2\pi)\cdot 50\,kHz$ and setting $\delta_1 = \delta_{ah,n} + \Delta_0$. In the experiment we linearly scan Δ_0 from 0 kHz (blue) via 180 kHz (green) to 360 kHz (red) in a modulation at 20 kHz to successively address the different levels. The crossings of the vertical lines with the colored curves give an estimate for the scattering rate of state n at given Δ_0.*

The inverse scaling with the repump power is due to the Quantum-Zeno like suppression [153, 154] of population from the $|2^*, n-1\rangle$ state. The $\alpha_{n,\mathrm{eff}}^{-1}$ dependency reflects the fact that many photons can get scattered for a single Raman transfer if the decay rate back to state $|1\rangle$ is low. Because the cooling rate is proportional to $\alpha\Gamma_{n,\mathrm{eff}}$, the cooling is unaffected by the branching α (assuming $\alpha_{n,\mathrm{eff}} \approx \alpha$) in this regime.

In the opposite limit (S), where the Raman coupling is strong compared to the decay rate Γ_{2^*}, one obtains a saturation of the scattering rate at half of Γ_{2^*} as the ground states fully mix.

$$\Gamma_{n,\mathrm{eff}} \overset{\Gamma\Omega_n \gg \omega_R^2}{=} \frac{\omega_R^2}{2\Gamma} \frac{\Omega_n^2}{\Omega_n^2(1+4\delta_2^2/\Gamma^2)+2\alpha_{n,\mathrm{eff}}\delta_1^2} \tag{4.3.12}$$

$$\frac{\omega_R^2\Omega_n^2}{\Gamma(\Omega_n^2(1+4\delta_2^2/\Gamma^2)+4\alpha_{n,\mathrm{eff}}\delta_1^2)} \tag{4.3.13}$$

$$\overset{\delta_1=\delta_2=0}{=} \frac{\omega_R^2}{2\Gamma} \tag{4.3.14}$$

Thus, the scattering rate goes to zero for very small and very strong repump couplings ω_R with a clear maximum at values on the order of $\sqrt{\Omega_n\Gamma}$ (see Fig. 4.4).

Because the Raman coupling increases with the level n while the repumper is independent of n, the repump power can not maximize the cooling on all levels simultaneously. The ideal repump power, thus, depends on the regime one wants to optimize. For fluorescence imaging it only matters not to occupy the large n values, therefore one chooses a repump power which for a given Raman couplings Ω_n puts the low n states into regime L, optimizes the medium n and puts the high n into regime S (see Fig. 4.4 A).

Next, we compare this cooling rate per level to the sum of all heating processes. Some of those are directly linked to the cooling process like the recoil of the scattered photon that closes one cooling cycle. Other like the off-resonant Raman scattering are only indirectly linked and show a different scaling with the input parameters e.g. the detuning or power of the Raman beams. Thus, those these allow for an optimization fo $\Lambda_{\mathrm{Cool}}/\Lambda_{\mathrm{heat}}$.

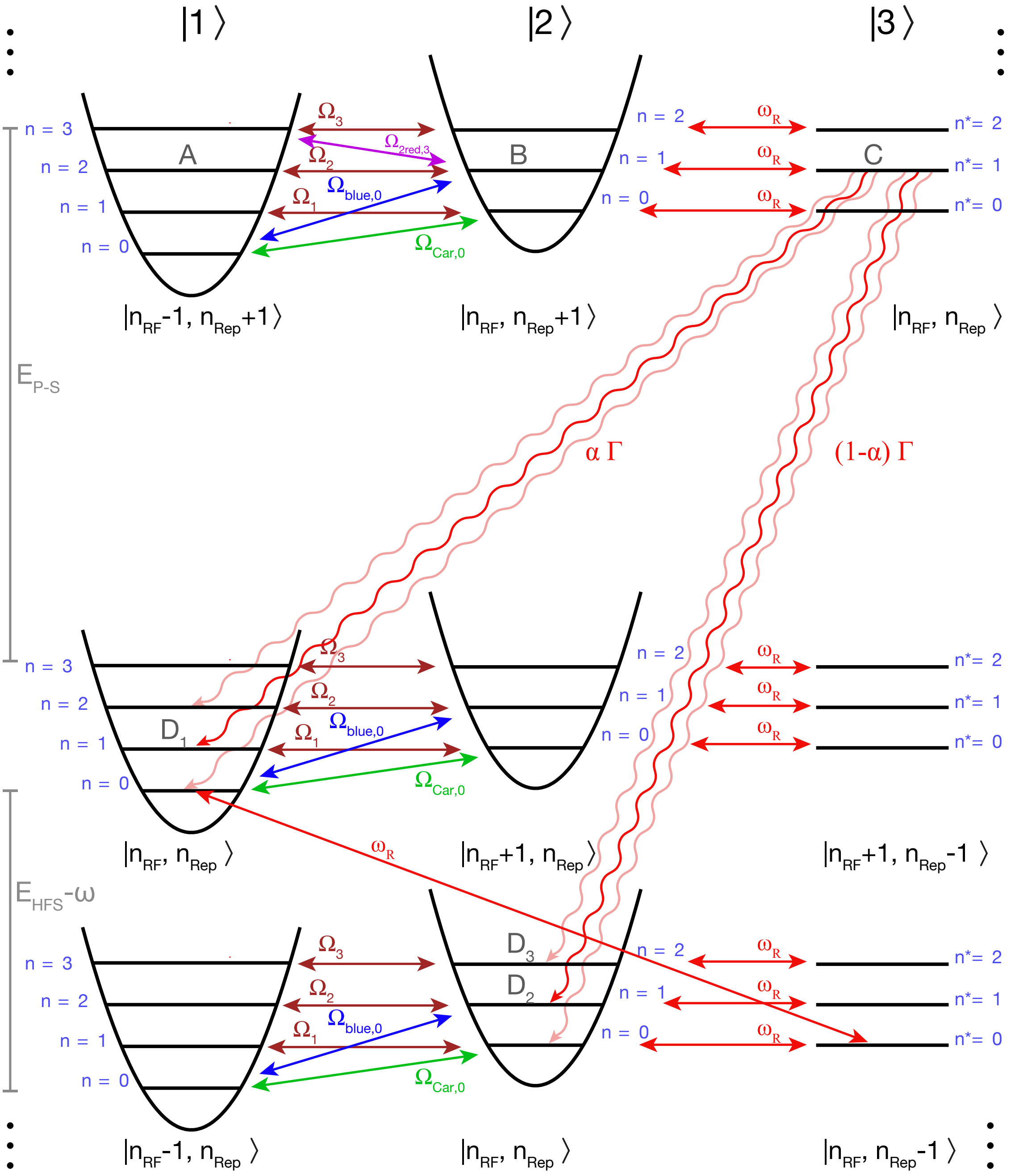

Figure 4.5. Illustration of couplings and decays for Raman sideband cooling. *Atomic states $|1\rangle$, $|2\rangle$ and $|3\rangle$, dressed with the effective second order Raman photons n_{RF} and the optical repump photon n_{Rep}, produce two ladders of states. Shown are three sets sorted by energy for $\delta_1 = 0$ and $\delta_2 = 0$. Horizontal couplings are resonant, while tilted arrows mark detuned couplings. Spontaneous decay exists for all excited states, with branching to the states $|1\rangle$ and $|2\rangle$ with a ratio α and between different h.o. levels with $\eta^{2|\Delta n|}n$. Only a selection of couplings is drawn.*
An atom starting e.g. in the state $|1, n = 2\rangle$ (A) is transferred to the $|2, n = 1\rangle$(B) via a Raman coupling Ω_2 and is then excited to state $|3, n^* = 1\rangle$(C). If it decays to $|1, n = 1\rangle$ (D_1), one cooling step was successful, but it can also decay to $|2, n = 1\rangle$ (D_2), where another repump photon is required, or to $|2, n = 2\rangle$ (D_3) on a sideband (light red).

4.4 Heating rates

In addition to the main cooling process considered in the last section, there are many inevitable heating processes associated with Raman cooling. Figure 4.5 gives an overview of resonant and off-resonant couplings, which lead to cooling but also to heatings. The following estimate of their heating rates shows that most of them are rather irrelevant in our parameter regime (see Table 4.1), but they should be considered in a general planning of a Raman cooling setup.

4.4.1 Photon recoil

Photon absorption Every photon absorbed by the atom leads to a kick due to the momentum $\hbar\mathbf{k}^\gamma$ of the photon. If the atom has initially a mean momentum $\mathbf{p}$, the final momentum is $\mathbf{p}+\hbar\mathbf{k}^\gamma$ and the energy changes by $E_r^\gamma + \hbar\mathbf{k}\cdot\mathbf{p}/m$. For an atom in any h.o. eigenstate $|n\rangle$, the initial momentum is zero, so the heating rate due to absorptions, Λ_{ar}, from the Raman cooling (repump beam) is one recoil energy times the total scattering rate $\Gamma_{n,\mathrm{eff}}$.

$$\Lambda_{ar} = \Gamma_{n,\mathrm{eff}} E_r^\gamma \tag{4.4.1}$$

It is, thus, directly proportional to the cooling rate Λ_{Cool}. Note that absorption heating is not isotropic but only affects the axis of the repump beam. In the case of insufficient cooling, this leads to a tunneling of the atoms in this direction once they reached high h.o. levels. This can be observed in tunneling measurements, where one sees the atoms being *pushed out* by the repump beam.

Photon emission Also the emitted photons have a recoil which heats the atom with the same strength as an absorbed photon, but isotropically with $\frac{1}{3}E_r^\gamma$ on average per h.o. axis.

$$\Lambda_{er} = \Gamma_{n,\mathrm{eff}} E_r^\gamma \tag{4.4.2}$$

4.4.2 P-state evolution

The optical potential due to the lattice felt by the excited P-state is different from the ground state because the P-state has a different polarizability. Thus, even without a momentum recoil the atom is not in an eigenstate of its potential once excited to the P-state. This leads to a time-evolution of the wave-function until it decays back into the ground state. In this following, we estimate this time evolution and its heating effect.

In the harmonic approximation, the 1d-Hamiltonian of the excited state can be written as

$$\hat{H}_P = \frac{\hat{p}^2}{2m} + \frac{1}{2}m\omega_P^2\hat{x}^2 = \hbar\omega_P\left(\hat{a}_P^\dagger\hat{a}_P + \frac{1}{2}\right) \tag{4.4.3}$$

$$= \frac{\hbar}{4\omega_0}\Big(2(\omega_P^2+\omega_0^2)\hat{a}^\dagger\hat{a} + (\omega_p^2-\omega_0^2)(\hat{a}^\dagger\hat{a}^\dagger + \hat{a}\hat{a})\Big) + c, \tag{4.4.4}$$

where in the last line the h.o. operators of the P-state $\hat{a}_P$ are replaced[1] by the ground state operators $\hat{a}$ and the constant term is called c. Such a Hamiltonian induces $n \to n\pm 2$ transitions. For lithium $\omega_P \approx 0.86\omega_0$ in a 1064 nm lattice, thus the effect is small. In the case of an

---

[1] $\hat{a}_P^\dagger = \frac{1}{2\sqrt{\omega_0\omega_P}}\left((\omega_P+\omega_0)\hat{a}^\dagger + (\omega_P-\omega_0)\hat{a}\right)$.

anti-confinement of the P-state (e.g. for near resonant optical lattices or 1064 nm lattices for potassium [31]), the trap frequency ω_P becomes complex and the heating effect can be detrimental.

For a harmonic potential the exact propagator is well known [155]

$$U(x,x',t) = \langle x'|e^{-i\hat{H}_p t/\hbar}|x\rangle = \left(\frac{m\omega_p}{2\pi i\hbar\sin\omega_p t}\right)^{1/2} \exp\left(\frac{i}{2\hbar\sin\omega_p t}\left((x^2+x'^2)\cos\omega_p t - 2xx'\right)\right). \tag{4.4.5}$$

With the h.o. wave functions of the ground state potential, $\Psi_n(x)$, one can calculate the transition matrix elements, $U^P_{n',n}$, after arbitrary times t. As the lifetime in the excited state $\tau = 1/\Gamma$ is short compared to typical trap frequencies, an expansion in $\omega^* t$ gives the relevant dynamics, where ω^* is the larger one of the two h.o.frequencies[1]:

$$U^P_{n,n+2}(t) = \int dx \int dx' \Psi^*_n(x')\Psi_{n+2}(x)U(x,x',t) \tag{4.4.6}$$

$$= i\frac{\sqrt{(n+1)(n+2)}}{4}\frac{\omega_0^2-\omega_p^2}{\omega_0}t + \mathcal{O}\left(\left(\frac{\omega_0^2-\omega_p^2}{\omega_0}t\right)^2\right) \tag{4.4.7}$$

All other matrix elements with even Δn scale with higher powers of $\omega^* t$ and all elements with Δn odd are zero due to parity. The heating rate Λ_P due to the P-state evolution can now be estimated by averaging the transition probabilities with the decay function $e^{-t/\tau}/\tau$ and multiplication with the scattering rate $\Gamma_{n,\mathrm{eff}}$ and energy gain $(2\hbar\omega_0)$:

$$\Lambda_{P,n} = \Gamma_{n,\mathrm{eff}} \int_0^\infty \frac{dt}{\tau}(2\hbar\omega_0)\left(\left|U^P_{n,n+2}(t)\right|^2 - \left|U^P_{n-2,n}(t)\right|^2\right)e^{-t/\tau} \tag{4.4.8}$$

$$= \left(n+\frac{1}{2}\right)\underbrace{\hbar\frac{(\omega_p^2-\omega_0^2)^2}{\omega_0}\tau^2}_{A_P}\Gamma_{n,\mathrm{eff}} + \mathcal{O}\left((\omega^*\tau)^4\right) \tag{4.4.9}$$

Once excited, the time-evolution happens in all three axis simultaneously, thus the total heating rate is

$$\Lambda_{P,\mathbf{n}} \backsimeq \left(n_x+n_y+n_z+\frac{3}{2}\right)A_P\Gamma_{n,\mathrm{eff}}. \tag{4.4.10}$$

For a given ratio of polarizabilities of S and P states $\chi \equiv \alpha_P/\alpha_S$, one obtains

$$A_P = (\chi-1)^2\hbar\omega_0(\omega_0\tau)^2 \tag{4.4.11}$$

because $\alpha_{S/P} \sim \omega^2_{0/P}$. The heating shows a strong ω_0^3 scaling with the on-site frequency leading to strong heating at a *small* Lamb-Dicke factor.

This analysis is based on time evolution in the P-state without laser couplings, so it is only valid for weak driving of the repumper ($\omega \ll \Gamma$). In the case of strong driving, one needs to consider the dressed state time-evolution instead, where the atom experiences an averaged S+P-potential. This allows to reduces this heating effect significantly with a strong, detuned repump beam as demonstrated for potassium [31]. Even imaging without cooling is possible in this case for very large positive χ as in ^{174}Yb [131, 156].

---

[1] For larger confinement in the ground state ($\omega_0 > \omega_p$), the almost free expansion of the wave packet given by ω_0 dominates, while for strong ω_p, the P-confinement gives the relevant time scale.

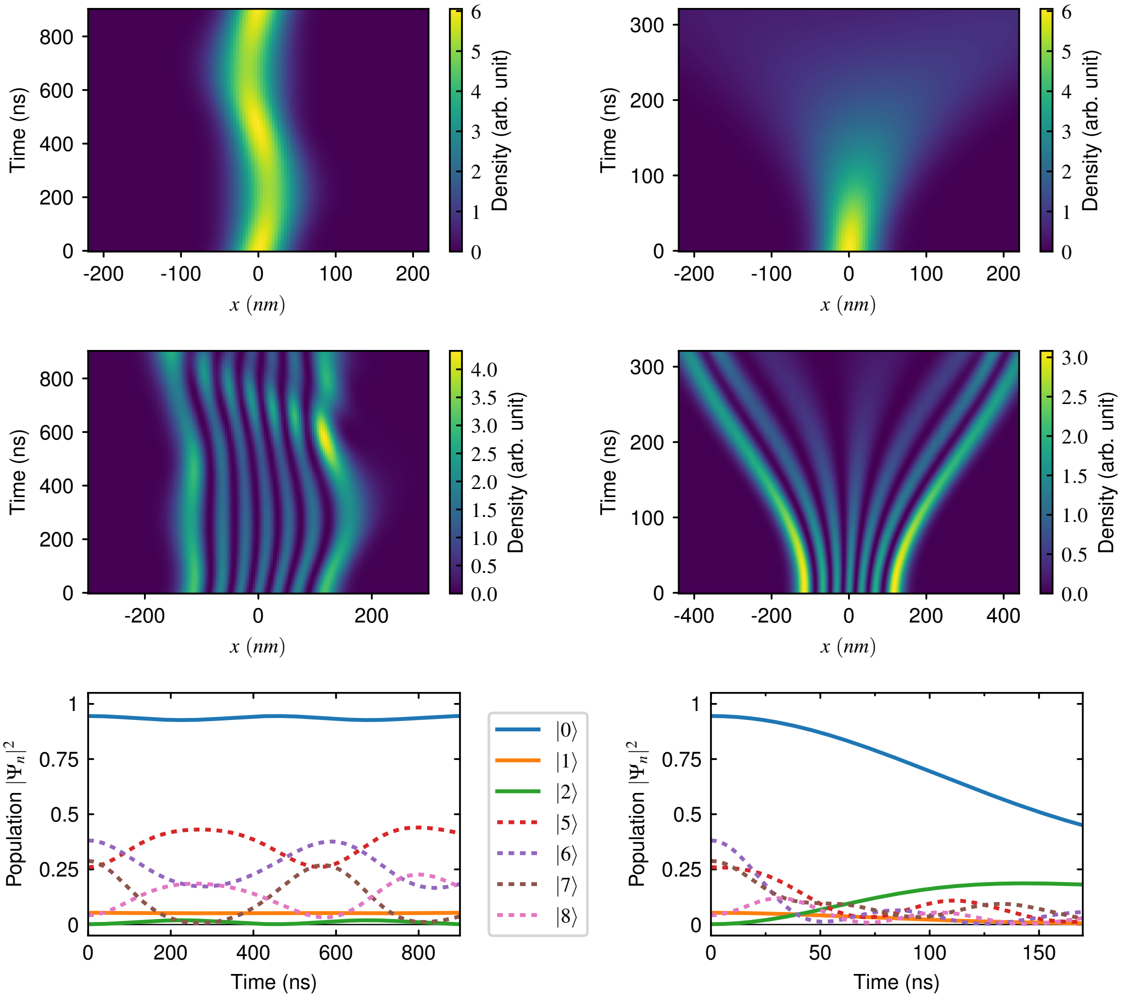

Figure 4.6. Time evolution of the P-state. *A ground state atom starting in an h.o. eigenstate* $n = 0$ ***(first row)*** *or* $n = 6$ ***(second row)*** *absorbs a photon a time* $t = 0$ *and is excited to the P state. In a 1064 nm lattice for lithium* ***(first column)*** *the optical potential is only 25% weaker than in the ground state. The time evolution of the real space density* $|\Psi_n(x)|^2$ *mainly reflects the momentum kick by the photon and shows a weak breathing due to the changed trap frequency. The evolution of the overlap with the S-state h.o. eigenstates* ***(bottom row)*** *shows how much stronger the levels mix for the initial* $n = 6$ *state (dashed) compared to* $n = 0$ *case (solid). The distribution at* $t = 0$ *is due to the recoil of the absorbed photon and the lifetime in the P-state is 27.1 ns. The* ***second column*** *shows the dramatic effect if the P-state potential is the inverse of the S-state potential (near resonant case). The unbound wave function rapidly expands and is even accelerated outwards, causing large heating in such a lattice.*
Simulation are done by exact diagonalization of 3 sites of a lattice with $d = 532$ *nm and 517* E_r^{Lat} *depth (in the S-state) with 3.8 nm grid and an energy cut at* $1700\,E_r^{\mathrm{Lat}}$.

Our system For lithium in a 1064 nm lattice $\chi = 0.75$ (based on [157]) and at $\omega_0 = 1.3\,\mathrm{MHz}$ one gets $A_P = 0.058\,E_r^{\gamma}$ from Eq. 4.4.9. Corrections at higher orders of τ in a h.o. reduce the value to $A_P = 0.051\,E_r^{\gamma}$. Due to the anharmonicity, the effect is higher for an atom in a lattice well. Numerics, which include the photon recoil at absorption, confirm the form of equation 4.4.10 and give $A_P = 0.11\,E_r^\gamma$ for the repump axis and $A_P = 0.067\,E_r^\gamma$ in the other two axes with our parameters.

In summary, an atom in state $|n_x, n_y, n_z\rangle$ suffers from a total energy increase due to momentum transfers of absorption and emission and from the P-state evolution for the scattering of a single photon given by

$$E_{ph} = 2E_r^\gamma + \left(n_x + n_y + n_z + \frac{3}{2}\right) A_P \Gamma_{n,\mathrm{eff}}. \tag{4.4.12}$$

Inserting our experimental number, one obtains[1]

$$\begin{aligned} E_{ph} &= \Big((1.38 + 0.11 n_x) + (0.36 + 0.067 n_y) + (0.36 + 0.067 n_z)\Big) E_r^\gamma && (4.4.13)\\ &= \Big(2.1 + 0.11 n_x + 0.07(n_y + n_z)\Big) E_r^\gamma. && (4.4.14)\end{aligned}$$

The distribution of the energy into the three axes (first line) shows that the majority of heating always goes to the repump axis. The additional heating caused by the P-state evolution is for us about 10% (65%) of a recoil energy per photon in the $n = 0$ ($n = 5$) state.

Near resonant pinning lattice However, in our first approach to single-atom imaging with lithium in the year 2014, we used a near resonant pinning lattice (few 10 GHz detuned). In that case $\chi = -1$ (two level atom) and the P-state heating per photon at high lattice depths is very strong. In good agreement with Eq. 4.4.11, numerics in such a lattice give (see Fig. 4.6)

$$\begin{aligned} E_{ph}^{\chi=-1} &\approx \left(8.6 + 3.6 \textstyle\sum_i n_i\right) E_r^\gamma \\ &\approx \left(0.49 + 0.21 \textstyle\sum_i n_i\right) \hbar\omega_0, \quad \text{at}\, \omega_0 = (2\pi\hbar)\cdot 1.3\,\mathrm{MHz}, \end{aligned} \tag{4.4.15}$$

where the first line expresses the heating in units of a photon recoil and the second in units of the level spacings. Already in the 2nd excited h.o. state, the heating almost cancels the maximum cooling of $1 \cdot \omega_0$ per photon, which makes Raman-cooling at these parameters impossible. Due to $A_P \sim \omega_0^3$ the effect strongly decreases with smaller trap frequencies, which we tried. But this results in a worse Lamb-Dicke parameter η and increases tunneling rates (see Sect. 4.5.3), which prevented us from successful imaging and let us switch to the high power, far-detuned lattice. We, however, did not try a detuned repump beam, which might have helped. Even though the anti-confinement for potassium at 1064 nm is much worse ($\chi = -5.4$ [31]), one needs to consider that the ratios of resonant p-heating to cooling are four times worse for a near resonant lithium lattice compared to potassium at the same η due to the much higher frequencies.

The general scaling of the relevance of the P-evolution is

$$\Lambda_P / \Lambda_{Cool} \propto (\chi - 1)^2 m^{-2} \eta^{-4}, \tag{4.4.16}$$

where m is the mass of the atom, $\chi = \alpha_P/\alpha_S$ is the ration of the polarizabilities and η is the Lamb-Dicke factor.

---

[1] Calling the repump axis x here.

4.4.3 Off-resonant scattering

There are additional heating effects due to off-resonant scattering from laser beams like the Raman beams or the lattice beams.

Raman beams The Raman beams cause an off-resonant scattering rate due to their finite detuning Δ_{Rm} from the D-lines. Every photon heats the atom by an energy E_{ph} as derived above. The heating rate is therefore given by

$$\Lambda_{\text{sc. Rm}} = \Gamma \frac{\Omega_{Rm,1}^2 + \Omega_{Rm,2}^2}{4\Delta_{Rm}^2} E_{ph} \tag{4.4.17}$$

with the single-photon Rabi frequencies $\Omega_{Rm,i}$ of the two Raman beams. For similar strength of the two Raman beams $\Omega_{Rm,1}^2 \approx \Omega_{Rm,1}^2$, this scales proportional to the 2-photon Raman coupling (cf. Eq. 4.2.1) $\Lambda_{\text{sc. Rm}} \sim \Omega_n/\Delta_{Rm}$, while for very different intensities there is a quadratic dependence $\Lambda_{\text{sc. Rm}} \sim \Omega_n^2/\Omega_{Rm,\text{weak}}^2$. Therefore, it is advisable to use similar strength in both beams.

Repump beam In addition, there is off-resonant scattering from the repump beam on the other F-manifold with a detuning $\Delta_R \approx E_{HFS}$ leading to a heating rate

$$\Lambda_{\text{sc. Rp}} = P_1 \Gamma \frac{\omega_R^2}{4\Delta_R^2} E_{ph} \tag{4.4.18}$$

where P_1 is the fraction of population in the $|1\rangle$ state, which is close to one for a good dark state $|1,0\rangle$. At an optimum repump coupling $\omega_R^2 \sim \Omega_n \Gamma$, this heating rate scales only like $\sim \Omega_n$ and, thus, slower than the cooling rate and it is therefore most relevant at low Raman couplings. But its absolute value is small even for lithium with its small hyperfine splitting (see Table 4.1).

Lattice beams The heating due to off-resonant scattering from the lattice beams is given by [84]

$$\Lambda_{\text{sc. Lat}} \simeq 3 \frac{\Gamma\, V_0}{\hbar \Delta_{\text{Lat}}} \left(\frac{\omega_{\text{Lat}}}{\omega_{\text{Atom}}} \right)^3 E_{ph}, \tag{4.4.19}$$

with the lattice depth V_0 per axis, the lattice laser detuning Δ_{Lat}, the atomic resonance frequency ω_{Atom} and the lattice laser frequency ω_{Lat}. The factor of 3 arises from the sum over three axes and the counter-rotating term has been ignored as the heating term is negligible in the far detuned case anyway. For our current setup, we get scattering from the lattice of only 2 Hz, so this contribution is ignored for the rest of the analysis.

4.4.4 Off-resonant Raman couplings

Carrier transitions The 2-photon Raman coupling also leads to transfers on the carrier ($n \to n$) which are detuned by one h.o. frequency ω_0. While the transfer conserves energy, there is heating from the repump photons. With the assumption that the carrier coupling $\Omega_{\text{carrier},n}$ is much smaller than the on-site frequency, one obtains with the decay rate of the dressed state $|2^*, n\rangle$ ($\Gamma_{2^*} \approx \omega_R^2/\Gamma$) state:

$$\Lambda_{\text{carrier}} = P_1 \frac{\omega_R^2}{\Gamma} \frac{\Omega_{\text{carrier},n}^2}{4\omega_0^2} E_{ph}. \tag{4.4.20}$$

Blue transitions In addition there can be detuned transfers on the blue sideband of the Raman process ($n \to n+1$). These heat by one h.o. quanta, but occur at a much lower rate given by the coupling $\Omega_{\text{blue},n}$ to the detuning $2\omega_0$

$$\Lambda_{\text{blue}} = P_1 \frac{\omega_R^2}{\Gamma} \frac{\Omega_{\text{blue},n}^2}{16\omega_0^2} \hbar\omega_0. \tag{4.4.21}$$

The recoil heating for the repump process has been ignored in this case.
Note that both of these processes scale like $\sim \Omega_n^2 \omega^2 \Gamma$, which becomes Ω_n^3 for a optimal repumper ($\omega^2 \sim \Omega_n \Gamma$). Thus, as soon as one of these processes dominates the heatings, the ratio of cooling to heating decreases quickly with stronger Raman coupling.
The contribution from even higher blue sidebands of the Raman coupling scale like $\frac{\eta^{2\Delta n}}{\Delta n} \binom{n+\Delta n}{n}$, so they are less relevant for $\eta \lesssim 0.5$ and can be ignored in most cases.

Cooling on doubly red transitions With the Raman beams tuned closed to the first red sideband, also couplings on the second red transition need to be considered. Here the energy is lowered by $2\hbar\omega_0$, but the coupling rate is a second order transfer $\Omega_{\text{2red},n} \approx \Omega_{\text{carrier},0} \eta^2 \sqrt{n(n-1)}$:

$$\Lambda_{\text{2red}} = P_1 \frac{\omega^2}{\Gamma} \frac{\Omega_{\text{2red},n}^2}{4\omega_0^2} \hbar\omega_0 \tag{4.4.22}$$

For simplicity we will treat this as a negative contribution to the heating rate.

4.4.5 Rescattering

An atom can scatter a photon that has been emitted from another atom. If the other atom has been excited resonantly followed by a decay to state i, the photon is resonant for state i. Summing over all occupied lattice sites (x,y) with relative distance d_{xy} one can estimate the heating rate by

$$\begin{aligned}
\Lambda_{\text{resc}} &= (P_1\alpha + P_2(1-\alpha))\Gamma_{\text{sc.total}} \sum_{x,y}^{\text{occ.}} \frac{\sigma}{4\pi d_{xy}^2} E_{ph} \\
&= (P_1\alpha + P_2(1-\alpha))\Gamma_{\text{sc.total}} \frac{\sigma\rho}{4\pi} \sum_{i,j\neq(0,0)}^{R} \frac{1}{i^2+j^2} E_{ph} \\
&\approx (P_1\alpha + P_2(1-\alpha))\Gamma_{\text{sc.total}} \frac{\sigma\rho}{2} \log(R) E_{ph}.
\end{aligned} \tag{4.4.23}$$

Here $\Gamma_{\text{sc.total}}$ is the total scattering rate per atom, $\sigma \approx 0.1 \cdot 3\lambda_{\text{Atom}}^2/2\pi$ is the scattering cross section of an atom for unpolarized light on the D_1 line, R denotes the radius of the atomic cloud in lattice spacings and ρ is the atomic 2d-density. In the last line the sum was approximated by an integral over an circle with radius R. In our system the rescattering has only a minor relevance, but for large systems with small lattice spacing or in 3d lattices it can become important.

4.4.6 Repumping of state 2^*

For $\alpha < 1$, it can take more than one photon to pump the atom back into state $|1\rangle$. Every time the atom is decaying from the excited state there a chance $(1-\alpha)$ to decay to the state $|2^*\rangle$,

Property level n	Level n 0	 1	 2	 5	 9	Unit
Recoil heating cooling cycle	0	251	491	1040	1060	μK/ms
P-state heating cooling cycle	0	41	123	526	904	μK/ms
Raman carrier	150	143	128	83	36	μK/ms
Raman blue	7	14	21	41	69	μK/ms
Raman off-resonant	32	34	35	40	47	μK/ms
Repump off-resonant	1	1	1	2	2	μK/ms
Rescattering	3	3	3	4	4	μK/ms
Repump 2^* state	29	225	442	1080	1360	μK/ms
Raman double-red	0	0	-2	-17	-72	μK/ms
SUM heating INT	0	486	1020	2610	3270	μK/ms
SUM heating EXT	221	226	220	192	135	μK/ms
Cooling	0	-3450	-6760	-14300	-14600	μK/ms
Anharmonicity	-	0	-32	-136	-302	$(2\pi\hbar)$ kHz
$\Gamma_{n,\text{eff}}$	0	9	17	36	37	(2π) kHz
Γ_{heat}	1.4	1.3	1.2	0.9	0.6	(2π) kHz

Table 4.1. Heating and cooling rates at Raman sideband cooling. *The cooling and heating rates in different levels, anharmonicities ($E_n - E_{n-1} - \hbar\omega_0$) of the wells as well as photon scattering rates. The values are calculated for our ^{6}Li system in a $517\,E_r^{Lat}$ deep 532-nm lattice ($V_0 = -730\,\mu K$, $\omega_0 = (2\pi)\cdot 1.3\,MHz$) with a Raman coupling $\Omega_1 = (2\pi)\cdot 50\,kHz$, whose 2-photon detuning is modulated between ω_0 and $\omega_0 - 360\,kHz$. The repumper has an intensity of 0.6 mW/cm^2 ($\omega_R = (2\pi)\cdot 1.1\,MHz$) and is resonant on the $|2\rangle \to |3\rangle$ transition including the light shift of the lattice. The Raman beams have intensities of 210 and 20 kW/cm^2 and are 7.3 GHz red detuned to the D_1 transition. For the rescattering rate a Mott insulator with 200 atoms in the 1.15 μm physics lattice is assumed. Values are given for the axis along the repump direction, which has the largest heatings. All heatings related to photon recoil are about a factor of 4 lower in the other 2 axis. To get the scattering rates from all axes the last two rows need to be multiplied by three.*

which is not part of the cooling cycle. Due to the decay rate Γ_{2^*}, it will quickly scatter another photon that can bring it back to a state $|1^*, n\rangle$. These repump photons have to be taken into account as a heating source

$$\Lambda_{\text{Repump}} = P_2 \Gamma_{2^*} E_{ph} \approx \frac{1-\alpha}{\alpha} \left(\Gamma_{n,\text{eff}} + \Gamma_{\text{heat}}\right) E_{ph} \tag{4.4.24}$$

The population P_2 of this state will be determined in the next section from the scattering rates (Eq. 4.5.7) and the last expression is valid for $\Gamma_{2^*} \gg \Gamma_{n,\text{eff}}$, when $P_2 \sim 1/\Gamma_{2^*}$. For definition of Γ_{heat} see Eq. 4.5.1.

4.4.7 Summary

Table 4.1 lists the heating and cooling rates in different levels for our system. For all but the lowest level the cooling is much stronger than the heating, so we are operating in a regime where hot atoms will on average be cooled down. The cooling actually exceeds the heating rates by almost an order of magnitude.

The main heating contributions arise from the scattering of photons in the cooling cycle. These are summed as heating INT as they are inevitably linked to the cooling rate and just lower the cooling per photon. The other heating rates are summed as heating EXT. These show different dependencies on the input parameters and their ratio to the cooling should be minimized. Note that the 2^*-repump contribution is split between INT and EXT. With our parameters, the Raman carrier coupling is the main external source of heating at $n < 6$.

Although we start in the lowest band and the cooling is much stronger than the heating, we see atoms that are lost or move during imaging. This counter-intuitive behavior can be resolved by considering that the cooling and heating rates are only statements about the mean of a distribution. Raman cooling is a driven system without a bath for thermalization. Therefore, the heating and cooling rates make no direct statement about the width of the distribution. Even with a very high ground state fraction, the distribution can show a finite population in the untrapped highly excited states. To investigate this, a full rate equation with $n \to n'$ couplings is analyzed in the next section.

4.5 Rate equation

4.5.1 Setup

A rate equation treats states and the classical incoherent transitions between them. In order to correctly include the coherent Raman couplings, we work with the dressed states introduced in section 4.3.2.

- The state $|1^*,n\rangle$ consists of the state $|1,n\rangle$ with an admixture of $|2,n-1\rangle$ from the Raman coupling and an admixture of $|3,n^*-1\rangle$ from the repumper. It has a scattering rate of $\Gamma_{n,\text{eff}}$ and preferentially decays to $|1^*,n-1\rangle$ in the deep Lamb-Dicke regime at large α. $|1^*,0\rangle = |1,0\rangle$ is the ground state, which is dark except for heating processes.
- The state $|2^*,n\rangle$ consists of the state $|2,n-1\rangle$ with an admixture of $|1,n\rangle$ from the Raman coupling and an admixture of $|3,n^*-1\rangle$ from the repumper. It has a scattering rate of Γ_{2^*} and preferentially decays to $|1^*,n-1\rangle$ in the deep Lamb-Dicke regime at large α.

These states are mainly coupled to other levels by the incoherent scattering of photons either in the cooling cycle or from one of the heating sources (Sect. 4.4). The coherent coupling e.g. on the Raman carrier transition can be treated as an incoherent scattering rate as well, as long as its coupling is weak compared to either the detuning ($\approx \omega_0$) or the decay rate Γ_{2^*} of the coupled state $|2^*\rangle$.

Instead of heating/cooling rates (energy/time), we turn to a description of rates between states (population/time). Thus, we combine all heating rates that are not directly linked to the cooling process (Off-resonant scatterings, off-resonant Raman couplings, rescattering)[1] into a single heating scattering rate Γ_{heat} per axis:

$$\Gamma_{\text{heat}} \equiv \left(\Lambda_{\text{sc. Rm}} + \Lambda_{\text{sc. Rp}} + \Lambda_{\text{carrier}} + \Lambda_{\text{blue}} + \Lambda_{\text{resc}} - \Lambda_{\text{2red}}\right) \frac{\alpha}{3E_{ph}} \tag{4.5.1}$$

The heating is only weakly dependent on the level n (see Table 4.1). Thus, it can be well approximated by the $n=0$ rate, where it is most relevant (approximation could easily be relaxed).

The cooling scattering rate $\Gamma_{n,\text{eff}}$ (Eq. 4.3.3) on the other hand has a strong dependence on n due to its sensitivity to the Raman coupling Ω_n and the detuning δ_1 as derived in section 4.3. As we are interested in hopping and loss processes that occur close to the lattice threshold, anharmonicities are non-negligible, which make the detunings δ_1 level-dependent.

With these rates, the time evolution of the populations $P_{1,n}$ and $P_{2,n}$ of the states $|1^*,n\rangle$ and $|2^*,n\rangle$ can be expressed as:

$$\begin{aligned} \partial_t P_{1,n}(t) = &-P_{1,n}(t)(\Gamma_{n,\text{eff}} + \Gamma_{\text{heat}}) \\ &+ \alpha \sum_m \left[P_{1,m}(t)\left(\Gamma_{m,\text{eff}} M_{n,m-1} + \Gamma_{\text{heat}} M_{n,m}\right) + P_{2,m}(t)\Gamma_{2^*} M_{n,m}\right] \end{aligned} \tag{4.5.2}$$

$$\begin{aligned} \partial_t P_{2,n}(t) = &-P_{2,n}(t)\Gamma_{2^*} \\ &+ (1-\alpha) \sum_m \left[P_{1,m}(t)\left(\Gamma_{m,\text{eff}} M_{n,m-1} + \Gamma_{\text{heat}} M_{n,m}\right) + P_{2,m}(t)\Gamma_{2^*} M_{n,m}\right] \end{aligned} \tag{4.5.3}$$

---

[1] The heating from repumping is not included because it is treated explicitly by including the states $|2^*,n\rangle$.

The negative terms describe the scattering out of the state $|i,n\rangle$ and the positive terms describe the scattering from a state $|i,m\rangle$ into the state $|i,n\rangle$ with probabilities given by the matrix elements of the single-photon scattering matrix M (see Sect. 4.5.2). The shift of the index is due to the Raman coupling that a state $|1,m\rangle$ scatters via state $|2,m-1\rangle$ in the cooling cycle with rate $\Gamma_{m,\mathrm{eff}}$ (see Sect. 4.3) and α is the branching to states 1^* and 2^*. Note that the recoil heating is included in the off-diagonal elements of M_{nm} and the repump process from state 2^* is written explicitly.

The coupled equations 4.5.2 and 4.5.3 are a set of linear first-order differential equation for the probability distributions $P_{1,n}(t)$ and $P_{2,n}(t)$, where $n = 0,1,\ldots,N_b$ is the h.o. level of the local well. The matrix elements M contain the full couplings between different h.o.-levels and the rates $\Gamma_{n,\mathrm{eff}},\Gamma_{\mathrm{heat}},\Gamma_{2^*}$ are the scattering rates in the cooling cycle, from perturbing heatings and of the state 2^*, respectively. We are interested in the time evolution starting from an initial state, where the atom is the ground state i.e. $P_{1,n}(t=0) = \delta_{n,0}$, $P_{2,n}(t=0) = 0$. The decay branching α between states 1^* and 2^* is assumed to be a level independent constant.

Elimination of state 2 In order to simplify the description, one can obtain an expression just in the h.o. level n. One can sum the repump process from state $|2^*,m\rangle$ to state $|1^*,n\rangle$ via all possible intermediate decays to states $|2^*,n'\rangle$. These processes leads to a geometric series that can easily be summed explicitly

$$\begin{aligned}\tilde{M}_{nm} &= M_{nm} + (1-\alpha)\sum_{n'}\left(M_{nn'}M_{n'm} + (1-\alpha)\sum_{n''}\left(M_{nn''}M_{n''n'}M_{n'm}+\ldots\right)\right)\\ &= \left(\frac{\mathbf{M}}{\mathbf{1}-(1-\alpha)\mathbf{M}}\right)_{nm} \qquad (4.5.4)\end{aligned}$$

Replacing $\mathbf{M}$ by $\tilde{\mathbf{M}}$ in Eq. 4.5.2 and dropping terms that depend on P_2, one obtains an effective rate equation just for the populations of state 1^*. Formally, this can be obtained by adiabatic elimination [158] of states $|2^*,n\rangle$: As we are interested in (almost) steady-state solutions one can approximate the change $\partial_t P_{2,n}(t)$ with zero and solve the matrix equation4.5.3 for $P_{2,n}$.

The final rate equation then reads:

$$\begin{aligned}\partial_t P_{1,n}(t) &= -P_{1,n}(t)(\Gamma_{n,\mathrm{eff}}+\Gamma_{\mathrm{heat}})\\ &\quad + \alpha\sum_m P_{1,m}(t)\left(\Gamma_{m,\mathrm{eff}}\tilde{M}_{n,m-1}+\Gamma_{\mathrm{heat}}\tilde{M}_{n,m}\right) \qquad (4.5.5)\\ \partial_t \mathbf{P}_1 &= \mathbf{R}\mathbf{P}_1. \qquad (4.5.6)\end{aligned}$$

In the last line it has been written in matrix form with the vector $\mathbf{P}_1$ and the square matrix $\mathbf{R}$. Note that the equation does not depend on Γ_{2^*} any more.

The populations of state 2 are related to those of state 1 via

$$P_{2,n} = \frac{1-\alpha}{\Gamma_{2^*}}\sum_m\left(\Gamma_{m,\mathrm{eff}}\tilde{M}_{n,m-1}+\Gamma_{\mathrm{heat}}\tilde{M}_{n,m}\right)P_{1,m} \qquad (4.5.7)$$

$$\mathbf{P}_2 = \frac{1-\alpha}{\alpha\Gamma_{2^*}}\left(\mathbf{R}+(\Gamma_{n,\mathrm{eff}}+\Gamma_{\mathrm{heat}})\mathbf{1}\right)\mathbf{P}_1 \approx \frac{1-\alpha}{\alpha}\frac{\Gamma_{n,\mathrm{eff}}+\Gamma_{\mathrm{heat}}}{\Gamma_{2^*}}\mathbf{P}_1, \qquad (4.5.8)$$

where the last approximation is valid for a (quasi) steady-state solution ($\mathbf{R}\mathbf{P}_1 \approx 0$). Due to the linear character of the equation, the ratio of population in state 2^* to state 1^* is simply the ratio of rates going from 1^* to 2^* and vice versa.

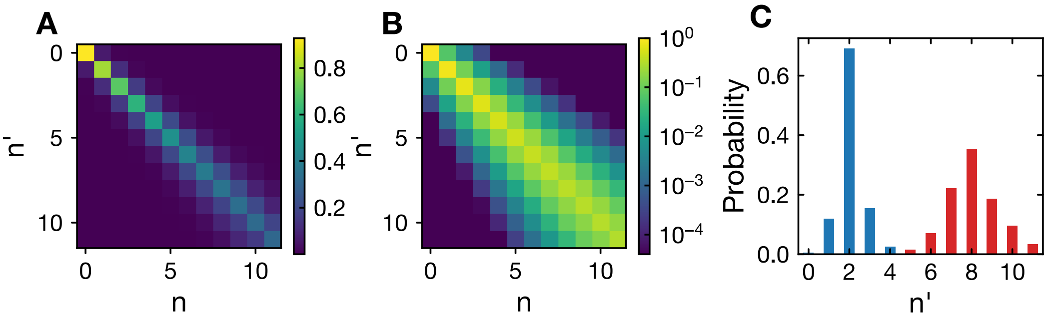

Figure 4.7. Single-photon coupling matrix M. *The probability distribution of the final state n' of a ^{6}Li atom starting in state n of a single well of a $517\,E_r^{Lat}$ lattice that scatters one photon at 671 nm with linear **(A)** and logarithmic **(B)** color scale. **(C)** Result for initial state $n = 2$ (blue) and $n = 8$ (red) i.e. vertical cuts of **M**.*

4.5.2 Matrix elements

In this paragraph, we turn to the explicit calculation of the matrix elements M_{nm} that couple the eigenstates of the lattice well. While the heating due to a photon recoil is independent of the initial level n, the distribution of final levels after absorption of one photon shows a strong dependence on n.

The transfer matrix element for a single recoil have been presented with the Raman coupling (Sect. 4.2).

The full scattering process of one photon consists of a momentum kick of the absorption, the P-state time-evolution and a second momentum kick of the emission. The main heating occurs in the axis of the repumper. For simplicity we consider only this axis and treat it as an axis of the lattice. As we are interested in the probability that an atom leaves its site during scattering, the loss rate in this axis should be good upper bound for the total loss rate. The matrix element for a $n \to n'$ transition at a single scattering event is

$$U_{n',n} = \langle n'|e^{ik\cos(\vartheta)\hat{x}} e^{i\hat{H}_P t/\hbar} e^{ik\hat{x}}|n\rangle = \langle n'|\hat{D}(i\eta\cos\vartheta)\hat{U}^P\hat{D}(i\eta)|n\rangle \tag{4.5.9}$$

where ϑ is the angle of the emitted photon relative to the repump axis and t is the time in the excited state (see Sect. 4.4.2), whose full cosine lattice potential is considered for the calculation.

The probability for a $n \to n'$ transition is, thus, given by averaging the squared matrix element over the time t and angle ϑ

$$M_{n',n} = \langle |U_{n',n}|^2 \rangle_{t,\vartheta} = \int_0^\pi d\vartheta \frac{\sin\vartheta}{2} \int_0^\infty \frac{e^{-t/\tau}}{\tau} |U_{n',n}|^2 \tag{4.5.10}$$

As a dimensionless number $M_{n',n}$ only depends on three values:

- The lattice depth measured in E_r^{Lat}.
- The ratio of the two length scales (the wavelength of the repump light λ and the lattice spacing d), which is of order one.
- The ratio of the decay rate Γ to the lattice frequency as measured by $A_P/\hbar\omega_0$ (see Eq. 4.4.11), which is often so close to zero, that it can be ignored.

The numerical calculation of the matrix elements is performed in real space in a 3-site lattice with localized Wannier states n, n'. For the matrix all states in the central well with $E_n < 0.9\,V_0$ are kept[1], while transition probabilities into other states are treated as hopping (neighboring wells) or losses (unbound states), which will both be called losses. Results for a $517\,E_r^{\mathrm{Lat}}$ lattice are shown in Figure 4.7. The contribution of the P-state evolution on the matrix-values is small (< 20%) for the numbers shown.

4.5.3 Loss rates

A direct calculation of time evolution during cooling with the ground state $|1,0\rangle$ as an initial state by equation 4.5.6 shows that the distribution $\mathbf{P}_1(t)$ approaches a quasi-steady-state distribution after less than 10 scattered photons. Due to a small but finite coupling to the untrapped states, the time evolution of the distribution shows after this initial phase a very slow constant decay.

This quasi-steady-state solutions of the equation 4.5.6, $\mathbf{P}_1^0$, can be obtained by diagonalization of $\mathbf{R}$. There is a single right eigenstate $\mathbf{P}_1^0$ of $\mathbf{R}$ with all positive entries, which is the only physical solution because the $P_{1,n}$ are probabilities. Its eigenvalue gives the loss rate of the system Γ_{loss}, so the rate in which the atom is transferred to states in the continuum or neighboring sites

$$\mathbf{R}\mathbf{P}_1^0 = \Gamma_{\mathrm{loss}}\mathbf{P}_1^0, \quad P_{1,n}(t) = P_{1,n}^0 e^{-\Gamma_{\mathrm{loss}}t}. \tag{4.5.11}$$

The total photon scattering rate is obtained from the (normalized[2]) eigenvectors $\mathbf{P}_1^0$ by multiplication with the scattering rates per state

$$\Gamma_{\mathrm{sc.total}} = \sum_n P_{1,n}^0 \frac{\Gamma_{\mathrm{heat}} + \Gamma_{n,\mathrm{eff}}}{\alpha}. \tag{4.5.12}$$

The factor α^{-1} describes the average number of photons scattered until the atom is back in state 1^* after being excited from state 1^*.[3] We are interested in the ratio of the loss rate to the scattering rate $\zeta = \Gamma_{\mathrm{loss}}/\Gamma_{\mathrm{sc.total}}$. It describes how many photons an atom can scatter on average before it is lost from the site. In figure 4.8, ζ is expressed as the number of atoms lost for one million scattered photons ($10^6 \cdot \Gamma_{\mathrm{loss}}/\Gamma_{\mathrm{sc.total}}$). In our experiment, we scatter about 5000 photons per atom during imaging, so a loss rate of 10 atoms per one million photons means a 95% imaging fidelity[4].

Results For our parameters (Table 4.1) the rate equation analysis predicts

$$\Gamma_{\mathrm{loss}} = (2\pi)\cdot 24\,\mathrm{mHz}, \quad \zeta = 9\cdot 10^{-6}, \quad \mathfrak{F}_{5000\,\mathrm{photons}} = 95.6\%, \quad P_{1,n=0} = 0.98 \tag{4.5.13}$$

The calculated fidelity $\mathfrak{F}$ is comparable to our experimental loss rates. $\mathfrak{F} = 95.6\%$ is only slightly worse than the best values we achieved in the lab (about 97.5%), which is a quite good

---

[1] Although states with $0.9\,V_0 < E_n < V_0$ are still bound, the next photon absorption excites the atom even further, which leas to a very high loss probability. The final results do not critically depend on this cutoff value.

[2] Normalization needs to include state 2^*. $\sum_n P_{1,n} + P_{2,n} = 1$, but for successful cooling the total fraction in state 2^* is typically only ~1%. For an eigenstate, $P_{2,n}^0$ is proportional to $P_{1,n}^0$.

[3] Mathematically α^{-1} arises from the summation of scattering from states 1^* and 2^* after proper normalization of $P_{1,n}^0$,$P_{2,n}^0$ via Eq. 4.5.7.

[4] The fidelity $\mathfrak{F}$ for imaging with N_{ph} scattered photons is related to the loss rates via $\mathfrak{F} = e^{-N_{ph}\zeta}$.

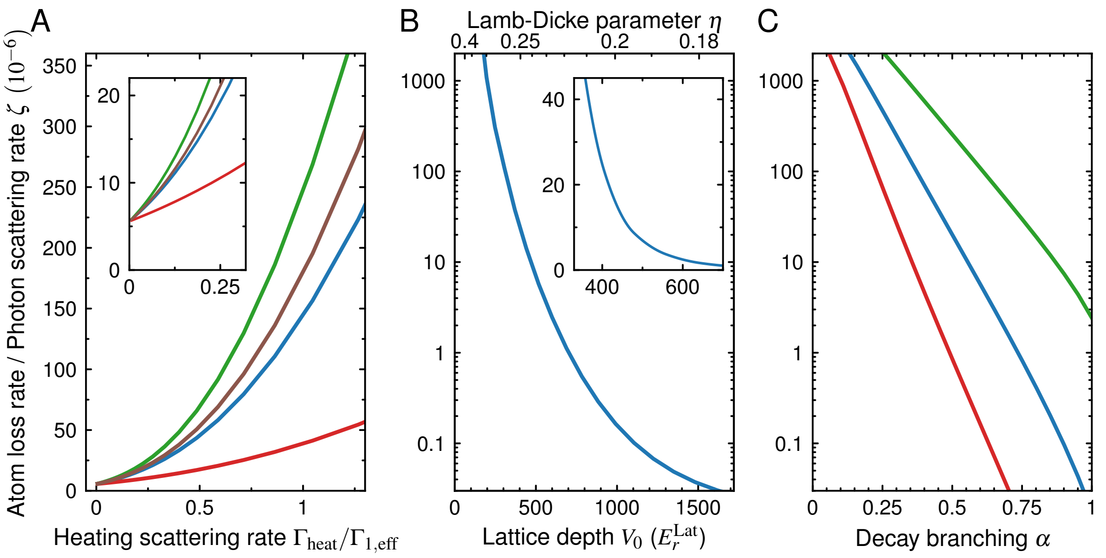

Figure 4.8. Hopping/loss of atoms. *The number of atoms that left its original site, normalized to the photon scattering rate as predicted from the rate equation.* ***(A)*** *The heating scattering rate* Γ_{heat} *measures how strong the Raman cooling system is perturbed relative to the cooling scattering rate* $\Gamma_{1,\text{eff}}$ *of the lowest* $1 \to 0$ *transition. Calculation has been done for a* $517\,E_r^{\text{Lat}}$ *deep lattice at branching* $\alpha = 0.6$ *with different scalings of the cooling rate* $\Gamma_{n,\text{eff}}$ *with the h.o. level n: Without anharmonicities and saturation of the Raman coupling the scaling is linear* $\Gamma_{n,\text{eff}} = n\Gamma_{1,\text{eff}}$ *(red), with the anharmonicities (blue curve on Fig. 4.4 B) the couplings decrease for large n leading to much stronger losses (brown). By including our modulation of the Raman frequency (values* $\Gamma_{n,\text{eff}}$ *in table 4.1) one can reduce the losses slightly*[1] *(blue), the green curves shows the result for* $\Gamma_{n,\text{eff}} = \Gamma_{1,\text{eff}}$ *constant. A zoom into the low heating region (inset) shows that all curves approach a common non-zero loss-rate of 5.7 atoms per one million scattered photons.* ***(B)*** *The relative loss rates for almost zero heating for different lattice depth* V_0 *at* $\alpha = 0.6$*. These can be seen as a lower bound for the achievable loss rate. A stronger lattice both reduces the Lamb-Dicke factor* η *(top) and increases the number of bound states. The inset is a zoom into the experimentally relevant regime in linear scale.* ***(C)*** *The relative loss rate for almost zero heating as a function of the repump efficiency* α *(probability to decay to state* $|1\rangle$*) also shows an exponential behavior. The lattice depths are* $300\,E_r^{\text{Lat}}$ *(green),* $517\,E_r^{\text{Lat}}$ *(blue), and* $1000\,E_r^{\text{Lat}}$ *(red). All calculations have been performed in dimensionless units with* $E_r^{\text{Lat}}/E_r^{\gamma} = 0.4$ *and* $\Gamma/E_r^{\gamma} = 200$ *(lithium values).*

agreement considering that the loss rate depends exponentially on most of the input values and no free parameter has been used. All input parameters are calculated from independently measured quantities or known properties of the atom.

Low heating regime For zero heating rate the $|1^*,0\rangle$ state is a dark state of the system. In this idealized situation both the scattering and the loss rate are zero. As seen in section 4.4, the heating rates can be made much lower than the cooling rate. It is, therefore, of interest to look at the results of the rate equation in the limit $\Gamma_{\text{heat}} \to 0$. In this case, the $\Gamma_{\text{loss}}/\Gamma_{\text{sc.total}}$ approaches a value ζ_0 that is independent of all the cooling strengths $\Gamma_{n,\text{eff}}$ and heating Γ_{heat}

---

[1] To allow for a comparison, the heating rate (x-axis) is in this case still normalized to the unmodulated scattering rate of $\Gamma_{1,\text{eff}} = (2\pi) \cdot 17\,\text{kHz}$.

(see inset of Fig. 4.8 A) and only depends on the matrix elements $M_{n',n}$ and the branching α.[1] Thus, there is a lower bound to the loss rate with respect to an optimization of cooling and heating rates.

This can be understood from a Monte-Carlo trajectory of an atom that is once excited from $|1^*,0\rangle$, but is otherwise only exposed to the cooling light: For every photon in the cooling cycle it will do a transition $n \to n'$ with probability $\tilde{M}_{n',n}$ until it ends up in the dark state or it is lost. The probability of a loss and the number of emitted photons will not depend on the rates $\Gamma_{n,\mathrm{eff}}$, but just on the branchings $M_{n',n}$ and α.

The numerical results are well approximated (better 25%) for a range of lattice depths from 200 to 1700 E_r^{Lat} by

$$\zeta^0_{\alpha=0.6}(V_0) = 10^{-6} \exp\left(100(1/\sqrt[4]{V_0} - 1/\sqrt[4]{700})\right). \tag{4.5.14}$$

The $V_0^{-1/4} \sim \eta$ dependence shows that $\log(\zeta) \sim \eta$ and emphasizes the relevance of a small Lamb-Dicke factor for successful imaging. A decrease of η by 0.01 results in a four times lower loss rate limit.

For a given lattice, the only remaining parameter of relevance in the low heating limit is the repump efficiency α (Figure 4.8 C) because it takes $(1/\alpha)$ scattered photons for one successful cooling step. Each of these photons has a small probability to raise the h.o. level, which in about N_b steps leads to the exponentially small but finite loss probability.

The importance of α explains why it is better to repump on the $F = 1/2$ state instead of the $F = 3/2$ state. In principle it would be beneficial to select an m_F-repump transition with the best branching. For ^{6}Li the $P_{1/2}F = 1/2$ states for example decay with 89% to the $F = 3/2$ ground state. But the very low coupling to the $F = 1/2$ states and the small hyperfine splitting of only 26 MHz to the $P_{1/2}F = 3/2$ states makes it impossible to get a good coupling to this state. In addition, the Raman dark states (Sect. 4.2.1) make it even more complicated to find a best choice for the geometry and polarization of the laser beams. An extended discussion of this is left to a future analysis.

For our lattice of about $520 E_r^{\mathrm{Lat}}$ depth, the calculation at $\alpha = 0.6$ predicts at least 5.7 lost atoms per one million scattered photons or a maximum fidelity of 97.2% for 5000 photons per atom. The greatest uncertainty of this prediction is from the value α, which depends on laser angles and polarizations.

4.5.4 Steady state distributions

The normalized eigenvector $P^0_{1,n}$ and the related occupation of the second state $P^0_{2,n}$ gives the quasi-steady-state probability distribution $P_n = P^0_{1,n} + P^0_{2,n}$ of the h.o.-levels n (Figure 4.9). The distribution does not follow a simple exponential decay, so the system is not thermal. Instead there is a fast decay (low temperature) for the states close to the ground state and a much slower decay for large n. Although up to 99% of the atoms are in the ground state, the population in the highly excited states is still large enough to produce the loss rates.

The distribution can phenomenologically be approximated by the sum of two thermal populations $f_T(n) \sim \exp(-E_n/T)$

$$P_{\mathrm{fit}}(n) = b f_{T_c}(n) + (1-b) f_{T_h}(n) \tag{4.5.15}$$

---

[1] For $\Gamma_{\mathrm{heat}} \to 0$ the matrix R factorizes $R_{n,m} = (M_{n,m-1} - \delta_{n,m})\Gamma_{m,\mathrm{eff}}$ and the eigenvalues of R are those of $M_{n,m-1} - \delta_{n,m}$.

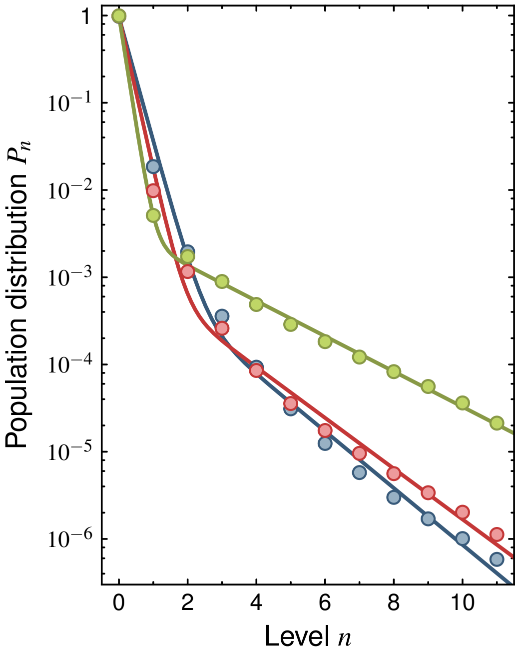

Figure 4.9. Distribution of level populations during Raman cooling from rate equation. *Solutions of equation 4.5.11 with our experimental parameters* $\Gamma_{n,\mathrm{eff}}$ *and* Γ_{heat}. *The (quasi) steady-state distribution of the level population shows a strong suppression already in the first excited state and a long tail to high excitations. Our measurement parameters (Table 4.1) have been experimentally optimized to minimize losses and the modulation of the Raman frequency provides cooling also at large n. The distribution (blue) shows in this case less than* $2 \cdot 10^{-6}$ *population in the lossy states close to the trap edge. Without the modulation (red) the distribution shows a faster initial decay, but then a less efficient cooling at large n leading to slightly worse loss rates. If Raman and repump parameters are optimized to ground state cooling (green), one can reach a ground state occupation of 99.2% at the cost of a ten-fold stronger tail. The solid lines are fits with the sum of two exponential terms (see main text).*

with a fraction b of the atoms at a temperature T_c and the rest at a hotter temperature T_h. For our parameter (Table 4.1), we obtain:

$$b = 0.997, \quad k_B T_c = 0.30\hbar\omega_0, \quad k_B T_h = 1.3\hbar\omega_0$$

The corresponding temperatures are 19 and 81 μK.

Such a long tail distribution has recently been investigated with an ion pair in a linear Paul trap [159]. In their case, a similar rate equation predicted a 99.9% ground state occupation and a 10^{-4} population in the tenth excited state. They could verify their model to high accuracy at low n, but had no experimental test for the long tail. This verification is provided naturally by our measurement of loss/hopping rates during the imaging.

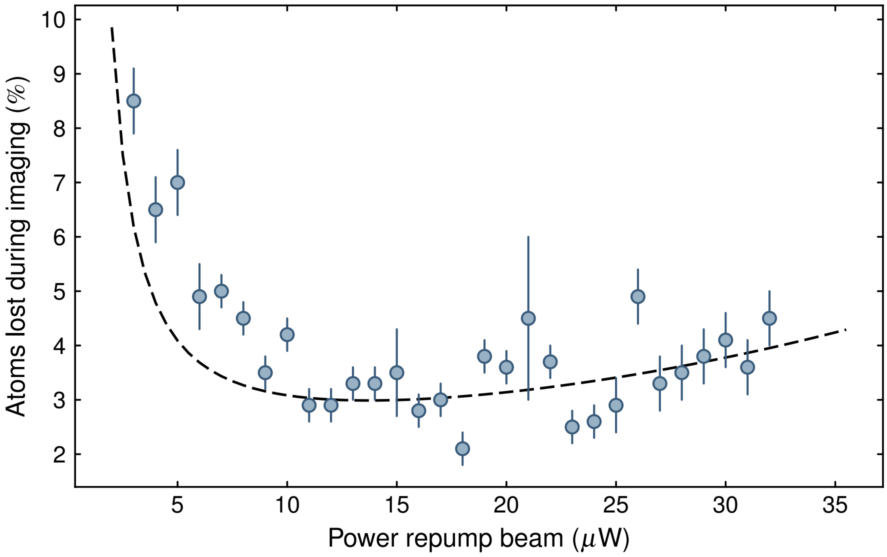

Figure 4.10. Loss rate vs power of the repump beam. *Measurement of the fraction of atoms which was lost or moved during a 600 ms fluorescence imaging (blue points) for different intensities of the repump beam i.e. different ω_R. The detected fluorescence level increases by about 50%, while increasing the repump power over the displayed range. The loss rate result of the rate equation is multiplied with the total photon count (per repump value) assuming 4% detected photons (black line). Simulation uses values of table 4.1 adjusted to the repump power. There is no free parameter in the calculation.*

4.6 Comparison to experimental results

We can compare the calculated loss rates from the rate equation to experimentally measured tunnelings and losses during imaging for different values of the experimental parameters. Experimentally losses are determined by taking two consecutive images of the same cloud and counting the number of atoms that moved or disappeared. We only look at the central part of the cloud (about 60% of all atoms) to exclude effects from finite beam sizes. Experimentally we find the expected linear scaling of losses with exposure time, thus, a constant loss rate.

The calculations are done with the parameters of table 4.1 adjusted to the experimental values, which includes the effects of the modulation of the Raman detuning. We calculate the eigenvalue of the (quasi) steady-state solution (Eq. 4.5.11) and the result (lost atoms per one million photons) is converted to a loss rate during imaging in percent by multiplication with the experimentally determined fluorescence rate and exposure time.

Repump Power As an example, we present a comparison for different powers (intensities) of the repump beam (see Fig. 4.10). There is a relatively weak dependence on this parameter with a broad optimum around 20 μW ($\omega_R = (2\pi)\cdot 1.1\,\text{MHz}$). We see an increase of detected photons per atom from 120 at 3 μW to 180 at 30 μW.

In the simulation the repump power enters mainly by its influence on the scattering rate $\Gamma_{n,\text{eff}}$ (see Sect. 4.3), while the effect on the heating Γ_{heat} via $\Lambda_{\text{sc. Rp}}$ is negligible at this parameter range. After multiplication with the experimental photons counts (assuming 4% detected photons), we find a fairly good agreement between the results of the rate equation and the measurement results. The higher losses at low repump power are due to a weaker cooling, while the higher losses at strong repump power are mainly due to the higher scattering rate. The loss rate per photon only increases by a few percent for 30 μW compared to 15 μW.

A detailed comparison of experimental loss and scattering rates to the model presented in this chapter for other parameters (e.g. Raman power, repump detuning, geometry of beams) is beyond the scope of this thesis and left to a future analysis.

4.7 Summary and conclusion

We analyzed in detail the Raman sideband cooling for fluorescence imaging, which we use to keep the atoms localized during imaging. We calculated the Raman coupling, that depends on the geometry and polarization of the two Raman beams, and found good agreement with measured Rabi oscillations. In order to compare the cooling strength to the heating rates, we first derived a cooling rate from a master equation of an effective three-level system. All associated heating rates (photon recoil, P-state evolution, off-resonant scattering, Raman carrier transitions) are much lower than the cooling in our case. Nevertheless, we always see some atoms that are lost or that tunnel during the imaging.

The heatings fall into two groups. Heating processes of the first group are linked to the cooling process and do not perturb the dark state, like the recoil of the photon that pumps the atom back into the initial state. The other heatings, that do affect the ground state, like the off-resonant Raman scattering, lead to a finite photon scatting rate, which we detect with the camera. But these rates are so small compared to the cooling, that they can almost be ignored apart from their effect on the ground-state.

The losses that we see are caused by the small but finite probability for each scattered repump photon to raise the harmonic oscillator level instead of decrease it.

The simple three-level picture of Raman sideband cooling is only valid for a small Lamb-Dicke parameter η *and* low harmonic oscillator levels n. The higher the n, the stronger are the $n \to n+1$ coupling elements. This leads to a non-thermal distribution of level occupancies, which show a low mean, but a long tail to high excited states.

We set up a rate equation for the h.o. levels and dressed atomic states, which allows to calculate these losses from the experimental parameters of the setup. For our measurement parameters we calculate a loss probability of about one atom for 100 000 scattered photons, which is close to the measured loss and tunneling rates of about 3 percent for imaging with 5000 photons scattered per atom. We compared the prediction of the rate equation to experimentally measured loss rates for different input values e.g. power of the beams and found reasonable agreement, which suggests that our model captures the essential aspects of this fairly complicated cooling method.

We conclude from the analysis presented in this chapter that there are two possible approaches to improve our imaging fidelity. With our current lattice and beam geometry, the losses can only be reduced, by reducing the number of photons scattered. In order to still obtain a single-atom resolved image, either the detection fidelity or the reconstruction algorithm needs to be improved. The next chapter presents our current image reconstruction protocol and we suggest some improvements. The other approach is to improve our Lamb-Dicke factor by making the lattice deeper or to increase our repump efficiency (α) by choosing a different Raman geometry or different states. A deeper pinning lattice is planned and will be implemented within the next year, but the total depth is still limited by the available laser power of high-power, low-noise laser sources.

Chapter 5

Image Reconstruction

This chapter describes the reconstruction of the fluorescence images of atoms in a square lattice, thus the analysis to convert an image with counts per pixel into a digitalized information of the atom number on every site. Because we encode the spin information in a positional information (see Sect. 3.4.3), this also reveals the spin of the atoms and the reconstruction can then be used to construct the full distribution in the lowest band. In addition, some properties characterizing the quality of our imaging are analyzed.

The analysis includes three steps. First the position of all physics lattice sites on the image are estimated (Sect. 5.1), then each collected photon is assign to one lattice site via a deconvolution algorithm (Sect. 5.2) and finally the number of photons per site are used to determine the atom number on each lattice site (Sect. 5.3).

The reconstruction of the lattice sites and some preliminary simulation of the fidelity of occupation reconstructions are summarized in the Bachelor's thesis of Michael Hoese [160].

Introduction A lattice image, $g(x,y)$, can be modeled as the convolution ($*$) of the distribution of atoms, $f(x,y)$, with the point-spread function (PSF) of our imaging system, $p(x,y)$,

$$g(x,y) = f(x,y) * p(x,y) \tag{5.0.1}$$

The position of an atom originally at physics lattice site (n,m) is given by $\mathbf{r}_i = \mathbf{R}_{n,m} + \boldsymbol{\xi}_{n,m} = n\mathbf{a}_1 + m\mathbf{a}_2 + \mathbf{b} + \boldsymbol{\xi}_{n,m}$ where $\mathbf{a}_1$ and $\mathbf{a}_2$ are the lattice vectors of the physics lattice, $\mathbf{b}$ is an offset vector pointing to site (0,0) and $\boldsymbol{\xi}_{n,m}$ is the displacement vector due to the pinning lattice on site (n,m) (cf. Sect. 3.4.4). The atomic distribution can be written as a sum over all atoms as

$$f(\mathbf{r}) = \sum_i \delta\left(\mathbf{r} - \mathbf{r}_i\right) \tag{5.0.2}$$

Effects ignored in the description are:

- The pinning lattice displaces the atom out of the 2d plane in z-direction by a distance Δz, which leads to a small change of the widths of the points spread function. As the maximum Δz is $d_{PL}\sqrt{2}/2 = 380\,\mathrm{nm}$ at our pinning lattice geometry (Sect. 3.4.4), the increase of the size of the PSF is less than 1.6%.

- The point spread function changes as a function of lattice position in the imaging plane due to image aberrations. Simulation with the Zemax-software gave an effect below 10% for the change of PSF waist at 100 μm displacement in the x-y plane.

- There is a positional dependence of the number of scattered photons per atom (see Sect. 4) due to the finite waist of the pinning lattice beams and Raman beams, which are affecting the on-site oscillator frequency and Raman coupling strength respectively.

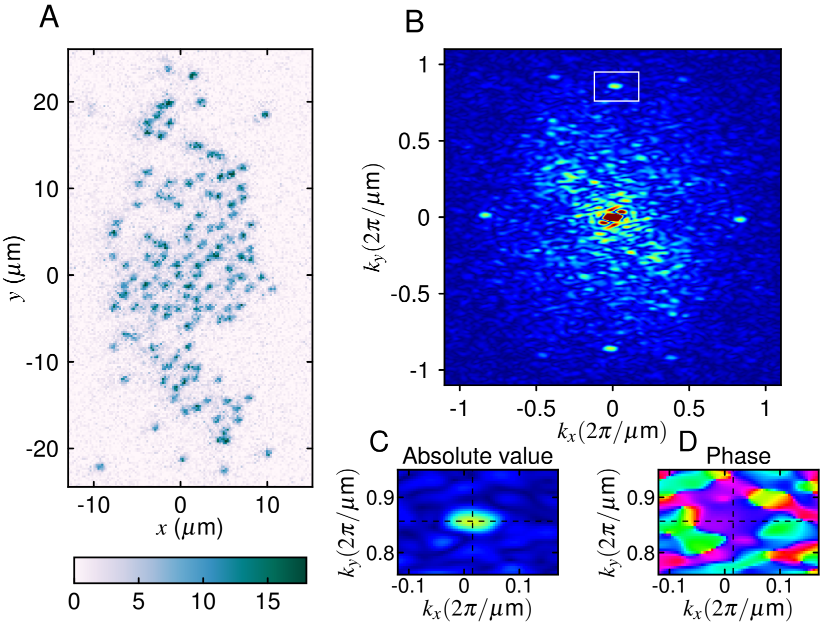

Figure 5.1. Lattice vectors and phases from Fourier transform. ***(A)*** *A single-site resolved image. The colorscale gives the photons per pixel.* ***(B)*** *Absolute value of the Fourier transform of the image. The peaks that correspond to the reciprocal lattice vectors of the physics lattice appear at* $(0.015, 0.857)$ *and* $(0.830, -0.014)$ $2\pi/\mu m$. ***(C)*** *Zoom of the upper peak (white rectangle). The cross-hair marks the peak position.* ***(D)*** *Phase of the Fourier transform in the same region*

5.1 Lattice reconstruction

Starting with an image like the one shown in figure 5.1A, we need to determine where exactly the lattice sites of the imaged lattice are located. Several approaches have been developed in the past to address this problem [25, 26], whose complexity is given by the ratio β of the widths of the point-spread-function[1] to the lattice constant. Due to our very good ratio of $\beta = 0.83(2)$, which is below one, the lattice modulation is visible by eye and we can use a simple 2d Fourier transform. For $\beta > 1$ this is not possible because a filled lattice (Mott insulator) results in an almost homogeneous count distribution with no signal in the Fourier transform.

Fourier Transform Figure 5.1B shows the results of a Fourier transform (FT) that has been obtained by a FFT-algorithm (scipy.fftpack). In order to obtain an image with a good resolution on a fix grid in k-space, the original image is cropped to the region of interest around the atoms, the background is subtracted and it is then placed in the center of an empty array of 1024×1024 pixels. Every pixel corresponds to 224(3) nm, resulting in a resolution of $(2\pi) \cdot 4.5\,\mathrm{nm}^{-1}$/pxl in k-space[2].

---

[1] We take the first minimum of the idealized Airy pattern as the widths, which corresponds to 2.905σ of the Gaussian waist σ.

[2] Images up to December 2015 have been taken with a different magnification and 380 nm/pxl.

5.1.1 Physics lattice sites

Lattice vectors The peaks in the Fourier transform that correspond to the reciprocal physics lattice vectors $(\boldsymbol{\alpha_1}, \boldsymbol{\alpha_2})$ are easily identified as the strongest peaks apart from $\mathbf{k} = (0,0)$. If one treats the local offsets $\boldsymbol{\xi}_{n,m}$ caused by the pinning lattice as a random variable with $\langle \xi_{n,m} \rangle_{n,m} = 0$ and $\langle \boldsymbol{\xi}^2_{n,m} \rangle_{n,m} = \bar{\xi}^2$, one arrives at a Fourier transform of $g(x,y)$

$$\tilde{g}(\mathbf{k}) = FT[g(x,y)] = \left(\tilde{h}(\mathbf{k}) * \tilde{\rho}(\mathbf{k})\right) \cdot \tilde{p}(\mathbf{k}) \cdot e^{-\frac{1}{2}\bar{\xi}^2 \mathbf{k}^2}, \tag{5.1.1}$$

where $\tilde{h}(\mathbf{k})$ is the reciprocal lattice with lattice vectors $\mathbf{G}$, $\tilde{\rho}$ is the FT of the density distribution $\rho(n,m)$, $\tilde{p}$ is the FT of the PSF p and the random offset lead to a reduction of the amplitude in analogy to a Debye-Waller factor[1] [85]. The first reciprocal lattice vectors thus appear as sharp peaks whose shape is given by the FT of the density distribution, while the finite PSF and the offset vectors just reduce the amplitude of these peaks.

The exact lattice vectors are estimated by first looking at the reciprocal pixel of maximum intensity close to the expected k-vectors, followed by a 2d Gaussian fit to obtain the center with subpixel resolution. Finally the real space lattice vectors are related to the reciprocal ones $(\boldsymbol{\alpha_1}, \boldsymbol{\alpha_2})$ via a matrix inversion

$$\begin{pmatrix} | & | \\ \mathbf{a}_1 & \mathbf{a}_2 \\ | & | \end{pmatrix} = \frac{1}{2\pi} \begin{pmatrix} - & \boldsymbol{\alpha}_1 & - \\ - & \boldsymbol{\alpha}_2 & - \end{pmatrix}^{-1}. \tag{5.1.2}$$

The uncertainty of this method on a single shot with about 100 atoms is about 1%. Typically the lattice vectors stay constant over weeks, thus they are calculated once with high accuracy on about 100 averaged raw images and then kept as fixed values in the analysis. Typical lattice vectors are

$$\mathbf{a_1} = \begin{pmatrix} 5.346(2) \\ -0.096(1) \end{pmatrix}, \quad \mathbf{a_2} = \begin{pmatrix} 0.102(1) \\ 5.209(2) \end{pmatrix}. \tag{5.1.3}$$

Numbers are in pixel and $1\,\mathrm{pxl} = 224(3)\,\mathrm{nm}$. Whenever we realign the lattice, these values are remeasured.

Lattice phases In order to assign the position of all lattice sites, the lattice phases i.e. the entries of the offset vector $\mathbf{b}$ are required in addition to the lattice vectors. This information is given by the phase of the FT at the position of the reciprocal lattice vector (see Fig. 5.1D). The FFT measures phases relative to the (0,0) pixel, which leads to trivial strong phase oscillations given by the center of mass vector in real space, $\mathbf{R}$

$$\tilde{g}(\mathbf{k}) = \tilde{g}'(\mathbf{k}) e^{-i\mathbf{R}\mathbf{k}}. \tag{5.1.4}$$

The phase of $\tilde{g}'(\mathbf{k})$ is typically smooth especially at a peak of the FT amplitude (see Fig. 5.1D). The phase value at the reciprocal lattice vectors is extracted by a simple 2d linear interpolation[2].

As the phases depend on the relative path length of the two interfering laser beams, it can fluctuate from shot to shot. Thus we determine the phase for every image independently.

---

[1] Random offsets reduce a FT of a lattice by $\left\langle e^{i\mathbf{k}\cdot\boldsymbol{\xi}} \right\rangle_\xi \approx e^{\frac{1}{2}\langle \mathbf{k}\cdot\boldsymbol{\xi} \rangle_\xi}$. Approximation valid for $k \lesssim \bar{\xi}^{-1} = (d_{PL}/\sqrt{12})^{-1} = 6.5\,\mu\mathrm{m}^{-1}$ with pinning lattice constant $d_{PL} = 532$ nm.

[2] Care needs to be with respect to the jump from π to $-\pi$, which must not occur within the values used for the interpolation.

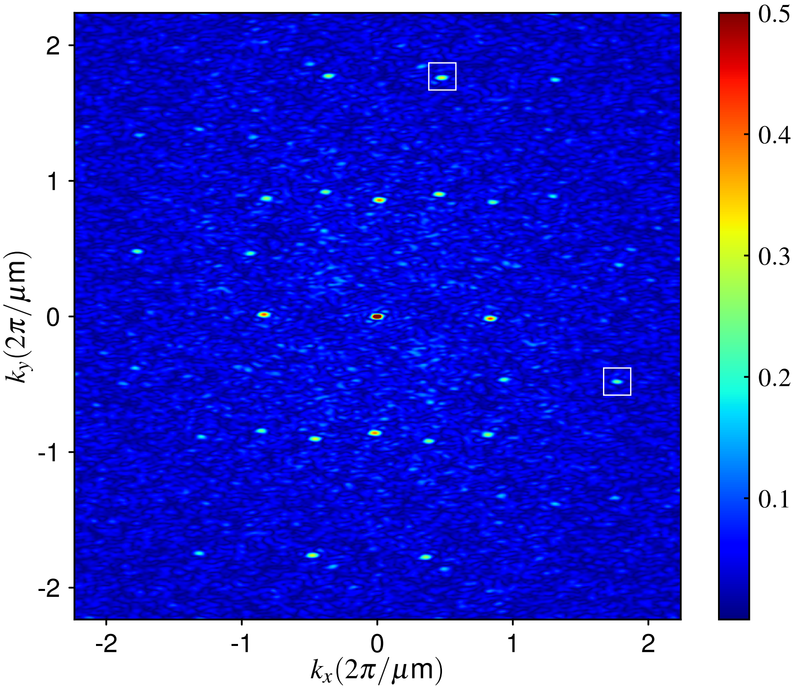

Figure 5.2. Fourier transform of deconvolved image. *After deconvolution (Sect. 5.2) the spatial size of the peak associated with one atom is very small (see inset of Fig. 5.4 B). Thus, its Fourier transform shows a lot more structure at large k-values. In addition to the peaks close to* $(0,\pm 1)$ *and* $(\pm 1,0)$ $(2\pi)\cdot\mu m^{-1}$*, which are from the physics lattice, there are peaks caused by the pinning lattice structure. The main reciprocal lattice vectors are marked with white squares. Other peaks are higher order combinations of this superposition of two square lattices (physics + pinning lattice). Color scale values are the modulus of the image in Fourier space normalized to the* $(0,0)$ *peak.*

5.1.2 Pinning lattice sites

The offsets, ξ_{nm}, due to the pinning lattice are in fact not random, but they are determined by the relative position of the physics and pinning lattice sites. Both of these are simple cubic lattices, but with different incommensurate lattice spacings (1150 nm, 532 nm) and relative angles (44°, 10°)[1]. This structure leads to additional peaks in the FT, some of which are already visible in figure 5.1B i.e. close to (0.5,0.9) $2\pi/\mu$m. A Fourier transform after deconvolution (see Sect. 5.2) shows a lot more peaks (Fig. 5.2) due to the much smaller residual point spread function. One can identify the reciprocal lattice vectors of the pinning lattice $(\alpha_{PL,1},\alpha_{PL,2})$ and linear combinations of α and α_{PL}. In principle this allows to determine the exact position of the pinning lattice sites on the image, which can be used in a future improved image reconstruction.

---

[1] The physics lattice is oriented (almost exactly) along the x,y,z corrdinates of the lab frame and the pinning lattice axis x',y',z' are obtained by a rotation of 44° around y, followed by a 10° rotation around z.

5.2 Image deconvolution

This section addresses the process to determine the number of atoms on each of the previously reconstructed physics lattice sites from a fluorescence image. Typically, this is achieved in a two-step procedure: First one needs to determine from which lattice site a given photon count originated and then one needs to map the photon number to an atom number on every site. The quality of an algorithm is measured by the lower threshold of photon numbers (exposure time) for which it still gives high-fidelity results.

The easiest approach for the first step is to connect every pixel of the image to its closest lattice site and then sum the counts on all pixel for every lattice site. This simple integration approach suffers from the disadvantage that, due to the finite point spread function size, some counts are wrongly assigned to neighboring lattice sites. It works well if the PSFs are small $\beta < 1$ and centered on the physics lattice sites. In our case the pinning shifts leads to quite substantial overlaps into the neighboring sites.

More sophisticated algorithms try to undo the convolution of the atomic position with the PSF to better localize the counts. Such a deconvolution is a classic task of image processing and returns the function $f(\mathbf{r})$ for a convolution equation:

$$g(\mathbf{r}) = f(\mathbf{r}) * p(\mathbf{r}) + \varepsilon(\mathbf{r}) \tag{5.2.1}$$

where $(\mathbf{r})$ runs over all pixel, $f(\mathbf{r})$ is the original atomic distribution, $p(\mathbf{r})$ is the point-spread function of the imaging system, $g(\mathbf{r})$ is the recorded image and $\varepsilon(\mathbf{r})$ are all deviations (errors, noise) from the ideal expression. Without noise, deconvolution is achieved by a simple division in Fourier space $\tilde{f} = \tilde{g}/\tilde{p}$. On real images this leads to amplification of noise in the high k modes due to the division by very small numbers and is not usable directly.

Noise There are several contributions to the *noise* on an image.

- *Photon shot noise*. This is the main source of noise on the images and arises directly from the photon quantization. It is strong because we detect less than 20 photons per pixel of the camera.

- *Background noise*. There is light that reaches the camera, which was not scattered by our atoms e.g. stray light from the glass cell or background light. We minimized this contribution to about 1.5 photons per pixel. Most of it is static, so we subtract an average background image from each new image before analyzing it. The shot-noise of the background counts remains.

- *Readout noise*. The conversion of electronic charge to digital counts has a noise that depends on the readout speed of the camera. We use a slow readout of 500 ms for the full frame and have negligible readout noise much below one photon due to a 50-fold amplification of the charge inside the camera before readout.

- *Camera defects.* Certain pixel of the camera give unreasonably high counts due to defects. We made a catalog of these pixels and replace their values by the mean of the surrounding pixels.

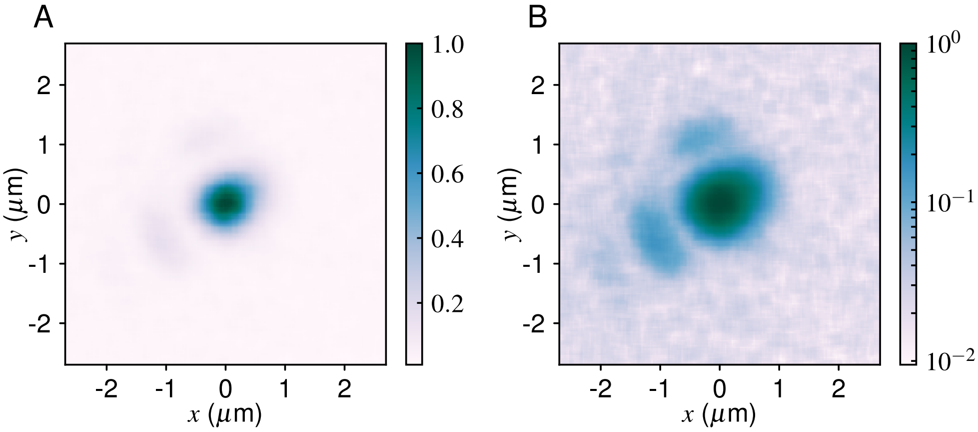

Figure 5.3. Point spread function. *The measured point-spread function of our imaging system with **(A)** linear colorscale and **(B)** logarithmic colorscale. The central peak has a Gaussian width of about 350 nm. The logarithmic plot shows residual imperfections of our imaging system, which deform the Airy ring into two stripes.*

5.2.1 Point-spread-function

With our single atoms, we are in the exceptional position to have an almost perfect point source at hand that can be used to experimentally determine the point-spread-function (PSF) of our imaging system.

Measurement of PSF In order to determine the PSF with good signal to noise ratio, the images of many isolated atoms are averaged. We thus evaporated the atomic cloud until only about ten atoms remained in the single plane of the z-lattice. Then we lower the confinement as much as possible without tunneling between the z-planes (15 E_r) in order to maximize the atom-atom distance. We take many of these picture, find all atoms with a “blob-detection” algorithm (*feature.blob_dog* from *scikit-image* package [161]) and crop the images around each atom keeping 24 by 24 pixel (5×5 μm) per atom. Each little image with one atom is fitted with a 2d Gaussian to determine its center. As the atoms are, of course, not centered with respect to the pixels, we upsample the images by a factor 8×8 without interpolation and then average all atoms centered on this reduced grid. In order to avoid perturbations of the true PSF, we enforce the following constraints on a detected blob to include it in the PSF average: (a) No other atomic blob is detected within a 4 μm radius, (b) The central pixel of the atom has at least 8 photons, (c) The blob is still present on a second image that is taken with a delay of 1 second, (e) The fitted Gaussian waist is less than 420 μm. The last two constraints try to filter out atoms that started to move or got lost during the exposure of the image.

Results The PSF of our imaging system is shown in figure 5.3. The central part is well described by a 2d Gaussian profile with $\sigma_1 = 310(3)\,\mathrm{nm}$ and $\sigma_2 = 368(5)\,\mathrm{nm}$ along their main axes, which are rotated by $30(1)^\circ$ w.r.t. the x-axis.

5.2.2 The Lucy-Richardson-algorithm

Given a measured image $g(\mathbf{r})$, a known point-spread function $p(\mathbf{r})$, and an error function that is *only* given by shot noise fluctuations on every pixel, one can find the most likely distribution $\phi^*(\mathbf{r})$, that could have generated the given $g(\mathbf{r})$.[1] Lucy [162] and Richardson [163] developed an iterative expectation maximization algorithm based on a Bayesian analysis.

Sketch of the derivation With Bayes' theorem the probability $P(\phi|g)$, that the atomic distribution was ϕ given a measured g, can be expressed based on the probability $P(g|\phi)$, that a distribution ϕ generates an image g,

$$P(\phi|g) = P(g|\phi)\frac{P(\phi)}{P(g)}, \tag{5.2.2}$$

where $P(\phi)\,(P(g))$ is the general probability that a distribution ϕ (an image g) occurs, i.e. without considering the current realization. If one assumes all distributions ϕ to be equally likely[2], i.e. $P(\phi) = c$, one can maximize $\log[P(g|\phi)]$ w.r.t. ϕ instead of $P(\phi|g)$. Based on the Poisson statistics of photon counts around the mean image $\phi * p$ generated by a ϕ, one can express the probability to get a certain g by

$$P(g|\phi) = \prod_{\mathbf{r}} \frac{(\phi * p)^g}{g!} e^{-\phi * p}, \tag{5.2.3}$$

with the factorial and the exponentials meant as operations per pixel $\mathbf{r}$. Taking the functional derivative of $\log[P(g|\phi)]$ with respect to ϕ and setting it to zero, one obtains[3] with $\hat{p}(\mathbf{r}) \equiv p(-\mathbf{r})$ and $\mathbf{I}$, the image with ones on each pixel:

$$\frac{\delta}{\delta\phi(\mathbf{r})}\log[P(g|\phi)] = \frac{\delta}{\delta\phi(\mathbf{r})}\left(\sum_{\mathbf{r}} g\log(\phi * p) - \phi * p\right) = \sum_{r}\Bigg(\overbrace{\frac{g}{\phi * p} * \hat{p}}^{C(\mathbf{r})} - \mathbf{I}\Bigg) \overset{!}{=} 0 \tag{5.2.5}$$

The solution of this equation $\phi = \phi^*$ is the *maximum likelihood* distribution, which is thus given by $C(\mathbf{r}) = 1$ on every pixel. Instead of solving $C(\mathbf{r}) = 1$ for $\phi(\mathbf{r})$, which involves a deconvolution, the Richardson-Lucy algorithm uses $C(r)$ as a correction factor on a previous guess ϕ_n to get an improved estimate ϕ_{n+1}

$$\phi_{n+1}(\mathbf{r}) = \phi_n(\mathbf{r})\,C_n(\mathbf{r}), \quad C_n(\mathbf{r}) = \frac{g(\mathbf{r})}{\phi_n(\mathbf{r}) * p(\mathbf{r})} * p(-\mathbf{r}). \tag{5.2.6}$$

Obviously, ϕ^* is a fix point of this iteration.

---

[1] For notational simplicity the dependence on $\mathbf{r}$ will be implied for the rest of the section.

[2] As we have a priori knowledge of the existence of a lattice structure, this is a simplification. Our additional knowledge could be used to improve the algorithm in the future (see Sect. 5.2.3).

[3] Note the general convolution identity for three functions of $\mathbf{r}$:

$$\sum_{\mathbf{r}} a\,(b * c) = \sum_{\mathbf{r}} b\,(a * \hat{c}) \tag{5.2.4}$$

and that $\mathbf{I} * p = \mathbf{I} * \hat{p} = \mathbf{I}$ because the PSF p is normalized.

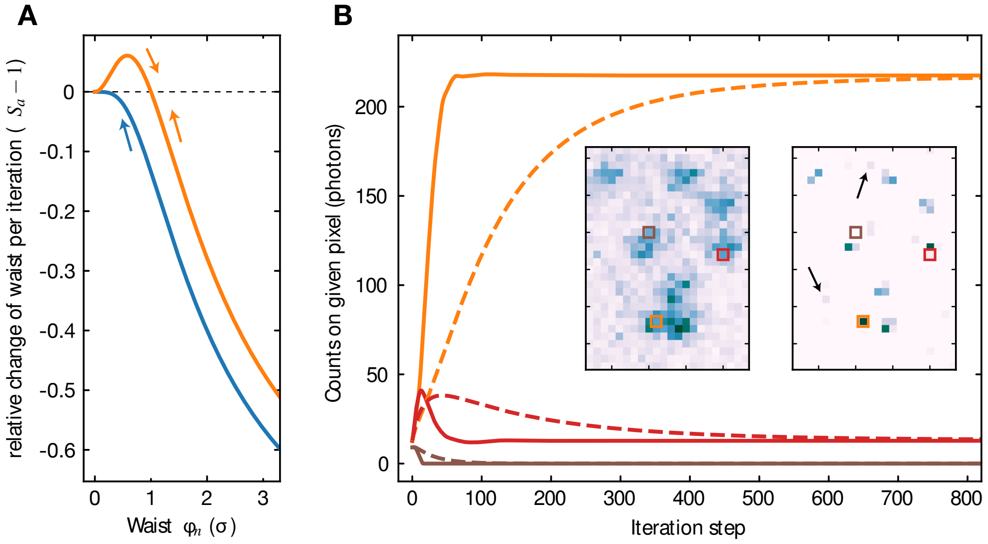

Figure 5.4. Richardson-Lucy deconvolution. ***(A)*** *Deconvolution of ideal Gaussian peaks with the R-L-algorithm. Relative change of the waist in one iteration step for an image with a blob of waist* σ *(blue) or* $\sqrt{2}\sigma$ *(orange) deconvolved with a PSF of waist* σ*. In the first case the fixed point* 0 *is approached slowly, while in the second case the fixed point* 1 *is reached quickly. Arrows give the direction of the iteration flow.* ***(B)*** *Example with an atom resolved image. The insets show a zoom into the initial image and the converged result of the deconvolution. The main plot shows the evolution of photon counts on marked pixels while the L-R iteration runs. Dashed lines are the bare algorithm and solid lines show the accelerated version. We typically use the accelerated algorithm and stop after 150 iterations. Arrows mark non-zero pixels which do not correspond to an atom, but result from the over-fitting of noise.*

Example: Gaussian blobs To get a feeling for the basic behavior of the algorithm it is instructive to consider the deconvolution of an image with a perfect 2d Gaussian $G(b\sigma)$ with waist $b\sigma$ by a Gaussian PSF $G(\sigma)$ with waist σ. Starting with $\phi_0 = G(a\sigma)$, one obtains after one iteration[1]

$$\phi_1 = G\left(S_a a\sigma\right) \equiv G\left(\frac{\sqrt{1+a^2\left(1+b^2\right)}}{1+a^2}a\sigma\right). \tag{5.2.7}$$

Thus the Gaussian shape is preserved and the waist changes by a factor S_a. To find the fixed points of the iteration, one sets $S_a = 1$ and finds $a_{fix} = 0$ and $a_{fix} = \sqrt{b^2-1}$. For $b > 1$ the second one is obviously the solution and it is the only attractive fixed point (see Fig. 5.4 A). The case $b = 1$ is the ideal scenario, where the deconvolution contracts the image to a delta-function. In this case, the convergence of the algorithm becomes very slow at the end ($\sigma_n \propto n^{-1/4}$, where n is the iteration number). The slow convergence of the ideal image is no practical problem as one can speed up the convergence (see Sect. 5.2.2) and stop the iteration once the waist is much smaller than one pixel. The case $b < 1$, which is a blob that is smaller than the PSF, has also $a_{fix} = 0$ as the only (real) fixed point and is thus contracted to a point.

---

[1] 2d Gaussian multiplication, division and convolution are given by $G(\sigma)G(\mu) \propto G(\sigma\mu/\sqrt{\sigma^2+\mu^2})$, $G(\mu)/G(\sigma) \propto G(\sigma\mu/\sqrt{\sigma^2-\mu^2})$ and $G(\sigma) * G(\mu) = G(\sqrt{\sigma^2+\mu^2})$.

Properties

- From equation 5.2.5 it is obvious that the fixed point of the iteration 5.2.6 is the optimum ϕ^*, which is not only a stationary point of $P(\phi|g)$, but even the global maximum likelihood solution[1] of the analysis [162].

- Due to its non-linear structure, the algorithm is capable of restoring structures with high k-vectors in the image. It even tends to a *sparse* solution i.e. one where the counts on many pixels are exponentially suppressed [164].

- If g, ϕ_0 and p have only positive entries, the algorithm ensures positivity for all ϕ_n and the sum of all counts remains equal to those of the image g.[2] This makes it very favorable for our application where we want to assign photons to localized point sources.

- One problem of the bare Richardson-Lucy algorithm without regularization is its remaining instability because of the division involved[3]. Due to the convolution in the denominator this is less dramatic than a direct division but the iterations can still produce pixel with unreasonable high counts. This can be avoided by a regularization [165] or an addition of a background value b in the algorithm, replacing the denominator by $\phi_n * p + b$ where b are the mean background counts on g, which can be either a constant value larger zero or a background image. This ensures that the denominator never gets too close to zero.

- A related issue of unregularized maximum-likelihood algorithm is the *overfitting* of noise. Given only a single g to reconstruct f, the algorithm tends to find structures in the noise that are unphysical. This can produce wrong peaks from regions with background counts only (see black arrow in Fig. 5.4 B). It can be avoided by either adding constraints to the iteration or by simply stopping the algorithm before it produces too strong features. In our images the background counts are sufficiently small, that these little peaks do not matter, especially after integration per lattice site area.

Speed up by linear extrapolation The bare algorithm is rather slow meaning that consecutive iterations do almost identical relative changes to ϕ. This can be employed to significantly speed up the algorithm by extrapolation [166]. The effect is presented in figure 5.4 B by tracking the value on some pixel while the iterations are performed with and without acceleration. Typically the acceleration reduces the time for the same result by a factor of five, because five times less steps are required[4].

---

[1] Note that this is not equivalent to minimizing the distance $\sum_{\mathbf{r}}(g - p * \phi_n)^2$.

[2] $\sum_{\mathbf{r}} \phi_{n+1}(\mathbf{r}) = \sum_{\mathbf{r}} \phi_n(\mathbf{r}) \frac{g(\mathbf{r})}{\phi_n(\mathbf{r})*p(\mathbf{r})} * p(-\mathbf{r}) = \sum_{\mathbf{r}} g \frac{\phi_n * p}{\phi_n * p} = \sum_{\mathbf{r}} g(\mathbf{r})$ using Eq. 5.2.4.

[3] Performing a division $y = a/x$, where x is a non-negative random number following some distribution with a *finite* density close to zero, the distribution for y has a heavy tail decaying with y^{-2} for large y and it has thus infinite mean and variance. This holds even if the probability around zero is exponentially small.

[4] Note that the run time per iteration is dominated by the calculation of the two convolutions. Here it is important to use fft-based convolutions (*scipy.signal.fftconvolve*) that outperform real space calculations (*scipy.signal.convolve2d*) for our image sizes by at least a factor of 50. Even faster is a direct calculation of the convolutions because it allows use a saved Fourier transform of the constant point-spread-function p, instead of calculating it twice per iteration step (once per call of fftconvolve).

5.2.3 Possible improvements

The current implementation of the deconvolution does not use any prior information apart from the point-spread-function. But we do have the additional a priori knowledge that our deconvolved image consists of point sources localized at the pinning lattice sites. This information can be used to restrict the space of possible outputs of the deconvolution algorithm to the ones that are physically reasonable. Our current algorithm finds the most likely ϕ^* from the space $(\mathbb{R}^+)^{\#\text{pixel}}$ because every pixel can show any positive real number. Instead one could directly search within the set of all atomic distributions $\{0,1,2\}^{\#\text{Lattice Sites}}$. The much smaller target space requires less input i.e. less photons to give high fidelity results. This allows in principle to overcome the diffraction limit in resolution [167], which we would need to achieve if we want to reconstruct on the pinning lattice sites. A practical implementation of such a Bayesian approach needs an efficient algorithm to find the maximum within the target space, that is still exponentially large.

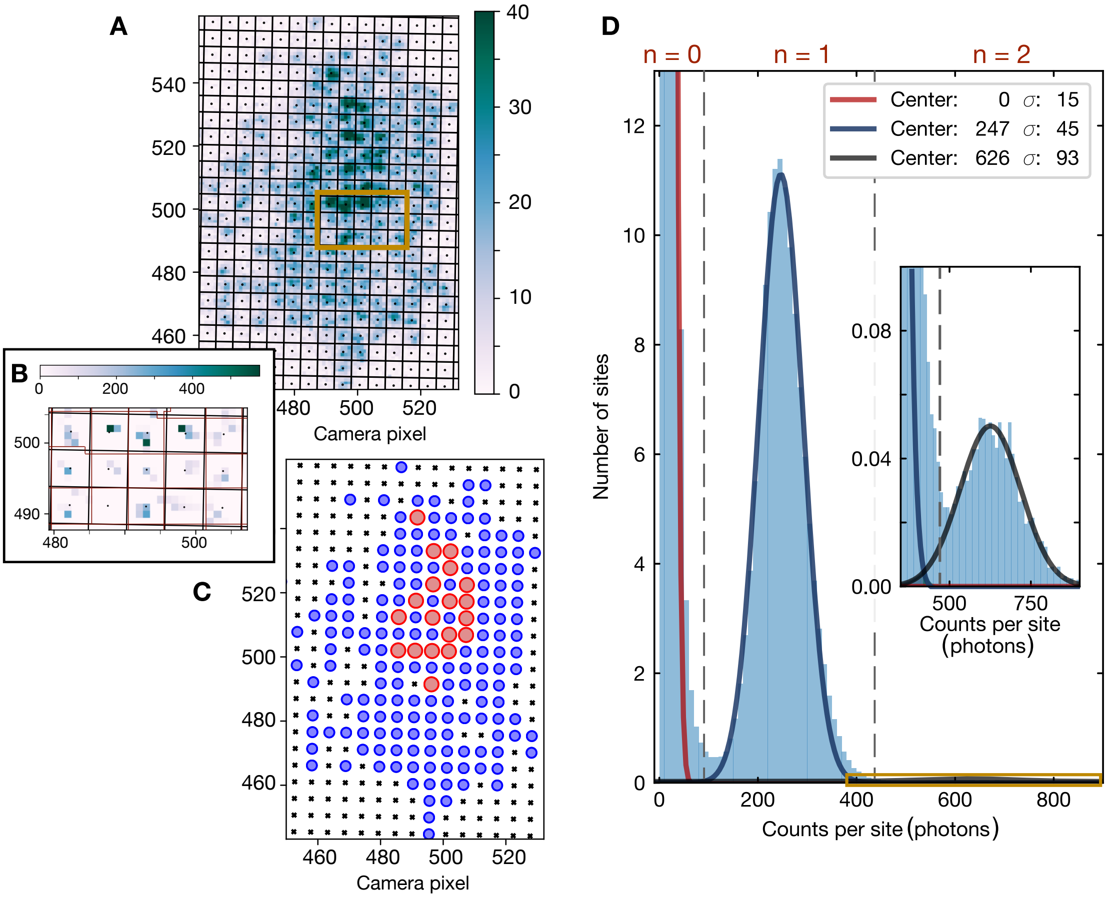

Figure 5.5. ***Photons per lattice site.*** ***(A)*** *A fluorescence image with photons detected per pixel during the 550 ms exposure. The reconstructed physics lattice sites are drawn as black dots. Black lines mark the lattice site areas.* ***(B)*** *Deconvolved image within the brown box of A. Red lines separate pixel that belong to different sites.* ***(C)*** *The reconstructed occupation per site with blue marking a single atom and red a doubly occupied site.* ***(D)*** *The histogram of counts per lattice site average over many shots (2500). The binning is over 10 photons. It shows a clear trimodal structure with peaks for 0,1 and 2 atoms per site. The colored curves are Gaussian fits to these peaks, while the vertical dashed lines separate the three regions. The inset is a zoom into the doublon peak (brown box).*

5.3 Lattice occupation

5.3.1 Integration of counts

After deconvolution of the recorded image, the majority of counts is bunched on single pixels (see Figs. 5.4B, 5.5B), but in principle the deconvolved image can still have counts on all pixels. To get a number of photons per lattice site, these have to be summed over the regions belonging to one lattice site. We define the area of a lattice site (n,m) as all points that are closer to $\mathbf{R}_{n,m}$ then to any other $\mathbf{R}_{n',m'}$. As the physics lattice grid is incommensurable with the pixel grid, one has to deal with counts on pixel whose area belongs to several lattice sites. Simulations showed that a higher reconstruction fidelity is reached when all counts from one pixel are assigned to the lattice site of the center of this pixel instead of splitting the counts and assigning them proportionally to all sites whose area overlaps with the pixel[1]. The assignment of counts to lattice sites is illustrated in figure 5.5 B.

5.3.2 Photon histograms

In a histogram of these photons per lattice site, one can see a trimodal structure (Fig. 5.5D). Lattice sites tend to have about 0 or around 250 or about 600 photons. This allows to assign the lattice occupation on every site. A detailed analysis of such a distribution shows that the number of photons (widths of the peaks) is far from shot-noise limited but follows a much broader distribution. One contribution of this broadening (see [89]) is the spatial inhomogeneous fluorescence rate over the size of the atomic cloud due to our pinning lattice beams of only about 60 μm waist. A full understanding of the distribution and its width is, however, still an open question. In the center the peaks are well described by Gaussians, but there are clear deviations on the wings.

5.4 Summary and outlook

We presented in detail the image reconstruction process, i.e. the algorithms to obtain the atom number per lattice site from the fluorescence images. First, we get the position of the lattice sites by analysis of the reciprocal lattice vectors in a Fourier transform of the image. Because the measured image is a convolution of the atomic distribution with the point-spread function of our imaging system, a deconvolution with the Richardson-Lucy-Algorithm localizes the photon counts per atom to an area much below the lattice spacing. This makes it possible to unambiguously connect almost every photon to the site it originated from. A count histogram finally allows to identify thresholds for zero, one and two atoms per site.

The algorithm works very reliably for images with at least 200 photons per atom. For lower fluorescence counts, we see a worse separation of the peaks in the histogram resulting in a lower reconstruction fidelity on some sites. We would like to reduce the required number of photons further because this can reduce the errors due to hopping and losses during imaging (see chapter 4). Because our counts per atom show a spatial dependence, a first improvement could be reached by defining count thresholds locally instead of globally. Further improvements are possible by assigning a probability to have e.g. zero or one atom on sites whose counts are close the defined thresholds. Instead of a number (zero, one, two), the reconstruction algorithm would assign e.g. 60% probability to be empty and 40% probability to be singly occupied. This could be carried to the further analysis of physical properties. Finally, the whole algorithm could be changed to Bayesian approach, where the a priori knowledge of a lattice structure and of atoms with given fluorescence strengths is taken into account from the beginning [167].

---

[1] This leads to a varying number of pixels per lattice site. In our case there can be between 25 and 36 pixel connected to one lattice site. Thus residual homogeneous background counts are unevenly distributed. But the splitting of signal counts from one pixel leads to much larger errors as it is almost impossible to have signal counts from two different lattice sites on the same pixel *after* deconvolution.

Chapter 6

Spin and Density Properties of Fermi-Hubbard Chains

This chapter presents an overview of measurements with our quantum gas microscope. After a general introduction into the analysis methods of site-resolved images (Sect. 6.1), the first half of the chapter focuses on observables related to the density of the atoms. Our trap can be treated as a varying chemical potential, which allows to extract thermodynamic relationships in the metallic and insulating phase from the averaged density per site (Sect. 6.2). In addition, our images provide full access to density fluctuations, which are suppressed in band- and Mott-insulating states. A comparison of these fluctuations to the compressibility allows us to confirm the fluctuation-dissipation theorem (Sect. 6.3).

In the second half of the chapter we turn to the analysis of spin correlations (Sect. 6.4). We present the first observation of antiferromgnetic spin correlations with ultracold atoms beyond nearest-neighbor distance in Hubbard chains. We study these correlations as a function of interaction strength and density and show that these measurements provide a thermometer for the spin sector of the system.

The results on ideal Fermi gases presented in this chapter are published in [32] and our first demonstration of antiferromagnetic spin correlations are published in [71]. Note that the data presented in this chapter is based on more recent measurements.

6.1 Analysis of site-resolved images

A quantum gas microscope offers vast new possibilities and options to analyze many-body systems. The traditional focus on local observables and two-point correlation functions is to a large extent caused by the experimental possibilities to measure bulk properties and response functions. Now, with the option to experimentally access higher order correlation functions, more complex tailored observables can be used to reveal effects of interest[1]. The development and proper understanding of the most suitable correlations for a given effect will present a significant challenge. Here also the limited amount of data and robustness to experimental errors need to be taken into account.

In this section, we present an overview of the observables used in this and the next chapter. Starting from simple local averages, we present correlation functions, spatial averages and conditional correlation functions.

Density and spin Using the reconstructed images (see Chap. 5) from the quantum gas microscope, any analysis starts with the digital information of atom number and spin on every site of the two-dimensional physics lattice for every image taken. These two three-dimensional arrays (density/spin vs site along x, site along y and image number) are the raw information (see Fig. 6.1) to calculate any observable that can be written as a combination of local particle number operators ($\hat{n}_{\uparrow,r}$, $\hat{n}_{\downarrow,r}$, $r=(x,y)$). With the density ($\hat{n}_r = \hat{n}_{\uparrow,r}+\hat{n}_{\downarrow,r}$) and spin operator ($\hat{S}^z_r = 1/2(\hat{n}_{\uparrow,r}-\hat{n}_{\downarrow,r})$), simple observables are the local density n_r and magnetization m_r:

$$n_r = \langle \hat{n}_r \rangle = \frac{1}{N_s}\sum_\tau n_{r,\tau}, \quad m_r = \left\langle \hat{S}^z_r \right\rangle = \frac{1}{N_s}\sum_\tau S^z_{r,\tau} \tag{6.1.1}$$

Here $\langle \dots \rangle$ describes the average over the N_s images labeled by τ. The local density and spin fluctuations are measured by the variance of the local distributions:

$$\delta n_r^2 = \left\langle (\hat{n}_r - n_r)^2 \right\rangle, \quad \delta m_r^2 = \left\langle (\hat{S}^z_r - m_r)^2 \right\rangle \tag{6.1.2}$$

In contrast to measurements that are limited to the parity of the local density, the density variance is an observable which provides information that is independent from the mean density, in our case. As both the density and the spin can take three different values in the single-band Hubbard model, the local distributions are fully characterized by these four observables.[2]

Singlon density Besides the density and the spin, an important local observable is the parity of the density

$$n^s_r = \langle \hat{n}^s_r \rangle, \quad \hat{n}^s_r = \hat{n}_{\uparrow,r} + \hat{n}_{\downarrow,r} - 2\hat{n}_{\uparrow,r}\hat{n}_{\downarrow,r} = 4\left(\hat{S}^z_r\right)^2. \tag{6.1.3}$$

The operator measures if a site is singly occupied and it is sometimes called *local moment* [170], but we prefer to call it singlon density in line with a hole and doublon density. Note that the definition above only applies if $\hat{n}_{\sigma,r}$ is restricted to zero and one[3].

---

[1] Such measurements are possible with any microscope that can resolve individual particles faster than their motion. Up to tenth-order correlations functions have been obtained in atom chip experiment [168] and also very different systems like the new XFEL X-ray laser will provide access to high-order correlation functions in space and time for molecules and other quantum materials [169].

[2] There are only 4 possible states (hole,↑,↓,doublon), so the distribution is fully given by three parameters. When one looks at spin and density separately, each sector is characterized by its mean and variance.

[3] Atoms in higher bands can produce pairs of atoms with the same spin on one site r.

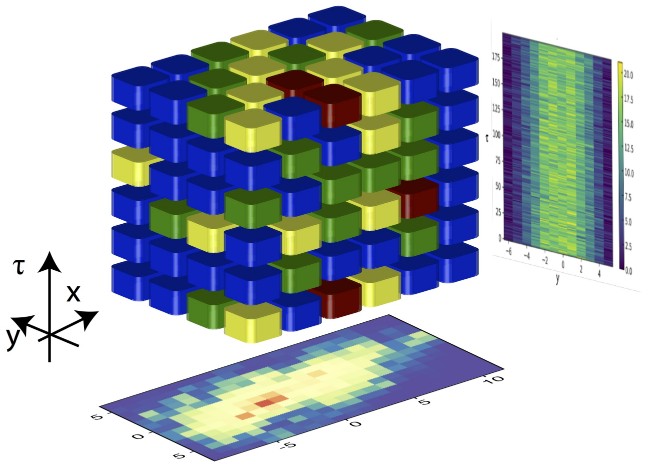

Figure 6.1. Cube of data. *Illustration of the raw data consisting of holes (blue), spin ups (yellow), spin downs (green) and doublons (red) on every site of the lattice (x,y) and on every image (τ). Averaging of the density along τ gives the mean density (bottom) and along x gives the atom number per chain per shot (right).*

It is the direct observable of quantum microscopes that suffer from parity projection, but we can calculate it from $\hat{n}_{\uparrow,r}$ and $\hat{n}_{\downarrow,r}$, of course. The advantage of $\hat{n}^s_r$ over $\hat{n}_r$ is that it respects the particle-hole symmetry around $n = 1$ of the FHM. For systems without doublons it is identical to the normal density $\hat{n}_r$, while for spin balanced non-interacting atoms[1] $n^s_r = \delta n^2_r$. It, thus, serves as a reference for density fluctuations i.e. $\delta n^2_r / n^s_r$ measures density fluctuations relative to the trivial case.

For many-body states, which are almost products of local quantum state, like a band- or a Mott insulator, the local statistics contain almost all informations. If, however, the tunneling between the sites is relevant, one can expect interesting correlations between the events on different sites.

Correlation functions In addition to the local observables, one can calculate spatial correlation functions. The most import ones are the density-density correlator $R(r,r')$ and the spin-spin correlator $C(r,r')$

$$R(r,r+d) = \langle \hat{n}_r \hat{n}_{r+d} \rangle - n_r n_{r+d}, \quad C(r,r+d) = 4\left(\left\langle \hat{S}^z_r \hat{S}^z_{r+d} \right\rangle - m_r m_{r+d}\right), \tag{6.1.4}$$

where the uncorrelated part has been subtracted and d is the relative distance. $R(r,r+d)$, thus, measures non-trivial density correlations like the density suppression around a particle due to Pauli's effect or repulsive interactions [171]. The spin correlator allows to detect antiferromagnetic effects i.e. the anti-alignment of neighboring spins. The factor four is a normalization such that a perfectly ordered Néel state has $C(0,d) = (-1)^d$.

---

[1] Because:

$$n^s_r = \langle (\hat{n}_{\uparrow,r} - \hat{n}_{\downarrow,r})^2 \rangle = \left\langle \left(\hat{n}_{\uparrow,r} - n_{\uparrow,r} + n_{\downarrow,r} - \hat{n}_{\downarrow,r}\right)^2 \right\rangle$$

$$= \left\langle \left(\delta \hat{n}_{\uparrow,r}\right)^2 + \left(\delta \hat{n}_{\uparrow,r}\right)^2 - 2\underbrace{\left(\hat{n}_{\uparrow,r} - n_{\uparrow,r}\right)\left(\hat{n}_{\downarrow,r} - n_{\downarrow,r}\right)}_{0} \right\rangle = \delta n^2_r \text{ for uncorrelated up- and down-spins.}$$

The related pair distribution function for fermions is defined as[1]

$$g^{(2)}_{\sigma,\sigma'}(r,r+d) = \frac{V^2}{N_\sigma(N_{\sigma'}-\delta_{\sigma,\sigma'})}\left(\langle\hat{n}_{\sigma,r}\hat{n}_{\sigma',r+d}\rangle - \delta_{\sigma,\sigma'}\delta_{0,d}\langle\hat{n}_{\sigma,r}\rangle\right), \tag{6.1.5}$$

where V is the volume (number of sites) and N_σ is the number of particles with spin σ. It measures the probability (times V^2) to find a particle with spin σ at site r and a *second* particle with spin σ' at site $r+d$. Correlations show up as deviations from $g^{(2)}_{\sigma,\sigma'} = 1$ and as a probability density $g^{(2)}(r,r')$ is normalized such that $1/V^2\sum_{r,r'} g^{(2)}(r,r') = 1$.

If one ignores the spin, the analogous distribution function reads[2]

$$g^{(2)}(r,r+d) = \frac{V^2}{N(N-1)}\left(\langle\hat{n}_r\hat{n}_{r+d}\rangle - \delta_{0,d}\langle\hat{n}_r\rangle\right) = \frac{N}{N-1}\frac{1}{n_r n_{r+d}}\left(\langle\hat{n}_r\hat{n}_{r+d}\rangle - \delta_{0,d}\langle\hat{n}_r\rangle\right). \tag{6.1.6}$$

The second expression allows for different local densities at r and $r+d$.

As we are working with an inhomogeneously trapped system, care has to be taken in the averaging of the positional argument r. In general, the correlation functions are treated as sets (with $0 \leq d \leq d_{max}$) of local observables e.g. $R_r(d)$ and we specify how to average over r depending on the circumstances.

As a comparison for our measurements, we give here the $g^{(2)}$ function of non-interacting fermions in 1d with density $n$at $T = 0$ in an infinite system, which shows the famous Pauli hole around $d = 0$:

$$g^{(2)}_{\sigma,\sigma',\mathrm{free}}(d) = 1 - \delta_{\sigma,\sigma'}\left(\frac{\sin(\pi n d)}{\pi n d}\right)^2 \tag{6.1.7}$$

This also leads to non-zero antiferromagnetic spin correlations even for non-interacting fermions.

Spatial averaging Local observables can be summed or averaged over sets of sites to give properties of the full cloud or specific subregions. We define the total atom number N_{tot} (total magnetization M_{tot}) of the cloud and the atom number (magnetization) per chain $N_c(y)$ ($M_c(y)$):

$$N_{\mathrm{tot}} = \langle\hat{N}_{\mathrm{tot}}\rangle = \left\langle\sum_r \hat{n}_r\right\rangle, \qquad M_{\mathrm{tot}} = \langle\hat{M}_{\mathrm{tot}}\rangle = \left\langle\sum_r \hat{S}^z_r\right\rangle \tag{6.1.8}$$

$$N_c(y) = \langle\hat{N}_c(y)\rangle = \left\langle\sum_x \hat{n}_{x,y}\right\rangle, \qquad M_c(y) = \langle\hat{M}_c(y)\rangle = \left\langle\sum_x \hat{S}^z_{x,y}\right\rangle \tag{6.1.9}$$

In addition, we have the possibility to choose the region for averaging of one operator based on the mean per site of a different quantity e.g. to analyze the density fluctuations δn_r^2 based on the mean density or the spin correlations based on the mean magnetization.

---

[1] The $(N-1)$ factor in the denominator is important in small systems because there are only $N-1$ particles left that can be found at $r+d$ if there is a particle at r and one is looking at identical particles.

[2] It can be derived from Eq. 6.1.5 by summing the four $g_{\sigma,\sigma'}$ terms, weighted by the probability to draw that spins combination $p_{\sigma\sigma'} = \frac{N_\sigma(N'_\sigma-\delta_{\sigma,\sigma'})}{N(N-1)}$.

Conditional observables and higher order correlation functions A powerful tool of the analysis is the calculation of conditional observables. We define in general

$$\mathscr{O} = \left\langle \hat{A} \right\rangle_{\hat{B}=b} = \frac{\left\langle \hat{P}_{\hat{B},b} \hat{A} \hat{P}_{\hat{B},b} \right\rangle}{\left\langle \hat{P}_{\hat{B},b} \right\rangle} \tag{6.1.10}$$

as the expectation of operator $\hat{A}$ on the subset of the data, where some condition is true i.e. $\hat{B}$ takes the value b as enforced by the projection operator $\hat{P}$. Some examples:

- For $A = \hat{S}^z_r$, $B = \hat{n}^s_{r'}$ and $b = 0$, $\mathscr{O}$ is the mean spin on site r given that site r' is empty or doubly occupied.
- In the case of $A = \hat{n}_{x,y}$, $B = \hat{N}_c(y)$ and $b = 10$, one obtains the density on site (x, y) under the condition that the chain y has 10 atoms in total.

The difference to the filtering of the last section is that here we select based on the outcome of an individual realization i.e. a selection in *time* not in space. Of course, one can also combine both by selected spatial averaging of a conditional observable.

There are many applications of such observables, which can unveil information that is otherwise hidden in the averaging by the measurement process. One can e.g. reduce the experimental fluctuations in the preparation of the system, filter out obvious errors or unwanted events or bin one observable by a second one. Care has to be taken, of course, to understand systematic effects induced by imposing any condition. In general, one can distinguish two cases. If the operator B of the condition commutes with the Hamiltonian, $\mathscr{O}$ simply measures within a separated subspace of the Hilbert space. The total atom number, for example, is a conserved quantity of the Hubbard model. A condition $\hat{N} = N$ changes the ensemble analyzed from the usual grand canonical to a canonical ensemble, but one can still expect thermal distributions. In the opposite case of an arbitrary condition that is not related to some conservation law, the conditional observable should rather be understood as a notation for a normalized higher order correlation function. The next chapter deals in detail with an analysis of spin correlations around holes, that fall into this category ($\hat{A} = \hat{S}^z_r \hat{S}^z_{r'}$, $\hat{B} = \hat{n}_{r''}$, $b = 0$).

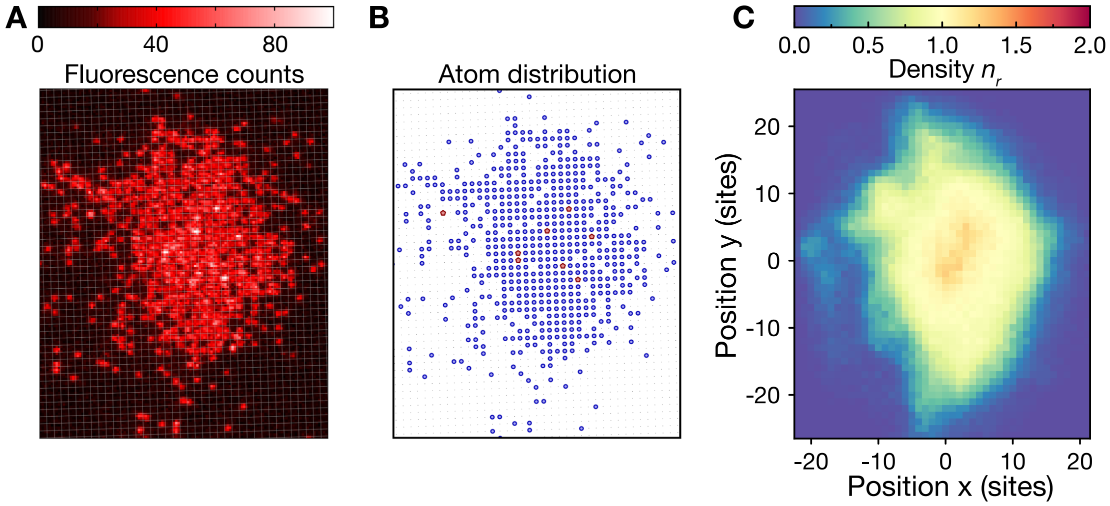

Figure 6.2. Single-site resolved density distribution. *(**A**) Fluorescence image of a cloud with about 750 non-interacting atoms. (**B**) Reconstructed distribution of atoms from (A) (**C**) Density distribution obtained from averaging 450 images.*

6.2 Density

The local particle density $\hat{n}_r$ is the most basic observable of our microscope. Thanks to the detection of more than one particle per site, we directly measure the true density and study the transition from Mott insulator to metal. The paramagnetic Mott insulating state has been observed in seminal ultracold atom experiments involving trap-averaged quantities and, recently, at the single-atom level [57, 58, 170, 172–176].

In a grand-canonical ensemble[1] the density is a function of the chemical potential and temperature. Within the local-density approximation (LDA), one can describe the inhomogeneous system locally by an infinite homogeneous system with the same density. The local chemical potential $\mu(r)$ is given by

$$\mu(N,r) = \mu(N) - V(r), \tag{6.2.1}$$

where $\mu(N)$ is the global chemical potential related to the atom number N and $V(r)$ is the local potential[2]. A measurement of the density as a function of the chemical potential and the temperature allows to construct the equation-of-state (EoS) of the system. Detailed experimental studies revealed the EoS for scale-invariant systems (unitary Fermi gas [24], BKT [177]) and for the density sector of the Fermi-Hubbard model for two [175] and more [178] spin states. In reverse, a known EoS allows to extract temperature and/or chemical potentials from measured density distributions.

6.2.1 Non-interacting fermions

We start our analysis with a simple cloud of spin-polarized fermions, which are always non-interacting in the ultracold regime. Figure 6.2 shows an example of an individual image, its

---

[1] The full system is closed, but sufficiently small parts of the system can be treated in the grand canonical ensemble with the rest serving as the bath.

[2] Depending on the system, N is the atom number per 1d chain or of the 2d cloud.

reconstruction and the spatial density distribution n_r, obtained by averaging the occupation of every site over several hundred images. The density distribution reflects the variation of the underlying potential of the laser beams. The density is highest in the center and then decreases to zero towards the edges. In addition, to the general harmonic confinement, we observe static imperfection on large scales, which produce the irregular structure. There are several phases present in different regions of the cloud. In the case of non-interacting spin-polarized fermions, these are

- A metal in the lowest band at densities below one particle per site (blue, green) on the outer ring.
- A band-insulator (BI) with a filled first band with a density of one (yellow). Due to its incompressibility there is a large area of constant density even in an inhomogeneous potential.
- A metal in the first excited band with densities between one and two (orange).

For atoms in the lowest band, the band-insulator is a direct consequence of Pauli blocking, which prevents more than one atom per lattice site, and it is thus a pure quantum effect. The quality of this band-insulator can be quantified by the density fluctuations, which tend to zero as the occupation is always one atom per site. Due to the second band and a finite temperature as well as due to experimental imperfections, we measured local fluctuations in the band-insulator of $\delta n_r^2/n_r = 0.06(3)$ which is an almost 12 dB suppression compared to classical particles, which would show $\delta n_r^2/n_r = 1$. The fluctuations correspond to an entropy per particle of only $0.3(1)k_B$. This low value can be reached because of the large gap to the next band. If one creates such a band insulator with two spin states in the superlattice, one can hope to adiabatically transfer the state with its low entropy into a Mott insulator by splitting each site [65]. For details of our analysis of the non-interacting system including an analysis of density correlations see [32, 89].

6.2.2 Interacting fermions

Non interacting atoms are great to benchmark an experimental setup or an analysis technique, but the interesting physics of quantum many-body systems requires interactions between the atoms.

With a $|1\rangle$, $|2\rangle$ mixture of lithium atoms in our physics lattice, we produced Hubbard systems in one and two dimensions with interactions up to $U/t = 18$[1]. We worked with spin balanced systems only so far and realized Mott insulator of up to 200 atoms.

Detailed characterizations of density related properties of the two-dimensional Fermi-Hubbard model down to temperature $T/t = 0.6$ have been performed recently in several groups [170, 174–176]. The measurement of density distributions requires high-resolution imaging, but not necessarily to the level of single sites. In this section, we present our analysis of a one-dimensional chain[2] at $U/t = 8$ highlighting our analysis method, which is unique to quantum

---

[1] Interaction U and hopping rate t are set by the lattice depth and the scattering length. At scattering lengths above $a_s \sim 2000 a_B$ we start to see three-body losses and very low hopping rates t require deep lattices, which lead to a strong confinements and thus small systems.

[2] We generated one-dimensional chains by splitting of our 2d cloud with a strong lattice in y-direction ($V_y = 17E_r^y$, $t_y \sim (2\pi\hbar)\cdot 5\,\mathrm{Hz}$) and worked for the experiment in this section at $t_x = (2\pi\hbar)\cdot 400\,\mathrm{Hz}$. Details of the preparation are given in Sect. 7.2.

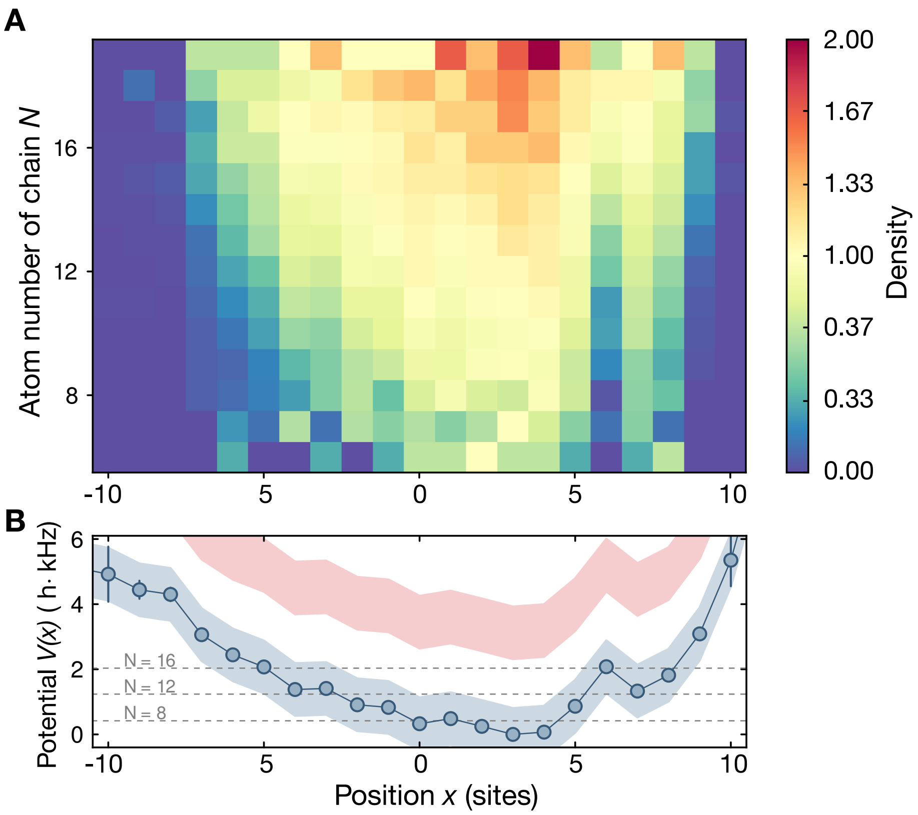

***Figure 6.3. Density in a single Hubbard chain vs total atom number. (A)** The local density in row $y = 0$ (cf. Fig. 7.3) for $N = 6 - 19$ atoms per chain. The density depends on the local chemical potential $\mu(N) - V(x)$ with a chemical potential $\mu(N) = 0.52(9)N$ that is almost proportional to the total atom number N. **(B)** The local potential $V(x)$ for the same chain (points) with reconstructed chemical potentials for given atom numbers (dashes lines). Deviations from a harmonic confinement are due to imperfections of our lattice beams. The blue and red shadings indicate the ground and Mott band with bandwidths of $(2\pi\hbar) \cdot 1.6\,kHz$.*

gas microscopes. It relies on the precise determination of the chemical potential μ for each atom number in the chain.

Density in Hubbard chains with N atoms We have access to the exact atom number per chain of every run. This allows to sort the data of one chain by its total atom N. For notational simplicity, we drop the index c in this section. The density

$$n(x,N) = \langle \hat{n}_x \rangle_{\hat{N}_c = N} \tag{6.2.2}$$

gives the mean occupation of site x for N atoms in the chain (Fig. 6.3A). Taking the known potential per site[1] (Fig. 6.3B) and a global chemical potential approximated[2] by $\mu(N) = \alpha(N-$

---

[1] We calibrate our potential $V(x,y)$ with single-site resolution by analysis of the density of a weakly interacting gas with known equation of state.

[2] In principle one can keep $\mu(N)$ completely arbitrary and determine a value for each N. But we found an almost linear relationship ($\mu(N) \propto N$) in all cases due to the constant density of states in 1d harmonic oscillators. So an expansion of $\mu(N)$ to second order around a central value e.g. $N_0 = 10$ is sufficient to capture our deviations from an harmonic potential.

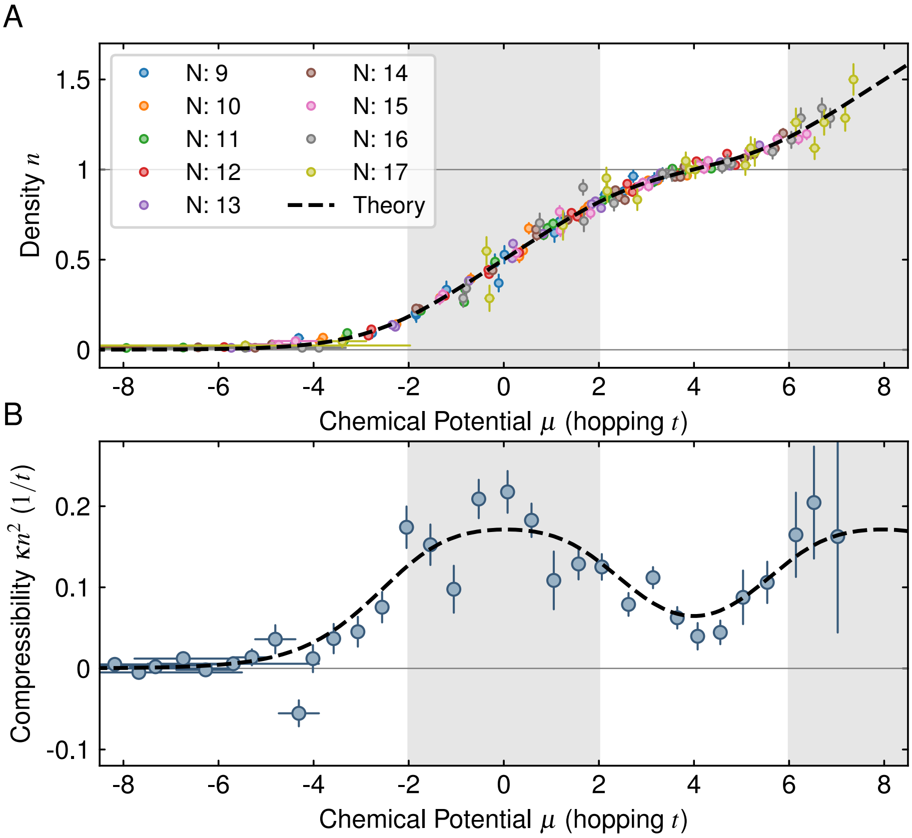

Figure 6.4. Density and compressibility vs chemical potential. *(**A**) The density as a function of the chemical potential obtained by plotting the entries of $n(N,x)$ in figure 6.3 vs $\mu(N)-V(x)$. The different colors correspond the different atom numbers per chain, N, and the gray shading indicates the width of the ground and Mott band. (**B**) The compressibility (times density squared) as a function of the chemical potential obtained from the derivative of (A). There is a clear dip at half filling ($\mu = U/2 \simeq 4t$) reflecting the low compressibility of a (thermal) Mott insulator. Black dashed curves are the theoretical predictions based on the two band model from Eq. 6.2.4 for a FHM at $U = 8t$ and a fitted $T = 0.94t$. All data is from the single line $y = 0$.*

$N_0) + \beta(N-N_0)^2$, equation 6.2.1 assigns a local chemical potential to every entry in the (x,N)-plane. Every column in figure 6.3A thus represents the density of the system at a position x for a scan of the chemical potential just with different offsets $V(x)$ per site. As $n(\mu)$ for $\mu = \mu(N) - V(x)$ should be a single curve independent of x and N, one can fit for α and β and obtain the equation of state (Fig. 6.4A). The data indeed collapses on a single line for $\alpha = 0.52(9)$ and $\beta = -0.002(7)$ $(N_0 = 6)$. While this equation of state has been measured before, we like to stress that the analysis used just 21 sites of a single chains at constant experimental parameters. The quite good resolution of the EoS results from the intermediate sorting of the data by chain atom number N.

Two band model One can calculate the density of the strongly repulsive system by a simple two band model. For $U \to \infty$ it is well known that bosons in one-dimension fermionize [179] i.e. most properties can be derived from identical fermions. The same is true for the charge properties of strongly repulsive spin-full fermions of the FHM, which can be mapped to spinless non-interacting fermions [104, 180]. At finite interaction $U \gg W = 4t$, one can introduce a second band (Mott band) shifted by energy U relative to the ground band (see illustration in Fig. 6.3B). Instead of two strongly interacting spin states, one has two non-interacting fermions, with chemical potentials that differ by U. For these, thermal properties can be simply calculated by integration over the Fermi distribution functions $f(k)$

$$f(k) = \frac{1}{e^{\beta(\varepsilon(k)-\mu)}+1}, \quad f_U(k) = \frac{1}{e^{\beta(U+\varepsilon(k)-\mu)}+1}, \quad \text{with: } \varepsilon(k) = -2t\cos(k), \tag{6.2.3}$$

where $\beta = 1/T$ and the wavevector k is measured in units of the lattice spacing. E.g. the density can be calculated numerically from a simple integral:

$$n(\mu,\beta) = \int_{-\pi}^{\pi} \frac{dk}{2\pi}\left(f(k)+f_U(k)\right) \tag{6.2.4}$$

This two band model is inaccurate when it predicts a particle of the upper band on a site that is not occupied by a particle of the lower band because physically the upper band only exists on occupied sites. Thus, the model works well for temperature $T \ll U$, where the lower band is almost filled before the upper band gets populated. In one-dimension it is expected to work especially well because the lowest corrections of order $J = \frac{4t^2}{U}$ do not affect the density due to spin-charge separation. This simple non-interacting model does not account for particle-hole fluctuations, so it is inaccurate for e.g. the variance of the density. Popular high-temperature expansion [181] in t/T and t/U, on the other hand, suffer from unphysical ringing[1] for $T < t$ even for the density.

We obtain very good agreement of our experimental density curve $n(\mu)$ with the two band model at a temperature of $T = 0.94(9)t$ (Fig. 6.4A). This is an important result because it confirms that the realizations with different atom numbers N_c are still described by the same temperature. This is not obvious because different atom numbers per chain can lead to different temperatures even if they are created from the same thermal two-dimensional cloud: We still change the lattice potential adiabatically after the different chains became disconnected. During this process not the temperature but the entropy is conserved and each N_c-ensemble can evolve differently.

6.2.3 Compressibility

The compressibility is related to the density via,

$$\kappa = \frac{1}{n}\frac{\partial n}{\partial P} = \frac{1}{n^2}\frac{\partial n}{\partial \mu}, \tag{6.2.5}$$

where P is the pressure and $dP = n\,d\mu$. From the $n(\mu)$ data one can thus obtain the compressibility $\kappa(\mu)$ by a derivative with respect to μ. To avoid the divergence for $n \to 0$, we look at a normalized compressibility κn^2 (Fig. 6.4B), which is obtained by averaging the density $n(\mu)$ in small bins of the chemical potential and calculating finite differences. The normalized compressibility peaks for a chemical potential of zero, which corresponds to quarter filling or

---

[1] A converging expansion $n(\mu, t/T) = \sum_i a_i(\mu)(t/T)^i$ with $t/T > 1$ shows unphysical oscillations in n if stopped at series element $i_{\max}$.

one atom per two sites, which is the expected behavior for spinless non-interacting fermions at this density. The compressibility shows the symmetry of the FHM around $\mu = U/2$.

Once again, we find excellent agreement with the two band model and the amplitude of the dip due to the Mott insulator at $\mu = U/2 \simeq 4t$ is in agreement with a charge temperature $T/U = 0.12(1)$. The compressibility vanishes completely only at $T = 0$ and $n = 1$, so strictly there is no Mott insulator at finite temperatures.

The large variance and uncertainty on the data points of the compressibility is a consequence of the derivative on noisy data[1].

Further thermodynamic properties can be derived from the equation of state. Experiments with potassium recently derived the pressure and the thermodynamic entropy from the $n(\mu)$ relation [182]. We will next turn to the analysis of fluctuations, which we can directly measure and thereby confirm the fluctuation-dissipation relations to the compressibility.

---

[1] With a different analysis methods smooth results could be obtained. If one first fits $n(\mu)$ with a spline (e.g. *scipy.interpolate.splrep*) and then takes the derivative of the spline function, the final compressibility curve is smooth. Of course, the uncertainty of the resulting curve remains.

6.3 Density fluctuations

In addition to the mean density, we have access to all orders of density fluctuations. One needs to distinguish between fluctuation due to unstable parameters or experimental imperfections and quantum or thermal fluctuations. The latter contain important information about the many-body wavefunction or the temperature of the system. Once all experimental fluctuations are controlled or can be measured, a fluctuation of some variable is a physical observable just like a mean. Typically the relevance of fluctuations scales with the inverse square root of the system size, so a single lattice site provides the largest possible fluctuation signal.

Fluctuation-dissipation relation Fluctuations of an equilibrium system are generally linked to the response of the system to weak external perturbations. First described by the Einstein-relation [183–185], which connects the friction in a liquid to the Brownian motion of a suspended particle, fluctuations-dissipation relations can be derived for many properties [186].

The density fluctuations are related to the compressibility, which is obvious from the expression of the density as a thermal average ($\beta = 1/T$)

$$\langle \hat{n}_r(T,\mu) \rangle = \frac{\mathrm{Tr}\, \hat{n}_r e^{-\beta(\hat{H}-\mu\hat{N})}}{\mathrm{Tr}\, e^{-\beta(\hat{H}-\mu\hat{N})}}. \tag{6.3.1}$$

The compressibility κ as the derivative with respect to μ is thus always proportional to the sum of all density correlations

$$n_r^2 \kappa_r = \frac{\partial \langle \hat{n}_r \rangle}{\partial \mu} = \frac{1}{T} \sum_{r'} \left(\langle \hat{n}_r \hat{n}_{r'} \rangle - \langle \hat{n}_r \rangle \langle \hat{n}_{r'} \rangle \right) \tag{6.3.2}$$

because the total particle number is $\hat{N} = \sum_r' \hat{n}_{r'}$. The ratio of compressibility to fluctuations is, therefore, a constant, which is given by the inverse of temperature times density square. It is important to note that the relation 6.3.2 is valid for each position r and does not rely on the homogeneity of the density.

We are in the positions to experimentally verify this relationship for a strongly interacting quantum system because we can measure

- the compressibility by taking the derivative of the measured density $n(\mu)$, where the chemical potential is derived from the analysis of atom number per chain and/or from the confining potential in LDA (see Sect. 6.2.3),
- the density fluctuations over arbitrary distances from a correlations analysis of the single-site resolved images,
- the temperature from the density distribution $n(\mu)$ by comparison to some theory e.g. in the low density wings.

For the FHM, the on-site fluctuations (variance) of the density (Eq. 6.1.2) have been measured for a large range of densities, interactions and temperatures by the group of M. Köhl [187]. They also had access to the compressibility and the temperature but they could not measure the non-local correlations $r \neq r'$. Instead they used equation 6.3.2 to derive these as the missing part to fulfill the relation.

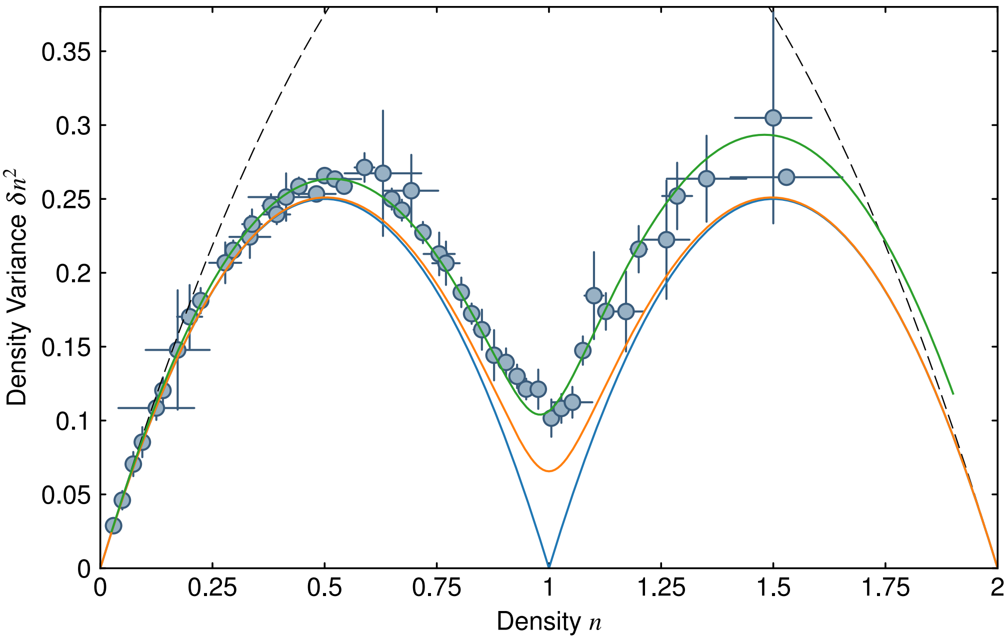

Figure 6.5. Density fluctuations. *The measured density variance δn^2 per site vs the measured density n of chain $y = 0$ (blue points). Data has been sorted by atom number per chain and binned with width 0.025 density. The variance for hard core fermions at $U \to \infty$ (blue line) expresses the simple $n(1-n)$ variance of a binomial distribution for holes and doublons. At finite T/U or t/U the lobes start to connect. The orange line has been calculated at the experimental values $U/t = 8$ and $T/t = 0.94$ from the two-band model. It shows the melting of the Mott insulator due to thermal excitations at $n = 1$. We can match our data well if we include to this result the variance due to hopping (2.5%) and losses (0.5%) during our imaging (green curve). The uncertainties of the data points (1 SEM) along the n and δn^2 axis are strongly correlated because no events can occur below the blue curve. The variance is much lower in comparison to non-interacting fermions (dashed line).*

Here, we present the confirmation of the fluctuation-dissipation relation for the density by obtaining all three contributions experimentally for a one-dimensional Hubbard systems at $U/t = 8$, $T/t = 0.94$ and mean densities up to 1.5 particles per site. In addition, a careful analysis of detection errors allows to obtain good agreement with theory.

6.3.1 Density variance

We can directly calculate the variance per site from the measured distribution of densities. Plotted against the local density (Fig. 6.5), we obtain a curve $\delta n^2(n)$. We see a double lobe structure of two binomial distributions with strongly reduced local fluctuations around a density of $n = 1$ due to the repulsion. The almost symmetric structure towards $n = 0$ and $n = 2$ is given by the particle-hole symmetry. At $U \to \infty$ the local density distribution of the FHM is given by two binomial distributions, one for the ground band and one for the Mott band. This fixes the variance as a function of density to two parabolic lobes. At finite interaction, thermal and quantum fluctuations increase the variance, especially around $n = 1$.

In the simplified model of an independent ground (G) and Mott band (U), the variance is given by (see Eq. 6.2.3):

$$\begin{aligned}\delta n^2 = \langle \hat{n}^2 \rangle - n^2 &= \int_{-\pi}^{\pi} \frac{dk}{2\pi} \left(\langle (\hat{n}_G(k) + \hat{n}_U(k))^2 \rangle \right) - n^2 \\ &= \int_{-\pi}^{\pi} \frac{dk}{2\pi} \left(f(k) + f_U(k) + 2 f(k) f_U(k) \right) - n^2 \\ &= n - n^2 + \underbrace{2 \int_{-\pi}^{\pi} \frac{dk}{2\pi} f(k) f_U(k)}_{\chi_\mu} \end{aligned} \qquad (6.3.3)$$

For $U \gg T$ the integral gives $\chi = (n-1)$ if $n > 1$ ($\mu > U/2$) and zero otherwise, which results in the double lobe structure shown in figure 6.5. This is the exact limit for $U \to \infty$ at fixed T and t, but misses the quantum fluctuations (particle hole pairs) for $T \to 0$ at nonzero t/U. The integral χ at finite T/U captures thermal excitations, which raise the variance around $n = 1$, but still give lower variance than the one observed.

Effect of detection errors The extra variance and the slight deviations from the symmetry around $n = 1$ in our data can be explained by the losses during the imaging (see Chap. 4). While a detection error on the order of a few percent has only small influence on the mean density, its contribution to the variance is substantial.

Given a probability p^- not to detect an atom on its correct site and a probability p^+ to detect an atom on a site[1], where it did not originate, the detected density[2] $\tilde{n}$ is related to the true density n via $\tilde{n} = n(1-p^-) + p^+$. The detected variance $\delta\tilde{n}^2$ can then be calculated as a function of the true variance δn^2 as

$$\delta\tilde{n}^2 = \delta n^2 \left(1 - p^-\right) + p^-(n^2 - \chi_{\mu(n)}) + p^+ \qquad (6.3.4)$$

$$= \tilde{n} - \tilde{n}^2 + \chi_{\mu(n(\tilde{n}))}(1 - 2p^-) + 2p^+\tilde{n}. \qquad (6.3.5)$$

In the second line, we re-expressed in terms of the measured density $\tilde{n}$ as plotted in figure 6.5. Note that $p^- > p^+$, $\tilde{n} < n$ for most densities, and $\chi_{\mu(n)} > \chi_{\mu(\tilde{n})}$, thus the detection errors always increase the variance, as one would expect. Including these detection error, the calculated variance matches the measured one very well (see Fig. 6.5).

A crucial step to obtain the low variance around $n = 1$ is the sorting by chain atom number N_c (see Sect. 6.2.2). This removes density fluctuations due to fluctuation of N_c leading to varying chemical potentials from shot to shot. These are large because of the relatively small size of our chain. We can i.e. consider a canonical instead of a grand-canonical ensemble[3]. The many-body wavefunction (or thermal density matrix) in the lattice prior to imaging is different for runs with different number of atoms in the same chain and the resulting variance of the density can be identified as a change of mean density instead of a thermal fluctuation of the 1d-system.

---

[1] p^- and p^+ are related to the hopping probability p_h and loss probability p_L per atom via $p^- = p_h + p_L$ and $p^+ = p_h\bar{n}$. Here $\bar{n} \approx 0.5$ is the mean density over a typical hopping distance.

[2] The notation is only used in this paragraph. Everywhere else, including in the figures, the measured density is labeled n.

[3] The local sites, however, are still described in a grand-canonical ensemble with the rest of the chain serving as the (finite) bath.

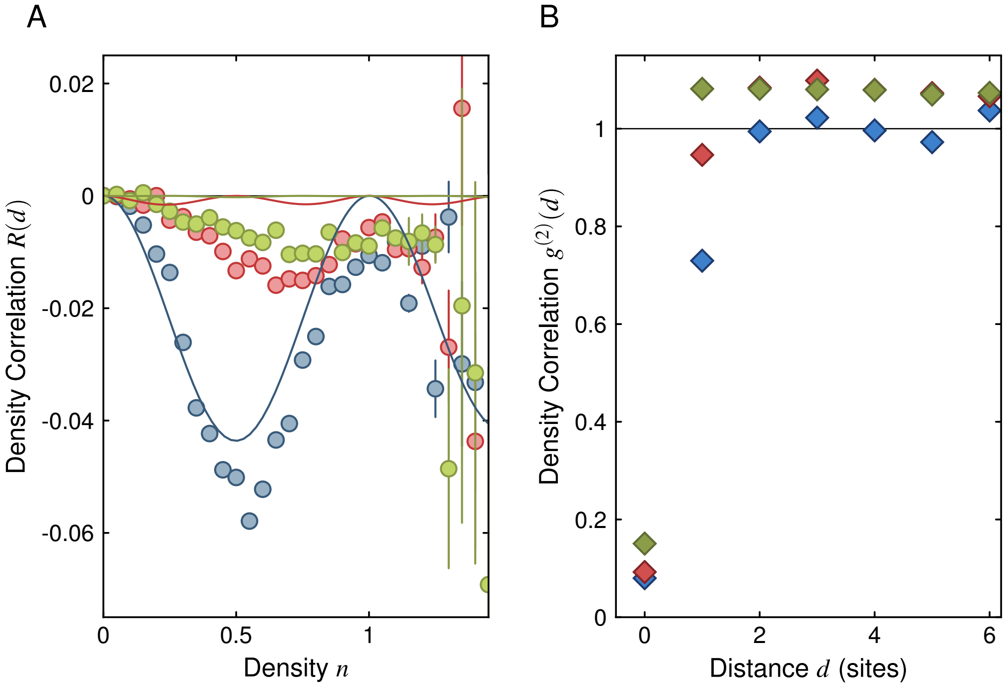

Figure 6.6. Density correlations. (A) *The density correlations* $R(d) = \langle \hat{n}_r \hat{n}_{r+d} \rangle - \hat{n}_r \hat{n}_{r+d}$ *vs measured density as defined in the main text. For distance* $d = 1$ *(blue) we see quite strong negative correlations as expected for repulsive fermions. Around density one, these are the particle-hole pairs of the Mott insulator and at lower densities they arise from tendency towards a charge density wave. The theoretical prediction from the two band model at* $U/t = 8$ *and* $T/t = 0.94$ *(solid lines) captures the basic trend, but can not account for all correlations because it does not include the particle-hole fluctuations nor our experimental imperfections. The obtained density correlations at* $d = 2$ *(red) and* $d = 3$ *(green) are weaker and they are dominated by a negative offset due to the analysis at fixed atom number (in analogy to the spin correlation offset in Appendix B.3). The large errorbars for* $n > 1.1$ *are due to low statistics at these densities.* ***(B)*** *The measured pair distribution function* $g^{(2)}(d)$ *for* $n = 0.4$ *(blue),* $n = 0.6$ *(red) and* $n = 1.0$ *(green). The strong correlation hole around* $d = 0$ *is due to repulsive interactions and the fermionic nature of the atoms. The negative systematic offset from (A) is no longer present due to the proper normalization (Eq. 6.1.6) and* $g^{(2)} \approx 1 + 1/L$ *is the limit for large distances in a system of size L. We do not expect to see Friedel-oscillations at our temperatures.*

6.3.2 Density correlations

The analysis of two-point density correlations $R(d)$ is straight forward from a given data set. We calculate $\langle \hat{n}_r \hat{n}_{r'} \rangle$ for all pairs (r, r') within the same chain where the average runs over all images with the same number of atoms in this chain. The resulting bare correlations thus depend on four indices $(y, x, x' = x + d, N_c)$. Each correlation is associated with the mean density n of the $d + 1$ sites connecting r and r' by averaging the occupations over the same subset of the data i.e. a different density for each (y, x, x', N_c). We then bin these densities for each relative distance d in groups of width Δn typically 0.05 and average the associated correlations within each bin. The resulting data now depends only on d and n.

The density-density correlation $R(d)$ (Eq. 6.1.4) for $d = 1$ are all negative and their magnitude shows a peak of $R(1) = -0.056$[1] at $n \approx 0.5$ (Fig. 6.6). This value needs to be compared with -0.25, which is the maximally possible correlation value[2] corresponding to a charge-density wave, where every atom is followed by a hole. Due to three reasons, we do not see correlations beyond $d = 1$, however: The finite temerature, the 1d-nature, which allows at the most for algebraically decaying correlations and the inhomogeneous density in our trap.

At low densities correlations scale like n^2 as expected for non-interacting atoms and at $n = 1$ we observe $R(1) = -0.011$, which we associate with the particle-hole pairs in the Mott-insulator [27]. Taking a first order estimate, we would expect a particle-hole probability $p_{d/h}$ of $2({}^t\!/\!_U)^2$ whenever the two neighboring atoms are of opposite spin. From our spin correlation measurements (see Fig. 7.5 for spin correlations of this data set) we know that anti-aligned spins on neighboring sites occur with a probability of about 65%. This gives $p_{d/h} \approx 2\%$, slightly higher than the observer value, which could be due to higher order corrections at $U/t = 8$.

The measured correlations $R(d > 1)$ are all negative, which has a simple statistical reason from the finite system size: If one detects a particle at r, there are only $N - 1$ particles left, so it is less likely to find a particle at r' compared to the unconditioned case.

Pair distribution function This effect is taken into account with the properly normalized pair distribution function $g^{(2)}(d)$ (Eq. 6.1.6). At $d = 0$ we see strong anti-correlations, which are nothing but the suppression of the variance (Fig. 6.5) below the value for independent particles. Non-interacting fermions have $g^{(2)}(0) = 0.5$ because identical fermions are fully anti-correlated $g^{(2)}_{\sigma,\sigma}(0) = 0$ and particles of different spin are uncorrelated $g^{(2)}_{\sigma,\bar{\sigma}}(0) = 1$. The suppression below 0.5 is thus due to the repulsive interactions and $g^{(2)}(0)$ would reach zero for $U \to \infty$.

This *correlation hole* extends to finite distance with a range of about $1/n$ (cf. Eq. 6.1.7). We see significant correlations only for $d = 1$ and find $g^{(2)}(d > 1) \gtrsim 1$. Values above one are expected in a finite system of size L with a correlation hole around zero because of the normalization: $\sum_d g^{(2)}(d) = L$.

6.3.3 Fluctuation-dissipation relation

We can now compare the compressibility (Sect. 6.2.3) to the sum of all density fluctuations (Fig. 6.7). To this end we multiply the compressibility $\kappa(n)n^2$ obtained in Sect. 6.2.3 with the temperature that we got from the comparison of the density distribution to the theory and compare to the on-site correlations δn^2, to the sum of non-local correlations $\sum_d R(d \neq 0)$ and to the sum of all correlations. While the on-site fluctuations are larger than the compressibility [187], the non-local contributions fill the difference and we can experimentally confirm the relation

$$\kappa(n)n^2T = \left\langle \sum_{r'=1}^{L} \langle \hat{n}_r \hat{n}_{r'} \rangle - \langle \hat{n}_r \rangle \langle \hat{n}_{r'} \rangle \right\rangle_{n(r)=n} \tag{6.3.6}$$

at $U/t = 8$, $T/t = 0.94$ and densities $0 < n < 1.2$ within the errorbars (~10%). Here r' runs over all sites of a Hubbard chain (including sites of different density) and the average over r

---

[1] We do not show uncertainties on these numbers because the statistical SEM is only about 0.0004 because more than 20 000 data points are averaged for each density value. Systematic effects thus dominate which are hard to quantify.

[2] In a system without doublons.

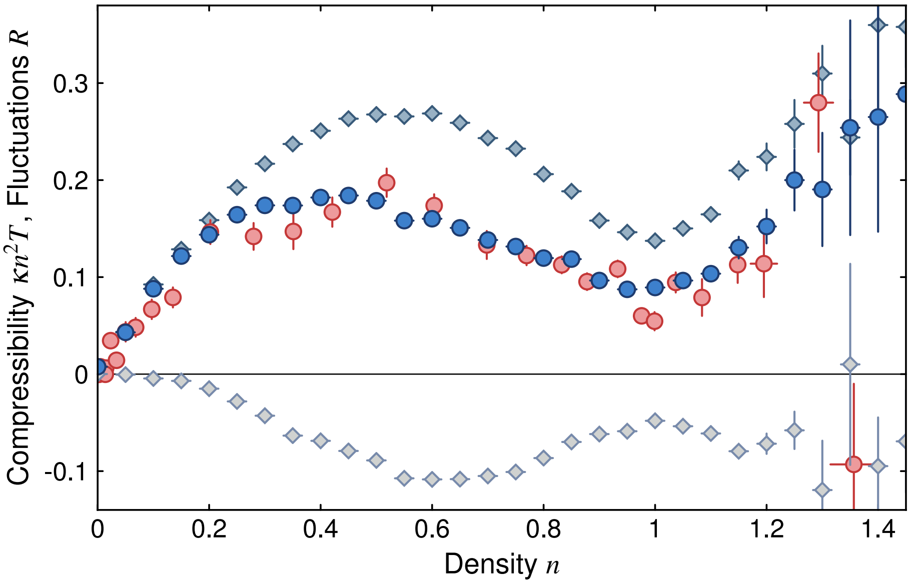

Figure 6.7. Compressibility and fluctuations. *Experimental confirmation of the relation (Eq. 6.3.2) between compressibility, density fluctuations and temperature. The compressibility $\kappa n^2 T$ (red circles) as a function of the local density n is calculated as the derivative of $n(\mu)$ for density data from the central three chains of the experiment (Sect. 6.2.3 and Fig. 6.4B). The on-site $R(d=0)$ (dark blue diamonds) and non-local $\sum_d R(d \neq 0)$ (light blue diamonds) correlations (Figs. 6.5,6.6A) can be added to give a line (blue circles), which matches the compressibility scaled with the temperature $T = t$ at all densities. This relates the response of the system to an external pressure with the equilibrium fluctuations of the many-body system.*

is taken within density bins as described in section 6.3.2. In order to increase the statistics, we combined data from the central three chains of the system, which show the same temperature $T/t = 0.94(5)$. We note a slight asymmetry of the correlation curve which peaks below $n = 0.5$ and we link this to a weak systematic effect at low densities.

Finally we like to stress the connecting of this relation to the order parameter of the Mott insulator. The Mott insulator is defined as the state with zero compressibility [1], so the sum over all correlations vanishes according to equation 6.3.6. The individual summand can still be non-zero due to quantum fluctuations, but all fluctuations have to occur as particle-hole *pairs* to keep the sum at zero. This is exploited in the construction of the Mott order parameter in terms of a string operator [27, 188, 189]

$$O(l) = \left\langle (-1)^{\sum_{x=x_0}^{x_0+l} (\hat{n}_x - n_x)} \right\rangle, \tag{6.3.7}$$

which stays finite even for l to infinity, i.e. $\lim_{l\to\infty} O(l) \neq 0$, because fluctuations only come as bound pairs at $T = 0$.

Model independent temperature One can invert the relation 6.3.6 and use the measurements of compressibility and correlations to derive the temperature T. This has the advantage that it does not depend on a model because both κ and $R(d)$ can be calculated from the data without any reference to theory [190], which might not be available for strongly interacting systems in higher dimensions. Using this approach, we obtain a temperature of $T/t = 0.99(15)$, which is only a factor of three less precise than the temperature derived from comparison to FHM calculations. The largest contribution to the uncertainties comes from the compressibility, which could be improved by more statistics or a more sophisticated method to take the derivative.

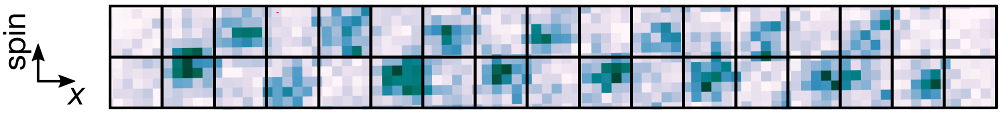

Figure 6.8. Image of a spin chain with antiferromagnetic correlations. *Spin chain with 15 spins that shows Néel order. The spin is encoded in the vertical direction due to our local Stern-Gerlach splitting. Such ordered realizations occur by chance*[1]*, because in one dimension the Heisenberg ground state differs from a Néel state by strong quantum fluctuations.*

6.4 Antiferromagnetic correlations in spin chains

The study of quantum magnetism with Fermions in optical lattices has been a central goal for more than one decade. The Hubbard model supports antiferromagnetic correlations below a "critical" entropy per particle of $s^* = S/Nk_B = \ln(2)$ [60, 191, 192] in all dimensions. The experimental realization of the required low entropy lattice fermions has proven to be extremely challenging, making the observation of longer ranged antiferromagnetism difficult. Important progress in revealing magnetic ordering in the Hubbard model has been reported with the observation of nearest-neighbor correlations via singlet-triplet spin oscillations [67, 193, 194] and short range correlations deduced from optical Bragg spectroscopy [68]. However, for global observables the detection of the onset of magnetic order is complicated by the inhomogeneity of the trapped samples, in which different phases coexist. Microscopic control or detection helps to overcome this limitation, and the analogue of antiferromagnetic correlations has been measured in small systems of up to three fermions [195]. Soon after the realization of Fermi microscopes [29–32, 123], we and three other groups succeeded to image spin correlations over several sites in Fermi-Hubbard systems [71–74] and even an antiferromagnetic phase has been demonstrated by now [75].

In this section, we report on a site- and spin-resolved study of antiferromagnetic correlations in one-dimensional spin-$1/2$ Hubbard chains. Importantly, true long range order is absent in the 1d Hubbard model even at zero temperature [54, 192], and the resulting algebraic decay of the correlations is significant even on a distance of a few sites [60, 196].

Our measurements reveal finite-range antiferromagnetic Heisenberg correlations extending over up to four sites. The results are in good agreement with quantum Monte Carlo simulations and can be described by the analytic expression from bosonization theory (Eq. 2.3.4). Furthermore, we measured the strength of the spin correlations for increasing interactions, which are consistent with isentropic lattice loading. Finally, we observed spin wave correlations away from half filling that are stretched in space by the amount of doping.

6.4.1 Spin correlations vs distance

First, we analyze the spin correlations $C(d) = 4(\langle \hat{S}_i^z \hat{S}_{i+d}^z \rangle - \langle \hat{S}_i^z \rangle \langle \hat{S}_{i+d}^z \rangle)$ between the spin operators $S_i^z = (\hat{n}_{i,\uparrow} - \hat{n}_{i,\downarrow})/2$ versus distance d. To this end, we fixed the s-wave scattering length to $2390(30)\, a_B$, where a_B is the Bohr radius, corresponding to $U/t = 8.2$ and took a high statistics dataset of 1900 individual pictures. Our first analysis of the Mott insulator involves all sites

---

[1] We find spins with perfect Néel order (along z) in $0.9(3)\%$ of all spin chains with 15 singly occupied sites. For random spins one expects only $2^{-14} = 0.006\%$ such events, while the overlap of the $L = 15$ Heisenberg chain with the Néel state is still only 6.3% (obtained by exact diagonalization).

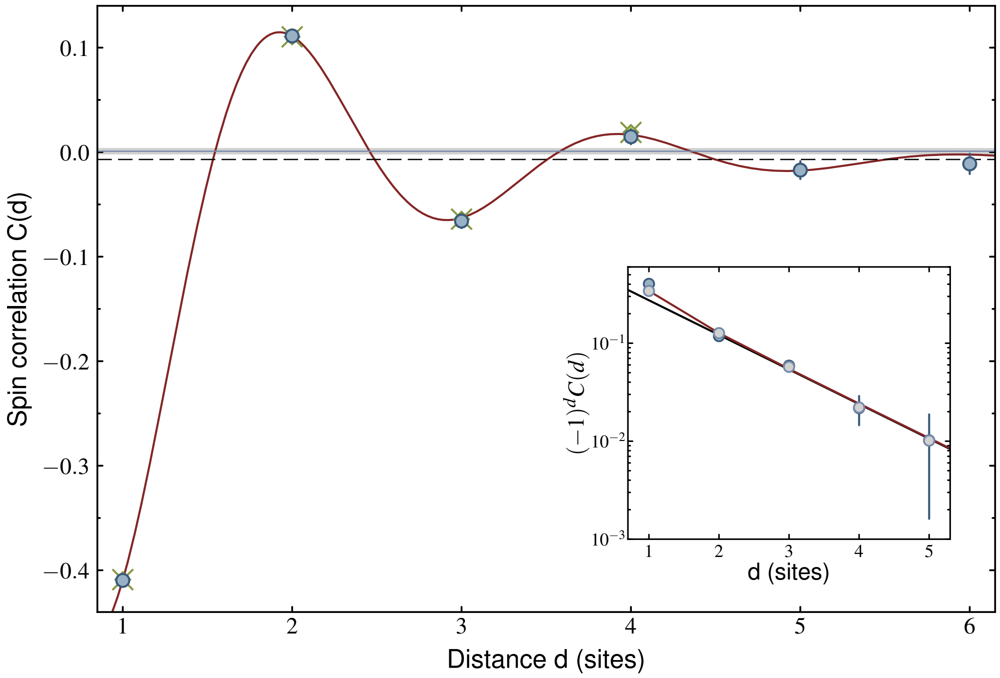

Figure 6.9. Antiferromagnetic spin correlations versus distance in spin chains. *Measured spin correlations $C(d)$ at U/t = 8.2 for a Mott insulator (density $n_r \in [0.95, 1.05]$) (blue circles). The staggered behavior directly visualizes the antiferromagnetic nature of the correlations. Correlations up to four sites are statistically significant. The transverse correlations (gray line) vanish within their 1 SEM uncertainty (light gray shading). The dashed black line gives the finite size offset (see Appendix B.3), which is subtracted before comparing to theory. The green crossed symbols behind the blue dots are QMC-results of the FHM for a homogeneous system at half-filling corresponding to entropies per particle of $s = 0.41(1)$ and the red line a is fit with the Luttinger expression (Eq. 6.4.1) consisting of a decaying term $A(d)$ and an decaying oscillatory term $B(d)(-1)^d$.* ***(Inset)*** *Staggered spin correlator $C_s(d) = (-1)^d C(d)$ (dark blue circles) in a logarithmic plot. The oscillating part $B(d)$ (light blue circles), obtained by subtraction of the fitted $A(d)$, shows an exponential decay $B(d) \propto \exp(-d/\xi)$, with a decay length of $\xi = 1.2(1)$ sites for $d > 1$. At $d = 1$ the deviation of the* sinh *(red line) from the simple exponential (black line) becomes visible. All error bars represent 1 SEM.*

with an average density in the range $n_r = 1 \pm 0.05$. Furthermore, we disregard some of the lattice sites, on which the Stern-Gerlach based spin detection is biased due to lattice inhomogeneities [71, 112]. The observed strong nearest-neighbor correlations of $C(1) = -0.410(5)$ correspond to 68% of the expected zero temperature signal in the Heisenberg limit [60, 196] (see Fig. 6.9). The absence of correlations between different chains in y-direction confirms the independence of the chains and serves as a check against systematic errors in the analysis. Due to the finite length of our chains and sub-shotnoise magnetization fluctuations ($4(\delta M_c)^2 < N_c$) the correlations show an offset, which we correct for (see Appendix B.3 for details).

Comparison to Quantum Monte Carlo Simulations To quantify our results, we compare the spin correlations to Quantum Monte Carlo (QMC) calculations[1] for the homogeneous Hubbard chain. We find an excellent agreement of the first four data points at $d = 1\dots4$ at a temperature of $T = 0.233(5)\,t = 0.48(1)\,J$, which corresponds to entropy per particle $s = 0.403(7)$ significantly below $s^* = \ln(2)$. Calculations are performed at thermal equilibrium between spin and charge degrees of freedom. There is strong evidence that our experimental measurements are performed with $T_\rho > T_\sigma$.[2] At half filling and $U \gtrsim 7$ the charge temperature however has almost no impact on spin correlations, so we believe our (spin) temperature estimate to be valid.

Correlation length A simple exponential fit to the rectified correlations $(-1)^d C(d)$ for $d > 1$ gives a correlation length $\tilde{\xi}$ of 1.27(15) sites (see inset of Fig. 6.9). The $d = 1$ correlations differ from this exponential by 0.14 or 28σ and also the other data points show a systematic oscillation around the exponential. These deviations from a simple exponential decay can be understood from bosonization theory.

Comparison to bosonization A treatment of the Fermi-Hubbard model based on bosonization (see Sect. 2.3 and Appx. A) predicts spin correlations (Eq. 2.3.4) that are the sum of a simple decaying term and an oscillating (antiferromagnetic) term. For half filling ($n = 1$) one obtains at finite temperatures[3]

$$C(d) = A(d) + B(d)(-1)^d = -\frac{A}{\sinh^2(d/\xi)} + \frac{B}{\sinh(d/\xi)}(-1)^d. \tag{6.4.1}$$

We fit the full data, including $C(1)$, with this expression and obtain a decay constant $\xi = 1.23(12)$ sites along with $A = 0.050(4)$ and $B = 0.31(5)$. The data points are now consistent with the fit within their error bars. The decay described by ξ is due to thermal spinon excitations and equation 2.3.5 relates the decay ξ to the spin temperature via the spinon velocity, $u_\sigma \approx \pi J/2$:

$$T_\sigma = \frac{u_\sigma}{\pi\xi} = \frac{J}{2\xi} = 0.41(4)\,J \tag{6.4.2}$$

The temperature obtained this way is smaller but still consistent with the QMC comparison above.

After subtraction of the fitted $A(d)$, the measured data thus falls on a straight line in a logarithmic plot for $d < 1$ (inset of Fig. 6.9). Even the expected deviation from the simple exponential for $d = 1$ is visible, which is thus a first glimpse of the algebraic decay behavior for zero temperature. Note that this is not a confirmation of the functional form predicted by bosonization but rather we show that our data can consistently be described by the expression 6.4.1 because we fitted three parameters to only five data points.

---

[1] The QMC calculations have been performed by J. Nespolo in the group of L. Pollet.

[2] Of course, one has to compare spin and charge temperature at the same measurement parameters. The dataset of Sect. 6.2 has been analyzed both for spin and charge temperatures and we find for the central chains $T_\sigma = 0.51(2)\,t$ from spin correlations and $T_\rho = 0.94(5)\,t$ from the density distribution in the trap.

[3] We are using Eq. 2.3.4 with $K_\rho = 0$ and $K_\sigma = 1$. Logarithmic corrections are ignored.

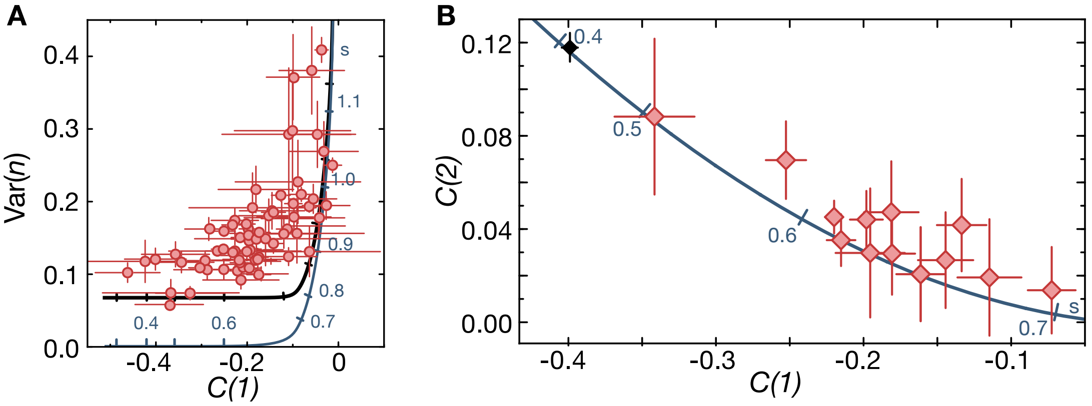

Figure 6.10. Spin and density correlations vs entropy. *Local density fluctuations and spin correlations are susceptible to temperature or entropy in different regimes.* ***(A)*** *Density fluctuations* δn^2 *versus spin correlator* $C(d=1)$ *for a density interval [0.9,1.1] at* $U/t = 10.3$ *at different temperatures. Density fluctuations rise steeply for low values of the spin correlator, signaling the saturation of the entropy in the spin sector. The solid lines are theory values combining QMC results (Fig. 2.3) with two band density calculation at* $n=1$ *(blue) for different entropies. The black line is corrected for 2% losses during imaging and the small deviation from* $n=1$*. The observed density fluctuations at given* $C(1)$ *are even higher signaling a hotter charge than spin temperature.* ***(B)*** *Spin correlations* $C(d)$ *for distances* $d=1$ *and* $d=2$ *of samples with different temperatures. The black point corresponds to the data of figure 6.9. The solid line is the prediction from QMC calculations with given entropies per particle. It was calculated for* $U/t = 10$ *and* $n=1$*, but is approximately valid for all* $U/t > 7$ *(see Sect. 2.2.3). The calculation contains no free parameter.*

6.4.2 Spin correlations as a thermometer

The magnitude of the spin correlations strongly depends on the temperature of the system, thus spin correlations can serve as a good thermometer at temperatures below t, while density fluctuations are a thermometer at larger temperatures.

To show this, we selected a density interval $\langle \hat{n}_i \rangle = 1 \pm 0.1$ and calculated the density fluctuations $\mathrm{Var}(\hat{n})/\langle \hat{n} \rangle$ for all sites with mean densities in this window. These density fluctuations reflect the entropy in the charge sector, while the nearest-neighbor spin correlations are a measure of the spin entropy and we show their mutual dependence in figure 6.10, identifying two distinct regimes of total entropy. In the regime below $s^* = \ln(2)$ ($C(1) \lesssim 0.15$), the density fluctuations are predicted to depend only weakly on the total entropy [60, 196], which in turn is stored in the spin fluctuations. Only when these are saturated at s^*, the density fluctuations grow, visible in their steep rise when the spin correlations are just below zero. This freezing of density fluctuations renders them useless as a thermometer in the low entropy regime, whereas the highly temperature-sensitive (and entropy-sensitive) spin correlations are ideal for this purpose down to $T = 0$ [60].

6.4.3 Spin correlations vs interactions

In order to explore the properties of the Hubbard chains at different interaction strengths U/t, we measured spin correlations for varying onsite interactions U, while keeping the lattice ramp and final lattice depth constant at $11\,E_r$.[1]

---

[1] The data of this subsection was measured before some of the improvements have been implemented. Thus the total temperatures are higher than in the rest of the spin analysis of this chapter.

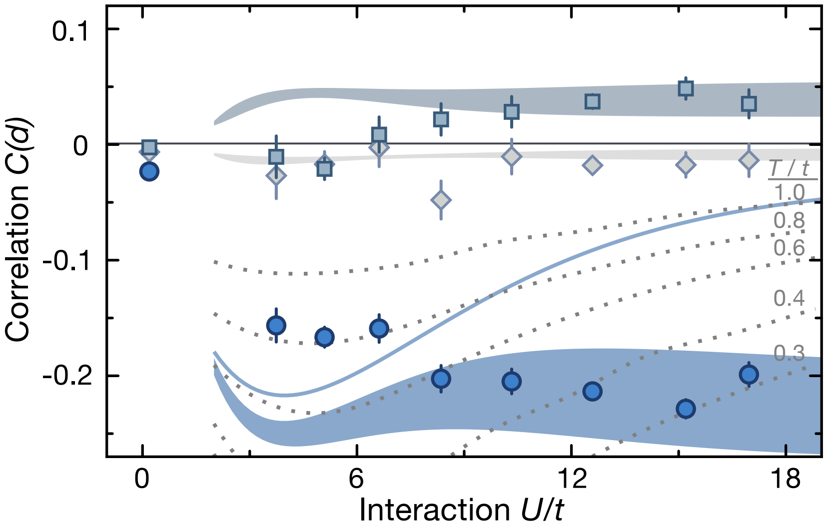

Figure 6.11. Spin correlations at different interaction strengths. *Spin correlations $C(d)$ for distances $d = 1$ (dark blue), 2 (light blue), and 3 (gray) versus interaction strength U/t. Starting close to zero at vanishing interactions, finite range spin correlations develop and saturate for interaction strengths $U/t > 8$. The shaded areas indicate the QMC predictions in a homogeneous system at half-filling for an entropy per particle between $s = 0.60$ (lower bound) and 0.65 (upper bound); the solid line is the prediction for C(1) at $s^* = \ln(2)$. Dotted lines are isothermals for $C(1)$ at the indicated temperatures. For large U/t, we observed adiabatic cooling, whereas both temperature and entropy decrease in the analyzed spatial region at intermediate U/t. The data is average over a density interval* $[0.7, 1.3]$.

We compared the measurements to QMC results for a homogeneous system at half-filling for different temperatures and entropies. The dependence of the correlations on the interactions is rather different when comparing isothermal and isentropic state preparation. In the former case, a maximum of the correlations is expected at intermediate interactions, where part of the entropy is carried by density modes [61], whereas at large interactions, the correlations decrease owing to the smaller energy scale of spin excitations given by the super-exchange coupling J. In the isentropic case of constant entropy, spin correlations saturate toward strong interactions, where the energetic gap between spin and density modes is large. At intermediate interaction strengths, the correlation behavior depends on the entropy, and a weakly pronounced maximum exists for intermediate entropies around $s^* = \ln(2)$ (Fig. 6.11), whereas below $s = 0.6$, a monotone increase of the correlations with interaction strength is expected.

Experimentally, we observed a saturation behavior of the spin correlations for $U/t > 8$. The inferred temperature dropped from $T = 0.6t$ to $0.3t$ while increasing U/t from 8 to 16, as expected for adiabatic cooling. At intermediate interactions, $U/t \approx 5$, we observed reduced spin correlations compared with the isentropic prediction at half-filling. We attribute this to a changing entropy distribution in the trap [172] and a measured weak increase of the mean density in the analyzed region by 5%.

6.4.4 Spin correlations vs density

Due to the confining potential, the density of our cloud changes continuously from zero in the wings to a peak value in the center (see Fig. 6.12A). Also the local spin correlators $C_r(d) = C(r, r+d)$ show a spatial dependence (Fig. 6.12C, E) with the strongest correlations in the Mott insulator and weaker values away from $n = 1$. This is a necessary consequence because

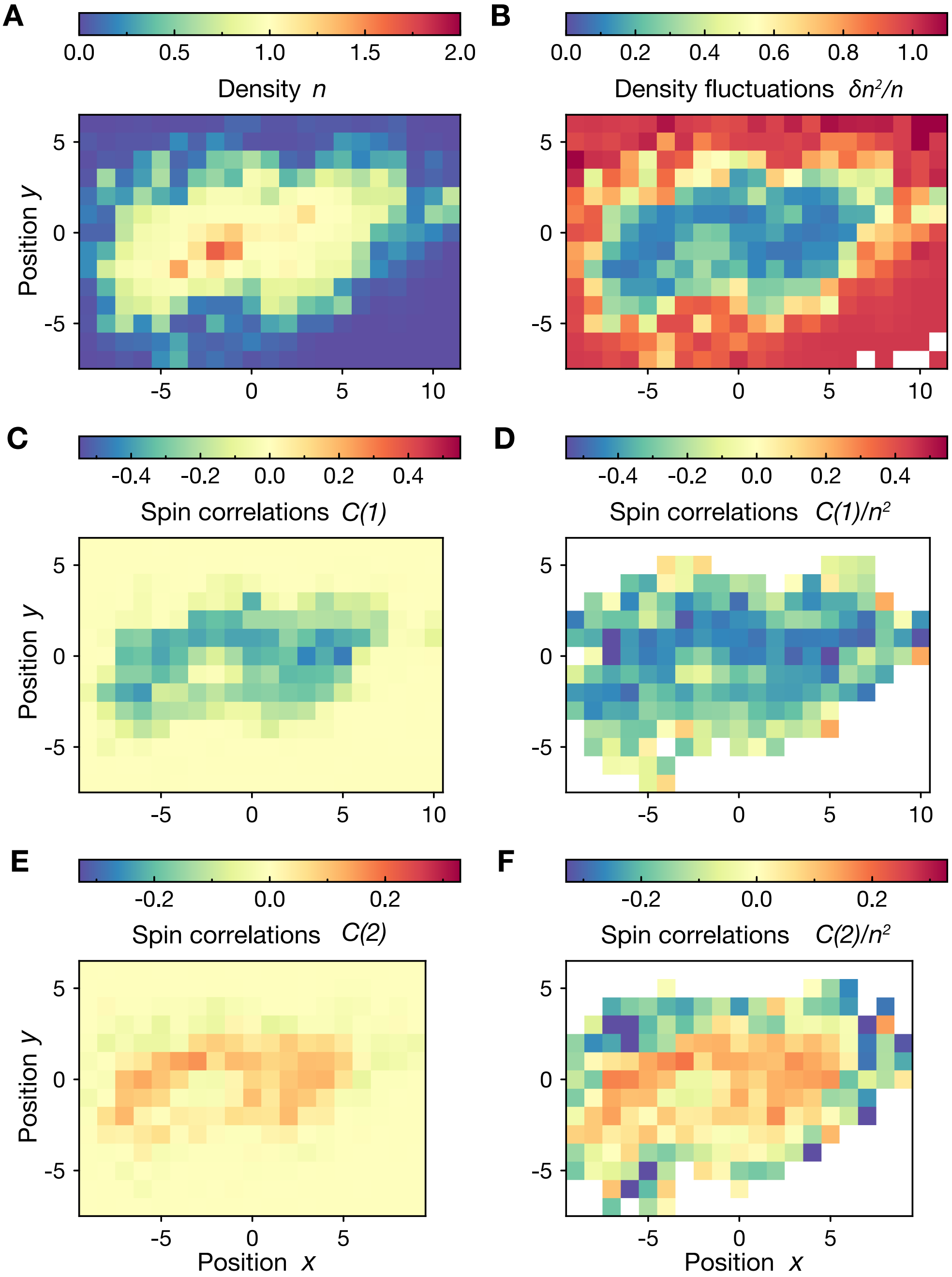

Figure 6.12. Overview of density and spin correlations. *The spatial distributions of (**A**) the local density* n_r *, **(B)** the on-site density fluctuations* $\delta n_r^2/n_r^s$*, **(C)** the bare nearest-neighbor spin correlations* $C_r(d_x = 1)$ *and **(D)** these normalized to (singlon) density squared* $C_r(d = 1)/(n_r^s)^2$*, **(E)** the bare next-nearest-neighbor spin correlations* $C_r(d = 2)$ *and **(F)** these normalized to density squared* $C_r(d = 2)/(n_r^s)^2$*. The region of the Mott insulator with density one (yellow in A) and low density fluctuations (blue in B) shows the strongest spin correlations (C,E). After normalization to density (D,F), larger regions show strong correlations demonstrating that spin correlations exist in the doped regime. White areas do not have sufficient statistics to display a result.*

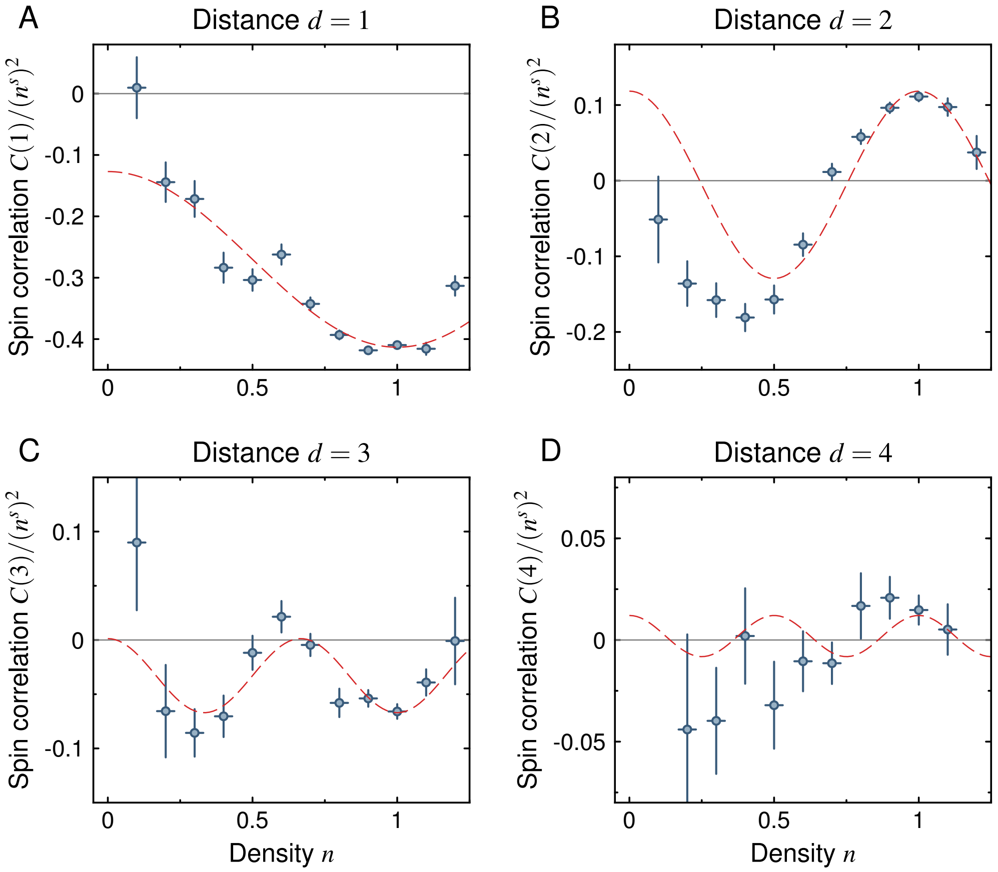

Figure 6.13. Spin correlations vs density. *Spin correlations $C(d)/(n^s)^2$ for distances $d = 1$ to $d = 4$. As expected the correlations show oscillations proportional to the Fermi wave-vector k_F. The fits (red lines) with the functional form of the zero temperature prediction from Luttinger liquid theory, $C(d) = A/d^2 + B/d\cos(\pi nd)$, show a qualitative match.*

a hole or doublon has always spin zero, leading to $C(d) \sim (n^s)^2$ with the singlon density n^s defined in (6.1.3). We thus look at $C_r(d)/(n_r^s)^2$ (Fig. 6.12D, F), where this dependence is divided out[1]. The $C_r(1)$ correlations now stay strongly negative over most of our cloud and only decrease for very weak densities. For $C_r(2)$ one can now clearly see a sign change from positive to negative correlations as one goes outwards from the trap center. The reason of this hole-induced change of the correlations is discussed in chapter 7.

We can bin our spatially resolved spin correlations by the density per site and compute a mean spin correlator $C(d)$ in each density bin. If the LDA holds, the result should resemble a homogeneous system at the given density. Because the spin correlations are given by (see Sect. A.3) $C(d) \sim \cos(\pi nd)$, we expect to see oscillations of $C(d)$ with n for fix distance d.

---

[1] In the data analysis we use directly the conditional correlator $\tilde{C}(d) = \left\langle \hat{S}^z_r \hat{S}^z_{r+d} \right\rangle_{\hat{n}^s_r=1,\hat{n}^s_{r+d}=1}$, which acts on singly occupied sites only. For $\left\langle \hat{n}^s_r \hat{n}^s_{r'} \right\rangle \approxeq \langle \hat{n}^s_r \rangle \left\langle \hat{n}^s_{r'} \right\rangle$, one gets $\tilde{C}(d) = C(d)/(n^s)^2$ (see Sect. 6.1) and we use both expressions interchangeable. The conditional expression is easier to evaluate because it avoids the division of two noisy observables $\hat{S}^z_r$ and $\hat{n}_r$, which are non-trivially correlated with each other.

Figure 6.13 gives an overview of our results for densities n up to 1.2 particles per site binned in intervals of 0.1 density. We nicely see the increasing number of oscillations with increasing d. For a qualitative comparison, we fit the curves with the zero temperature expression[1] from Luttinger liquid theory:

$$C(d,n) = A'_d + B'_d \cos(\pi n d) \tag{6.4.3}$$

and find decent agreement. Quantitative comparisons would require to take into account the finite temperature and higher order corrections in k_F as well as in the system size.

Our density resolution is limited by the size of the density regions within our cloud. For large distances it, thus, becomes harder to resolve the oscillations. In addition, the distance d starts to correlate sites that can no longer be approximated by a constant density[2].

6.5 Summary

We have shown single-atom, single-site, and spin resolved measurements of density and spin properties of Hubbard systems.

In the density sector, we constructed the equation of state for density as a function of chemical potential and used it to derive the local compressibility and temperature. With the measurement of the local and non-local fluctuations, we could experimentally confirm the fluctuation-dissipation relation for compressibility.

Using our spin resolution, we could directly measure antiferromagnetic spin-spin correlations up to four sites in one-dimensional chains and confirm entropies as low as 0.4 k_B per particle in the center of the trap. In the Mott insulator, we observed adiabatic cooling of the spin degree of freedom while increasing the interactions. In a final analysis of spin correlation vs distance, the stretching of the spin wave with decreasing density could be confirmed.

We demonstrated how the access to the full counting statistics not only allows to calculate maps with single-site resolution, but also how one can construct correlation functions for different densities. In addition, the possibility to sort the data by conserved quantities, like total atom number, allows to reduce fluctuations from the preparation and work in a canonical instead of grand canonical ensemble. This opens the path to many new and fascinating possibilities like the study of stochastic thermodynamics [197], where we could investigate non-equilibrium relations of fluctuations like the Jarzynski and Crooks equalities [198–200]. The implementation of entropy redistribution techniques [75] will allow to reach even lower temperature with spin correlations that spread through the full system. In one dimension, this could be used to directly measure the algebraic scaling and infer the value of the Luttinger parameters.

In the next chapter we will see how an analysis of spin-hole correlations in our systems reveals hidden correlations and confirms spin-charge separation.

---

[1] A comparison to the finite temperature expression 2.3.4 would be more appropriate. But both the parameter K_ρ and the velocities u_ρ and u_σ are density dependent, leading to a complicated functional form of the finite temperature result. Here we merely want to show that the number of oscillations matches with the theory.

[2] We use the mean density of the $d+1$ sites to assign a density to the correlations as in Sect. 6.3.2.

Chapter 7

Non-local Spin Correlations in Doped Hubbard Chains

This chapter is organized as follows: After a general introduction to doped spin systems and an overview of the results (Sect. 7.1), we give a brief description of aspects of the experimental setup, which are specific to the measurements in this chapter (Sect. 7.2). The presentation of measurement results starts with a detailed analysis of the spin correlations around single holes (Sect. 7.3). Then we turn to the correlations in systems with many holes, which appear hidden, and discuss their characterization with string correlators (Sect. 7.4.2). Finally an analysis in "squeezed space" leads to a successful description of spin correlations in terms of a Heisenberg model (Sect. 7.5). The chapter ends with a brief summary and an outlook to future experiments (Sect. 7.6).

This chapter is based on the publication [82].

7.1 What happens when you dope an antiferromagnet?

This is one of the central questions in strongly correlated electron systems leading to the puzzle of High-T_c superconductivity [4, 202]. In the cuprate systems, the two-dimensional antiferromagnetic (AFM) order decreases upon doping with holes, giving rise to a competition of several phases with strong correlations and leading ultimately to the famous d-wave superconducting phase around an optimum doping of 15% [3].

A small review of this physics of doped antiferromagnets is given chapter 1. Due to the competition of hole delocalization and spin order, holes tend to attract each other [39]. It can even be favorable for holes to form stripes within the AFM [203] (Fig. 7.1A). Such ordered stripes have been measure in certain doped cuprate materials [201], where they suppress superconductivity. These stripes are one-dimensional subsystem and within the stripes the holes can move freely and, thus, minimize their energy. This is possible because of the effect of spin-charge separation in one dimension as presented in section 2.3 and appendix A. The free motion of a hole can be easily understood from figure 7.1B because a moving hole in 1d just shifts atoms without changing their order.

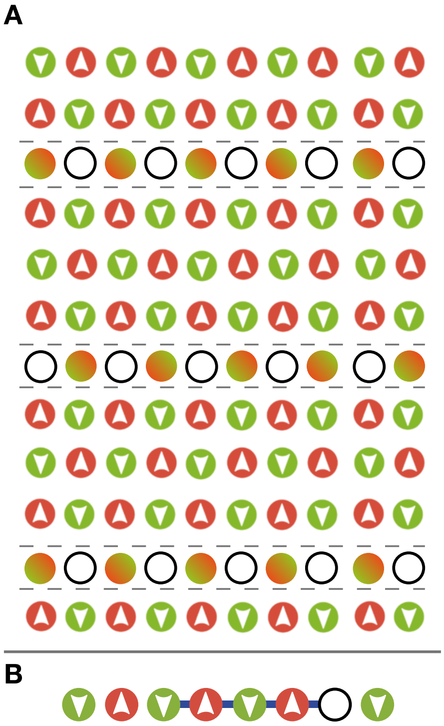

Figure 7.1. Striped phase. ***(A)*** *Illustration of stripes of holes in AFM background at 1/8 doping as found in* $(La_{1.28}Nd_{0.6}Sr_{0.12})CuO_4$ *[201]. The holes are mobile along the horizontal stripes forming 1d-subsystems with spin-charge separation. The two-colored circles are spins, which are aligned along the horizontal direction but not along the vertical direction due to their delocalization.* ***(B)*** *In a one-dimensional AFM background a hole can move without energy cost as indicated by the blue track of the hole.*

7.1.1 One-dimensional systems

Already the Hamiltonian of a 1d system can be split into a spin and a charge part, which are independent of each other. The motion of holes (missing charges) does not affect the correlations of the spin sector and the holes can fully delocalize leading to a minimal (kinetic) energy. Thus, 1d doped systems are fundamentally different from systems in higher dimensions.

In this section, we present results from true[1] one-dimensional doped spin chains. With our ultracold atoms observed by a spin-resolved quantum gas microscope [32, 71], we are in a

---

[1] The chains are fully one-dimensional in a sense that no corrections caused by inter-chain couplings have to be considered on the scale of the experimental accuracy. Residual coupling between chains are about $\sim (2\pi\hbar)\cdot 5\,\mathrm{Hz}$, which is small compared to the 15 ms we hold the spin-chains before imaging. But this time is long compared to the decoherence between different chains, such that the system lost its memory of the initial 2d cloud.

unique position to experimentally probe the interplay of spin correlations and holes in a clean 1d chain and to study the effects of spin-charge separation. So far, experimental evidence of this foundational phenomenon was based on spectroscopic [77–79] or transport measurements [80, 81] in condensed matter systems. Although one would expect the spin correlations to be independent of doping, the quasi long-range antiferromagnetic order appears to be suppressed by a finite hole density in the system, when it is measured by two-point spin correlation functions. However, thanks to the independence of the spin and charge sectors, the order is not truly reduced, but rather hidden [204–206]. It can be revealed by measurements over an extensive part of the system allowing one to construct string correlation functions. In analogy to the spin-1 Haldane phase [207–209], this requires measuring all spins in the chain.

A closely related way to unveil the hidden order is to work directly in "squeezed space", where empty sites are completely removed from the system [104–107]. In traditional condensed matter systems, string order cannot be measured, nor is squeezed space accessible to experiments. Our measurements, in contrast, give access to snapshots of the full spin and density distribution, such that non-local correlation functions can be extracted. Measurement of a non-local order parameter have first been demonstrated with spinless bosons [27] and they find potential applications in many strongly correlated systems. For a quantum gas microscope such many-point correlation functions are a natural observable because they are as easily extracted as standard two-point correlations and allow to observe properties, that are hidden to simple correlators.

7.1.2 Overview

We probed the physics of the doped one-dimensional Fermi-Hubbard model using a balanced spin mixture of our ^{6}Li atoms trapped in a single plane of a two-dimensional optical lattice. Our versatile quantum gas microscope allowed for the simultaneous local detection of both spin states, as described in chapter 3 and illustrated on figure 3.8. By controlling the lattice depths in the different spatial directions, we created independent one-dimensional systems described by the single-band Hubbard Hamiltonian (Eq. 2.2.1). At half filling in the strong coupling limit ($U/t \gg 1$), the Fermi-Hubbard model reduces to a Heisenberg spin chain with $J = 4t^2/U$ and supports quasi long-range antiferromagnetic order at zero temperature [96].

The doped system is described at long wavelength by Luttinger liquid theory (Appendix A), which predicts at zero temperature an algebraic decay of the spin correlations with distance that is faster than the one of the Heisenberg model (see Eq. A.3.2). This decay can be understood from spin-charge separation, allowing holes to freely move in the AFM spin-chain. Consequently, the spins around the hole are anti-aligned and the sign of the staggered magnetization $(-1)^i S_i^z$, called AFM parity, changes (Fig. 7.2B). This implies that a hole acts as a domain wall of the AFM parity, which reduces the spin correlations. The spin order however, is still present and can be revealed either in squeezed space by effectively removing the holes in the analysis (Fig. 7.2D) or by evaluating string correlators, which take the AFM parity domain walls into account by flipping the sign of the correlator (Fig. 7.2C). Analytic and numerical studies [107] have shown that at zero temperature, the two-point spin correlations in squeezed space are comparable to the ones of a pure Heisenberg chain, for any doping and any repulsive interaction U. This is readily understood in the $U/t \to \infty$ limit, where the many-body wave function $\Psi(\{x_{j,\nu}\}) = \Psi_\rho(\{x_j\})\Psi_\sigma(\{\tilde{x}_{j,\nu}\})$ factorizes exactly into a density Ψ_ρ and a

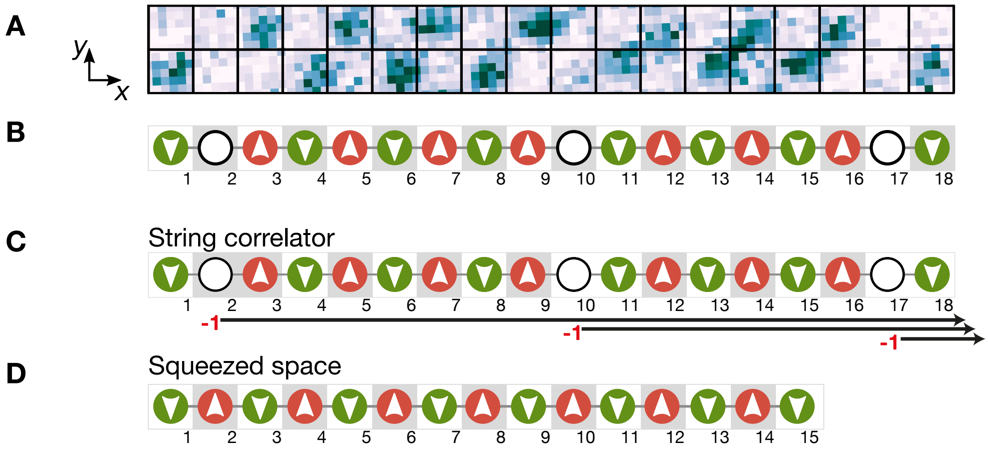

Figure 7.2. Analysis of a doped Hubbard chain. *(**A**) Spin and density resolved image of a single, lightly doped Hubbard chain after a local Stern-Gerlach-like detection. (**B**) Reconstructed spin and density distribution of the image above. The hole-induced AFM parity flips are highlighted by the background shading relative to the spin orientation. (**C**) String correlator analysis. In the string correlator analysis, the flip in the AFM parity is canceled by a multiplication of (-1) for each hole illustrated by the switched background shading. (**D**) Squeezed space analysis. Squeezed space is constructed by removing all sites with holes from the chain. The site indices refer to distances in squeezed space different from the real space distances. Comparing either of these analyses to the conventional two-point correlator reveals the hidden finite-range AFM order in the system. Additional parity flips due to thermal spinons and quantum fluctuations are present on most snapshots of the system (not shown).*

spin Ψ_σ part [104, 210] for all length scales[1]. The spin degree of freedom is described by a Heisenberg model in squeezed space with the spins "living" on a lattice defined by the positions of spinless, non-interacting fermions [105]. Distances in squeezed space $\tilde{x} = x - N_h$ are shorter by the number of holes N_h within this distance, leading on average to a rescaling by the spinless fermion density $\tilde{x} \sim nx$. Even at non-zero temperature and finite interactions, the spin correlations in squeezed space are governed by a Heisenberg model that obtains renormalized exchange couplings $J_{\text{eff}}(n)$, which depend on the original density n.

---

[1] Note the difference to the Luttinger liquid description, which applies at all interaction strength, but only for the leading long-wavelength contributions.

7.2 The experimental system

7.2.1 Preparation sequence

Each experimental cycle starts with an all-optical generation of a degenerate Fermi gas of 10^5 ^{6}Li atoms at $T/T_F = 0.15$ in a crossed dipole trap. With a tightly confined elliptical dimple beam, we can directly transfer about 8000 atoms into a single plane of the vertical-lattice (spacing $a_z = 3.1\,\mu$m), where the temperature is further reduced by an evaporation step with a steep magnetic gradient, that pulls out atoms along the plane. The number of atoms in the resulting two-dimensional degenerate two-component Fermi gas can be precisely controlled with the strength of the gradient (see Chapter 3). Using the large spacing component of the optical superlattice ($a_{\mathrm{sl}} = 2.3\,\mu$m), the system was divided into about ten independent one-dimensional tubes. The Fermi-Hubbard chains were then realized using a lattice of $1.15\,\mu$m spacing along the tubes. The atom number was set such that the maximum density in the chains was typically just below unity. At the end of the lattice ramps, the tunneling amplitude reached $t = h \times 400\,$Hz, and the confinement caused by the lattice beams fixed the length of the central chain to about 15 sites. The onsite repulsion U was tuned to $h \times 2.9\,$kHz using the broad Feshbach resonance between the hyperfine states $|\downarrow\rangle = |F, m_F\rangle = |1/2, -1/2\rangle$ and $|\uparrow\rangle = |1/2, 1/2\rangle$ to set a scattering length of 2000 Bohr radii at the end of the lattice ramps resulting in an exchange interaction of $J = h \times 220\,$Hz. These parameters and the lattice ramps have been optimized to produce cold, strongly repulsive, doped Hubbard chains (For details see appendix B.1).

7.2.2 Properties of the atomic cloud

The prepared clouds contained in total 131 ± 5.5 atoms with a global magnetization of $\frac{1}{2}(N_\uparrow + N_\downarrow) = +1.2 \pm 2.9$ compatible with zero, where the uncertainties are the standard deviations of the distributions, i.e. not the usual standard error of the mean. The sub-shot-noise fluctuations are attributed to our magnetic gradient assisted evaporation in a stiff optical trap, which cuts into the Fermi sea [211]. The Gaussian intensity profiles of the lattice beams introduced an additional confining potential, which led to an inhomogeneous density distribution (Fig. 7.3A). The atom number was chosen to obtain $N \lesssim N_0 = 2\sqrt{\frac{4t}{\frac{1}{2}m\bar{\omega}^2 a_l^2}} \simeq 13$ in most chains, corresponding to a filling lower than one atom per site [212]. Here, the frequency corresponding to the harmonically approximated confinement along the chains is $\bar{\omega} \approx 2\pi \times 300\,$Hz. The atom number distribution in the chains is shown in Fig. 7.3B.

Atom number and magnetization fluctuations per chain Equipped with the measurement of the full counting statistics, we binned the 38 000 chains from all shots of the dataset by their number of atoms $N = \langle \sum_i (\hat{n}_{i\uparrow} + \hat{n}_{i\downarrow}) \rangle$, where i runs over all sites of the chain. For each bin of fixed N, we analyzed the magnetization $\hat{M} = \sum_i \hat{S}_i^z$ and magnetization fluctuations $\langle \hat{M}^2 \rangle$. For typical atom numbers of $N = 7$ to 15, we observed less than half a spin of net magnetization $\langle \hat{M}/N \rangle = 0.023(1)$ and on average sub-shot-noise fluctuations $\langle 4\hat{M}^2/N \rangle = 0.52(1)$ per chain, which is about half the value expected for uncorrelated spins. This is not a surprise because the atoms are already strongly interacting when the system is split into chains. This suppression of fluctuations is roughly constant for average length chains and stronger (weaker) for very long (short) chains (see Fig. 7.3C). These fluctuations were taken into account when comparing to numerical predictions.

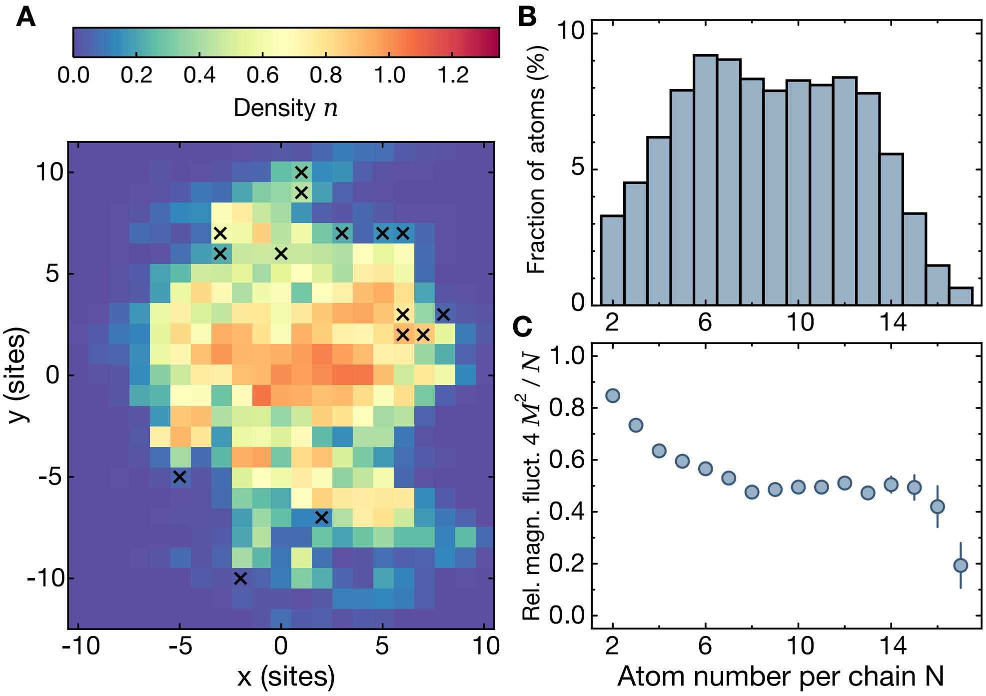

Figure 7.3. Cloud properties. *(**A**) Density distribution of the cloud obtained by averaging* 2700 *experimental runs. The decoupled chains run along the x-direction. Each pixel corresponds to a lattice site and black crosses identify sites which were filtered out because spin detection failed due to optical potential imperfections. (**B**) Distribution of the atoms into chains of different atom number. The typical accessible chain length is* 15 *sites, leading to a broad distribution of different densities in every shot. (**C**) Magnetization fluctuations* M^2 *per chain normalized to the expected value for uncorrelated fluctuations* $N/4$.

Temperature From comparison of the measured spin-correlations at half filling to Quantum Monte-Carlo results (cf. Chapter 6), we estimated the temperature in the central chains to be $0.51(2)t$ or $0.90(3)J$, which corresponds to an entropy per particle of $0.63(2)k_B$. This is higher than the temperatures reached in experiments with large Mott isolators (see Sect. 6.4), but corresponds to a similar mean global entropy per particle because the entropy distribution is more uniform in the current system, which is mainly metallic. A significant fraction of the entropy is carried by the charge, resulting in sufficiently strong spin correlation signals.

7.2.3 Systematic corrections

The fidelity of the spin resolved imaging depends on the phase fluctuations of the superlattice in y-direction. In 3% of the experimental runs, we detected unusually large global spin imbalances. We attribute these to a detection error caused by superlattice phase fluctuations, which can occur due to air turbulence or mechanical vibrations. Thus, runs with more than 16 excess spins (up or down) in the entire cloud have been discarded.

In addition, short scale imperfections in the trapping potential (visible in Fig. 7.3A) affect our spin detection. Small fringes on the lattice beams generate local potential gradients which result in a consistent failure of spin detection on some sites (see SI of [71]). While the precise superlattice phase control ensured a local mean spin of $S_i^z = 0.004(3)$ for typical "good" sites, we filtered out sites with a detected mean spin of more than $|S_i^z| > 0.025$ on a 3.5σ level. This concerns 15 lattice sites out of about 300 (Fig. 7.3A). In about 1% of the chains we detected one or more sites occupied by two atoms of the same spin. These events can be caused by the small chance of having atoms in the second band or by the residual weak hopping during the imaging. We removed all those lines from the dataset. We ensured that none of the filters discussed above critically affect the results reported in this chapter.

Detection errors From the careful analysis of our imaging method (Chapter 4), we know that our detection fidelity is about 97%[1]. This means that some of the holes we detect are not physical. This limits the analysis of systems with very low hole-doping as the relative fraction of wrong holes is large in this case. Thus most of the data presented in this chapter has been taken at 20 - 40% doping, where the error is small. We included a systematic correction for the fraction of wrong holes in quantitative comparisons.

Finite size correction There is a finite size effect from the residual magnetization, which affects the analyzed spin-spin correlation functions. It adds an offset of order $1/N$ relative to the correlation values expected in infinite spin chains. We correct for this effect with a procedure described in Appendix B.3.

---

[1] A large fraction of these detection errors occur at the edges of our images, resulting in an even better fidelity in the central parts of the clouds.

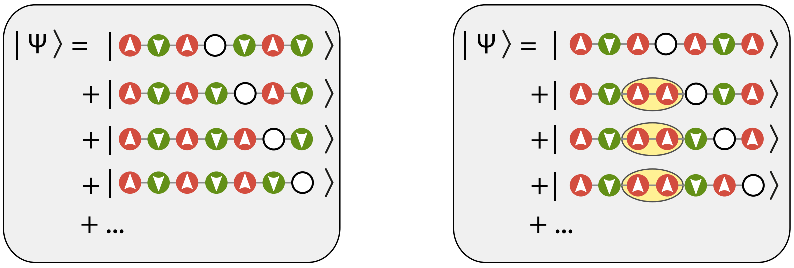

Figure 7.4. Aligned vs anti-aligned spins around a hole. *For a delocalized hole in an AFM spin background the spins around the hole are anti-aligned (left). Aligned spins around a hole correspond to a spinon (right), which is obvious as soon as the hole moves away. Illustrated here for a Néel background, but the same argument holds for a doped Heisenberg AFM state just with non-unity probability. Delocalization of the spinon is not drawn.*

7.3 Spin correlation around a single hole

7.3.1 Introduction to spin correlations in doped spin chains

Two-point spin correlations in undoped Hubbard chains have been discussed in detail in chapter 6. What is the effect of holes on these correlations? The main effect of a density $n < 1$ on the standard $\left\langle S_i^z S_j^z \right\rangle$ correlator is a trivial reduction of the correlation value $\left\langle \hat{S}_i^z \hat{S}_j^z \right\rangle \sim n^2$ because $\hat{S}_l^z$ returns zero whenever site l is empty (or doubly occupied[1]). As this contains no information about the correlations of the spins that are present in the system, we generalize the spin-spin correlation function for the doped case to[2]

$$C(d) = 4\Big(\langle \hat{S}_i^z \hat{S}_{i+d}^z \rangle_{\bullet_i \bullet_{i+d}} - \langle \hat{S}_i^z \rangle_{\bullet_i} \langle \hat{S}_{i+d}^z \rangle_{\bullet_{i+d}} \Big). \tag{7.3.1}$$

The circular indices describe the condition that the correlator is evaluated only if sites i and $i+d$ are singly occupied, which is a pictorial notation of the conditional correlations introduced in section 6.1. The condition circumvents the trivial reduction and effectively amounts to a normalization by n^2 (see Appendix B.2 for detailed definitions of all conditional correlation functions used in this chapter). Because we do not directly measure the correlation function, but take bare snapshots of the system, such a conditional correlation function is easily evaluated from the data. In addition, there is no limitation to two-point correlators for high-resolution images.

To approach the question of the effect of holes from a microscopic point of view, one can consider the alignment of spins around a single hole. There are two possible configurations, which are illustrated in figure 7.4. Either the spins are aligned or anti-aligned. The removal of a single spin from an AFM chain corresponds to the aligned case. However, the empty site is in both cases surrounded by two opposite spins after a single hopping of the hole. Therefore, the anti-aligned case is expected to be much more likely as long as the spins show (some) nearest-neighbor AFM correlations. In addition, the energy of the aligned case is higher. The

---

[1] In this chapter, we are working with hole doped system. The number of doublons is, therefore, negligible and we do not distinguish between the density n and the singlon density n^s (Eq. 6.1.3) in the notation.

[2] An average over the index i is implied in all averages.

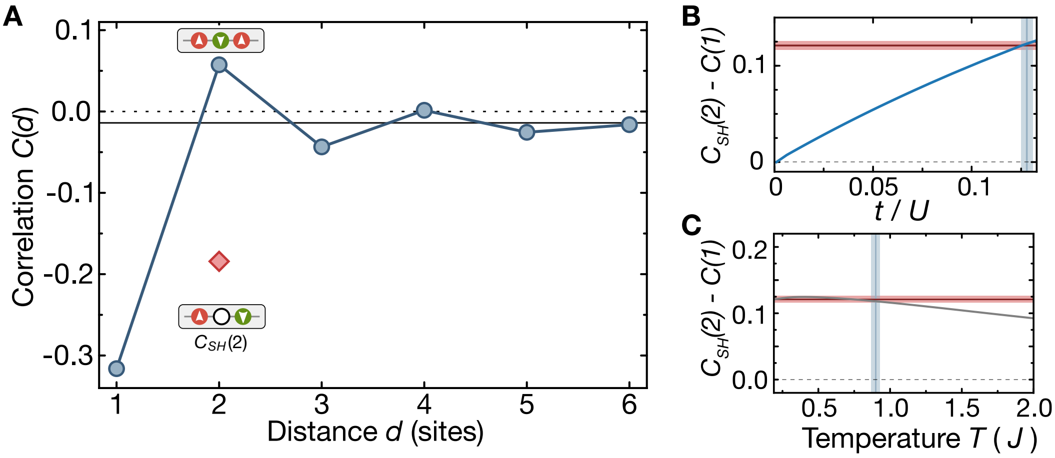

Figure 7.5. ***Revealing the magnetic environment around holes.*** ***(A)*** *Connected two-point spin correlation function $C(d)$ analyzed on occupied sites only (blue). The finite range AFM order without holes asymptotically falls off with an exponential decay length of* 1.3(2) *sites. The spin correlations at a distance of two sites switch sign in the presence of a hole as measured by $C_{SH}(2)$ (red diamond) demonstrating an AFM environment surrounding the hole. The solid black line indicates the finite-size offset (see Appx. B.3), the blue line is a guide to the eye and statistical uncertainties are smaller than the symbol sizes.* ***(B,C)*** *Comparison of experimental values (red lines) of $C_{SH}(2) - C(1)$ with results for different interactions (B) and temperature (C) from exact diagonalization (blue, gray curves). Vertical blue lines (shadings) indicate experimental values (uncertainties). The systematic error due to a finite atom loss rate of up to 3% during imaging is negligible compared to a mean doping of* 0.35.

removal of a particle that has charge and spin is an excitation both in the charge and the spin sector. As soon as the hole moves, the spinon-excitation is visible as two aligned spins on adjacent sites. So for a Néel AFM state, aligned spins around a hole have a higher energy (of order J).

To study such correlations we define a three point correlator[1]

$$C_{SH}(d,s) = 4\left\langle \hat{S}^z_i \hat{S}^z_{i+d} \right\rangle_{\bullet_i \circ_{i+s} \bullet_{i+d}} \qquad (7.3.2)$$

which measures the spin-spin correlation on sites i and $i+d$ given that site $i+s$ is empty. As the correlator is conditioned on i and $i+d$ being occupied and $i+s$ being empty, it is undefined for $s = 0$ and $s = d$.[2]

7.3.2 Nearest-neighbor spin-hole correlations

To investigate the magnetic environment around a hole, we calculate the conditional three-point spin-hole correlation function $C_{SH}(2) = C_{SH}(d = 2, s = 1)$ defined in equation 7.3.2. The correlator indeed reveals anti-alignment of the spins around individual holes ($C_{SH}(2) < 0$). Figure 7.5 highlights the hole induced sign change by comparison to the standard two-point

---

[1] To lighten the notation, the subtraction of the disconnected spin part $-\langle \hat{S}^z_i \rangle_{\bullet_i} \langle \hat{S}^z_{i+d} \rangle_{\bullet_{i+d}}$ is not written explicitly. We do subtract these terms, but their values are close to zero in our system anyway (within their errorbars). Other disconnected parts are not subtracted unless written explicitly.

[2] In addition, we ignore the trivial $C_{SH}(0,s) = 1$.

correlator $C(d)$ of an undoped spin chain. To obtain unity filling, the latter was evaluated on a hole-free subset of the data. The measured modulus of the correlation around a hole is $|C_{SH}(2)| = 0.184(4)$, which is considerably larger than $C(2) = 0.057(3)$ and about half of the next-neighbor value of $|C(1)| = 0.316(2)$.

At zero temperature for $U/t \to \infty$ one expects $|C_{SH}(2)| = |C(1)|$, as the hole has no effect on the magnetic alignment of its surrounding spins. To understand the measured difference $|C_{SH}(2)| - |C(1)|$, we calculated this value by exact diagonalization of the t-J model in a 15 site system at different temperatures and interactions U [82]. We found good agreement at a matching temperature $0.9J$ and at our interaction value $U = 7.8t$ (Fig. 7.5B,C). These calculations, which take the experimental fluctuations of the magnetization per chain into account, show that this is not a finite temperature effect, but caused by the finite interactions. Intuitively, the difference is caused by spinons, which are (virtually) bound to the hole, because the configuration has an energy which is lower by J compared to a spatially separated hole and spinon (cf. Fig. 7.4). Such an effect is a correction to spin-charge separation, which is consistent because the difference vanishes for $U \to \infty$, where the separation becomes exact on all length scales.

Connected three point correlations To show that the correlator $C_{SH}(d)$ contains information that goes beyond two-point correlations, one can calculate the connected part of the three point correlator: $C^c_{SH}(d) = A\Big(\langle \hat{S}^z_i \hat{n}^h_{i+s} \hat{S}^z_{i+d}\rangle - \langle \hat{S}^z_i\rangle\langle \hat{n}^h_{i+s} \hat{S}^z_{i+d}\rangle - \langle \hat{S}^z_i \hat{n}^h_{i+s}\rangle\langle \hat{S}^z_{i+d}\rangle - \langle \hat{S}^z_i \hat{S}^z_{i+d}\rangle\langle \hat{n}^h_{i+s}\rangle$ $+2\langle \hat{S}^z_i\rangle\langle \hat{n}^h_{i+s}\rangle\langle \hat{S}^z_{i+d}\rangle\Big)$. Here $A^{-1} = \langle \hat{n}^s_i \hat{n}^h_{i+s} \hat{n}^s_{i+d}\rangle \approx n_i(1 - n_{i+s})n_{i+d}$ is the normalization due to the condition $\bullet_i \circ_{i+1} \bullet_{i+2}$ and $\hat{n}^h_i$ detects the presence of a hole. In a spin balanced system, we have $\langle \hat{S}^z \rangle = 0$ independently of any holes, so

$$C^c_{SH}(d) = A\left(\left\langle \hat{S}^z_i \hat{n}^h_{i+s} \hat{S}^z_{i+d}\right\rangle - \left\langle \hat{S}^z_i \hat{S}^z_{i+d}\right\rangle\left\langle \hat{n}^h_{i+s}\right\rangle\right) = C_{SH}(d) - C(d). \tag{7.3.3}$$

So the connected part is nothing but the difference of $C_{SH}(d)$ to $C(d)$, which is clearly non-zero i.e. $C_{SH}(2) - C(2) = 0.241(7)$.

7.3.3 Full spin-hole-spin correlations

In order to further confirm the independence of the spin and density sectors, we want to analyze the full three point correlator $C_{SH}(d,s)$ (Eq. 7.3.2), which measures the spin-spin correlation of distance d given that there is a single hole at distance s from the first spin (see Fig. 7.6A). Ideally, this would be measured in spin chains that only contain a single hole to exclude the effect of other holes. As we cannot prepare chains with a deterministic number of holes yet[1] and such a three point-correlator needs a lot of statistics, we had to include chains with more than one hole in the analysis. The main effect of the other holes (the parity flip) can be removed by inserting a tailored charge string[2] (see discussion of string correlations in Sect. 7.4.2):

---

[1] A local addressing with a digital micromirror device (DMD) to remove single atoms from a Mott insulator will be installed in late 2017.

[2] The charge string removes the parity flip for all holes but the one at $i+s$. As this analysis wants to show that the parity flip is the only effect of a delocalized hole, this approach is valid only a posteriori. In addition, it is justified by the independent spin-string analysis of section 7.4.

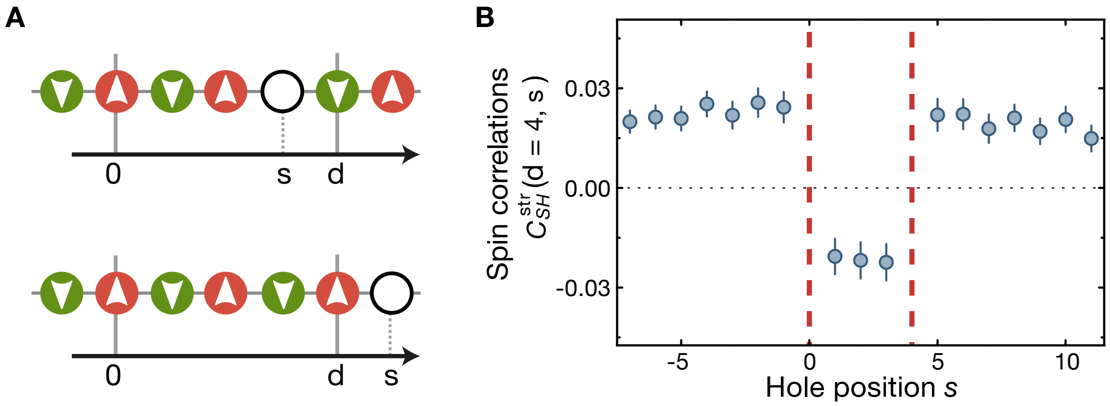

Figure 7.6. Spin-Hole-Spin Correlator. ***(A)*** *Illustration of the three-point spin-hole-spin correlator with spin-spin distance d and spin-hole distance s for $d = 4$ and $s = 3, 5$ (top, bottom)* ***(B)*** *Spin-hole-spin correlator at $d = 4$ with domain walls indicated by dashed lines. The constant correlations within the domains can be interpreted as a direct measurement of the independence of the spin and charge sector. This is a vertical cut of figure 7.7.*

$$C^{\mathrm{str}}_{SH}(d,s) = 4 \left\langle \hat{S}^z_i \left(\prod_{j=1, j\neq s}^{d-1} (-1)^{(1-\hat{n}_{i+j})} \right) \hat{S}^z_{i+d} \right\rangle_{\bullet_i \circ_{i+s} \bullet_{i+d}} \tag{7.3.4}$$

For a system with a single hole, this correlator is identical to the three-point correlation function $C_{SH}(d,s)$.

Figure 7.6B displays the experimental result with a fixed spin-spin distance $d = 4$. For $s = 0$ and $s = d$ the hole crosses one of the two spins, which causes the discussed AFM parity flip. Apart from this, the correlation signal is almost independent of the position of the hole. This observation emphasizes spin-charge separation by the absence of polaron-like effects, which would result in a local change of the spin correlations around the hole.

The full dependence of $C^{\mathrm{str}}_{SH}(d,s)$ on the spin separation d and the position of the hole in the string s is shown in Fig. 7.7A. Each row shows the AFM spin correlations for a fixed hole position and each column contains a parity flip, when the hole is inbetween the spins. The rectified correlator $(-1)^d C^{\mathrm{str}}_{SH}(d, s - d/2)$ in Fig. 7.7B highlights the two domains of opposite AFM parity, demonstrating that the hole acts as a domain wall for the magnetic order [203]. To emphasize the symmetries of the three-point correlator, the position of the hole is measured here relative to the center of mass of the two spins.

7.3.4 Implication from spin-charge separation

Traditionally, spin-charge separation is mainly discussed as the separation of a spin-full fermion into a spin- and a charge-wave (packet), which propagate with two different velocities and thus separate in space after some time. This effect is rooted in the structure of the effective Hamiltonian that describes the low-energy dynamics of the system - the Luttinger Hamiltonian A.1.6. As shown in appendix A, this Hamiltonian separates into a charge part ρ and a spin part σ. The waves are the lowest excitations of the associate bosonic fields $\phi_\rho(x)$ and $\phi_\sigma(x)$.

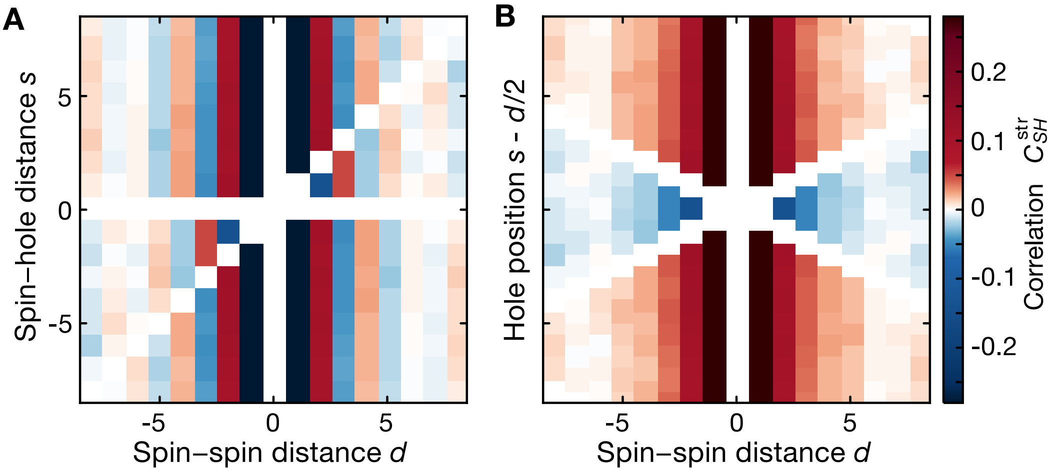

Figure 7.7. Single holes as domain walls for the AFM order. (A) *Tailored string correlator* $C_{SH}^{str}(d,s)$ *measuring the effect of a single hole on the doped Hubbard-chain. As expected for separated spin and charge sectors, the correlations are independent of the distance s between the hole and the spin, except for the opposite sign when the hole sits in between the two spins at relative distance d. In addition, there is a dynamic picture to the measurements shown here. Interpreting the vertical axis as time, one obtains the picture of a delocalized hole freely propagating through an antiferromagnetic background. The correlator* $C_{SH}^{str}(d,s)$ *is set to zero whenever two operators are evaluated at the same site.* ***(B)*** *Rectified correlator* $(-1)^d C_{SH}^{str}(d,s-d/2)$ *of the same data with hole position referenced to the center of the spin positions. The hole associated AFM parity flips are directly visible by the different domains. The expected parity is observed consistently for spin-spin distances of up to eight sites. The point symmetry around the origin is by construction of the correlator.*

There are, however, other consequences of the separation of the Hamiltonian, i.e. the expectation value of any correlation function which is a product of spin and charge observables, i.e. $f(\phi_\rho,\phi_\sigma) = f_\rho(\phi_\rho) f_\sigma(\phi_\sigma)$, factorizes into a spin and a charge part:

$$\left\langle f(\phi_\rho,\phi_\sigma)\right\rangle = \left\langle f_\rho(\phi_\rho)\right\rangle_\rho \left\langle f_\sigma(\phi_\sigma)\right\rangle_\sigma \tag{7.3.5}$$

This product form is also a direct result of spin-charge separation and its measurement can thus be interpreted as a direct measurement of spin-charge separation in the system.

The oscillatory part of the spin-hole correlator $C_{SH}(d,s)$ expressed in the bosonic fields is given by (see Eq. A.3.1)

$$\begin{aligned} C_{SH,2k_F}(x,s) \sim \Big\langle &\cos\left(2k_F x - \sqrt{2}\phi_\rho(x)\right) \sin\left(-\sqrt{2}\phi_\sigma(x)\right) \\ &\cos\left(-\sqrt{2}\phi_\rho(0)\right) \sin\left(-\sqrt{2}\phi_\sigma(0)\right)\Big\rangle_{\bullet_0 \circ_s \bullet_x} . \end{aligned} \tag{7.3.6}$$

To evaluate this expression, we look at the influence of a hole on the field ϕ_ρ. This field shows a kink, i.e. for a hole at position s, the charge field changes from $\phi_\rho(x)$ to $\phi_\rho(x) + \pi/\sqrt{2}\,\Theta_{x-s}$, where Θ_x is the Heaviside step function. Insertion into (7.3.6) gives (for $x > 0$):

$$\begin{aligned} C_{SH,2k_F}(x,s) &\sim \left\langle (1-2(\Theta_{x-s}-\Theta_x)) \cos\left(2k_F x - \sqrt{2}\phi_\rho(x)\right) \cos\left(-\sqrt{2}\phi_\rho(0)\right)\right\rangle_\rho \\ &\quad \cdot \left\langle \sin\left(-\sqrt{2}\phi_\sigma(x)\right) \sin\left(-\sqrt{2}\phi_\sigma(0)\right)\right\rangle_\sigma \qquad (7.3.7) \\ &\sim \underbrace{(1-2(\Theta_{x-s}-\Theta_x))}_{\text{Sign flip for } 0<s<x} \underbrace{\cos(2k_F x) \left\langle \sin\left(-\sqrt{2}\phi_\sigma(x)\right) \sin\left(-\sqrt{2}\phi_\sigma(0)\right)\right\rangle_\sigma}_{C_{2k_F}(x)} . \end{aligned}$$

$$(7.3.8)$$

Equation 7.3.8 follows if there are no other holes in the system i.e. $\phi_\rho = 0$. Here the oscillatory part of the normal spin-spin correlation $C_{2k_F}(x)$ in a spin chain without holes has been identified. $C_{SH,2k_F}(x,s)$ is thus a product of the charge part, which produces the sign flips, and the regular spin part. Our measurement in figure 7.7 shows exactly this pattern.

Dynamic interpretation Although we did not measure the propagation of holes through an AFM background directly, there is, in addition, a classical dynamic interpretation of the data:

For a spin-up on site i, the correlator C just gives the mean orientation of a spin at site $i+d$. Owing to spin-charge separation, a hole can move through the spins by simply shifting them one by one. This effect is visible on the diagonal of figure 7.7A if one interprets $s = u_\rho t$ as time. Every row looks like the one below except for a single shifted spin next to the hole. Since the measurements are static, the hole velocity u_ρ is of course not observed.

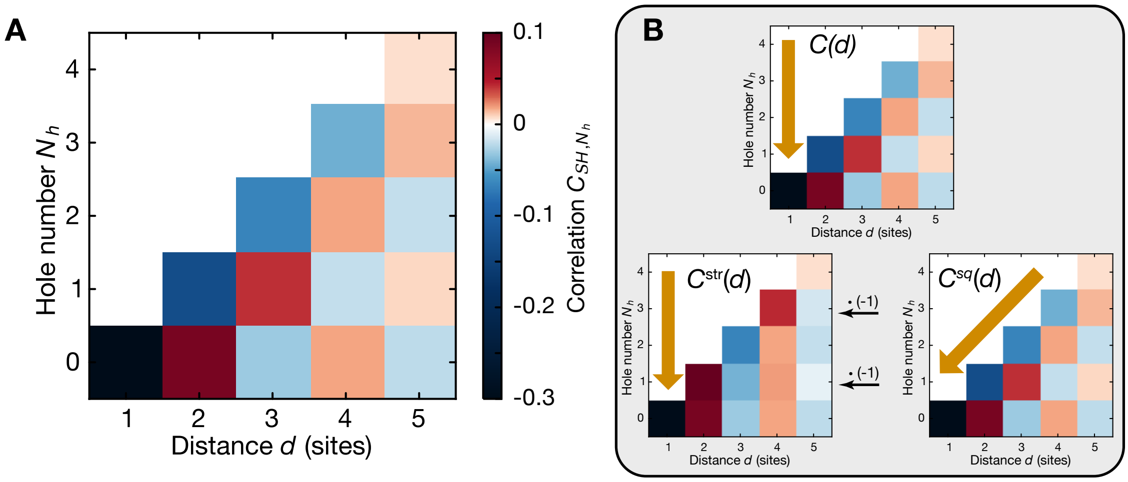

Figure 7.8. Spin correlations and hole numbers. ***(A)*** *Amplitude of the correlation function* $C_{SH,N_h}(d)$ *as a function of distance d and the number of holes* N_h *in the string between the two spins. The parity of the AFM order flips with every hole. The finite size offset (Appendix B.3) has been subtracted.* ***(B)*** *Illustrations of how the two-point correlator* $C(d)$*(top), the spin-string correlator* $C^{str}(d)$ *(bottom left) and the squeezed space correlator* $C^{sq}\left(\tilde{d}\right)$ *(bottom right) can be obtained from* $C_{SH,N_h}(d)$ *by averaging (big arrows) along* N_h *or along each diagonal. Black arrows indicate multiplications of rows by* (-1) *due to the charge string.*

7.4 Revealing hidden correlations

After the detailed analysis of the effects of a single hole on an antiferromagnetic spin chain, we now turn to measurements with several holes. There are two complementary ways to characterize the number of holes. One is the standard thermodynamic approach to characterize the system as a function of the mean density n. Making use of the local density approximation, every site is assigned a density $n(x,y)$ (see Fig. 7.3). We associate a correlator $C(d)$ with the mean density of the $d+1$ sites it spans because in a system with only local interactions, the correlations build up through all these sites. A second, microscopic approach, which directly generalizes the analysis of the last section, is to explicitly count the number of holes present on the sites between the two operators of a correlator in each realization.

The results presented in this and the next section show that only a combination of both approaches finally leads to a simple characterization of the spin correlations of a doped spin chain. The exact number of holes determines the number of parity flips, while the mean density sets the strength of the correlations at finite temperature. This results in a description of the spin sector in terms of a Heisenberg model with an effective coupling J_{eff}.

7.4.1 Spin correlations for many holes

Following the microscopic approach, the influence of larger doping on the spin order is revealed by studying the correlations as a function of the number of holes between the two spins, that is by evaluating

$$C_{SH,N_h}(d) = 4\,\langle \hat{S}^z_i \hat{S}^z_{i+d} \rangle_{\bullet_i \{\circ\}_{N_h} \bullet_{i+d}} \tag{7.4.1}$$

with exactly N_h holes on the otherwise singly occupied string of length $d+1$. To connect with the previous results, one can note that $C_{SH,N_h=0}(d) = C(d)$ at the absence of holes (blue line in Fig. 7.5A) and $C_{SH,1}(2) = C_{SH}(2)$.

The results of this analysis shown in Fig. 7.8A reveal a sign change of C_{SH,N_h} at fixed distance d for each newly introduced hole and antiferromagnetic correlations versus distance for fixed hole number N_h. Thus, each hole indeed corresponds to a flip of the antiferromagnetic parity, which we measured up to $N_h = 3$.

In a thermodynamic ensemble at $n < 1$, the hole number between the two measured spins fluctuates. The spin correlator $C(d)$ is independent of the number of holes and its value is thus given by a (weighted) average of C_{SH,N_h}:

$$C(d) = \sum_{N_h} C_{SH,N_h}(d) P_{n,d}(N_h) \tag{7.4.2}$$

where $P_{n,d}(N_h)$ is the probability to have N_h holes on the $d-1$ sites for a mean density n.[1] The sum includes contributions with alternating signs for different hole numbers (Fig. 7.8B), which is the microscopic origin of the stronger decay of spin correlations due to a fluctuating charge sector (see Eq. A.3.2) even in a system showing spin-charge separation.

7.4.2 String correlator

The mixing of contribution with different numbers of parity flips directly explains the suppression of magnetic correlations with hole doping that we measure with the normal spin correlator $C(d)$ (cf. Fig. 7.9A). At spin-spin distance one, there can never be a hole between the spins, but for all larger distances the contribution from even and odd hole numbers cancel. The effect is enhanced by averaging over different densities present in our system.

The strong reduction of spin correlations caused by hole fluctuations does not imply the absence of magnetic order in the system, but rather suggests that it is hidden by the fluctuations in the position of the atoms.

String-order in the spin-1 Haldane chain This situation is similar to the famous Haldane phase of spin-1 chains [207, 208]. The ground state of this model is the AKLT state [209], which is a superposition of all states consisting of spins $|\uparrow\rangle$, $|\downarrow\rangle$ and $|0\rangle$, such that every $|\uparrow\rangle$ is followed by a $|\downarrow\rangle$, which is followed by an $|\uparrow\rangle$, but with an arbitrary number of $|0\rangle$s in between the $|\uparrow\rangle$ and $|\downarrow\rangle$s. The $|0\rangle$ spins hide correlations between the $|\uparrow\downarrow\rangle$ components leading to exponentially decaying local correlators. The intrinsic AFM order is unveiled by a non-local correlation function [204] :

$$\lim_{|i-j|\to\infty} \left\langle \hat{S}_i^z \prod_{l=i}^{j} (-1)^{\hat{S}_l^z} \hat{S}_j^z \right\rangle \neq 0 \tag{7.4.3}$$

This operator is able to see the AFM order because it replaces the rectifying $(-1)^d$-factor with a string, that only flips the sign for $S_l^z = \pm 1$.

---

[1] If one ignores density correlations, which are weak, $P_{n,d}(N_h)$ follows a binomial distribution $B(d-1, n)$.

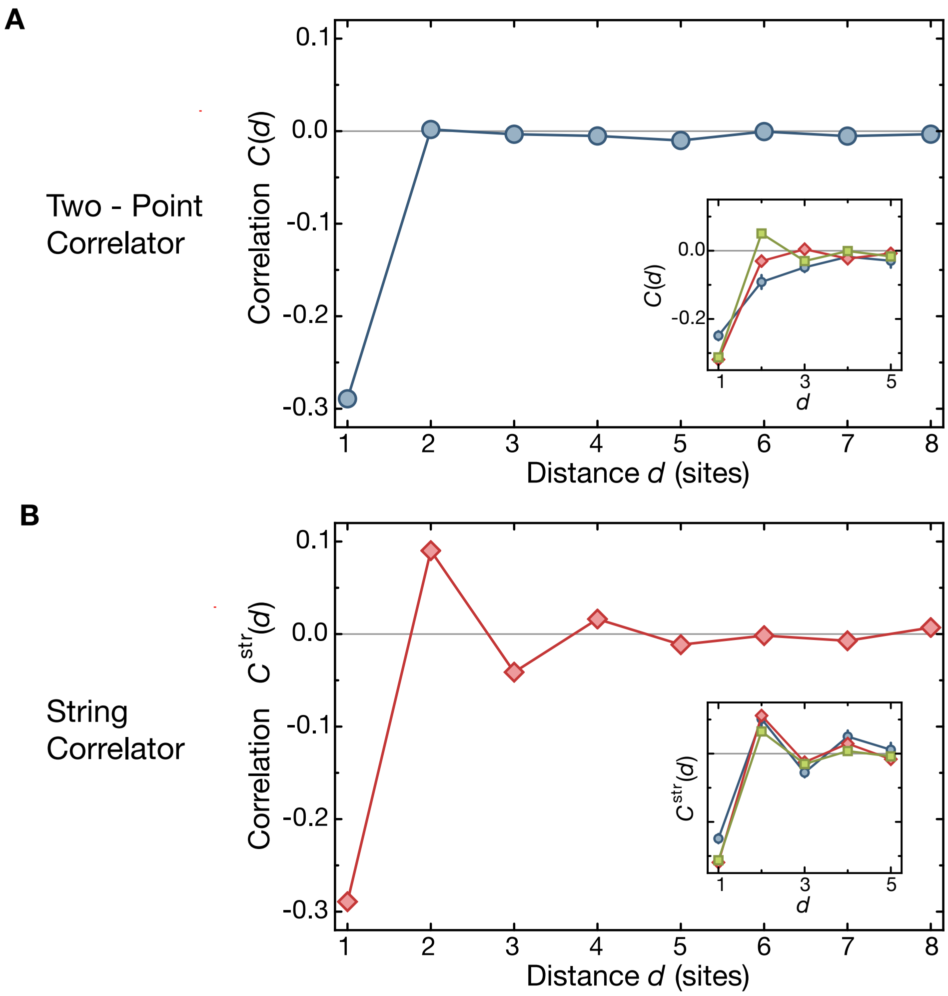

Figure 7.9. Effect of hole doping on spin order. *Comparison of **(A)** the spin correlation function* $C(d)$ *and **(B)** the spin-string correlation function* $C^{str}(d)$ *averaged over all local densities in the trap. The insets show the data binned by density (bin widths* 0.1*) for* $\langle n\rangle = 0.4$ *(blue),* $\langle n\rangle = 0.7$ *(red) and* $\langle n\rangle = 1$ *(green). (A) The conventional two-point spin correlations vanish for* $d > 1$ *in the inhomogeneous system due to the presence of holes. (B) The hidden spin correlations of the data can be revealed by disentangling spin and charge sector with the string correlator. The extracted exponential decay length of* $1.2(1)$ *sites matches the one extracted at unity filling (cf. Fig. 7.5). Finite range AFM order in the conventional correlator* $C(d)$ *is present at* $\langle n\rangle = 1$*, whereas it quickly gets suppressed when the system is doped away from half filling (A). In contrast, string correlations* $C^{str}(d)$ *only marginally depend on density (B). Solid lines are guides to the eye. All correlations shown are corrected for the constant finite size offset (Appendix B.3) and the data in the main plot is averaged over the entire cloud leading to statistical uncertainties smaller than the point sizes.*

Measurement of string correlators By identifying double occupancies and holes with spin $|\rightarrow\rangle$ states, one can use the same procedure to construct a string correlator that probes the underlying spin order in the doped Hubbard chain [107]:

$$C^{\mathrm{str}}(d) = 4\left\langle \hat{S}_i^z \left(\prod_{j=1}^{d-1}(-1)^{(1-\hat{n}_{i+j})}\right)\hat{S}_{i+d}^z\right\rangle_{\bullet_i\bullet_{i+d}} \tag{7.4.4}$$

This string correlator takes the antiferromagnetic parity flips into account by a corresponding sign flip for each hole (cf. Fig. 7.2C). The unique ability to detect the spin and density locally on single images enables the direct measurement of the string correlator $C^{\mathrm{str}}(d)$ for different densities. The dependence of the string correlator on distance reported in Fig. 7.9 is in stark contrast with the standard two-point spin correlation function $C(d)$. Whereas $C(d)$ quickly vanishes when the data is analyzed over different densities, staggered correlations at distances up to four sites are detected with the string correlator $C^{\mathrm{str}}(d)$. The string correlations show an amplitude and a decay at all dopings, which are almost the same as the ones of the normal spin correlator at density one (Fig. 7.5A).

When binning the data in regions of fixed density (see insets of Fig. 7.9), we observe two effects: The normal correlator $C(d)$ shows an increasing periodicity of the AFM correlations with decreasing density. This is expected from Luttinger theory (Eqs. A.3.2 and 2.3.4), where the oscillatory term depends on $k_F \sim n$. For the string correlator, on the other hand, the oscillation period is always two because all parity flips have been removed. In addition, the amplitude of the string correlations is larger and it even shows an increase with stronger doping, in contrast to the usual decrease of spin correlations with doping. The reason for this effect is that due to the high mobility of the holes, correlations across a hole are stronger in magnitude than across a spin. This was observed in figure 7.5 comparing $|C(2)| < |C_{SH}(2)|$. Stated differently: the strong $|C_{SH}(2)|$ correlations across a hole physically rather correspond to a nearest-neighbor than to a next-nearest-neighbor spin correlation and should thus be included in a $C(1)$ correlator (cf. Fig. 7.8B). This can be achieved with a squeezed space analysis presented in section 7.5.

7.4.3 String correlations in bosonization

In the Luttinger liquid description, spin-charge separation is present on the level of the Hamiltonian. As discussed in section A.3, the influence of the charge sector on the two-point spin correlation function

$$\begin{aligned} C(x) =& \frac{2}{\pi^2} \left\langle \nabla\phi_{\sigma,0} \nabla\phi_{\sigma,x} \right\rangle \\ &+ n^2 \cos(\pi n x) \left\langle \cos\left(\sqrt{2}\phi_{\rho,0}\right) \cos\left(\sqrt{2}\phi_{\rho,x}\right) \right\rangle \left\langle \sin\left(\sqrt{2}\phi_{\sigma,0}\right) \sin\left(\sqrt{2}\phi_{\sigma,x}\right) \right\rangle \end{aligned} \tag{7.4.5}$$

is explicit in the ϕ_ρ dependence. Thus, the measured spin correlations also depend on charge fluctuations. The string correlator (Eq. 7.4.4) can written as $C^{\mathrm{str}}(x) = \left\langle \hat{C}(x)\hat{D}(x) \right\rangle$ with the additional string factor $\hat{D}(x) = \prod_{j=0}^{x}(-1)^{(1-\hat{n}_j)}$. To express $C^{\mathrm{str}}(d)$ in bosonized form, we first rewrite $\hat{D}$ using the expression of the density in terms of the bosonic fields [107, 213]:

$$\begin{aligned} \hat{D}(x) &= \cos\left(\pi \sum_{j=0}^{x} (1-\hat{n}_j)\right) = \cos\left(\pi \int_0^x dz \left(1 - n + \sqrt{2}/\pi \nabla\phi_\rho(z)\right)\right) \\ &= \cos\left(\pi(1-n)x + \sqrt{2}\phi_\rho(x) - \sqrt{2}\phi_\rho(0)\right) \\ &= \cos\left(\pi(1-n)x\right) \cos\left(\sqrt{2}\phi_\rho(0)\right) \cos\left(\sqrt{2}\phi_\rho(x)\right) + \ldots \end{aligned} \tag{7.4.6}$$

The irrelevant combinations[1] of cos() and sin() have been dropped in the last line. The non-local operator $\hat{D}$ thus has a local representation in terms of the field ϕ_ρ, which is possible because of the non-locality of ϕ_ρ itself. Due to its dependence on the field ϕ_ρ only, the operator $\hat{D}(x \to \infty)$ serves as an order parameter of the Mott phase [27, 189]. But here we are interested in how the string influences the spin correlator in the metallic Luttinger phase. Upon multiplication with $\hat{D}$, the oscillatory part of the correlator obtains terms $\cos^2 \phi_\rho = \frac{1}{2}(1 + \cos 2\phi_\rho)$, which are strictly positive and thus insensitive to the fluctuations of $\phi_\rho(x)$. In addition the $\cos(\pi(1-n)x)$-factor changes the period of the oscillation from $\cos(\pi n x)$ to $\cos(\pi x)$, which is the AFM staggering that we observed (Fig. 7.9). The string correlator thus contains the following dominant term

$$C^{\text{str}}(x) \sim n^2 \Big(\cos\left(\pi x\right) + \cos\left(\pi(2n-1)x\right)\Big) \Big\langle \sin\Big(\sqrt{2}\phi_\sigma(0)\Big) \sin\Big(\sqrt{2}\phi_\sigma(x)\Big)\Big\rangle + \mathscr{O}\left(x^{-2}\right) \tag{7.4.7}$$

$$\sim \left(\cos\left(\pi x\right) + \cos\left(\pi(2n-1)x\right)\right) \frac{1}{x} \log(x^{-1})^{1/2} + \mathscr{O}\left(x^{-2}\right), \tag{7.4.8}$$

where the average has been taken in the Luttinger phase at zero temperature to show the algebraic $1/x$ decay known from a pure spin model (Heisenberg) [54]. At finite temperature, this corresponds to a smaller exponential decay constant. The density dependent second cos-term is a correction with larger wavelength, which is hard to observe in our small systems.

Finally, we like to emphasize the connection to the Haldane phase once more. Upon a trivial shift $\phi_\sigma \to \phi_\sigma + \pi/\sqrt{8}$, the $\sin\sqrt{2}\phi_\sigma$ turns into a $\cos\sqrt{2}\phi_\sigma$. The ϕ_σ-dependence is then identical to the ϕ_ρ-dependence of $\hat{D}$, which was the order parameter of the Mott phase. In analogy, $C^{\text{str}}(x)$ thus serves as an order parameter for the AFM spin order. This was already clear from the comparison to the Haldane chain, where this operator measured the hidden order. In contrast to the Haldane phase, where the spin sector is long-range ordered and the "charge" sector is truly disordered (exponentially decaying spin-0 correlations), our doped Hubbard chains show spin and a charge sectors with both algebraic order at zero temperature. Our analysis to reveal the hidden correlations is thus in one-to-one correspondence to an analysis of the spin-1 chain, which would detect the hidden *long range* order. So our experiment demonstrates how to directly measure hidden topological order in spin systems.

---

[1] Upon averaging $\langle \ldots \rangle$ over all fields ϕ_χ terms that change sign under $\phi_\chi \to -\phi_\chi$ vanish. Non-zero contribution are collected from term like $\nabla\phi_\chi(0)\nabla\phi_\chi(x)$ or $\cos\phi_\chi(0)\cos\phi_\chi(x)$.

7.5 Squeezed space analysis

7.5.1 Introduction of squeezed space

The concept of squeezed space is closely connected to the Luttinger description (see Appx. A). It is based on the unique labeling of particles by the spatial order in one dimension. The labeling field $\phi_l(x)/2\pi$ (Eq. A.1.1) is treated as the position $\tilde{x}$ of a particle in squeezed space. So the j-th particle (to the right of an arbitrary particle zero) is located at position j in squeezed space and its real space lattice site is neglected. Of course, one obtains by this construction a lattice where all sites are occupied and only the spin degree of freedom is left.

Ogata and Shiba [104, 210] have shown that, in the limit of infinite repulsive interaction, this construction allows to exactly factorize the ground state many-body wavefunction $\Psi(\{x_{j,\sigma}\})$ of the 1d Hubbard model into a charge part Ψ_ρ and a spin part Ψ_σ:

$$\Psi(\{x_{j,\nu}\}) = \Psi_\rho(\{x_j\})\,\Psi_\sigma(\{\tilde{x}_{j,\nu}\})\,. \tag{7.5.1}$$

While the charge-wavefunction is the one of spin-polarized non-interacting fermions, the spin-wavefunction is the ground state of a Heisenberg model living *on the occupied sites*. By this we mean that for a system with N spins, N_h holes[1] and $L = N + N_h$ sites, squeezed space has only N sites indexed by $\tilde{x}$. The relation between x and $\tilde{x}$ involves the position of all holes, but the description in squeezed space is independent of the holes. This is illustrated in figure 7.2D. The exact separation of equation 7.5.1 is due to the difference in energy scales. As the interaction approaches infinity, the exchange interaction J gets much smaller than the bandwidth $W = 4t$ and the linearization around the Fermi points[2] becomes exact.

But even away from infinite interactions, squeezed space (like the Luttinger liquid) remains a useful concept and correctly predicts the leading low energy behavior of the spin correlations that we call $C^{sq}(\tilde{d})$.

At large distance (long wavelength) and any interaction U, the squeezed space prediction for spin correlations are actually identical to the ones obtained by the string analysis (last section) [107]:

$$C^{\mathrm{str}}(d \gg 1) = C^{sq}(nd \gg 1) \tag{7.5.2}$$

The density factor n provides the mean conversion from real to squeezed space. At short distances, the two correlators are however different. This is illustrated conceptually in figure 7.8B and measurements of $C^{sq}(\tilde{d})$ and $C^{\mathrm{str}}(d)$ are compared in figure 7.12.

---

[1] We focus on hole doping. Due to the particle-hole symmetry of the Fermi-Hubbard model, one could equally well analyze a system with doublons. So in general N_h is the sum of holes and doublons. Note that N becomes the number of singly occupied sites in this case (unpaired spin).

[2] Note that these are the Fermi points of the effective spin-polarized system at density $n = n_\uparrow + n_\downarrow$.

7.5.2 Effective Heisenberg model

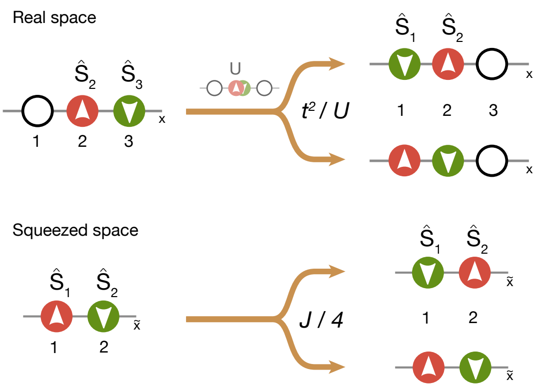

Figure 7.10. Hole induced spin flips. *By a second order hopping process a hole can induce a spin flip. In squeezed space only the spin flip remains. The process is of order J and thus needs to be included in a large U description of doped spin chains.*

The Hamiltonian governing the spin physics of squeezed space can be analytically derived from the FHM for large interactions. The full derivation can be found in the supplementary material of [82]. It shows that the spins follow a simple Heisenberg Hamiltonian with reduced exchange interaction J:

$$\hat{H}^{sq} = J_{\text{eff}}(n) \sum_{\langle \tilde{i},\tilde{j} \rangle} \hat{\vec{S}}_{\tilde{i}} \cdot \hat{\vec{S}}_{\tilde{j}}. \tag{7.5.3}$$

Indices $\tilde{i}, \tilde{j}$ refer to squeezed space and values of $J_{\text{eff}}(n)$ are shown in figure 7.11B. Intuitively, the reduced coupling can be understood from the delocalization of the holes. Whenever two nearest-neighbor spins in squeezed space are not separated by a hole in real space they interact with a bare J, but when they are split by a hole there is no spin interaction. $J_{\text{eff}}(n)$ averages both cases by taking the charge distribution at a given density into account. At large U the density sector is effectively non-interacting and $J_{\text{eff}}(n)$ becomes [82]:

$$J_{\text{eff}}(n,T) = \frac{J}{n} \langle \hat{n}_i \hat{n}_{i+1} \rangle - \frac{J}{2n} \left\langle \hat{n}_i \left(\hat{a}^\dagger_{i-1} \hat{a}_{i+1} + \hat{a}^\dagger_{i+1} \hat{a}_{i-1} \right) \right\rangle \tag{7.5.4}$$

$$= Jn \left[1 - \frac{1}{\pi n} \int_0^\pi dk \, \cos(2k) \, n_k^F(n,T) \right]. \tag{7.5.5}$$

Here $n_k^F(n,T)$ is the Fermi-Dirac distribution of free spinless fermions in a lattice with density n and temperature T. The two terms in equation 7.5.4 correspond to the two bare processes that induce spin flips. The first is the usual exchange interaction on two occupied sites. The second is a hole induced spin flip illustrated on figure 7.10. First a fermion hops from site 3 onto another fermion on site 2, where a virtual two-fermion state with energy U is formed. Then one of the two fermions hops from site 2 to site 1. No double-occupancies remain now, and the hole has effectively moved to site 2. The energy scale for this process is also set by J, and it is a relevant part of the t-J^* Hamiltonian [96].

Effect of temperature At zero temperature, the strength of the effective spin interaction does not matter because there is no second energy scale to compare it with. So in this case, the spin correlations are fully independent of the density, which of course directly follows from the factorization of the wavefunction (Eq. 7.5.1).

At finite temperature, the properties of the spin system depend on J/T. Via the density dependence of J_{eff}, the spin sector in squeezed space obtains a dependence on the original density n. This is easily understood because at low densities the spins barely see each other and interact only weakly, leading to lower degree of spin order. The temperature dependence of spin correlations in squeezed space is thus two-fold: The charge temperature enters into

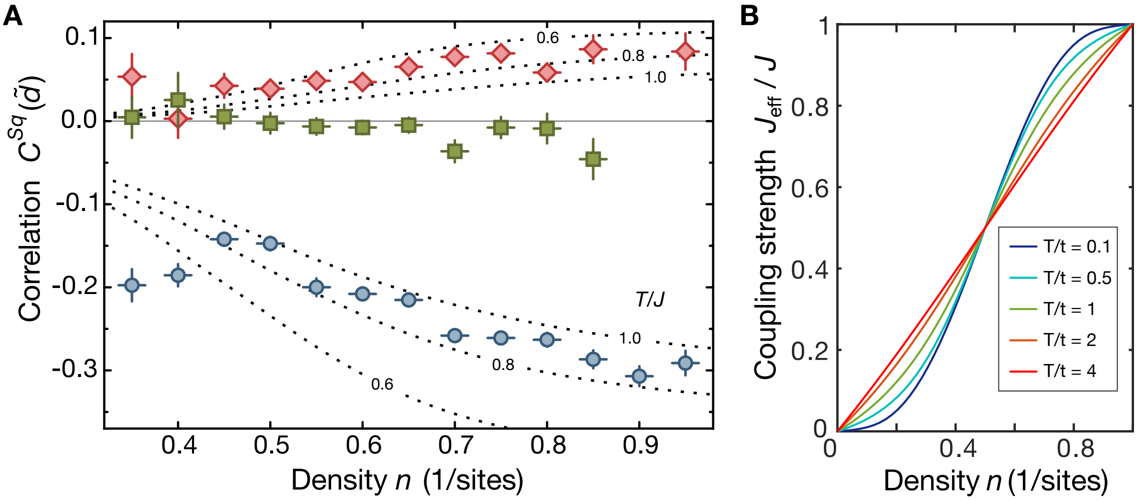

Figure 7.11. Spin correlations in squeezed space. ***(A)*** *Spin correlation measured directly in squeezed space for* $\tilde{d} = 1$ *(blue),* $\tilde{d} = 2$ *(red) and* $\tilde{d} = 3$ *(green) as a function of density n (bin widths* 0.05*). Dotted lines represent spin correlations* $C(1)$ *and* $C(2)$ *in the Heisenberg model for temperatures* $T/J = 0.6, 0.8, 1.0$ *obtained by exact diagonalization with a coupling constant* $J_{\mathit{eff}}(n)$*. The correlation decreases with increasing ratio* $T/J_{\mathit{eff}}(n)$*.* ***(B)*** *Dependency of the effective Heisenberg coupling* $J_{\mathit{eff}}(n)$ *on charge density at strong interactions (*$U \gg t$*). At high temperature, charge correlations vanish, leading to a linear dependence on density, while at low temperature, the algebraic charge order changes* J_{eff}*. Curves are based on analytic calculation in the non-interaction charge sector.*

the value of $J_{\rm eff}$ and the spin temperature sets the number of excitations with $J_{\rm eff}$. In principle, these two temperature could be different, because spin and charge are only weakly coupled, but we restrict our equilibrium analysis to identical spin and charge temperatures. But a direct extraction of two temperatures should be possible and marks an interesting extension of our work especially for quench experiments.

7.5.3 Experimental results

An analysis of the correlations directly in squeezed space is possible with the quantum gas microscope by removing the empty and doubly occupied sites in the analysis before evaluating the standard two-point correlator $C(d)$. This corresponds to a weighted summation along the diagonals of Fig. 7.8B, and thus mixes events that had different distances in real space. Similar to the string correlator, the squeezed space analysis (Fig. 7.11) reveals the finite-range hidden antiferromagnetic order. A quantitative comparison to the Heisenberg model with renormalized coupling $J_{\rm eff}(n)$ agrees well at a temperature of $T = 0.87(2)\ J$, consistent with temperatures obtained independently. This demonstrates that the concept of squeezed space can be successfully applied even away from the $U/t \to \infty$ limit [102]. Here, $J_{\rm eff}$ was determined independently from the microscopic parameters of the Hubbard model. The discrepancy between theory and experiments at densities below 0.45 might arise from the adiabatic cooling when we decreased the density during the preparation of the chains (see Appendix B.1). In chains at the wings of the cloud, the adiabatic deconfinement is much larger compared to the central chains, which should thus lead to lower spin entropy. Experiments with even higher doping could clarify this. Owing to the growing distances in real space, we could only analyze

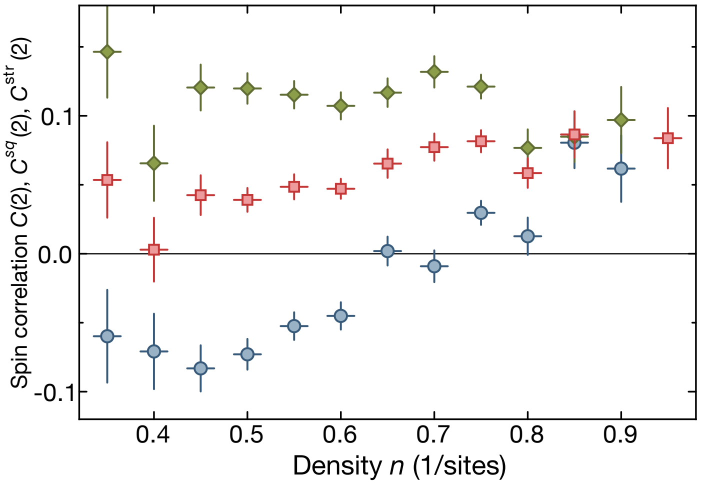

Figure 7.12. Comparison of spin correlations. *Spin correlation $C(d=2)$ in blue, spin string correlations $C^{str}(d=2)$ in green and squeezed space correlations $C^{sq}(\tilde{d}=2)$ in red as a function of local density.*

squeezed space correlations up to $\tilde{d}=3$. To probe the nature of the decay of the correlations with distance, larger and more homogeneous systems are required.

7.5.4 Comparison of correlation functions

We analyzed three types of spin correlation functions, the conventional connected two-point correlation function $C(d)$, the string correlation function $C^{\mathrm{str}}(d)$ and the squeezed space correlation function $C^{sq}(\tilde{d})$. Without any holes, all of these correlators give the same results. To emphasize the difference between them at finite doping, Fig. 7.12 shows an exemplary direct comparison of the $C^{\mathrm{x}}(2)$ values as a function of density. The conventional correlation function $C(d)$ is very sensitive to doping due to the discussed AFM parity flips and $C(2)$ even changes sign at $n=0.71(3)$, when the contribution from spin-hole-spin events $C_{SH,N_h=1}(d=2)$ dominates over events without a hole $C_{SH,N_h=0}(d=2)$.[1] The spin string correlation function, on the other hand, is insensitive to the hole induced AFM parity flips, thus, $C^{\mathrm{str}}(2)$ stays positive and even increases slightly in magnitude with decreasing density owing to the effectively shorter spin-spin distance in squeezed space. The squeezed space correlation function $C^{sq}(\tilde{d}=2)$ is also insensitive to the AFM parity flips and stays positive, but decreases with doping at finite temperature due to the decreasing effective coupling strength between the spins (see Sect. 7.5.2).

---

[1] Bosonization predicts the zero crossing of $C(1)$ at a density of about $n=0.75$, where $\cos(\pi n x)=0$ (cf. Eq. A.3.2).

7.6 Summary and outlook

Through the analysis of various local and non-local correlation functions, our measurements revealed striking equilibrium signatures of spin-charge separation in one-dimensional doped Hubbard chains. We explored the spin correlations around individual holes and demonstrated that each hole acts as a domain boundary of the AFM parity. Building upon this information, a string correlation function was constructed to characterize the spin sector independent of charge fluctuations. By removing the holes in the analysis of the data, measurements in an artificial squeezed space have been obtained. Good agreement with an effective Heisenberg description was found over a large range of dopings. The results showed that effects of spin-charge separation are visible in equilibrium correlation measurements.

The measurement demonstrated the new possibilities of quantum gas microscopes to characterize a system beyond the standard two-point correlators. Even in a theoretically well understood system like a one-dimensional spin chain, non-local correlations need to be employed to fully decompose the spin and charge pattern into their microscopic constituents. Due to the finite temperature of $T \sim J$ and the finite system size of about 15 sites, the analysis could not reach the scaling limit. Nevertheless, the precise analysis of short range correlations provided valuable information about the microscopic origin of effects observed on long wavelength and it is therefore complementary to measurements e.g. in solid state systems.

An interesting extension of this work would be the detection of dynamic signatures of spin-charge separation in quench experiments through the measurements of different spin and charge velocities [214, 215] or Green's function [216]. Using a local addressing laser, we plan to create deterministic holes and to observe the simultaneous spreading of a spinon and a holon wave through the chain. In higher dimensions the experimental evaluation of non-local correlations in synthetic hole doped antiferromagnetic materials is also of prime interest for the investigation of exotic many-body phases relevant to high temperature superconductors [217, 218]. The extension to two-dimensional Hubbard system could allow to directly see a local ferromagnetic environment around individual holes in an AFM background and the associated attraction of holes. In frustrated quantum magnets our measurement would, for example, enable the detection of skyrmions[1] and their role in quantum phase transitions [219]. Hence, our experiments mark a first step towards experimental studies of emergent gauge structures and topological order [220].

---

[1] Skyrmions are the topological excitations of a 2 d spin system ($\mathbb{R}^2 \to S^2$) where e.g. the central spins points down and all spins at $|r| \to \infty$ point up with a continuous change of spin directions inbetween.

Chapter 8

Summary and Outlook

In this thesis, we have demonstrated a versatile quantum gas microscope for ultracold fermions and the detection of antiferromagnetic spin correlations in the Fermi-Hubbard model over several sites. In one dimension, we found this spin order to be robust against hole-doping due to the effect of spin-charge separation.

Our single-atom resolved imaging, which can detect the full counting statistics including spin and doublons on every site, offers many new possibilities to analyze complex many-body states. In addition to the average density and spin with single-site resolution, it gives access to all orders of fluctuations and correlations. These correlations and the full underlying distribution function fully characterize the properties of a many-body system. In addition, the measurements allows us to employ powerful post-selections, which, if carefully applied, can reveal effects otherwise hidden in the noise.

With the measurement of the full atom number of a closed system on each realization, we observed the change of density by adding single atoms to the system and could work in a canonical ensemble despite natural shot-to-shot fluctuations. We employed this to study the equation of state of the one-dimensional Fermi-Hubbard model at intermediate interaction strength and could experimentally confirm the relation of compressibility to density fluctuations as given by the fluctuation-dissipation theorem.

In these lattice systems, we could realize antiferromagnetic (AFM) spin correlations over at least four sites in one-dimensional systems with entropies down to $0.4\,k_B$ per particle. We measured a constant strength of these spin correlation for increasing interactions indicating adiabatic cooling with decreasing exchange coupling J [71]. For densities below one, we observed incommensurate spin correlations, which are qualitatively described by a Luttinger liquid.

The simultaneous measurements of spins and holes is the core requirement for our analysis of spin-hole correlations and the evaluation of non-local string correlators. In doped spin chains, we confirmed that holes act as domain walls of the AFM parity and thereby reduce the spin correlations as measured by conventional two-point correlators. But due to spin-charge separation the spin order is not destroyed but merely hidden. With a non-local string correlation function, we were able to reveal these hidden correlations, which are described by an effective Heisenberg model [82].

These were merely the first experiments with our new advanced imaging technique, which has already proven to be a valuable improvement to the first quantum gas microscopes, that can measure the parity of the density only. In the future, we plan to extend these studies to doped two-dimensional systems and we will start to investigate non-equilibrium behavior and topology.

Technical improvements

The setup of our quantum gas microscope included many technological challenges. Especially the site-resolved imaging of a light atom like lithium turned out to be difficult due to the large photon recoil and limited available laser power. Our spin-resolved imaging relies on our large scale lattice produced by interfering beams, which are sent through the high-resolution objective. Related to this, we still face two problems, which are not detrimental, but which we would like to improve on: Our confining potential is not fully harmonic, but shows weak fringes and distortions, and our detection fidelity during imaging is only about 97%.

The imperfection of the potential are most likely caused by tiny errors in the laser beam profile, which get imaged onto the atoms with the high NA objective. Similar problems have been reported for the bosonic microscope in Harvard [129] and recently in a 1d optical lattice in Paris, which both also send the lattice beams through strong lenses. In the short term, we plan to minimize these fringes by compensation with a digital mirror device (DMD), which can shape the potential with single-site resolution [75, 221]. But in the long run, we have planned to built a new optical superlattice from two colors with beams which are sent to the atoms without passing through the objective.

With the detailed analysis of Raman sideband coooling, we can understand our small residual loss rate of atoms due to heating in the fluorescence process. Although the mean cooling is much stronger than all heating processes combined, the distribution of occupied levels shows a long tail to weakly bound states because the system leaves the Lamb-Dicke regime for highly excited harmonic oscillator states. The loss is less then 10 atoms for one million scattered photons, but we detect only 4% of the scattered light and need about 200 photons per atom on the camera, which results in a few percent detection error. Possible improvements can be reached with a deeper pinning lattice or with a more efficient repumping scheme. A new laser setup, which will provide about 20% more power is currently under construction and we will try to optimize the cooling by working in a weak magnetic offset field.

Future experiments

The dynamic measurement of spinon and holon propagation in a one-dimensional chain is a natural extension of our measurement of spin-charge separation with equilibrium correlations. It requires a local excitation of these modes e.g. by removal of a single spin in the center of a spin chain. We are currently implementing such an addressing with a DMD and plan to directly observe the propagation of the missing spin and charge in real time [215]. While the position of a single hole in a Mott insulator is easily identified on each picture, the excess spin is only revealed on many averaged pictures because of our finite spin correlation strength. Our estimation indicates that at least the short time behavior should be clearly measurable.

Our analysis of *hidden* spin correlations (Chapter 7) had a direct analogy to the spin-1 Haldane chain, but our system did not contain the non-trivial topology of this system. However, the Haldane chain can be simulated with ultracold Fermions in an optical lattice by including the p-band (first excited state along x, y, z) of the lattice [222, 223]. With four particles per site, the s-band is filled and the two atoms in the p-band form a spin-1. Our ability to measure both the spin and doubly occupied sites puts us in the unique position to resolve all these states in a single shot and thereby study a real Haldane chain.

With our experiments in one-dimensional spin chains, we demonstrated that we can reach low temperatures and analyze the interplay of spin and charge. Next, we want to apply this to the more complex situation of two-dimensional doped spin systems. We already measured antiferromagnetic correlations in 2d Mott insulators of similar length as in 1d case i.e. up to four sites. This correlation strength might already be sufficient to see some of the intersting microscopic behavior of holes in an AFM background. Contrary to 1d, holes in two dimensions are expected to be surrounded by a local ferromagnetic environment, which should be measurable with our microscope. At very strong repulsive interaction, a single hole even drives the full system into a Nagaoka ferromagnetic state [224, 225], whose observation would be a major step in the study of itinerant ferromagnetism [226–228]. In a next step, we will look for an effective attraction of pairs of holes by studying hole-hole correlation functions. After the realization of an AFM, such a measurement would be a major step towards the disputed d-wave pairing. In principle, the attraction of holes is a local process, which does not rely on full long-range antiferromagnetic order, but might already be observable with our current AFM correlations of several sites.

In addition, there are several ideas how to further reduce the temperature of our systems. Recently the group in Harvard created a bucket potential with a DMD and reached temperatures of $0.25t$ at $U/t = 7.2$ in 2d [75]. Another approach, which we will attempt with our current setup, is the adiabatic connection from a band insulator to a Mott insulator by splitting each site with the superlattice [65]. Because the entropies per particle in band insulator can be very low, we hope to reach very low temperatures in the Mott insulator this way. With an additional potential from a DMD one could even separate or remove the surrounding metallic entropy reservoir.

Although we are just starting to explore the analysis possibilities with spin and density correlations functions of arbitrary order, one may look ahead and address the question on how to implement fundamentally different observables or correlations in time. With many-body Ramsey interferrometry one can measure the *dynamic* many-body Green's function of spin systems [216] and gains direct information about the excitation spectrum. This proposal requires a local spin adressing, which has been demonstrated for Rubidium [125], and a full spin resolution as present in our machine. Another proposal involves a measurement with electromagnetically-induced-transparency [229]. The interference of two copies of the many-body system presents a different approach to observables beyond the combinations of density operators. A prominent example is the direct measurement of entropy, which has been shown for small bosonic systems [230].

Furthermore, there has been great progress in the last years to implement artificial gauge fields in optical lattices [231]. Recently these approaches have been combined with a quantum gas microscope [232] and effects in interacting systems are studied.

It becomes clear, that the prospects for interesting experiments with quantum gas microscopes are rich for years to come and I am convinced that more and more fascinating ideas will be developed to fully use the power of these experiments. Within the last three years the number of microscopes which published first images has grown from two [25, 26] to ten [29–32, 74, 123, 156, 233] and many more are under construction or in planning stage. Single-particle resolved images of ultracold atoms are, thus, certain to have a major impact on the investigation of strongly correlated quantum systems in the near future.

Appendices

Appendix A

Luttinger Liquid Theory

A.1 Introduction

One-dimensional interacting systems show very different properties compared to systems of higher dimensions. While most many-body systems in two or more dimensions are described by Fermi liquid theory [91], which shows quasi-particle excitations that can be adiabatically connected to free Fermions, most one-dimensional systems can be described by a harmonic-fluid approach [97–99]. Its basic excitations are collective waves with a simple linear dispersion. In contrast to higher dimensions, these excitations are bosonic and show negligible overlap with the microscopic fermions. Such systems have been termed *Luttinger liquids* [100, 101] and an extensive coverage of this theory can be found in the book by T. Giamarchi [54], whose notation we follow in this thesis.

As particles in one dimension can be uniquely labeled by their spatial integer index j per spin, one can define a monotonically increasing counting function (labeling field) $\hat{\phi}_l(x)$ that increases by 2π at the position of each particle, i.e. $\hat{\phi}_l(x_j) = 2\pi j$. Subtraction of the mean slope (given by the mean density ρ_0) leads to the function $\phi(x)$, which measures the displacement of particles from the crystalline position [54]:

$$\hat{\phi}_l(x) = 2\pi\rho_0 x - 2\hat{\phi}(x) \tag{A.1.1}$$

Thus e.g. $\phi(x) = 0$ describes an unperturbed crystal with spacing ρ_0^{-1}, $\phi(x) = \pi/2$ is the same crystal shifted by half a spacing, $\phi(x) = \pi\zeta x$ is a crystal with density $\rho_0 - \zeta$ and $\phi(x) = \zeta\pi\sin(kx)$ describes a density wave with amplitude ζ around ρ_0. Figure A.1 illustrates the concept with two examples. The counting field allows to express the density operator by

$$\begin{aligned}\hat{\rho}(x) &= \sum_j \delta(x - \hat{x}_j) = \sum_j \nabla\hat{\phi}_l(x)\delta(\hat{\phi}_l(x) - 2\pi j) \\ &= \left(\rho_0 - \frac{1}{\pi}\nabla\hat{\phi}(x)\right)\sum_p e^{i2p(\pi\rho_0 x - \hat{\phi}(x))},\end{aligned} \tag{A.1.2}$$

where p is an integer. In the first step $\delta(f(x)) = \delta(x - x_0)/|\nabla f(x)|$ was used and in last step the δ-function has been rewritten with its Poisson sum and (A.1.1) was inserted. The term in brackets describes the smooth variation of the density, while the sum of oscillating term are the fourier decomposition of the specific particle positions.

With this expression, the fermionic single-particle creation operators can be written in real space as an amplitude related to $\hat{\phi}(x)$ times a phase factor $\hat{\theta}(x)$

$$\hat{a}_x^\dagger = \sqrt{\hat{\rho}(x)}e^{-i\hat{\theta}(x)}e^{\frac{1}{2}\hat{\phi}_l(x)} \sim \left(\rho_0 - \frac{1}{\pi}\nabla\hat{\phi}(x)\right)^{1/2}\sum_p e^{i\hat{\theta}(x) + i(2p+1)(\pi\rho_0 x - \hat{\phi}(x))}, \tag{A.1.3}$$

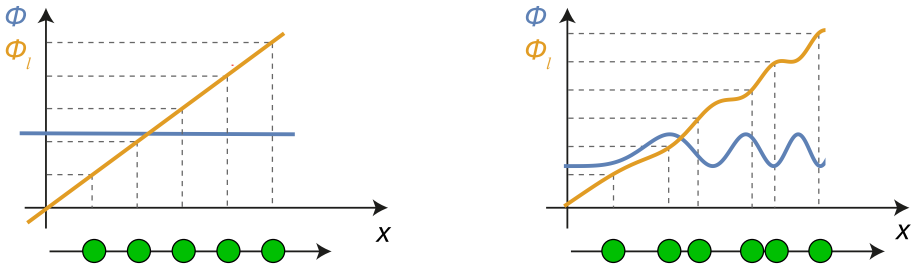

Figure A.1. Luttinger labeling field. *Illustration of the labeling fields $\phi_l(x)$ and $\phi(x)$. For crystallized particles $\phi_l(x)$ grows linearly and $\phi(x)$ is constant. Different functions allow to describe any particle distribution. Note that density fluctuations are proportional to the gradient of ϕ, $(\rho(x)-\rho_0)\sim -\nabla\phi(x)$.*

The last expression is equal up to a constant because the square root of a delta function is a delta function times a normalization. The extra $e^{\frac{1}{2}\hat{\phi}_l(x)}$ term is the Jordan-Wigner transformation [155] that ensures the proper fermionic anti-commutation relation of $\hat{a}_x^\dagger$ even though the fields $\hat{\phi}(x)$ and $\hat{\theta}(x)$ are bosonic[1].

So far the description of fermions in terms of bosonic fields is exact and general. Typically one is interested in the low energy, large wavelength description of a system. The representation in equation A.1.3 has the advantage of a natural *coarse graining* procedure by restriction of the sum to small values of p. This leads to a simplified expression for the density $\hat{\rho}$ from (A.1.2) with $p=-1,0,1$

$$\hat{\rho}_{x,\nu} = \left(\rho_0 - \frac{1}{\pi}\nabla\phi_\nu(x)\right)\left(1+\cos\left(2k_F x - 2\phi_\nu(x)\right)\right), \tag{A.1.4}$$

where we introduced a spin index $\nu=\uparrow,\downarrow$ to describe systems with spin.

Luttinger Hamiltonian To derive the Hamiltonian of the low-energy properties one can insert (A.1.3) per spin ($\phi_\uparrow$,$\phi_\downarrow$) into an interacting one-dimensional Hamiltonian and expand in powers of $\nabla\phi$ and $\nabla\theta$. Note that we only discuss the thermodynamic limit in this section. Finite size corrections are covered e.g. in [234]. Dropping all quickly oscillating terms[2] and inserting fields for spin and charge[3]

$$\phi_\rho = \frac{1}{\sqrt{2}}\left(\phi_\uparrow+\phi_\downarrow-\pi/2\right), \quad \phi_\sigma = \frac{1}{\sqrt{2}}\left(\phi_\uparrow-\phi_\downarrow\right), \tag{A.1.5}$$

one obtains the general Luttinger liquid Hamiltonian describing a gapless, spin-balanced, one-dimensional system

$$\begin{aligned} H_{LL} = &\frac{1}{2\pi}\int dx \left(u_\sigma K_\sigma \left(\nabla\theta_\sigma(x)\right)^2 + \frac{u_\sigma}{K_\sigma}\left(\nabla\phi_\sigma(x)\right)^2\right) \\ &+\frac{1}{2\pi}\int dx \left(u_\rho K_\rho \left(\nabla\theta_\rho(x)\right)^2 + \frac{u_\rho}{K_\rho}\left(\nabla\phi_\rho(x)\right)^2\right). \end{aligned} \tag{A.1.6}$$

---

[1] From here on we are going to drop the operator hats on the bosonic fields.

[2] Upon integration/summation oscillating terms give negligible contributions, but care has to be taken with certain commensurate effects. I.e. $\sum_n e^{ikn}$ does not vanish for $k=2\pi$.

[3] The $\pi/2$ phase has no physical relevance, but highlights some spin-charge symmetries.

The parameters $(u_\sigma, u_\rho, K_\sigma, K_\rho)$ encode the low-energy properties and they are in general non-trivially related to the microscopic parameters of the system. This quadratic Hamiltonian is a sum of density terms (that depend on θ_ρ, ϕ_ρ) and spin terms $(\theta_\sigma, \phi_\sigma)$ that both describe non-interacting simple waves. So even for a strongly interacting system, the low energy physics is given by plane wavelike spin and charge excitations, which are non-local in the original particles (encoded in the non-locality of ϕ and θ). The charge (spin) velocity u_ρ (u_σ) gives the velocity of those density (spin) waves of the system and thus set the energy of excitations, $E_q = u\,|q|$ without a gap. The Luttinger parameter K_ρ (K_σ) is related to the compressibility κ_ρ (magnetic susceptibility κ_σ) and to the charge (spin) stiffness D of the system, which are given by

$$\kappa_\rho \equiv \frac{\partial(n_\uparrow + n_\downarrow)}{\partial\mu} = \frac{2K_\rho}{\pi u_\rho}, \qquad \kappa_\sigma \equiv \frac{1}{2g\mu_B}\frac{\partial(n_\uparrow - n_\downarrow)}{\partial B} = \frac{K_\sigma}{2\pi u_\sigma}. \tag{A.1.7}$$

$$D_\rho \equiv \pi L \frac{\partial J}{\partial \Phi} = 2u_\rho K_\rho, \quad D_\sigma \equiv \frac{1}{L}\frac{\partial^2 E_0}{\partial \gamma^2} = 2u_\sigma K_\sigma \tag{A.1.8}$$

The charge stiffness is the change of current J for a change of magnetic flux Φ through a loop of size L and the spin stiffness can be defined as the change in energy E_0 for a twist of the spins by an angle γ.

The Luttinger parameters K are, thus, a measure for the strength of the response of the system to an external perturbation. In general, $K_\rho < 1$ describes a repulsive system, $K_\rho > 1$ an attractive one and $K = 1$ a non-interacting free *fermionic* system. Due to the *fluctuation-dissipation-theorem* K_ρ (K_σ) is also governing the strength of the density (spin) correlations, which are primary observables in our experiments. For the analytic form of the correlation functions of the Luttinger liquid see section A.3.

A.2 Fermi-Hubbard model

The Hamiltonian of the single band Fermi-Hubbard model (FHM) is given by equation 2.2.1. Written in the bosonized notation the Hamiltonian of the FHM conisists of the general H_{LL} (Eq. A.1.6) and additional terms; one to describe the (varying) chemical potential[1], one for an external magnetic field B as well as two terms that are needed to describe the phase transitions to gapped phases, which exist in the FHM:

$$\begin{aligned} H_{FHM,LL} = H_{LL} & \\ + \frac{1}{\pi}\int dx & \left(\sqrt{2}\mu(x)\nabla\phi_\rho(x) + \frac{g\mu_B B}{\sqrt{2}}\nabla\phi_\sigma(x)\right) \\ + \frac{2U}{(2\pi\alpha)^2}\int dx & \left(\cos(\sqrt{8}\phi_\sigma(x)) - \cos(\sqrt{8}\phi_\rho(x))\right) \end{aligned} \tag{A.2.1}$$

The second line of equation A.2.1 describes the effect of an external chemical potential $\mu(x)$ and magnetic field B. The nonlinearities in the third line[2] are due to the lattice potential ($\phi_\rho(x)$-term) describing *umklapp* - scattering[3] and the interaction between the left and right Fermi

---

[1] A constant chemical potential can always be absorbed into a redefinition of ϕ_ρ via a different ρ_0.

[2] This line is written for a system where $\phi_\uparrow$ and $\phi_\downarrow$ (Eq. A.1.1) are defined at half filling for $\rho_{0,\uparrow} = \rho_{0,\downarrow} = 1/2$. In the other cases, additional oscillatory factors arise, which make the terms less relevant.

[3] Umkapp - scattering events are scatterings in momentum space, which violate total momentum conservation and only conserve the quasi momentum of the lattice i.e. $P_1 + P_2 \to P_3 + P_4 + Q$, where Q is a lattice momentum.

point ($\phi_\sigma(x)$-term) are *backscattering* events[1]. The Hamiltonian in this form is the symmetric sum of two *sine-Gordon* Hamiltonians, one for the charge sector and one for the spin sector.

Spin-charge separation Note that there is no term coupling the spin and charge sector, so the spin fields are independent of the charge fields. This is a peculiarity which is very common in one dimension: Although the bare particles are fermions with a given spin and charge, a proper physical description separates spin from charge and treats both independently. This is known as *spin-charge separation* and the effect is already visible on the level of the Hamiltonian. For a discussion of the accuracy of this effect see section 2.3.

Spin-charge separation and the Hamiltonian above are no longer valid at strong magnetic fields (large polarization) because of the different sizes of the original Fermi seas. In this case, the Hamiltonian still separates in two independent sectors, but each is a linear superposition of spin and charge [54].

Phases

Depending on the values of K_ρ, K_σ, μ and B, each of the cos-terms in the Hamiltonian A.2.1 can drive the system into a gapped phase via a quantum phase transition. If both are irrelevant[2], the system stays in the metallic Luttinger liquid phase, described by H_{LL}, with renormalized parameters K, u. If one of the terms is a relevant perturbation, the system becomes massive in this sector i.e. it develops a gap (the corresponding field ϕ localizes in one minimum of the cosine).

The bare parameters (u, K) for the Fermi-Hubbard model can be obtained from an explicit derivation of equation (A.1.6) from (2.2.1) and are given by [54]:

$$u_\chi = v_F \left(1 \pm \frac{U}{\pi v_F}\right)^{1/2}, \quad K_\chi = \left(1 \pm \frac{U}{\pi v_F}\right)^{-1/2}, \quad v_F = 2t\sin(\pi n/2) \tag{A.2.2}$$

with plus (minus) sign for $\chi = \rho$ (σ). Note that $K_\rho > 1$ for attractive interactions and $K_\rho < 1$ for repulsive interactions and reversed for the spin. Due to the non-linear cos-terms these bare parameters get renormalized however and the values above are thus not the values which allow to directly calculate observables.

We list here a few results of such renormalization calculations for $T = 0$ with the relevant values of K and u after renormalization i.e. for H_{LL} without the extra terms of equation A.2.1. Due to the symmetry of the Hamiltonian, each property of the spin/charge sector at repulsive interactions has a symmetric correspondence in the charge/spin at attractive interactions [93].

Repulsive interactions

- At half filling ($|\mu| < \mu_c = \Delta_\rho$) the *umklapp* term is relevant and drives the system to a Mott insulator at arbitrary $U > 0$. The gap Δ_ρ is given by U for strong interaction and $\propto U^{1/2}e^{-v_F/U}$ for weak interactions. Within the Mott state, the field $\phi_\rho(x)$ is constant except for local fluctuations, which are the Doublon-Hole pairs. Because $\phi_\rho \sim \int dx\,\rho$ is a non-local field, only a string operator can measure the order [27, 189].

---

[1] Backscattering refers to collisions that conserve the total momentum, but exchange momentum between the ↑ and ↓ population.

[2] In a renormalization calculation, perturbing operators are classified as irrelevant or relevant. Irrelevant terms do not change the overall phase of the system, but only renormalize the parameters of the Hamiltonian, while relevant operators drive the system into a new phase with different properties (e.g. a gap) [235].

- In the unpolarized case ($B = 0$), the $\cos(\sqrt{8}\phi_\sigma(x))$ is marginally[1] irrelevant due to the spin SU(2) symmetry. This leads to $K_\sigma = 1$ for any doping with logarithmic corrections to the correlation functions.
- At finite doping there can be no Mott insulator and $0.5 < K_\rho < 1$ approaching $K_\rho = 0.5$ for any $U > 0$ close to an empty, half filled or filled band and for any doping at strong repulsions.
- Both charge[2] and spin show critical fluctuations with an algebraic decay of the density-density and spin-spin correlation functions[3]. The measurements of these spin correlations (at finite T) are a central part of the experimental results of this thesis.

Attractive interactions

- In the unpolarized case ($B = 0$), the spin-sector orders (ϕ_σ) for arbitrary $U < 0$ due to the backscattering term. The spins tend to pair in singlets with a spin-gap $\Delta_\sigma \propto U^{1/2}e^{-v_F/U}$ [236] for small $|U|$ and $\Delta_\sigma = |U|$ for strong attraction. This phase is known as a Luther-Emery liquid [237] and within this phase ϕ_σ is constant up to local fluctuations [189].
- At half filling, the *umklapp* term is marginally irrelevant leading to $K_\rho = 1$. At an arbitrary chemical potential, one gets $1 < K_\rho < 2$ with $K_\rho \to 2$ for almost full or empty bands at any $U < 0$.
- At a finite polarization, there is no spin gap and $0.5 < K_\sigma < 1$.
- There are critical fluctuations, i.e. correlations with only algebraic decay, towards singlet pairing in k-space (BCS) and towards a charge density wave.

The effective parameters (u,K) in the Luttinger phase can be obtained from comparison to numerical or analytic calculations. With the Bethe-ansatz [238], there exist an exact solution of the Fermi-Hubbard model [239], which allows to calculate the Luttinger parameters for repulsive [103] as well as attractive [240] interactions at various densities.

A.3 Correlation functions

The experimental observables are the spin and density. With equations A.1.4 and A.1.5, one can express the density $\hat{\rho} = \hat{\rho}_\uparrow + \hat{\rho}_\downarrow$ and the spin $\hat{S}^z = \frac{1}{2}(\hat{\rho}_\uparrow - \hat{\rho}_\downarrow)$ with the fields ϕ_ρ and ϕ_σ. It is instructive to look at the leading oscillatory terms with wavevector $2k_F = \pi(n_\uparrow + n_\downarrow)$:

$$\begin{aligned} \hat{\rho}_{2k_F}(x) &\sim \sin\left(2k_F x - \sqrt{2}\phi_\rho(x)\right)\cos\left(\sqrt{2}\phi_\sigma(x)\right) \\ \hat{S}^z_{2k_F}(x) &\sim \cos\left(2k_F x - \sqrt{2}\phi_\rho(x)\right)\sin\left(-\sqrt{2}\phi_\sigma(x)\right) \end{aligned} \tag{A.3.1}$$

---

[1] The term *marginal* describes that the system is right on the boundary to a spin ordered state. If the spin interaction in one axis were slightly larger than in the other, the spin sector would obtain a gap.

[2] Outside of the Mott insulator.

[3] These are the strongest correlations one can expect because the Mermin-Wagner theorem [92] prevents long range order (charge density wave, spin density wave) in infinite 1d systems.

From these expressions it becomes clear that ϕ_ρ acts as the phase of both the spin and charge waves and ϕ_σ is related to the amplitude of those waves.

It is important to note that, while the fields ϕ_ρ and ϕ_σ are independent in a Hamiltonian like Eq. A.2.1, the local physical observables always mix both fields. A central challenge in the analysis of doped spin chains (Chapter 7) was therefore to find a combination of local spin and density operators that isolate e.g. the spin properties of the system.

From equation A.3.1 it becomes clear that long ranged ordered spin or density waves would require both the fields ϕ_ρ and ϕ_σ to order i.e. to stay close to a constant value. As outlined in the last section, this never occurs in the FHM, which is of course required by the Mermin-Wagner-Theorem (in 1+1 dimensions).[1] A fluctuating field ϕ leads to correlations of only finite length as the phase difference accumulates over larger distances.

The density-density as well as the spin-spin correlation function can be expressed in terms of the bosonic fields θ, ϕ and their form can be evaluated analytically. At zero temperature for $U \geq 0$ the (equal time) correlation functions in the Luttinger phase are [54]:

$$\begin{aligned} R(x) = \quad & \langle n_0 n_x \rangle - \langle n_0 \rangle \langle n_x \rangle = -\frac{K_\rho}{\pi^2 x^2} + \tilde{A}_2 \frac{n^2 \cos(\pi n x)}{x^{K_\rho + K_\sigma^*}} \log^{-3/2}(x) \\ C(x) = & 4 \left(\langle S_0^z S_x^z \rangle - \langle S_0^z \rangle \langle S_x^z \rangle \right) = -\frac{K_\sigma}{\pi^2 x^2} + \tilde{A}_2' \frac{\cos(\pi n x)}{x^{K_\rho + K_\sigma^*}} \log^{1/2}(x) \end{aligned} \tag{A.3.2}$$

where x is the relative distance in units of the lattice spacing and $\tilde{A}_2, \tilde{A}_2'$ are constants that depend on the microscopic physics of the system. The renormalization of the spin parameter for a $SU(2)$ symmetric interaction leads to $K^* = 1$ and logarithmic corrections.
The first term of (A.3.2) is a simple $1/r^2$ -decay arising from pairs of atoms at the same Fermi point, while the second term oscillates with twice the Fermi-wavevector due to contributions from both Fermi points separated by $2k_F$ in k-space. This describes the tendency of the system to form a charge (spin) density wave. At half filling $\cos(\pi n x) = (-1)^x$ and one obtains antiferromagnetic correlations[2]. Due to the log corrections, the spin correlations decay slightly slower than the density ones. The absolute amplitude of the spin oscillations is, in addition, much stronger i.e. $A_2' \gg A_2$. A close look at equation A.3.1 shows that the relative amplitudes of the density and spin correlations are given by $\cos(\sqrt{2}\phi_\sigma)$ and $\sin(-\sqrt{2}\phi_\sigma)$. Even though the field ϕ_σ is fluctuating, the backscattering term $U\cos(\sqrt{8}\phi_\sigma)$ still tends to localize its value around $(1+2m)\pi/\sqrt{8}$. This leads to weak density correlations and strong spin correlations. At half filling these are the antiferromagnetic correlations of the Heisenberg model that decay with $1/r$ (using $K_\sigma = 1$ for SU(2) symmetric spin and $K_\rho = 0$ in a Mott insulator).

Finite doping The periodicity of the oscillations in equation A.3.2 is $2\pi/(2k_F) = 2/n$. At finite hole doping the wavelength of the spin and charge oscillations thus increases due to the dilution of the chain with holes. In addition, the amplitude of the oscillations decays faster compared to the Mott phase because $K_\rho \geq 0.5$. This can be attributed to the following processes: While the holes move through a spin chain, they shift the positions of the spins. This does not change the sequence of spins, but adds uncertainty to their position on the lattice. This effect is analyzed in detail in chapter 7.

---

[1] In a system that breaks SU(2) spin symmetry, a long range ordered state is possible. Ordered $\phi_\rho(x) = 0$ and $\phi_\sigma(x) = \pi/\sqrt{8}$ describe an Ising antiferromagnet.

[2] The charge sector is in a Mott insulator in this case, so (A.3.2) does not apply.

Finite temperatures At finite temperatures thermal excitations (spinons, holons, doublons) reduce the spin and charge correlations. These excitations are collective waves with wavevectors k and energies $E_{\text{holon}} = u_\rho\,|k|$, $E_{\text{spinon}} = u_\sigma\,|k|$. The leading terms of the spin and charge correlation functions of the Luttinger liquid at finite temperature are given by [1]

$$\begin{aligned} R(x) &= -\frac{K_\rho}{(\pi x_\rho \sinh(x/x_\rho)^2} + A_2 \frac{\cos(\pi n x)}{\left(x_\rho \sinh(x/x_\rho)\right)^{K_\rho} (x_\sigma \sinh(x/x_\sigma))^{K_\sigma}} \\ C(x) &= -\frac{K_\sigma}{(\pi x_\sigma \sinh(x/x_\sigma)^2} + A_2' \frac{\cos(\pi n x)}{\left(x_\rho \sinh(x/x_\rho)\right)^{K_\rho} (x_\sigma \sinh(x/x_\sigma))^{K_\sigma}} \end{aligned} \tag{A.3.3}$$

where $x_\chi = u_\chi/(\pi T)$ ($\chi = \rho, \sigma$) are characteristic thermal length scales of the charge and spin sector. At distances $x > x_\chi$ the correlations decay exponentially due to thermal excitation. At shorter distances, the correlations, however, decay algebraically because excitations with high energy are not thermally activated and long wavelength excitations do not affect short distances.

Although spin and charge excitations are decoupled, the spin and charge correlation functions are each affected by both sectors, which can be seen from the dependence on K_ρ, K_σ in equations A.3.2 and A.3.3. The mixing can be understood from the shifting of spins due to the free motion of holes. The normal two-point correlations given above show asymptotically an exponential decay with a decay constant ξ,

$$C(d) \sim \exp(-x/\xi), \quad \text{with:} \quad \xi^{-1} = \left(\frac{u_\rho}{\pi K_\rho T}\right)^{-1} + \left(\frac{u_\sigma}{\pi K_\sigma T}\right)^{-1}. \tag{A.3.4}$$

Note that the spin velocity ($u_\sigma \sim J$ at large U) is smaller than the charge velocity ($u_\rho \sim t$), so the decay is dominated by the spinons. Nevertheless, the additional effect of the charge sector is quite strong as demonstrated in the experiments described in chapter 7. A measurement of stronger spin correlations that only depend on the spin sector can be achieved with non-local correlators (same chapter).

---

[1] The logarithmic corrections have been neglected.

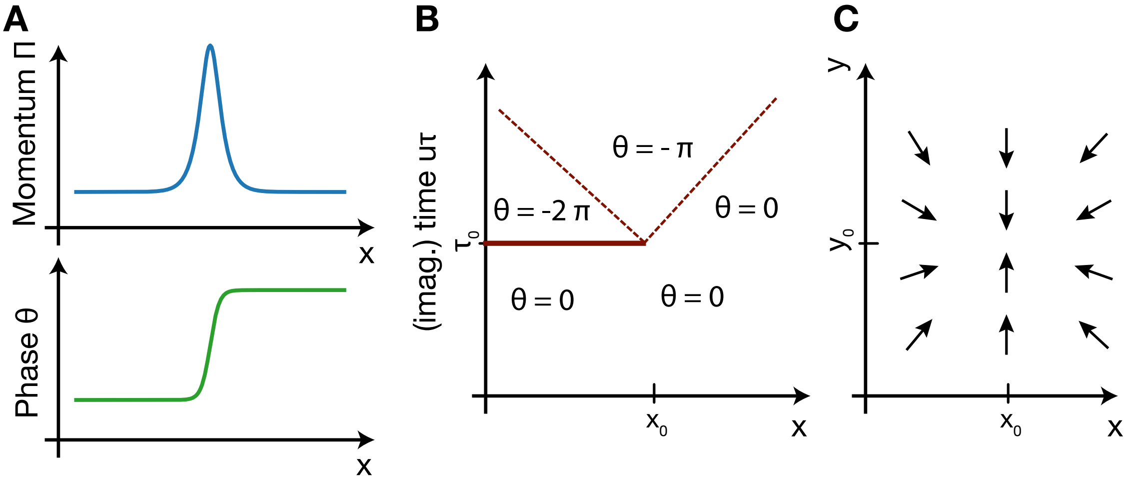

Figure A.2. Vortex in the Luttinger liquid A *A localized momentum (top) is associated with a kink in the phase θ_ρ.* ***B*** *A momentum kick $e^{i2\phi_\rho}$ at time τ_0 and position x_0 thus changes the phase $\theta_\rho = 0$ by -2π for $x < x_0$. The excitation spreads with time, leading to a winding of the phase θ_ρ around (x_0, τ_0). Such momentum kicks are generated by umklapp scattering events in a lattice, when two particles with quasi momenta q_1, q_2 scatter into q_3, q_4 with $\sum_i q_i = Q$, where Q is a lattice momentum. These processes drive the system into a Mott insulator.* ***C*** *The θ_ρ-vortex is topologically equivalent to a vortex in a classical spin XY-model, so the Mott transition in one-dimension is in the universality class of the BKT-transition [54].*

A.4 Connection to BKT-physics

Due to the correspondence of zero temperature d-dimensional quantum system to a (d+1)-dimensional classical system [241], there is a direct link of the discussed phases and correlations of the Luttinger liquid (as described by the sine-Gordon Hamiltonian in Eq. A.2.1) to the Berezinskii–Kosterlitz–Thouless (BKT) phase in two dimensions. Both fall into the universality class of the two-dimensional XY-model[1] with a phase transition driven by the binding of vortices [242, 243]. The connection is given by associating the phase θ_ρ with the angle of the XY-spins[2]. The quadratic Luttinger liquid (obtained for attractive interactions $K_\rho > 1$) correspond to the free spin-waves of the low temperature phase BKT phase, with no free vortices. The Mott phase, where ϕ_ρ orders and θ_ρ is disordered, is connected to the high-temperature phase of unbound vortices. The Luttinger parameter K_ρ thus has its correspondence in the inverse classical temperature T^{-1} and the transition is driven by the umklapp scattering term $\cos(\sqrt{8}\phi_\sigma(x))$. This allows to identify the *vortices* of the 1d system as these umklapp scattering events in a (ut, x)-plane (see Fig. A.2). The bound vortices in the critical low-temperature BKT-phase are therefore the absence of the umklapp scatterings (or their paring of with lattice momenta $+Q, -Q$) allowing the particles to spread through the system.

---

[1] Together with the two-dimensional Coulomb plasma.

[2] The focus here is on the charge sector and the Mott transition (ordered ϕ_ρ), but due to the duality the same is true for the spin sector and the transition to the Luther-Emery liquid.

Appendix B

Supplementary Material for Chapter 7

B.1 Preparation of doped spin chains

We started from a quasi two-dimensional degenerate mixture of the two lowest energy Zeeman states of ^{6}Li in a single plane of an optical lattice with $3.1\,\mu$m spacing in the vertical direction. The vertical lattice depth was $110\,E_r^z$ and the scattering length was set to $530\,a_B$. Here $E_r^i = h^2/8ma_i^2$ is the recoil energy for a lattice of period a_i in the i-direction, m the atomic mass and a_B the Bohr radius. Next, the preparation of about 10 Fermi-Hubbard chains started with ramping up the large scale component of an optical superlattice ($a_{sl} = 2.3\,\mu$m) in the y-direction in 15 ms to a depth of $18\,E_r^y$. A lattice of period $a_l = 1.15\,\mu$m along x was then ramped up in 15 ms to $3\,E_r^x$ and finally to $5\,E_r^x$ in 80 ms, while the lattice depth in z-direction was linearly decreased to $17\,E_r^z$ in 50 ms. Simultaneously the lattice in y-direction was increased to $27\,E_r^y$ in 60 ms. Using a magnetic offset field of 714 G near the broad Feshbach resonance located at 834.1 G [127] the scattering length was linearly increased during these ramps to $2000\,a_B$. The lattice and the low peak densities of about one atom per site ensured collisional stability by suppressing three-body recombination losses. At the end of the ramps, the onsite interaction energy was $U = h \times 2.9\,$kHz, as estimated from Wannier function calculations without taking into account finite band gap corrections [244]. The tunneling amplitude was $t = h \times 400\,$Hz and the exchange energy $J = 4t^2/U = h \times 220\,$Hz.

B.2 Definitions of correlation functions

An empty or doubly occupied site has spin zero and thus these sites reduce the magnitude of spin correlations trivially. In order to compare spin correlations at different densities, we evaluate the spin operators on singly occupied sites only. The conventional connected spin correlation function including this condition can be written as

$$C(d) = 4\,\langle \hat{S}_i^z \hat{S}_{i+d}^z \rangle_{\bullet_i \bullet_{i+d}} \equiv 4 \frac{\langle \hat{S}_i^z \hat{S}_{i+d}^z \rangle}{\langle \hat{n}_i^s \hat{n}_{i+d}^s \rangle} \approx \frac{4}{n_i n_{i+d}} \langle \hat{S}_i^z \hat{S}_{i+d}^z \rangle,$$

where we defined the "singlon" operator $\hat{n}_i^s = \hat{n}_{i,\uparrow} + \hat{n}_{i,\downarrow} - 2\hat{n}_{i,\uparrow}\hat{n}_{i,\downarrow}$. The first relation is the definition of the conditional correlation function $C(d)$, which we directly measured experimentally. The doublon fraction as well as density correlations beyond one site were negligible, which justifies the approximation of the "singlon-singlon" correlations in the denominator by the measured densities resulting in a simple normalized spin-spin correlator. These last expressions are just given for clarity, they have not been used in the analysis.

In the same spirit, the spin-hole correlation function, which selects on two occupied and one empty site, can be rewritten as a normalized three-point correlator:

$$C_{SH}(d,s) = 4\,\langle \hat{S}^z_i \hat{S}^z_{i+d} \rangle_{\bullet_i \circ_{i+s} \bullet_{i+d}} \equiv 4 \frac{\langle \hat{S}^z_i \hat{n}^h_{i+s} \hat{S}^z_{i+d} \rangle}{\langle \hat{n}^s_i \hat{n}^h_{i+s} \hat{n}^s_{i+d} \rangle} \approx \frac{4}{n_i (1-n_{i+s}) n_{i+d}} \langle \hat{S}^z_i \hat{n}^h_{i+s} \hat{S}^z_{i+d} \rangle,$$

where the hole operator $\hat{n}^h_i = (1-\hat{n}_{i,\uparrow})(1-\hat{n}_{i,\downarrow}) \approx (1-n_i)$ detects the presence of a hole at site i.

The measured non-local correlation functions can equivalently be expressed in terms of unconditional spin and density correlation functions,

$$\begin{aligned}
C^{\mathrm{str}}(d) &= 4 \left\langle \hat{S}^z_i \left(\prod_{j=1}^{d-1} (-1)^{(1-\hat{n}_{i+j})} \right) \hat{S}^z_{i+d} \right\rangle_{\bullet_i \bullet_{i+d}} \\
&\equiv \frac{4}{\langle \hat{n}^s_i \hat{n}^s_{i+d} \rangle} \left\langle \hat{S}^z_i \left(\prod_{j=1}^{d-1} (-1)^{(1-\hat{n}_{i+j})} \right) \hat{S}^z_{i+d} \right\rangle \\
C^{\mathrm{str}}_{SH}(d,s) &= 4 \left\langle \hat{S}^z_i \left(\prod_{j=1, j\neq s}^{d-1} (-1)^{(1-\hat{n}_{i+j})} \right) \hat{S}^z_{i+d} \right\rangle_{\bullet_i \circ_{i+s} \bullet_{i+d}} \\
&\equiv \frac{4}{\langle \hat{n}^s_i \hat{n}^h_{i+s} \hat{n}^s_{i+d} \rangle} \left\langle \hat{S}^z_i \hat{n}^h_{i+s} \left(\prod_{j=1, j\neq s}^{d-1} (-1)^{(1-\hat{n}_{i+j})} \right) \hat{S}^z_{i+d} \right\rangle .
\end{aligned}$$

When studying both local and non-local spin correlations at large distances, the presence of the trap complicates the definition of density. For the data presented in the main text in Fig. 3 we defined the density n as the mean density over all the sites connecting the two operators evaluated at sites i and $i+d$: $n = \frac{1}{d+1} \sum_{k=i}^{i+d} \langle \hat{n}_k \rangle$.

B.3 Correction for finite size effects

In each chain, the atom number and magnetization weakly fluctuate from shot-to-shot, but for a single realization the atom number $N = \langle \sum_i \hat{n}_i \rangle = N_\uparrow + N_\downarrow$ and magnetization $M = \langle \sum_i \hat{S}^z_i \rangle = \frac{1}{2}(N_\uparrow - N_\downarrow)$ are fixed. A fixed magnetization M in a single spin-$1/2$ chain without holes or doublons (length $L = N$) acts as a constraint on the spin-spin correlations because of the following exact sum rule:

$$\begin{aligned}
4\hat{M}^2 &= 4 \left\langle \sum_{i,j} \hat{S}^z_i \hat{S}^z_j \right\rangle = 4 \sum_i \left\langle \left(\hat{S}^z_i \right)^2 \right\rangle + 8 \sum_{d=1}^{N-1} \sum_{i=1}^{N-d} \langle \hat{S}^z_i \hat{S}^z_{i+d} \rangle \\
&= \hat{N} + 2 \sum_{d=1}^{N-1} (N-d) \hat{C}(d) \qquad \text{(B.3.1)}
\end{aligned}$$

Here, the line average of the spin correlation operator $\hat{C}(d) = 4/(N-d) \sum_{i=1}^{N-d} \hat{S}^z_i \hat{S}^z_{i+d}$ has been introduced in the last step.

Even for completely uncorrelated spins in the chain, the correlations are thus non-zero and their value $C(d) = 4M^2/(N^2-N) - 1/(N-1)$ is necessarily constant with distance d. This effect only vanishes in the case of Poisson (shot-noise) magnetization fluctuations $4M^2 = N$,

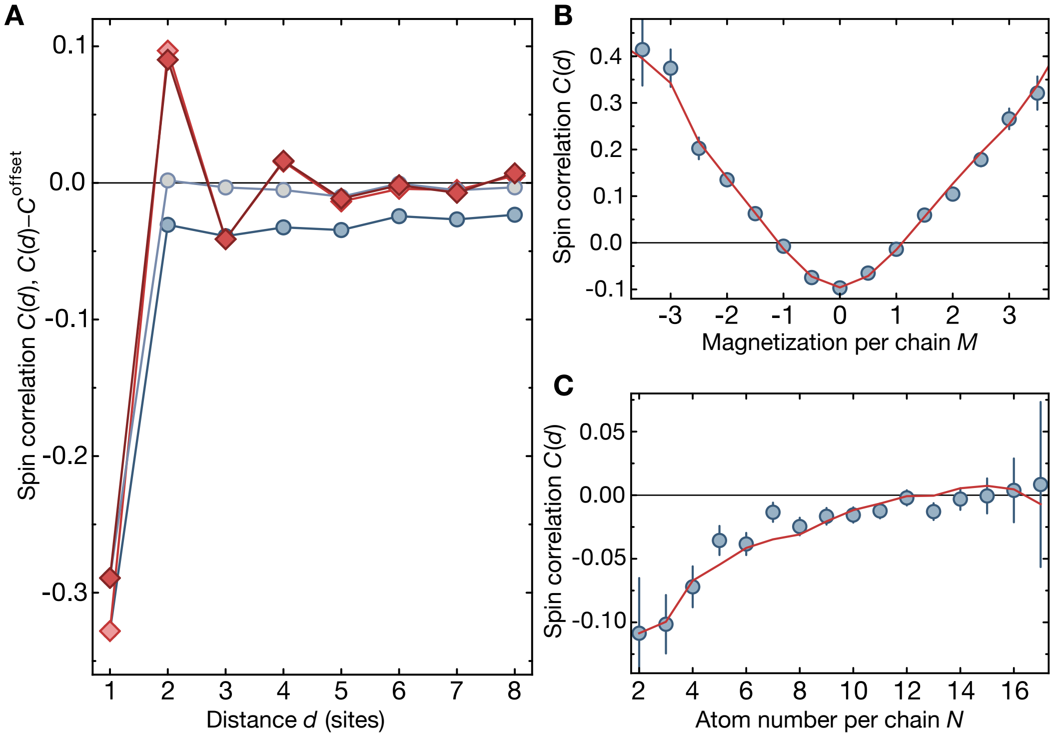

Figure B.1. Finite size offset analysis. ***(A)*** *Effect of offset subtraction. The spin correlation function* $C(d)$ *(dark blue) shows a clear offset that is expected in finite size systems with squeezed magnetization fluctuations. Subtraction of this offset leads to a correlation function which decays to zero (light blue). The spin string correlation function,* $C^{str}(d)$ *(red), is almost unaffected (light red) because of the changing signs* $(-1)^{N_h}$ *in the definition. Measured correlation values for large distances* $C(d>6)$ *(blue points), which we attribute fully to the offset, as a function of* ***(B)*** *chain magnetization* M *and* ***(C)*** *atom number* N*. The estimated offset corrections* $C^{offset}(M,N)$ *(red lines) from Eq. B.3.2 with* $A=-0.045$ *averaged over experimental atom number (B) or magnetization (C) distribution captures the experimental offset well.*

or in the infinite system size limit assuming non-extensive fluctuations. For sub-shot-noise fluctuations of the magnetization this offset is negative, in agreement with our experimental and numerical observations.

For systems with non-trivial correlations C^{corr} we assume a constant additive offset $C(d) = C^{\text{corr}}(d) + C^{\text{offset}}(N,M)$ due to this finite size effect. Solving Eq. B.3.1, reveals an offset $C^{\text{offset}}(N,M)$ depending on the correlations:

$$C^{\text{offset}}(N,M) = \frac{4M^2}{N^2-N} - \frac{1}{N-1} - \underbrace{\sum_{d=1}^{N-1} \frac{2(N-d)}{N(N-1)} C^{\text{corr}}(d)}_{A} \tag{B.3.2}$$

Experimentally, we find that our data is well described by $C^{\text{offset}}(N,M)$ with constant $A = -0.045(5)$ obtained from the correlations for $d > 6$, where we do not observe any staggered correlations in the conventional spin correlator (Fig. S2 B,C). In order to reveal the non-trivial staggered spin correlations, we measured the atom number and magnetization for each chain, calculated $C^{\text{offset}}(N,M)$ using the experimental value for A, and finally subtracted it from each single outcome contributing to $\langle \hat{S}_i^z \hat{S}_{i+d}^z \rangle$ before averaging spatially and over different experimental runs. This procedure was followed for all different versions of correlation functions, even though the string correlators are largely insensitive to the offset (Fig. S2A).

Appendix C

Timeline of the Experiment

2011

Spring	Christian Gross (group leader) joins the MPQ, planning of a new ^{6}Li quantum gas microscope
Summer	First test setup of the lattice with interference under an angle
September	Ahmed Omran (PhD student) and Timon Hilker (diploma student) join the team. Official start in the empty lab
October	Michael Lohse (diploma student) and Thomas Gantner (diploma student) join the team
November	Martin Boll (PhD student) joins the team
Fall	Laser setup for $^6\mathrm{Li}$, $^7\mathrm{Li}$ dual Zeeman Slower and MOT
	Winding coils for Zeeman slower, MOT, Magnetic trap, Feshbach field

2012

Winter	Setup of the interferometer for the physics superlattice
	Development of the jump-start electronics for the magnetic trap, Feshbach field
March	The last parts of our vacuum chamber arrive from CERN with 3 month delay
	Assembly of the vacuum chamber, baking, pumping: pressure great!
April	First MOTs of $^7\mathrm{Li}$ and $^6\mathrm{Li}$!
Summer	MOT optimization, implementation of our new experimental control system, setup magnetic trap
October	Timon Hilker becomes a PhD student
	Loading of the magnetic trap, first RF-evaporation
	Problems with clogged oven, several vacuum issues, re-baked oven section of vacuum chamber
November	Thomas Gantner leaves the team, Thomas Reimann (master student) joins the team
Fall	Two month search to close the Majorana hole of the magnetic trap with a green plug laser
	Stronger plug required (Verdi V18)

2013

Winter	Evaporation in the magnetic trap, loading of the dipole trap, but very unstable and 90 sec cycle time
February	Michael Lohse leaves the team, Konrad Viebahn (undergraduate) joins the team
Spring	Building of near resonant pinning lattice (3 tapered amplifiers)
	First test setup with a digital micromirror device (not implemented)
April	Decision to remove the magnetic trap and build a UV-MOT for $^6\mathrm{Li}$ instead
Summer	Setup of a UV laser from two infrared sources, bow-tie cavity
	Setup of a second MOT stage and a 100W dipole trap laser, rebuilding of the magnetic quadrupole trap into a second Feshbach field
September	Alexander Keesling (internship) joins the team
Fall	Cooling in the UV MOT, Evaporation in the new dipole trap
November	First degenerate Fermi gas!
	Thomas Reimann leaves the team
December	First optical transport to the science cell

2014

Winter	Setup and alignment of our z-lattice
March	Leo Stenzel (undergraduate) joins the team
Spring	Phase feedback for superlattice implemented
Spring + Summer	Raman sideband cooling in a near resonant pinning lattice (10-200 GHz detuning), but lifetimes never above 100 ms
June	Leo Stenzel, Alexander Keesling leave the team
August	Decision to remove the near resonant pinning lattice and to build a high power pinning lattice instead
September	Katharina Kleinlein (PhD student) joins the team
Fall	Setup of three 50 W pinning lattice axes
	Problems with breaking fiber amplifiers and thermal drifts
December	Guillaume Salomon (PostDoc) joins the team

2015

Winter	Raman sideband cooling in the new pinning lattice
	Preparation of a single plane with magnetic gradient and RF slicing
March	Michael Höse (undergraduate) joins the team
April	First image with single atoms!
Spring	Development of the image reconstruction algorithm
Summer	First alignment of imaging objective to optimize atom point-spread functions
August	Measurements Pauli blocking

September	First Mott insulator (2d), but troubles with fringes on the lattice
October	Paper on Pauli blocking submitted
Fall	Realignment of physics lattice and imaging objective
	Larger magnification of the imaging implemented
	Improved dimple trap allows to directly load a single plane, replaces unstable RF-slicing
December	Katharina Kleinlein leaves the team

2016

Winter	Improved phase stabilization of superlattice requires very stable temperatures and zero air flow
March	Implemented spin resolved imaging by local Stern-Gerlach splitting
April	Jayadev Vijayan (Master student) joins the team
	First antiferromagnetic spin correlations!
May	Paper on antiferromagnetic correlations submitted
September	Ahmed Omran leaves the team, Joannis Koepsell (PhD student) joins the team, Jayadev Vijayan becomes a PhD student
October	Zeeman window coated with lithium (OD 3). Window exchanged, pumping, pressure fine
Fall	Measurements of doped spin chains, spin-hole correlations
November	Martin Boll leaves the team

2017

February	Paper on hidden correlations submitted
April	Michael Höse starts his master's thesis
Mai	First spin correlations over system size
September	Analysis of charge fluctuations + compressibility
	Observation of incommensurate spin correlations in partly polarized chains

Bibliography

[1] I. Bloch, J. Dalibard, and W. Zwerger. *Many-body physics with ultracold gases*. Reviews of Modern Physics **80**, 885 (2008). (Cited on pages **1**, **12**, and **93**)

[2] R. P. Feynman. *Simulating physics with computers*. International Journal of Theoretical Physics **21**, 467 (1982). (Cited on pages **1** and **4**)

[3] J. G. Bednorz and K. A. Müller. *Possible high Tc superconductivity in the Ba-La-Cu-O system*. Zeitschrift für Physik B Condensed Matter **64**, 189 (1986). (Cited on pages **1**, **3**, and **104**)

[4] P. A. Lee, N. Nagaosa, and X.-G. Wen. *Doping a Mott insulator: Physics of high-temperature superconductivity*. Reviews of Modern Physics **78**, 17 (2006). (Cited on pages **1**, **3**, and **104**)

[5] T. Hänsch and A. Schawlow. *Cooling of gases by laser radiation*. Optics Communications **13**, 68 (1975). (Cited on page **1**)

[6] A. Ashkin. *Atomic-beam deflection by resonance-radiation pressure*. Physical Review Letters **25**, 1321 (1970). (Cited on page **1**)

[7] D. J. Wineland, R. Drullinger, and F. Walls. *Radiation-pressure cooling of bound resonant absorbers*. Physical Review Letters **40**, 1639 (1978). (Cited on page **1**)

[8] W. Neuhauser, M. Hohenstatt, P. Toschek, and H. Dehmelt. *Optical-sideband cooling of visible atom cloud confined in parabolic well*. Physical Review Letters **41**, 233 (1978). (Cited on pages **1** and **35**)

[9] W. D. Phillips and H. Metcalf. *Laser deceleration of an atomic beam*. Physical Review Letters **48**, 596 (1982). (Cited on pages **1** and **27**)

[10] E. Raab, M. Prentiss, A. Cable, S. Chu, and D. Pritchard. *Trapping of neutral sodium atoms with radiation pressure*. Physical Review Letters **59**, 2631 (1987). (Cited on page **1**)

[11] M. H. Anderson, J. R. Ensher, M. R. Matthews, C. E. Wieman, and E. A. Cornell. *Observation of bose-einstein condensation in a dilute atomic vapor.* Science **269**, 198 (1995). (Cited on page **1**)

[12] C. Bradley, C. A. Sackett, J. Tollett, and R. G. Hulet. *Evidence of Bose-Einstein condensation in an atomic gas with attractive interactions*. Physical Review Letters **75**, 1687 (1995). (Cited on page **1**)

[13] K. Davis, M. Mewes, M. Andrews, N. van Druten, D. Durfee, D. Kurn, and W. Ketterle. *Bose-Einstein condensation in a gas of sodium atoms*. Physical Review Letters **75**, 3969 (1995). (Cited on page **1**)

[14] B. DeMarco and D. S. Jin. *Onset of Fermi degeneracy in a trapped atomic gas*. Science **285**, 1703 (1999). (Cited on page **1**)

[15] F. Schreck, G. Ferrari, K. Corwin, J. Cubizolles, L. Khaykovich, M.-O. Mewes, and C. Salomon. *Sympathetic cooling of bosonic and fermionic lithium gases towards quantum degeneracy*. Physical Review A **64**, 011402 (2001). (Cited on page **1**)

[16] D. Jaksch, C. Bruder, J. I. Cirac, C. Gardiner, and P. Zoller. *Cold bosonic atoms in optical lattices*. Physical Review Letters **81**, 3108 (1998). (Cited on page **1**)

[17] M. Greiner, O. Mandel, T. Esslinger, T. W. Hänsch, and I. Bloch. *Quantum phase transition from a superfluid to a Mott insulator in a gas of ultracold atoms*. Nature **415**, 39 (2002). (Cited on page **1**)

[18] S. Inouye, M. R. Andrews, J. Stenger, H.-J. Miesner, D. M. Stamper-Kurn, and W. Ketterle. *Observation of Feshbach resonances in a Bose–Einstein condensate*. Nature **392**, 151 (1998). (Cited on page **1**)

[19] C. Chin, P. Julienne, and E. Tiesinga. *Feshbach resonances in ultracold gases*. Reviews of Modern Physics **82**, 1225 (2010). (Cited on pages **1** and **11**)

[20] I. Shvarchuck, C. Buggle, D. S. Petrov, K. Dieckmann, M. Zielonkowski, M. Kemmann, T. G. Tiecke, W. von Klitzing, G. V. Shlyapnikov, and J. T. M. Walraven. *Bose-Einstein condensation into nonequilibrium states studied by condensate focusing*. Physical Review Letters **89**, 270404 (2002). (Cited on page **2**)

[21] S. Tung, G. Lamporesi, D. Lobser, L. Xia, and E. A. Cornell. *Observation of the presuperfluid regime in a two-dimensional Bose gas*. Physical Review Letters **105**, 230408 (2010). (Cited on page **2**)

[22] Y.-i. Shin, C. H. Schunck, A. Schirotzek, and W. Ketterle. *Phase diagram of a two-component Fermi gas with resonant interactions*. Nature **451**, 689 (2008). (Cited on page **2**)

[23] S. Nascimbène, N. Navon, K. J. Jiang, F. Chevy, and C. Salomon. *Exploring the thermodynamics of a universal Fermi gas*. Nature **463**, 1057 (2010). (Cited on page **2**)

[24] M. J. H. Ku, A. T. Sommer, L. W. Cheuk, and M. W. Zwierlein. *Revealing the superfluid lambda transition in the universal thermodynamics of a unitary Fermi gas*. Science **335**, 563 (2012). (Cited on pages **2** and **82**)

[25] W. S. Bakr, J. I. Gillen, A. Peng, S. Fölling, and M. Greiner. *A quantum gas microscope for detecting single atoms in a Hubbard-regime optical lattice.* Nature **462**, 74 (2009). (Cited on pages **2**, **23**, **35**, **66**, and **129**)

[26] J. F. Sherson, C. Weitenberg, M. Endres, M. Cheneau, I. Bloch, and S. Kuhr. *Single-atom-resolved fluorescence imaging of an atomic Mott insulator.* Nature **467**, 68 (2010). (Cited on pages **2**, **23**, **35**, **66**, and **129**)

[27] M. Endres, M. Cheneau, T. Fukuhara, C. Weitenberg, P. Schauss, C. Gross, L. Mazza, M. C. Banuls, L. Pollet, I. Bloch, S. Kuhr, P. Schauß, C. Gross, L. Mazza, M. C. Bañuls, L. Pollet, I. Bloch, and S. Kuhr. *Observation of correlated particle-hole pairs and string order in low-dimensional Mott insulators*. Science **334**, 200 (2011). (Cited on pages **2**, **92**, **93**, **105**, **120**, and **136**)

[28] M. Cheneau, P. Barmettler, D. Poletti, M. Endres, P. Schauss, T. Fukuhara, C. Gross, I. Bloch, C. Kollath, S. Kuhr, P. Schauß, T. Fukuhara, C. Gross, I. Bloch, C. Kollath, and S. Kuhr. *Light-cone-like spreading of correlations in a quantum many-body system*. Nature **481**, 484 (2012). (Cited on page **2**)

[29] E. Haller, J. Hudson, A. Kelly, D. A. Cotta, B. Peaudecerf, G. D. Bruce, and S. Kuhr. *Single-atom imaging of fermions in a quantum-gas microscope*. Nature Physics **11**, 738 (2015). (Cited on pages **2**, **26**, **36**, **95**, and **129**)

[30] M. F. Parsons, F. Huber, A. Mazurenko, C. S. Chiu, W. Setiawan, K. Wooley-Brown, S. Blatt, and M. Greiner. *Site-resolved imaging of fermionic Li 6 in an optical lattice*. Physical Review Letters **114**, 213002 (2015). (Cited on pages **2**, **36**, **95**, and **129**)

[31] L. W. Cheuk, M. A. Nichols, M. Okan, T. Gersdorf, V. V. Ramasesh, W. S. Bakr, T. Lompe, and M. W. Zwierlein. *Quantum-gas microscope for fermionic atoms*. Physical Review Letters **114**, 193001 (2015). (Cited on pages **2**, **36**, **49**, **51**, **95**, and **129**)

[32] A. Omran, M. Boll, T. A. Hilker, K. Kleinlein, G. Salomon, I. Bloch, and C. Gross. *Microscopic observation of Pauli blocking in degenerate fermionic lattice gases*. Physical Review Letters **115**, 263001 (2015). (Cited on pages **2**, **23**, **36**, **77**, **83**, **95**, **104**, and **129**)

[33] A. Georges, W. Krauth, and M. J. Rozenberg. *Dynamical mean-field theory of strongly correlated fermion systems and the limit of infinite dimensions*. Reviews of Modern Physics **68**, 13 (1996). (Cited on page **3**)

[34] N. F. Mott. *Metal-insulator transition*. Reviews of Modern Physics **40**, 677 (1968). (Cited on page **3**)

[35] K. Andres, J. E. Graebner, and H. R. Ott. *4f-Virtual-Bound-State Formation in Ce*Al_3 *at Low Temperatures*. Physical Review Letters **35**, 1779–1782 (1975). (Cited on page **3**)

[36] F. Steglich, J. Aarts, C. D. Bredl, W. Lieke, D. Meschede, W. Franz, and H. Schäfer. *Superconductivity in the Presence of Strong Pauli Paramagnetism:* $\mathrm{CeCu_2Si_2}$. Physical Review Letters **43**, 1892–1896 (1979). (Cited on page **3**)

[37] S. Yamada, T. Imamura, and M. Machida. *16.447 TFlops and 159-Billion-dimensional exact-diagonalization for trapped Fermion-Hubbard model on the earth simulator*. In *Proceedings of Supercomputing 2005* (2005). (Cited on page **3**)

[38] E. Loh, J. Gubernatis, R. Scalettar, S. White, D. J. Scalapino, and R. Sugar. *Sign problem in the numerical simulation of many-electron systems*. Physical Review B **41**, 9301 (1990). (Cited on page **3**)

[39] F.-C. C. Zhang, C. Gros, T. M. Rice, and H. Shiba. *A renormalised Hamiltonian approach to a resonant valence bond wavefunction*. Superconductor Science and Technology **1**, 36 (1988). (Cited on pages **3** and **104**)

[40] G. Kotliar and J. Liu. *Superexchange mechanism and d-wave superconductivity*. Physical Review B **38**, 5142 (1988). (Cited on page **3**)

[41] D. A. Wollman, D. J. Van Harlingen, W. C. Lee, D. M. Ginsberg, and A. J. Leggett. *Experimental determination of the superconducting pairing state in YBCO from the phase coherence of YBCO-Pb dc SQUIDs*. Physical Review Letters **71**, 2134 (1993). (Cited on page **3**)

[42] C. C. Tsuei and J. R. Kirtley. *Pairing symmetry in cuprate superconductors*. Reviews of Modern Physics **72**, 969 (2000). (Cited on page **3**)

[43] P. W. Anderson. *The resonating valence bond state in* La_2CuO_4 *and superconductivity*. Science **235**, 1196 (1987). (Cited on page **3**)

[44] S. A. Kivelson, I. P. Bindloss, E. Fradkin, V. Oganesyan, J. M. Tranquada, A. Kapitulnik, and C. Howald. *How to detect fluctuating stripes in the high-temperature superconductors*. Reviews of Modern Physics **75**, 1201 (2003). (Cited on page **3**)

[45] E. H. da Silva Neto, P. Aynajian, A. Frano, R. Comin, E. Schierle, E. Weschke, A. Gyenis, J. Wen, J. Schneeloch, Z. Xu, S. Ono, G. Gu, M. Le Tacon, and A. Yazdani. *Ubiquitous interplay between charge ordering and high-temperature superconductivity in cuprates*. Science **343**, 393 (2014). (Cited on page **3**)

[46] H. Bertrand and A. Sevrin, editors. *Quantum theory of condensed matter*. World Scientific Publishing Co. (2010). (Cited on page **3**)

[47] T. Timusk and B. Statt. *The pseudogap in high-temperature superconductors: an experimental survey*. Reports on Progress in Physics **62**, 61 (1999). (Cited on page **3**)

[48] H. Ebrahimnejad, G. A. Sawatzky, and M. Berciu. *The dynamics of a doped hole in a cuprate is not controlled by spin fluctuations*. Nature Physics **10**, 951 (2014). (Cited on page **3**)

[49] E. Gull, O. Parcollet, and A. J. Millis. *Superconductivity and the pseudogap in the two-dimensional Hubbard model*. Physical Review Letters **110**, 216405 (2013). (Cited on page **3**)

[50] H.-C. Jiang, M. S. Block, R. V. Mishmash, J. R. Garrison, D. N. Sheng, O. I. Motrunich, and M. P. A. Fisher. *Non-Fermi-liquid d-wave metal phase of strongly interacting electrons*. Nature **493**, 39 (2013). (Cited on page **3**)

[51] D. J. Scalapino, E. Loh, and J. E. Hirsch. *d-wave pairing near a spin-density-wave instability*. Physical Review B **34**, 8190 (1986). (Cited on page **4**)

[52] J. Schrieffer. *Theory of superconductivity*. Advanced Book Program Series. Avalon Publishing (1983). (Cited on pages **4** and **15**)

[53] J. Zaanen and O. Gunnarsson. *Charged magnetic domain lines and the magnetism of high-Tc oxides*. Physical Review B **40**, 7391 (1989). (Cited on page **4**)

[54] T. Giamarchi. *Quantum physics in one dimension*. International Series of Monographs on Physics. Clarendon Press (2003). (Cited on pages **4**, **5**, **15**, **17**, **95**, **120**, **133**, **136**, **138**, and **140**)

[55] J. Hubbard. *Electron correlations in narrow energy bands*. Proceedings of the Royal Society A: Mathematical, Physical and Engineering Sciences **276**, 238 (1963). (Cited on pages **4** and **12**)

[56] U. Schneider, L. Hackermüller, J. P. Ronzheimer, S. Will, S. Braun, T. Best, I. Bloch, E. Demler, S. Mandt, D. Rasch, and A. Rosch. *Fermionic transport and out-of-equilibrium dynamics in a homogeneous Hubbard model with ultracold atoms*. Nature Physics **8**, 213 (2012). (Cited on page **4**)

[57] R. Jördens, N. Strohmaier, K. J. Günter, H. Moritz, and T. Esslinger. *A Mott insulator of fermionic atoms in an optical lattice.* Nature **455**, 204 (2008). (Cited on pages **4** and **82**)

[58] U. Schneider, L. Hackermüller, S. Will, T. Best, I. Bloch, T. A. Costi, R. W. Helmes, D. Rasch, and A. Rosch. *Metallic and insulating phases of repulsively interacting fermions in a 3D optical lattice.* Science **322**, 1520 (2008). (Cited on pages **4** and **82**)

[59] R. Staudt, M. Dzierzawa, and A. Muramatsu. *Phase diagram of the three-dimensional Hubbard model at half filling*. The European Physical Journal B **17**, 411 (2000). (Cited on pages **4** and **14**)

[60] E. V. Gorelik, D. Rost, T. Paiva, R. Scalettar, A. Klümper, and N. Blümer. *Universal probes for antiferromagnetic correlations and entropy in cold fermions on optical lattices*. Physical Review A **85**, 061602 (2012). (Cited on pages **4**, **5**, **95**, **96**, and **98**)

[61] F. Werner, O. Parcollet, A. Georges, and S. Hassan. *Interaction-induced adiabatic cooling and antiferromagnetism of cold fermions in optical lattices*. Physical Review Letters **95**, 056401 (2005). (Cited on pages **5**, **14**, and **99**)

[62] B. Gadway, D. Pertot, J. Reeves, and D. Schneble. *Probing an ultracold-atom crystal with matter waves*. Nature Physics **8**, 544 (2012). (Cited on page **5**)

[63] D. C. Mckay and B. DeMarco. *Cooling in strongly correlated optical lattices: prospects and challenges*. Reports on Progress in Physics **74**, 054401 (2011). (Cited on page **5**)

[64] J.-S. J.-S. Bernier, C. Kollath, A. Georges, L. De Leo, F. Gerbier, C. Salomon, and M. Köhl. *Cooling fermionic atoms in optical lattices by shaping the confinement*. Physical Review A **79**, 061601 (2009). (Cited on page **5**)

[65] M. Lubasch, V. Murg, U. Schneider, J. I. Cirac, and M.-C. Bañuls. *Adiabatic preparation of a Heisenberg antiferromagnet using an optical superlattice*. Physical Review Letters **107**, 165301 (2011). (Cited on pages **5**, **83**, and **129**)

[66] C. J. M. Mathy, D. A. Huse, and R. G. Hulet. *Enlarging and cooling the Néel state in an optical lattice*. Physical Review A **86**, 023606 (2012). (Cited on page **5**)

[67] D. Greif, T. Uehlinger, G. Jotzu, L. Tarruell, and T. Esslinger. *Short-range quantum magnetism of ultracold fermions in an optical lattice.* Science **340**, 1307 (2013). (Cited on pages **5** and **95**)

[68] R. A. Hart, P. M. Duarte, T.-L. Yang, X. Liu, T. Paiva, E. Khatami, R. T. Scalettar, N. Trivedi, D. A. Huse, and R. G. Hulet. *Observation of antiferromagnetic correlations in the Hubbard model with ultracold atoms*. Nature **519**, 1 (2015). (Cited on pages **5** and **95**)

[69] J. Simon, W. S. Bakr, R. Ma, M. E. Tai, P. M. Preiss, and M. Greiner. *Quantum simulation of antiferromagnetic spin chains in an optical lattice.* Nature **472**, 307 (2011). (Cited on page **5**)

[70] J. Struck, C. Ölschläger, R. Le Targat, P. Soltan-Panahi, A. Eckardt, M. Lewenstein, P. Windpassinger, and K. Sengstock. *Quantum simulation of frustrated classical magnetism in triangular optical lattices.* Science **333**, 996 (2011). (Cited on page **5**)

[71] M. Boll, T. A. Hilker, G. Salomon, A. Omran, J. Nespolo, L. Pollet, I. Bloch, and C. Gross. *Spin- and density-resolved microscopy of antiferromagnetic correlations in Fermi-Hubbard chains*. Science **353**, 1257 (2016). (Cited on pages **5**, **17**, **77**, **95**, **96**, **104**, **108**, and **127**)

[72] M. F. Parsons, A. Mazurenko, C. S. Chiu, G. Ji, D. Greif, and M. Greiner. *Site-resolved measurement of the spin-correlation function in the Fermi-Hubbard model*. Science **353**, 1253 (2016). (Cited on pages **5** and **95**)

[73] L. W. Cheuk, M. A. Nichols, K. R. Lawrence, M. Okan, H. Zhang, E. Khatami, N. Trivedi, T. Paiva, M. Rigol, and M. W. Zwierlein. *Observation of spatial charge and spin correlations in the 2D Fermi-Hubbard model*. Science **353**, 1260 (2016). (Cited on pages **5** and **95**)

[74] P. T. Brown, D. Mitra, E. Guardado-Sanchez, P. Schauß, S. S. Kondov, E. Khatami, T. Paiva, N. Trivedi, D. A. Huse, and W. S. Bakr. *Spin-imbalance in a 2D Fermi-Hubbard system*. Science **357**, 1385 (2017). (Cited on pages **5**, **36**, **95**, and **129**)

[75] A. Mazurenko, C. S. Chiu, G. Ji, M. F. Parsons, M. Kanász-Nagy, R. Schmidt, F. Grusdt, E. Demler, D. Greif, and M. Greiner. *A cold-atom Fermi–Hubbard antiferromagnet*. Nature **545**, 462 (2017). (Cited on pages **5**, **95**, **102**, **128**, and **129**)

[76] D. Mitra, P. T. Brown, E. Guardado-Sanchez, S. S. Kondov, T. Devakul, D. A. Huse, P. Schauss, and W. S. Bakr. *Quantum gas microscopy of an attractive Fermi-Hubbard system*. ArXiv:1705.02039 (2017). (Cited on page **5**)

[77] C. Kim, A. Y. Matsuura, Z.-X. Shen, N. Motoyama, H. Eisaki, S. Uchida, T. Tohyama, and S. Maekawa. *Observation of spin-charge separation in one-dimensional $SrCuO_2$*. Physical Review Letters **77**, 4054 (1996). (Cited on pages **5** and **105**)

[78] P. Segovia, D. Purdie, M. Hengsberger, and Y. Baer. *Observation of spin and charge collective modes in one-dimensional metallic chains*. Nature **402**, 504 (1999). (Cited on pages **5** and **105**)

[79] B. J. Kim, H. Koh, E. Rotenberg, S.-J. Oh, H. Eisaki, N. Motoyama, S. Uchida, T. Tohyama, S. Maekawa, Z.-X. Shen, and C. Kim. *Distinct spinon and holon dispersions in photoemission spectral functions from one-dimensional SrCuO*$_2$. Nature Physics **2**, 397 (2006). (Cited on pages **5** and **105**)

[80] O. M. Auslaender, H. Steinberg, A. Yacoby, Y. Tserkovnyak, B. I. Halperin, K. W. Baldwin, L. N. Pfeiffer, and K. W. West. *Spin-charge separation and localization in one-dimension*. Science **308**, 88 (2005). (Cited on pages **5** and **105**)

[81] Y. Jompol, C. J. B. Ford, J. P. Griffiths, I. Farrer, G. a. C. Jones, D. Anderson, D. A. Ritchie, T. W. Silk, and A. J. Schofield. *Probing spin-charge separation in a Tomonaga-Luttinger liquid*. Science **325**, 597 (2009). (Cited on pages **5** and **105**)

[82] T. A. Hilker, G. Salomon, F. Grusdt, A. Omran, M. Boll, E. Demler, I. Bloch, and C. Gross. *Revealing hidden antiferromagnetic correlations in doped Hubbard chains via string correlators*. Science **357**, 484 (2017). (Cited on pages **5**, **103**, **112**, **122**, and **127**)

[83] H. J. Metcalf and P. van der Straten. *Laser cooling and trapping*. Springer, New York (1999). (Cited on page **9**)

[84] R. Grimm, M. Weidemüller, and Y. B. Ovchinnikov. *Optical dipole draps for neutral atoms*. Advances in Atomic, Molecular, and Optical Physics **42**, 95 (2000). (Cited on pages **9** and **52**)

[85] N. Ashcroft and N. Mermin. *Solid state physics*. Saunders College, Philadelphia (1976). (Cited on pages **10** and **67**)

[86] J. C. Slater. *A soluble problem in energy bands*. Physical Review **87**, 807 (1952). (Cited on page **10**)

[87] M. F. Parsons. *Probing the Hubbard model with single-site resolution*. PhD thesis, Harvard (2016). (Cited on page **11**)

[88] C. Pethik and H. Smith. *Bose-Einstein Condensation in dilute gases*. Cambridge University Press, Cambridge, 2nd edition (2008). (Cited on page **11**)

[89] A. Omran. *A microscope for Fermi gases*. PhD thesis, Ludwig-Maximilians-Universität München (2016). (Cited on pages **12**, **21**, **25**, **27**, **33**, **39**, **40**, **76**, and **83**)

[90] T. Esslinger. *Fermi-Hubbard physics with atoms in an optical lattice*. Annual Review of Condensed Matter Physics **1**, 129 (2010). (Cited on page **13**)

[91] L. D. Landau. *The theory of a Fermi liquid*. Soviet Physics Jetp **3**, 920 (1957). (Cited on pages **14**, **17**, and **133**)

[92] N. D. Mermin and H. Wagner. *Absence of ferromagnetism or antiferromagnetism in one- or two-dimensional isotropic Heisenberg models*. Physical Review Letters **17**, 1133 (1966). (Cited on pages **14** and **137**)

[93] A. Ho, M. Cazalilla, and T. Giamarchi. *Quantum simulation of the Hubbard model: The attractive route*. Physical Review A **79**, 033620 (2009). (Cited on pages **14**, **15**, and **136**)

[94] C. A. Regal, C. Ticknor, J. L. Bohn, and D. S. Jin. *Creation of ultracold molecules from a Fermi gas of atoms*. Nature **424**, 47 (2003). (Cited on page **15**)

[95] W. Zwerger, editor. *The BCS-BEC crossover and the unitary Fermi gas*, volume 836 of *Lecture Notes in Physics*. Springer Berlin Heidelberg, Berlin, Heidelberg (2012). (Cited on page **15**)

[96] A. Auerbach. *Interacting electrons and quantum magnetism*. Springer Science & Business Media (1994). (Cited on pages **15**, **105**, and **122**)

[97] S. Tomonaga. *Remarks on Bloch's method of sound waves applied to many-fermion problems*. Progress of Theoretical Physics **5**, 544 (1950). (Cited on pages **17**, **18**, and **133**)

[98] J. M. Luttinger. *An exactly soluble model of a many-fermion system*. Journal of Mathematical Physics **4**, 1154 (1963). (Cited on pages **17**, **18**, and **133**)

[99] D. C. Mattis and E. H. Lieb. *Exact solution of a many-fermion system and its associated boson field*. Journal of Mathematical Physics **6**, 304 (1965). (Cited on pages **17** and **133**)

[100] F. D. M. Haldane. *Effective harmonic-fluid approach to low-energy properties of one-dimensional quantum fluids*. Physical Review Letters **47**, 1840 (1981). (Cited on pages **17** and **133**)

[101] F. D. M. Haldane. *'Luttinger liquid theory' of one-dimensional quantum fluids. I. Properties of the Luttinger model and their extension to the general 1D interacting spinless Fermi gas*. Journal of Physics C: Solid State Physics **14**, 2585 (1981). (Cited on pages **17**, **18**, and **133**)

[102] A. Imambekov, T. L. Schmidt, and L. I. Glazman. *One-dimensional quantum liquids: Beyond the Luttinger liquid paradigm*. Reviews of Modern Physics **84**, 1253 (2012). (Cited on pages **18** and **123**)

[103] H. J. Schulz. *Correlation exponents and the metal-insulator transition in the one-dimensional Hubbard model*. Physical Review Letters **64**, 2831 (1990). (Cited on pages **18**, **19**, and **137**)

[104] M. Ogata and H. Shiba. *Bethe-ansatz wave function, momentum distribution, and spin correlation in the one-dimensional strongly correlated Hubbard model*. Physical Review B **41**, 2326 (1990). (Cited on pages **18**, **86**, **105**, **106**, and **121**)

[105] Y. Ren and P. W. Anderson. *Asymptotic correlation functions in the one-dimensional Hubbard model with applications to high-T_c superconductivity*. Physical Review B **48**, 16662 (1993). (Cited on pages **18**, **105**, and **106**)

[106] J. Zaanen, O. Y. Osman, H. V. Kruis, Z. Nussinov, and J. Tworzydlo. *The geometric order of stripes and Luttinger liquids*. Philosophical Magazine Part B **81**, 1485 (2001). (Cited on pages **18** and **105**)

[107] H. V. Kruis, I. P. McCulloch, Z. Nussinov, and J. Zaanen. *Geometry and the hidden order of Luttinger liquids: The universality of squeezed space*. Physical Review B - Condensed Matter and Materials Physics **70**, 1 (2004). (Cited on pages **18**, **19**, **105**, **118**, **119**, and **121**)

[108] T. A. Hilker. *Laser cooling of bosonic and fermionic lithium*. Diploma thesis, Technische Universität München (2012). (Cited on pages **21** and **27**)

[109] M. Lohse. *Large-spacing optical lattices for many-body physics with degenerate quantum gases*. Diploma thesis, Karlsruher Institut für Technologie (2012). (Cited on pages **21**, **28**, and **29**)

[110] T. Gantner. *Magnetic trapping of lithium-6 and lithium-7*. Diploma thesis, Technische Universität München (2012). (Cited on page **21**)

[111] T. Reimann. *An optical lattice for Raman sideband-cooling and fluorescence imaging of fermionic lithium*. Master's thesis, Ludwig-Maximilians-Universität München (2013). (Cited on page **21**)

[112] M. Boll. *Spin and density resolved microscopy of Hubbard chains*. PhD thesis, Ludwig-Maximilians-Universität München (2016). (Cited on pages **21**, **29**, **31**, and **96**)

[113] G. Audi, O. Bersillon, J. Blachot, and A. H. Wapstra. *The Nubase evaluation of nuclear and decay properties*. Nuclear Physics A **729**, 3 (2003). (Cited on page **24**)

[114] R. Weast, M. Astle, and W. Beyer, editors. *CRC handbook of chemistry and physics*. CRC Press, Boca Ratons, 64th edition (1983). (Cited on page **24**)

[115] E. Arimondo, M. Inguscio, and P. Violino. *Experimental determinations of the hyperfine structure in the alkali atoms*. Reviews of Modern Physics **49**, 31 (1977). (Cited on page **24**)

[116] C. Sansonetti, C. Simien, J. Gillaspy, J. Tan, S. Brewer, R. Brown, S. Wu, and J. Porto. *Absolute transition frequencies and quantum interference in a frequency comb based measurement of the 6,7 Li D lines*. Physical Review Letters **107**, 023001 (2011). (Cited on page **24**)

[117] W. I. McAlexander, E. R. I. Abraham, and R. G. Hulet. *Radiative lifetime of the 2 state of lithium*. Physical Review A **54**, R5–R8 (1996). (Cited on page **24**)

[118] T. Ault, K. Brozek, L. Fan, M. Folsom, J. Kim, and J. Zeismer. *Lithium isotope enrichment: Feasible domestic enrichment alternatives*. Report UCBTH-12-005, University of California Berkeley. (Cited on page **23**)

[119] P. Lett, R. Watts, C. Westbrook, W. D. Phillips, P. Gould, and H. Metcalf. *Observation of atoms laser cooled below the Doppler limit*. Physical Review Letters **61**, 169 (1988). (Cited on page **25**)

[120] J. Dalibard and C. Cohen-Tannoudji. *Laser cooling below the Doppler limit by polarization gradients: simple theoretical models*. Journal of the Optical Society of America B **6**, 2023 (1989). (Cited on pages **25** and **35**)

[121] A. T. Grier, I. Ferrier-Barbut, B. S. Rem, M. Delehaye, L. Khaykovich, F. Chevy, and C. Salomon. *Λ-enhanced sub-Doppler cooling of lithium atoms in D_1 gray molasses*. Physical Review A **87**, 063411 (2013). (Cited on page **25**)

[122] G. Morigi, J. Eschner, and C. H. Keitel. *Ground state laser cooling using electromagnetically induced transparency*. Physical Review Letters **85**, 4458 (2000). (Cited on pages **26** and **35**)

[123] G. J. A. Edge, R. Anderson, D. Jervis, D. C. Mckay, R. Day, S. Trotzky, and J. H. Thywissen. *Imaging and addressing of individual fermionic atoms in an optical lattice*. Physical Review A **92**, 063406 (2015). (Cited on pages **26**, **36**, **95**, and **129**)

[124] R. Wei and E. J. Mueller. *Magnetic-field dependence of Raman coupling in alkali-metal atoms*. Physical Review A **87**, 042514 (2013). (Cited on pages **26** and **38**)

[125] C. Weitenberg, M. Endres, J. F. Sherson, M. Cheneau, P. Schauß, T. Fukuhara, I. Bloch, and S. Kuhr. *Single-spin addressing in an atomic Mott insulator*. Nature **471**, 319 (2011). (Cited on pages **26** and **129**)

[126] E. L. Hazlett, Y. Zhang, R. W. Stites, and K. M. O'Hara. *Realization of a resonant Fermi gas with a large effective range*. Physical Review Letters **108**, 45304 (2012). (Cited on page **26**)

[127] G. Zürn, T. Lompe, A. N. Wenz, S. Jochim, P. Julienne, and J. M. Hutson. *Precise characterization of Li 6 Feshbach resonances using trap-sideband-resolved RF spectroscopy of weakly bound molecules*. Physical Review Letters **110**, 135301 (2013). (Cited on pages **26** and **141**)

[128] P. M. Duarte, R. A. Hart, J. M. Hitchcock, T. a. Corcovilos, T.-L. L. Yang, a. Reed, and R. G. Hulet. *All-optical production of a lithium quantum gas using narrow-line laser cooling*. Physical Review A **84**, 061406 (2011). (Cited on page **27**)

[129] W. S. Bakr, A. Peng, M. E. Tai, R. Ma, J. Simon, J. I. Gillen, S. Folling, L. Pollet, and M. Greiner. *Probing the superfluid-to-Mott insulator transition at the single-atom level*. Science **329**, 547 (2010). (Cited on pages **29** and **128**)

[130] C. Regal. *Interfering and entangling single neutral atoms*. Conference talk, Atomic Phyics Gordon Reseach Conference (2017). (Cited on page **31**)

[131] M. Miranda, R. Inoue, N. Tambo, and M. Kozuma. *Noncooled site-resolved imaging of a Mott insulator*. ArXiv:1704.07060 (2017). (Cited on pages **35** and **49**)

[132] R. Yamamoto, J. Kobayashi, K. Kato, T. Kuno, Y. Sakura, and Y. Takahashi. *Site-resolved imaging of single atoms with a Faraday quantum gas microscope*. Physical Review A **96**, 033610 (2017). (Cited on page **35**)

[133] F. Diedrich, J. C. Bergquist, W. M. Itano, and D. J. Wineland. *Laser cooling to the zero-point energy of motion*. Physical Review Letters **62**, 403 (1989). (Cited on page **35**)

[134] J. D. Teufel, T. Donner, D. Li, J. W. Harlow, M. S. Allman, K. Cicak, A. J. Sirois, J. D. Whittaker, K. W. Lehnert, and R. W. Simmonds. *Sideband cooling of micromechanical motion to the quantum ground state*. Nature **475**, 359 (2011). (Cited on page **35**)

[135] M. Aspelmeyer, T. J. Kippenberg, and F. Marquardt. *Cavity optomechanics*. Reviews of Modern Physics **86**, 1391 (2014). (Cited on page **35**)

[136] M. Takamoto, F.-L. Hong, R. Higashi, and H. Katori. *An optical lattice clock*. Nature **435**, 321 (2005). (Cited on page **35**)

[137] M. M. Boyd, T. Zelevinsky, A. D. Ludlow, S. M. Foreman, S. Blatt, T. Ido, and J. Ye. *Optical atomic coherence at the 1-second time scale*. Science **314**, 1430 (2006). (Cited on page **35**)

[138] Y. Castin, J. I. Cirac, and M. Lewenstein. *Reabsorption of light by trapped atoms*. Physical Review Letters **80**, 5305 (1998). (Cited on page **35**)

[139] C. Monroe, D. M. Meekhof, B. E. King, S. R. Jefferts, W. M. Itano, D. J. Wineland, and P. Gould. *Resolved-sideband raman cooling of a bound atom to the 3D zero-point energy*. Physical Review Letters **75**, 4011 (1995). (Cited on page **35**)

[140] H. Perrin, A. Kuhn, I. Bouchoule, and C. Salomon. *Sideband cooling of neutral atoms in a far-detuned optical lattice*. Europhysics Letters **42**, 395 (1998). (Cited on page **35**)

[141] S. E. Hamann, D. L. Haycock, G. Klose, P. H. Pax, I. H. Deutsch, and P. S. Jessen. *Resolved-sideband raman cooling to the ground state of an optical lattice*. Physical Review Letters **80**, 4149 (1998). (Cited on page **35**)

[142] V. Vuletic, C. Chin, A. J. Kerman, and S. Chu. *Degenerate raman sideband cooling of trapped cesium atoms at very high atomic densities*. Physical Review Letters **81**, 5768 (1998). (Cited on page **35**)

[143] B. J. Lester, A. M. Kaufman, and C. A. Regal. *Raman cooling imaging: Detecting single atoms near their ground state of motion*. Physical Review A **90**, 011804 (2014). (Cited on page **36**)

[144] Y. S. Patil, S. Chakram, L. M. Aycock, and M. Vengalattore. *Nondestructive imaging of an ultracold lattice gas*. Physical Review A **90**, 033422 (2014). (Cited on page **36**)

[145] Y. Yu, N. R. Hutzler, J. T. Zhang, L. R. Liu, T. Rosenband, and K.-K. Ni. *Motional ground state cooling outside the Lamb-Dicke regime*. ArXiv:1708.03296 (2017). (Cited on page **36**)

[146] I. H. Deutsch and P. S. Jessen. *Quantum-state control in optical lattices*. Physical Review A **57**, 1972 (1998). (Cited on page **37**)

[147] A. J. Kerman. *Raman sideband cooling and cold atomic collisions in optical lattices*. PhD thesis, Stanford (2002). (Cited on page **38**)

[148] M. Fleischhauer, A. Imamoglu, and J. Marangos. *Electromagnetically induced transparency: Optics in coherent media*. Reviews of Modern Physics **77**, 633 (2005). (Cited on pages **39** and **43**)

[149] D. J. Wineland and W. M. Itano. *Laser cooling of atoms*. Physical Review A **20**, 1521 (1979). (Cited on page **41**)

[150] M. Abramowitz. *Handbook of mathematical functions, with formulas, graphs, and mathematical tables,*. Dover Publications, Incorporated (1974). (Cited on page **41**)

[151] Y. Wan, F. Gebert, F. Wolf, and P. O. Schmidt. *Efficient sympathetic motional-ground-state cooling of a molecular ion*. Physical Review A **91**, 043425 (2015). (Cited on page **41**)

[152] C. Cohen-Tannoudji, J. Dupont-Roc, and G. Grynberg. *Atom-photon interactions*. Wiley Science Paperback Series. Wiley (1998). (Cited on page **42**)

[153] D. Leibfried, R. Blatt, C. Monroe, and D. Wineland. *Quantum dynamics of single trapped ions*. Reviews of Modern Physics **75**, 281 (2003). (Cited on page **45**)

[154] Y. S. Patil, S. Chakram, and M. Vengalattore. *Measurement-induced localization of an ultracold lattice gas*. Physical Review Letters **115**, 140402 (2015). (Cited on page **45**)

[155] A. Altland and B. Simons. *Condensed matter field theory*. Cambridge University Press (2010). (Cited on pages **49** and **134**)

[156] M. Miranda, R. Inoue, Y. Okuyama, A. Nakamoto, and M. Kozuma. *Site-resolved imaging of ytterbium atoms in a two-dimensional optical lattice*. Physical Review A **91**, 1 (2015). (Cited on pages **49** and **129**)

[157] M. S. Safronova, U. I. Safronova, and C. W. Clark. *Magic wavelengths for optical cooling and trapping of lithium*. Physical Review A **86**, 042505 (2012). (Cited on page **50**)

[158] E. Brion, L. H. Pedersen, and K. Mølmer. *Adiabatic elimination in a lambda system*. Journal of Physics A: Mathematical and Theoretical **40**, 1033 (2007). (Cited on page **57**)

[159] J. S. Chen, S. M. Brewer, C. W. Chou, D. J. Wineland, D. R. Leibrandt, and D. B. Hume. *Sympathetic ground state cooling and time-dilation shifts in an* $^{27}Al^{+}$ *optical clock*. Physical Review Letters **118**, 1 (2017). (Cited on page **62**)

[160] M. Höse. *Image-analysis of single lithium-6 fermions in an optical lattice*. Bachelor's thesis, Ludwig-Maximilians-Universität München (2015). (Cited on page **65**)

[161] S. van der Walt, J. L. Schönberger, J. Nunez-Iglesias, F. Boulogne, J. D. Warner, N. Yager, E. Gouillart, T. Yu, and the scikit-image contributors. *scikit-image: image processing in Python*. PeerJ **2**, e453 (2014). (Cited on page **70**)

[162] L. B. Lucy. *An iterative technique for the rectification of observed distributions*. The Astronomical Journal **79**, 745 (1974). (Cited on pages **71** and **73**)

[163] W. H. Richardson. *Bayesian-based iterative method of image restoration*. Journal of the Optical Society of America **62**, 55 (1972). (Cited on page **71**)

[164] E. Shaked and O. Michailovich. *Regularized Richardson-Lucy algorithm for sparse reconstruction of Poissonian images*. ArXiv:1004.1215 (2010). (Cited on page **73**)

[165] V. Kempen and V. Vliet. *The influence of the regularization parameter and the first estimate on the performance of Tikhonov regularized non-linear image restoration algorithms*. Journal of Microscopy **198**, 63 (2000). (Cited on page **73**)

[166] D. S. C. Biggs and M. Andrews. *Acceleration of iterative image restoration algorithms*. Applied Optics **36**, 1766 (1997). (Cited on page **73**)

[167] Y. Ashida and M. Ueda. *Diffraction-unlimited position measurement of ultracold atoms in an optical lattice*. Physical Review Letters **115**, 095301 (2015). (Cited on pages **74** and **76**)

[168] T. Schweigler, V. Kasper, S. Erne, I. Mazets, B. Rauer, F. Cataldini, T. Langen, T. Gasenzer, J. Berges, and J. Schmiedmayer. *Experimental characterization of a quantum many-body system via higher-order correlations*. Nature **545**, 323 (2017). (Cited on page **78**)

[169] A. Madsen, A. Fluerasu, and B. Ruta. *Structural dynamics of materials probed by X-Ray photon correlation spectroscopy*, page 1. Springer International Publishing, Cham (2014). (Cited on page **78**)

[170] L. W. Cheuk, M. A. Nichols, K. R. Lawrence, M. Okan, H. Zhang, and M. W. Zwierlein. *Observation of 2D fermionic Mott insulators of* ^{40}K *with single-site resolution*. Physical Review Letters **116**, 235301 (2016). (Cited on pages **78**, **82**, and **83**)

[171] F. Schwabl. *Advanced quantum mechanics*. Advanced texts in physics. Springer (2005). (Cited on page **79**)

[172] R. Jördens, L. Tarruell, D. Greif, T. Uehlinger, N. Strohmaier, H. Moritz, T. Esslinger, L. De Leo, C. Kollath, A. Georges, V. Scarola, L. Pollet, E. Burovski, E. Kozik, M. Troyer, and R. Joerdens. *Quantitative determination of temperature in the approach to magnetic order of ultracold fermions in an optical lattice*. Physical Review Letters **104**, 180401 (2010). (Cited on pages **82** and **99**)

[173] S. Taie, R. Yamazaki, S. Sugawa, and Y. Takahashi. *An SU(6) Mott insulator of an atomic Fermi gas realized by large-spin Pomeranchuk cooling*. Nature Physics **8**, 825 (2012). (Cited on page **82**)

[174] P. M. Duarte, R. A. Hart, T.-L. Yang, X. Liu, T. Paiva, E. Khatami, R. T. Scalettar, N. Trivedi, and R. G. Hulet. *Compressibility of a fermionic Mott insulator of ultracold atoms*. Physical Review Letters **114**, 70403 (2015). (Cited on pages **82** and **83**)

[175] E. Cocchi, L. A. Miller, J. H. Drewes, M. Koschorreck, D. Pertot, F. Brennecke, and M. Köhl. *Equation of state of the two-dimensional Hubbard model*. Physical Review Letters **116**, 175301 (2016). (Cited on pages **82** and **83**)

[176] D. Greif, M. F. Parsons, A. Mazurenko, C. S. Chiu, S. Blatt, F. Huber, G. Ji, and M. Greiner. *Site-resolved imaging of a fermionic Mott insulator*. Science **351**, 953 (2016). (Cited on pages **82** and **83**)

[177] R. Desbuquois, T. Yefsah, L. Chomaz, C. Weitenberg, L. Corman, S. Nascimbène, and J. Dalibard. *Determination of scale-invariant equations of state without fitting parameters: Application to the two-dimensional Bose gas across the Berezinskii-Kosterlitz-Thouless transition*. Physical Review Letters **113**, 020404 (2014). (Cited on page **82**)

[178] C. Hofrichter, L. Riegger, F. Scazza, M. Höfer, D. R. Fernandes, I. Bloch, and S. Fölling. *Direct probing of the Mott crossover in the SU(N) Fermi-Hubbard model*. Physical Review X **6**, 021030 (2016). (Cited on page **82**)

[179] M. Girardeau. *Relationship between systems of impenetrable bosons and fermions in one dimension*. Journal of Mathematical Physics **1**, 516 (1960). (Cited on page **86**)

[180] G. Zürn, F. Serwane, T. Lompe, A. N. Wenz, M. G. Ries, J. E. Bohn, and S. Jochim. *Fermionization of two distinguishable fermions*. Physical Review Letters **108**, 075303 (2012). (Cited on page **86**)

[181] J. Oitmaa, C. Hamer, and W. Zheng. *Series expansion methods for strongly interacting lattice models*. Cambridge University Press (2006). (Cited on page **86**)

[182] E. Cocchi, L. A. Miller, J. H. Drewes, C. F. Chan, D. Pertot, F. Brennecke, and M. Köhl. *Measuring entropy and short-range correlations in the two-dimensional Hubbard model*. Physical Review X **7**, 031025 (2017). (Cited on page **87**)

[183] A. Einstein. *Über die von der molekularkinetischen Theorie der Wärme geforderte Bewegung von in ruhenden Flüssigkeiten suspendierten Teilchen*. Annalen der Physik **322**, 549 (1905). (Cited on page **88**)

[184] W. Sutherland. *LXXV. A dynamical theory of diffusion for non-electrolytes and the molecular mass of albumin*. Philosophical Magazine **9**, 781–785 (1905). (Cited on page **88**)

[185] M. von Smoluchowski. *Zur kinetischen Theorie der Brownschen Molekularbewegung und der Suspensionen*. Annalen der Physik **326**, 756 (1906). (Cited on page **88**)

[186] R. Kubo. *The fluctuation-dissipation theorem*. Reports on Progress in Physics **29**, 306 (1966). (Cited on page **88**)

[187] J. H. Drewes, E. Cocchi, L. A. Miller, C. F. Chan, D. Pertot, F. Brennecke, and M. Köhl. *Thermodynamics versus local density fluctuations in the metal-Mott-insulator crossover*. Physical Review Letters **117**, 1 (2016). (Cited on pages **88** and **92**)

[188] S. P. Rath and R. Schmidt. *Field-theoretical study of the Bose polaron*. Physical Review A **88**, 1 (2013). (Cited on page **93**)

[189] A. Montorsi and M. Roncaglia. *Nonlocal order parameters for the 1D Hubbard model*. Physical Review Letters **109**, 236404 (2012). (Cited on pages **93**, **120**, **136**, and **137**)

[190] Q. Zhou and T. L. Ho. *Universal thermometry for quantum simulation*. Physical Review Letters (2011). (Cited on page **94**)

[191] J. Sirker and A. Klümper. *Thermodynamics and crossover phenomena in the correlation lengths of the one-dimensional t - J model*. Physical Review B **66**, 245102 (2002). (Cited on page **95**)

[192] F. H. L. Essler, H. Frahm, F. Göhmann, A. Klümper, and V. E. Korepin. *The one-dimensional Hubbard model*. Cambridge University Press (2005). (Cited on page **95**)

[193] S. Trotzky, Y.-A. Chen, U. Schnorrberger, P. Cheinet, and I. Bloch. *Controlling and detecting spin correlations of ultracold atoms in optical lattices*. Physical Review Letters **105**, 265303 (2010). (Cited on page **95**)

[194] D. Greif, G. Jotzu, M. Messer, T. Esslinger, R. Desbuquois, and T. Esslinger. *Formation and dynamics of antiferromagnetic correlations in tunable optical lattices*. Physical Review Letters **115**, 260401 (2015). (Cited on page **95**)

[195] S. Murmann, A. Bergschneider, V. M. Klinkhamer, G. Zürn, T. Lompe, and S. Jochim. *Two Fermions in a double well: Exploring a fundamental building block of the Hubbard model*. Physical Review Letters **114**, 80402 (2014). (Cited on page **95**)

[196] B. Sciolla, A. Tokuno, S. Uchino, P. Barmettler, T. Giamarchi, and C. Kollath. *Competition of spin and charge excitations in the one-dimensional Hubbard model*. Physical Review A **88**, 1 (2013). (Cited on pages **95**, **96**, and **98**)

[197] S. Ciliberto. *Experiments in stochastic thermodynamics: Short history and perspectives*. Physical Review X **7**, 021051 (2017). (Cited on page **102**)

[198] C. Jarzynski. *Nonequilibrium equality for free energy differences*. Physical Review Letters **78**, 2690 (1997). (Cited on page **102**)

[199] G. E. Crooks. *Nonequilibrium measurements of free energy differences for microscopically reversible Markovian systems*. Journal of Statistical Physics **90**, 1481 (1998). (Cited on page **102**)

[200] C. Jarzynski. *Equalities and inequalities: Irreversibility and the second law of thermodynamics at the nanoscale*. Annual Review of Condensed Matter Physics **2**, 329 (2011). (Cited on page **102**)

[201] X. J. Zhou. *One-dimensional electronic structure and suppression of d-wave node state in* $(La_{1.28}Nd_{0.6}Sr_{0.12})CuO_4$. Science **286**, 268 (1999). (Cited on page **104**)

[202] B. Keimer, S. A. Kivelson, M. R. Norman, S. Uchida, and J. Zaanen. *From quantum matter to high-temperature superconductivity in copper oxides.* Nature **518**, 179 (2015). (Cited on page **104**)

[203] J. Zaanen. *Current ideas on the origin of stripes*. Journal of Physics and Chemistry of Solids **59**, 1769 (1998). (Cited on pages **104** and **113**)

[204] M. den Nijs and K. Rommelse. *Preroughening transitions in crystal surfaces and valence-bond phases in quantum spin chains*. Physical Review B **40**, 4709 (1989). (Cited on pages **105** and **117**)

[205] T. Kennedy and H. Tasaki. *Hidden* $Z_2 \times Z_2$ *symmetry breaking in Haldane-gap antiferromagnets*. Physical Review B **45**, 304 (1992). (Cited on page **105**)

[206] H. V. Kruis, I. P. McCulloch, Z. Nussinov, and J. Zaanen. *Geometry and topological order in the Luttinger liquid state*. Europhysics Letters **65**, 512 (2004). (Cited on page **105**)

[207] F. Haldane. *Continuum dynamics of the 1-D Heisenberg antiferromagnet: Identification with the O(3) nonlinear sigma model*. Physics Letters A **93**, 464 (1983). (Cited on pages **105** and **117**)

[208] F. D. M. Haldane. *Nonlinear field theory of large-spin Heisenberg antiferromagnets: Semiclassically quantized solitons of the one-dimensional easy-axis Néel state*. Physical Review Letters **50**, 1153 (1983). (Cited on pages **105** and **117**)

[209] I. Affleck, T. Kennedy, E. H. Lieb, and H. Tasaki. *Rigorous results on valence-bond ground states in antiferromagnets*. Physical Review Letters **59**, 799 (1987). (Cited on pages **105** and **117**)

[210] F. Woynarovich. *Excitations with complex wavenumbers in a Hubbard chain. II. States with several pairs of complex wavenumbers*. Journal of Physics C: Solid State Physics **15**, 97 (1982). (Cited on pages **106** and **121**)

[211] F. Serwane, G. Zurn, T. Lompe, T. B. Ottenstein, A. N. Wenz, and S. Jochim. *Deterministic preparation of a tunable few-fermion system*. Science **332**, 336 (2011). (Cited on page **107**)

[212] M. Rigol, A. Muramatsu, G. G. Batrouni, and R. T. Scalettar. *Local quantum criticality in confined fermions on optical lattices*. Physical Review Letters **91**, 130403 (2003). (Cited on page **107**)

[213] M. Endres. *Probing correlated quantum many-body systems at the single-particle level*. PhD thesis, Ludwig-Maximilians-Universität München (2014). (Cited on page **119**)

[214] A. Recati, P. O. Fedichev, W. Zwerger, and P. Zoller. *Spin-charge separation in ultracold quantum gases*. Physical Review Letters **90**, 020401 (2003). (Cited on page **125**)

[215] C. Kollath, U. Schollwöck, and W. Zwerger. *Spin-charge separation in cold Fermi gases: A real time analysis*. Physical Review Letters **95**, 176401 (2005). (Cited on pages **125** and **128**)

[216] M. Knap, A. Kantian, T. Giamarchi, I. Bloch, M. D. Lukin, and E. Demler. *Probing real-space and time-resolved correlation functions with many-body Ramsey interferometry*. Physical Review Letters **111**, 147205 (2013). (Cited on pages **125** and **129**)

[217] E. W. Carlson, S. A. Kivelson, D. Orgad, and V. J. Emery. *Concepts in high temperature superconductivity*, page 275. Springer, Berlin, Heidelberg (2004). (Cited on page **125**)

[218] Y. Zhang, E. Demler, and S. Sachdev. *Competing orders in a magnetic field: Spin and charge order in the cuprate superconductors*. Physical Review B **66**, 094501 (2002). (Cited on page **125**)

[219] T. Senthil, A. Vishwanath, L. Balents, S. Sachdev, and M. P. A. Fisher. *Deconfined quantum critical points*. Science **303**, 1490 (2004). (Cited on page **125**)

[220] X.-G. Wen. *Quantum field theory of many-body systems*. Oxford University Press (2004). (Cited on page **125**)

[221] J.-y. Choi, S. Hild, J. Zeiher, P. Schauss, A. Rubio-Abadal, T. Yefsah, V. Khemani, D. A. Huse, I. Bloch, and C. Gross. *Exploring the many-body localization transition in two dimensions*. Science **352**, 1547 (2016). (Cited on page **128**)

[222] K. Kobayashi, M. Okumura, Y. Ota, S. Yamada, and M. Machida. *Nontrivial Haldane phase of an atomic two-component Fermi gas trapped in a 1D optical lattice*. Physical Review Letters **109**, 235302 (2012). (Cited on page **128**)

[223] V. Bois, S. Capponi, P. Lecheminant, M. Moliner, and K. Totsuka. *Phase diagrams of one-dimensional half-filled two-orbital SU(N) cold fermion systems*. Physical Review B **91**, 075121 (2015). (Cited on page **128**)

[224] Y. Nagaoka. *Ferromagnetism in a narrow, almost half-filled s band*. Physical Review **147**, 392 (1966). (Cited on page **129**)

[225] J. von Stecher, E. Demler, M. D. Lukin, and A. M. Rey. *Probing interaction-induced ferromagnetism in optical superlattices*. New Journal of Physics **12**, 055009 (2010). (Cited on page **129**)

[226] E. C. Stoner. *Ferromagnetism*. Reports on Progress in Physics **11**, 43 (1947). (Cited on page **129**)

[227] G.-B. Jo, Y.-R. Lee, J.-H. Choi, C. A. Christensen, T. H. Kim, J. H. Thywissen, D. E. Pritchard, and W. Ketterle. *Itinerant ferromagnetism in a Fermi gas of ultracold atoms*. Science **325**, 1521 (2009). (Cited on page **129**)

[228] G. Valtolina, F. Scazza, A. Amico, A. Burchianti, A. Recati, T. Enss, M. Inguscio, M. Zaccanti, and G. Roati. *Exploring the ferromagnetic behaviour of a repulsive Fermi gas through spin dynamics*. Nature Physics **13**, 704 (2017). (Cited on page **129**)

[229] H. H. Jen and D.-W. Wang. *Extracting dynamical Green's function of ultracold quantum gases via electromagnetically induced transparency*. Journal of the Optical Society of America B **31**, 2931 (2014). (Cited on page **129**)

[230] A. M. Kaufman, M. E. Tai, A. Lukin, M. Rispoli, R. Schittko, P. M. Preiss, and M. Greiner. *Quantum thermalization through entanglement in an isolated many-body system*. Science **353**, 794 (2016). (Cited on page **129**)

[231] M. Aidelsburger, M. Atala, S. Nascimbène, S. Trotzky, Y.-A. Chen, and I. Bloch. *Experimental realization of strong effective magnetic fields in an optical lattice*. Physical Review Letters **107**, 255301 (2011). (Cited on page **129**)

[232] M. E. Tai, A. Lukin, M. Rispoli, R. Schittko, T. Menke, D. Borgnia, P. M. Preiss, F. Grusdt, A. M. Kaufman, and M. Greiner. *Microscopy of the interacting Harper-Hofstadter model in the few-body limit*. Nature Publishing Group **546**, 519 (2016). (Cited on page **129**)

[233] R. Yamamoto, J. Kobayashi, T. Kuno, K. Kato, and Y. Takahashi. *An ytterbium quantum gas microscope with narrow-line laser cooling*. New Journal of Physics **18**, 023016 (2016). (Cited on page **129**)

[234] A. E. Mattsson, S. Eggert, and H. Johannesson. *Properties of a Luttinger liquid with boundaries at finite temperature and size*. Physical Review B **56**, 15615 (1997). (Cited on page **134**)

[235] N. Goldenfeld. *Lectures on phase transitions and the renormalization group*. Frontiers in physics. Addison-Wesley, Advanced Book Program (1992). (Cited on page **136**)

[236] A. I. Larkin and J. Sak. *Boundary conditions for renormalization-group equations in one-dimensional Fermi gas*. Physical Review Letters **39**, 1025 (1977). (Cited on page **137**)

[237] A. Luther and V. J. Emery. *Backward scattering in the one-dimensional electron gas*. Physical Review Letters **33**, 589 (1974). (Cited on page **137**)

[238] H. Bethe. *Zur Theorie der Metalle*. Zeitschrift für Physik **71**, 205 (1931). (Cited on page **137**)

[239] E. H. Lieb and F. Y. Wu. *Absence of Mott transition in an exact solution of the short-range, one-band model in one dimension*. Physical Review Letters **20**, 1445 (1968). (Cited on page **137**)

[240] T. Giamarchi and B. S. Shastry. *Persistent currents in a one-dimensional ring for a disordered Hubbard model*. Physical Review B **51**, 10915 (1995). (Cited on page **137**)

[241] S. Sachdev. *Quantum phase transitions*. Cambridge University Press (2011). (Cited on page **140**)

[242] V. L. Berezinskii. *Destruction of long-range order in one-dimensional and two-dimensional systems having a continous symmetry group I. classical systems*. Soviet Physics JETP **32**, 493 (1971). (Cited on page **140**)

[243] M. Kosterlitz and D. J. Thouless. *Ordering, metastability and phase transitions in two-dimensional systems*. Journal of Physics C: Solid State Physics **6**, 1181 (1973). (Cited on page **140**)

[244] H. P. Büchler. *Microscopic derivation of Hubbard parameters for cold atomic gases*. Physical Review Letters **104**, 090402 (2010). (Cited on page **141**)

Acknowledgments

After five years of PhD and six years at the MPQ, the number of people that deserve my gratitude are almost too many to be listed. In no particular order, I like to thank them for what they have done for me and for the time spent together. None of the results would have been possible without them.

First and foremost, I like to thank my supervisor, Immanuel Bloch, for giving me the opportunity to work in his group and for all the support to build the experiment. He is a truly inspiring physicists, who realized an encouraging, creative atmosphere in his group. He always granted me the freedom to try out new ideas, when I needed it. Thank you, also, for the generous support at many conferences and schools.

Equally, my thank goes to our group leader, Christian Gross, who taught me everything I know about setting up a new experiment and writing successful publications. Without his hands-on approach to solve all the every-day problems, the experiment would have never been completed.

My fellow PhD student, Ahmed Omran, for all he has done to make this experiment come to live. He guided me at my first steps in the lab and it has been a great pleasure to work with him over all the years. Especially, I like to thank him for his technical expertise and all the lively discussions we had, that made me think very hard about the physics we are dealing with.

I also like to thank the other PhD student, Martin Boll, that I shared the lab with for five years. We had a lot of great time together in and outside the lab. In particular, I am very thankful to him for giving me a place to finish this thesis.

I am very grateful to our PostDoc, Guillaume Salomon. Much of what is written in this thesis originated from the stimulating discussions we had at any time of the day.

I thank all the diploma, master, bachelor and other students who worked in the lithium lab on many valuable projects over all these years, especially Thomas Gantner, Michael Lohse, Thomas Reimann, Konrad Viebahn, Leo Stenzel, Alex Keesling, Daniela Köck, Katharina Kleinlein and Michael Höse.

And I wish the next generation of lithium students the best of luck with our experiment. I am convinced that Joannis Koepsel and Jayadev Vijayan are going to successfully study a lot of exciting physics.

I like to thank all the members from the Bloch group for the time spent together, for the helpful hands, for borrowed equipment, for late night dinners, useful discussions and all the fun we had together. Especially, I like to thank Johannes Zeiher, Peter Schauß, Sebastian Hild, Michael Lohse, Nico Buchheim, Zhenkai Lu, Christoph Gohle, Sebastian Blatt, Ulrich Schneider and Simon Fölling.

I am also deeply thankful to Eugene Demler for his ability to explain complicated physics in a way that an experimentalist can understand, for his generous support during my stay in Harvard and for the recommendation letters he supplied, when I needed them. A special thanks goes to Fabian Grusdt for his contribution to our work and for all his exciting ideas and the helpful discussions about the future of the experiment.

I like to thank Lode Pollet very much for agreeing to serve as the Zweitkorrektor for this thesis and I thank him and Jacopo Nespolo for our successful collaborations and for their useful calculations.

My thanks goes to Markus Greiner, Daniel Greif and Christoph Weitenberg for many interesting discussions on fluorescence imaging and current and future experiments with quantum gas microscopes.

I thank Carsten Förster, Olivia Mödl, and Bodo Hecker for their great help with many electronic projects and Anton Mayer for his invaluable assistance to all our mechanical constructions. Without them the experiment would have never run.

Also Kristina Schuldt, Marianne Kargl, Ildiko Kecskesi and Frauke Logermann deserve thanks for all the administrative help. I know it is not always easy to look after a group of physicist. I also thank the MPQ administration for all organisational matters.

I also like to thank the people who taught me everything I know about physics, especially Wilhelm Zwerger, Stephan Dürr, Martin Brandt, Christian Pfleiderer, Brian DeMarco, Nigel Goldenfeld, Eduardo Fradkin and David Ceperly.

A special thanks goes to Ahmed Omran, Michael Lohse, Joannis Koepsel, Jayadev Vijayan, Guillaume Salomon, Bernhard Frank, Johannes Lang and Christian Gross for proofreading parts of this thesis and for their valuable feedback.

Of course, I am very grateful to my family and specially to my parents for their continuous support. I know I can always rely on them.

Finally, I like to thank Ursula for the years spent together. You have been the joy of my life!